



Title	Fabrication and Characterization of New Nanocomposite Materials Based on Transition Metal Cluster
Author(s)	NGUYEN, Thi Kim Ngan
Citation	北海道大学. 博士(総合化学) 甲第13227号
Issue Date	2018-03-22
DOI	10.14943/doctoral.k13227
Doc URL	http://hdl.handle.net/2115/69949
Type	theses (doctoral)
File Information	Nguyen_Thi_Kim_Ngan.pdf



[Instructions for use](#)

Doctoral Thesis

**FABRICATION AND CHARACTERIZATION OF NEW
NANOCOMPOSITE MATERIALS BASED ON TRANSITION
METAL CLUSTER**

Thi Kim Ngan NGUYEN

March, 2018

**Materials Chemistry and Engineering Course
Graduate School of Chemical Sciences and Engineering
Hokkaido University**

Abstract

Chapter 1

Nowadays, the functional material-coated glasses with specific characteristics including self-cleaning, UV-NIR light blocking or electrochromic property have widely been studied in smart window applications. Most studies have reported the optimization and possibility of the fabrication processes in order to enhance the intrinsic properties and reduce the production cost. The octahedral metal clusters based on molybdenum and tantalum transitional metals exhibit interesting photochemical, oxidation-reduction and prominent optical properties that are potentially applicable in energy, photocatalyst or biotechnology fields. The application fields of the metal cluster would be extended by applying some coating techniques, preparing the nanocomposites based on the inorganic and organic support, or synthesizing the hybrid with directly polymerization. In this thesis, the main expectation is to immobilize the metal cluster on supporting material as glass, silica or polymer, however, the last materials have to retain the specific characteristics of metal cluster. For these purposes, the essential techniques to fabricate the materials based on metal cluster are colloidal solution chemistry, electrophoretic deposition (EPD) and vacuum impregnation process (VIP).

The electrophoretic deposition (EPD) process, a fairly rapid and low cost two-step process well-known for ceramic shaping, conductive surface coating and easily scalable to industrial level thin, have been applied to prepare an octahedral metal cluster homogeneous film on the ITO-coated glass. The impressive advantage of this technique is to bring out the pure octahedral metal cluster film without counter cation that changes a cluster framework, following the modification of the optical property. In addition, the EPD process is useful to consume a small cluster concentration on a large area of the glass that reduces producing cost. The optimizations of the suspension and EPD parameters were investigated to obtain the octahedral cluster thin films with the best quality. A lots of techniques were used to characterize the colloidal suspensions (zeta potential, conductivity and particle size), the homogeneity, surface morphology and thickness (color 3D laser microscopy, FE-SEM, STEM), chemical property or crystal pattern (X-Ray diffraction, Fourier Transfer Infrared, X-ray fluorescence, X-ray Photoelectron Spectroscopy) and optical property (UV-Vis-NIR spectroscopy, high performance fluorescence spectroscopy, micro photoluminescence (PL) system, PL quantum yield spectrometer, CL measurement).

Chapter 2

The cluster films based on face capped $\text{Mo}_6\text{L}^i_8\text{L}^a_6$ units with i = inner ligands and a = apical ligands ($\text{L}^i = \text{L}^a = \text{Cl}, \text{Br}, \text{I}$) were fabricated by the EPD process. Photoluminescence property characterized by multicomponent emission in the deep-red/ near infra-red (NIR) region with a continuous excitation window from UV to visible as well as photo catalytic activity of the molybdenum octahedral cluster is particular interest for the application in biotechnologies, lighting and displays. The stabilization of the cluster solutions during EPD is very important to obtain high quality film. Several kinds of liquid, distilled water, ethanol, 1-propanol, acetone, methyl-ethyl ketone (MEK) and acetyl acetone, were

selected as dispersing media of the Mo₆ cluster compound. Homogeneous, transparent [Mo₆Brⁱ₈Br^a₆] cluster films with prominent luminescent property were obtained on conductive ITO-coated glass by the EPD process when dissolving the Cs₂Mo₆Brⁱ₈Br^a₆ precursor in MEK. The UV-Vis absorption spectra exhibited a high transparency in the visible light range (500 – 850 nm) accompanied by many peaks in the wavelength range from 400 nm to 2000 nm due to light interference. For the first time, the mechanism of deposition process is proposed, based on results obtained by the combination of X-ray analysis, electron microscopy and optical characterization. The Mo₆ film exhibiting Br rich layer, quickly deposited on ITO-coated glass at the first stage of the EPD process, followed by the formation of a multilayered structure composed of two types of clusters compounds [Mo₆Brⁱ₈Br^a₄(H₂O)₂] and [H₃O]₂[Mo₆Brⁱ₈Br^a₄(OH)₂]. Thanks to a nanometric size and the synergy of specific optical properties of metal atom clusters and substrate, the films with high transparency in the visible range and strong absorption in UV and IR range are obtainable.

Chapter 3

Due to the limitation of the stabilization of the octahedral cluster film in the air, organic supporting materials (polymer) were used to simultaneously fabricate or coat on the Mo₆ cluster film. The results conclude that poly dimethyl siloxane as an excellent top coating and poly methyl methacrylate, cellulose acetate phthalate (CAP) or polyvinylpyrrolidone (PVP) as a prominent dispersing medium significantly improved the stabilization of the octahedral cluster film during or after the EPD process.

Chapter 4

The potential of luminescent silica nanoparticle has been widely studied in the field of biological science as cancer diagnosis, optical imaging and biosensor. In this study, in order to promote the luminescent or UV absorption ability of the octahedral molybdenum clusters in the luminescent bioapplication, the Cs₂Mo₆Clⁱ₈Cl^a₆ and Cs₂Mo₆Iⁱ₈(OCOC₂F₅)^a₆, exhibiting excellent luminescent characteristic, were incorporated with hollow silica nanoparticles by a vacuum impregnation process. The prepared luminescent silica nanocomposite film has been prepared by the EPD process on ITO-coated glass or coated on sodium glass by dip coating with the support of the top coat solution.

Chapter 5

The octahedral Ta₆Br₁₄·8H₂O or [Ta₆Brⁱ₁₂(H₂O)^a₆]Br₂ cluster, one of the popular clusters of [M₆Lⁱ₁₂L^a₆]ⁿ⁻/_{n+} octahedron family (M = Nb, Ta; Lⁱ= inner halogen or chalcogen, L^a= apical halogen or functional group), exhibits interesting oxido-reduction and optical properties in the solution, which were investigated to fabricate the Ta₆ cluster film by EPD process for the expectation to block the UV and NIR light on low-emissivity window. The application of the {Ta₆Brⁱ₁₂}²⁺ core cluster species has been potentially studied in biotechnologies, optical devices, photovoltaic cells and UV blocking devices. The interesting characteristic has been recognized that the green {Ta₆Brⁱ₁₂}²⁺ core (adsorbing ultra-visible range) easily transfers to brown {Ta₆Brⁱ₁₂}^{3+/4+} core (absorbing near-infrared range) when dissolved in different solvents. Due to the interesting characterization of the green {Ta₆Brⁱ₁₂}²⁺ core species, the selection of the dispersing medium and optimization of the concentration of the Ta₆Br₁₄·8H₂O cluster in a solvent are the main purpose of the study in order to obtain the green homogeneous Ta₆ film. In

addition, the EPD parameters such as applied voltage and deposition time were investigated to fabricate the $\{\text{Ta}_6\text{Br}_{12}\}^{2+}$ green film that was confirmed through the FE-SEM image and optical characterization. By the EPD process, the green film based on the $\{\text{Ta}_6\text{Br}_{12}\}^{2+}$ core species was successfully fabricated, however, the stability of the oxidation state and transmittance of the Ta_6 octahedral cluster film were limited. For this reason, poly vinyl pyrrolidone (PVP) was used to improve the dispersion of the $\{\text{Ta}_6\text{Br}_{12}\}^{2+}$ green octahedral cluster in the EPD suspension for reducing the crystal size and preventing the interaction of the green $\{\text{Ta}_6\text{Br}_{12}\}^{2+}$ octahedral cluster in the deposition film with oxygen in air. As the result, thin and high transmittance Ta_6 cluster@PVP film with emeral-green color exhibiting the strong UV absorption under 400 nm was successfully fabricated.

Acknowledgments

I have been finished my thesis for three years with a lots of the support from nice supervisors, friends, colleagues, sisters, brothers and my big family. I would like to say thank to all of my dear companies whom give me the best motivation.

First of all, I am strongly thankful to my supervisor, Prof. Dr. Tetsuo UCHIKOSHI for nice support during 3 years with the best condition to study, work and live in Tsukuba city. He gave me a lots of motivation to finish the outstanding topics which are big challenges to my major. Importantly, his assistance, guidance, advice, encouragement, patience and sincere cooperation throughout this research is very helpful to extremely finish my thesis.

I am thankful to the strong supports of Prof. Dr. Kiyoharu TADANAGA, Prof. Dr. Toshihiro SHIMADA, and Prof. Dr. Yukio HINATSU who gave me a lots of nice reviewing, helpful advice and valuable suggestion to finish the thesis perfectly.

Most of the experiments in this thesis were performed at the National Institute for Materials Science (NIMS) under the strong support from the collaboration between NIMS (Japan), CNRS (France), Foundation Langlois, RENNES 1 University (France) and Saint-Gobain Company (France). Therefore, I honestly thank to the office and laboratory of Fine Particle Engineering group of National Institute for Materials Science (NIMS) gave me permission to carry out the experiments with strongly training a lots of the high technical equipment and supporting the professionally working place. I wish to thank Prof. Dr. Stéphane CORDIER, Dr. Fabien GRASSET, Dr. David LECHEVALIER, Prof. Dr. Naoki OHASHI and Dr. Mari KONO of Saint-Gobain KK (Tokyo, Japan) involved in LINK and related activities that cover fully financial support to finish my thesis. I thank to Ms. Yoko WATANABE for the full help during living in Tsukuba. Her help made my life smooth and convenient. I also thank to my kind colleagues, Dr. Yoshio MATSUI, Dr. Chika MATSUNAGA, Dr. Chenning ZHANG, Dr. Wanghui CHEN, Dr. Benjamin DIERRE, Dr. Norio SAITO and Dr. Hirohito OHATA for training some measurements and giving me a lots of kind advices to perform the experiments smoothly.

I gratefully thank to Prof. Dr. Stéphane CORDIER for giving me a change to visit the laboratory in University of Rennes 1 for three months in order to study the synthesis method of the metal clusters. I give a lots of thank to Dr. Marian AMELA-CORTES, Dr. Yann MOLARD, Dr. Adèle RENAUD, Mr. Maxence WILMET, and Ms. Noee DUMAIT whom help me so much during my visiting at the University of Rennes 1.

I thank to relating divisions of the Hokkaido University with the strong financial support for the travel and completion of the lecture smoothly.

The last, I would like to thank my family in Viet Nam and my friends in Japan. They encourage and support me very much when I have trouble and follow my dreams.

For all of the big success, I wish to express my heartfelt respects and gratitude to all of you!

Nguyễn Thị Kim Ngân

Contents

Chapter 1	2
Literature review	2
1.1. Application of nano-architected composite materials	2
1.2. A new class of nanomaterials based on metal atom clusters	3
1.2.1. Metal atom cluster	3
1.2.2. Octahedral metal cluster	4
1.2.3. Three band model – the reason of redox, spectroscopic, and photophysical characteristics of the octahedral cluster	8
1.3. Methodology - electrophoretic deposition process	13
1.4. Objective of the thesis	15
Chapter 2	26
Electrophoretic deposition of Octahedral Molybdenum Metal Clusters	26
2.1. Fabrication of the metal cluster and methodology	26
2.1.1. Fabrication of the hexamolybdenum clusters	26
2.1.2. The EPD system	27
2.2. Characterization techniques of the EPD suspension and the Mo ₆ film	28
2.2.1. Suspension	28
2.2.2. Morphology of thin film	28
2.2.3. Chemical characterization	28
2.2.4. Optical characterization	29
2.3. The thin, homogeneous and transparent Mo ₆ film by EPD process	29
2.3.1. Preparation of the Mo ₆ cluster solution and fabrication of the thin films by electrophoretic deposition (EPD)	29
2.3.2. Characterization of the suspension, the Mo ₆ film and optical properties	30
2.3.3. Conclusions	41
2.4. Formation mechanism of transparent Mo ₆ metal atom cluster film prepared by electrophoretic Deposition	41
2.4.1. Preparation suspensions and the Mo ₆ cluster films by EPD process	41
2.4.2. Formation mechanism of transparent Mo ₆ metal atom cluster film	42

2.4.3. Conclusions	50
References	50
Chapter 3	54
Stabilization of the hexamolybdenum cluster by incorporation with polymer.....	54
3.1. Stabilization of the Mo ₆ cluster film by top coating with poly dimethyl siloxane (PDMS).....	54
3.1.1. Preparation of the suspension and fabrication of film by EPD	54
3.1.2. Optimization of the PDMS coating condition on the Mo ₆ film.....	55
3.1.3. Characterization of the PDMS-coated Mo ₆ cluster film.....	57
3.1.4. Coating mechanism of PDMS on the Mo ₆ cluster film	60
3.1.5. Optical property of the PDMS-coated Mo ₆ cluster film.....	61
3.1.6. Conclusions	62
3.2. Stabilization of the Mo ₆ cluster film by directly fabrication with ketone polymer by EPD process.	63
3.2.1. Chemicals and preparation the Mo ₆ film by EPD process	64
3.2.2. EPD of Cs ₂ Mo ₆ I ₈ (OCOC ₂ F ₅) ₆ cluster precursor.....	65
3.2.3. EPD of Mo ₆ @polymer nanocomposite	67
3.2.4. Conclusions	76
References	77
Chapter 4	81
Fabrication and characterization of the Mo ₆ -incorporated hollow silica nanoparticles	81
4.1. Fabrication and characterization of the Mo ₆ @HSNs nanocomposite	82
4.1.1. Characteristic of materials.....	82
4.1.2. Preparation of suspensions and vacuum impregnation process.....	83
4.2. Characteristic of the Mo ₆ -incorporated silica nanoparticle.....	84
4.2.1. Morphology and chemical property	84
4.2.2. The thermal stability of the Mo ₆ -incorporated silica nanoparticle.....	86
4.2.3. Optical property stabilization of the Mo ₆ -incorporated silica nanoparticle	89
4.2.4. Conclusions	94
4.3. The Mo ₆ @HSNs film by EPD process.....	95
4.3.1. Preparation of suspension and setup of EPD.....	95
4.3.2. Optimization of the Mo ₆ @HSNs suspensions for EPD process.....	96

4.3.3. Characterization of the Mo ₆ @HSNs film by the EPD	99
4.4. Fabrication and characterization the Mo ₆ @HSNs film by dip coating	101
4.4.1. Mechanical properties	101
4.4.2. Optical property.....	103
4.5. Conclusions	104
Reference.....	105
Chapter 5	109
Fabrication of Octahedral Tantalum Cluster Film by Electrophoretic Deposition.....	109
5.1. Fabrication of the {Ta ₆ Br ⁱ ₁₂ (H ₂ O) ^a ₆ }Br ₂ cluster film by EPD process.....	109
5.1.1. Synthesis of the {Ta ₆ Br ⁱ ₁₂ (H ₂ O) ^a ₆ }Br ₂ cluster precursor.....	109
5.1.2. Preparation of the EPD suspension	110
5.1.3. The fabrication of the green Ta ₆ film by the EPD process	112
5.1.4. Characterization.....	113
5.2. Characterization of the {Ta ₆ Br ⁱ ₁₂ (H ₂ O) ^a ₆ } ⁿ⁺ cluster film.....	113
5.2.1. Optimization of the {Ta ₆ Br ⁱ ₁₂ (H ₂ O) ^a ₆ }Br ₂ cluster suspension.....	113
5.2.2. Optimization of the ratio of the {Ta ₆ Br ⁱ ₁₂ (H ₂ O) ^a ₆ }Br ₂ cluster and water in EPD suspension ..	116
5.2.3. Optimization of the EPD process to fabricate {Ta ₆ Br ⁱ ₁₂ (H ₂ O) ^a ₆ } ²⁺ cluster film.....	119
5.3. Fabrication of the {Ta ₆ Br ⁱ ₁₂ (H ₂ O) ^a ₆ } ²⁺ @PVP film by EPD process	121
5.4. Conclusions.....	126
References	127
Chapter 6	130
Conclusions and outlooks.....	130
6.1. Conclusions	130
6.2. Outlooks	132
Achievements.....	133

Chapter 1

Literature review

Chapter 1

Literature review

1.1. Application of nano-architected composite materials

The development of energy management systems is always the key interest on the world because the depletion of raw material sources from fossil fuel, the use of the efficient energy and negative impacts to the living environment have affected to the life quality of human. The consequences were significantly caused from the use of energy relating to the local pollution and global warming by CO₂ emission that proceeds the focus of the researchers to figure out the energy storage technologies for sustainable power networks ^[1, 2]. Many solutions have been explored to enhance the energy efficiency in buildings or constructions, to establish effective process in industrial production with less energy and raw material use and to improve recyclability. From this background, new multi-functional materials for saving and recycling energy have been aggressively studied on ^[3]. The average commercial building wastes about 40 % of the total energy it consumes, involving about 30 % CO₂ emission ^[4, 5, 6], which is one of the crucial cause of the global warming. Understanding the demand of saving energy for buildings, a number of the studies have been carried out to discover new multi-functional materials for comfort residence with the improvement of air quality, thermal insulation and lighting quality.

Currently, the innovation of the electrochromic smart window, which enables to vary the transmittance of visible light and solar energy by the application of an electrical voltage ^[7], has brought about the effective use of the energy and improved the amenity in office environment ^[8-14]. In addition, the heating and cooling systems of the office buildings, one of the significant energy-consuming sources, have been improved to raise their energy efficiency via the introduction of smart building energy management systems ^[15]. Beside the improvement of the insulation management systems, the task to search for new materials suitable for blocking the UV radiation and a portion of the NIR radiation and/or to convert a portion of the sunlight to thermal energy or electric power has been pursued for a long time ^[8, 16].

The excellently functional materials such as thermo-insulation materials ^[17] and reflection materials for residential environment, electrochromic or thermo-chromic materials ^[18], photovoltaic material ^[9], water flow-based materials for storing the building energy ^[12] have been studied. At the beginning, nanomaterials based on metal oxides have attracted huge attention as the ingredients in order to fabricate electrochromic devices for smart windows, sensors for air quality, and photo-catalysts for air cleaning ^[19]. Currently, nano-architected composite materials, a new class of the nanostructures entities compose of various dissimilar nanoscale building blocks including clusters, particles, wires and platelets (**Fig.1.1**) ^[20], have been fabricated to aim at realizing multifunctional systems with enhanced mechanical, physicochemical and structure properties. From a single molecule, a network of the molecules could be built via many different routes to form the flexible structures and bring out the excellent characteristics.

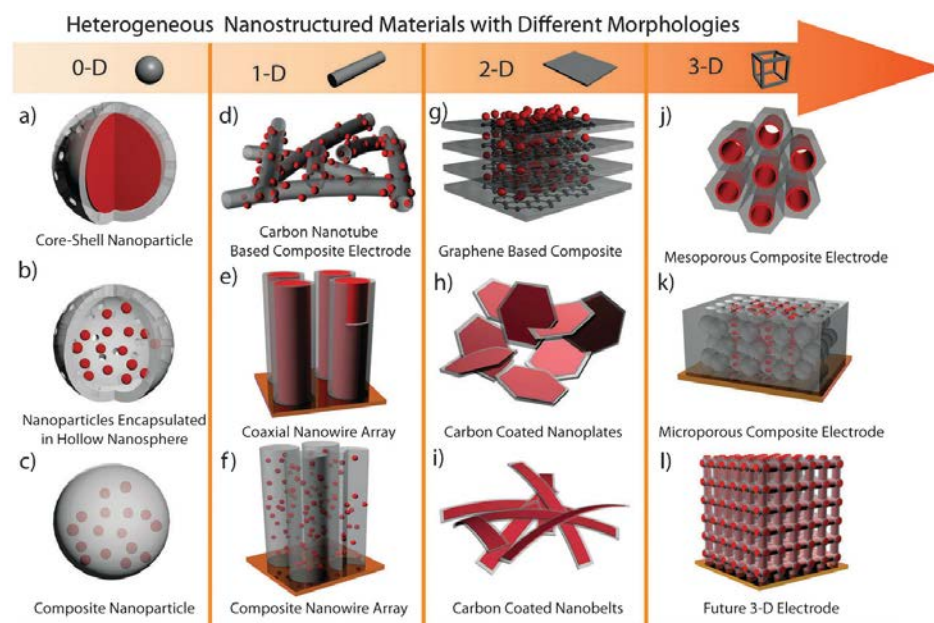


Fig. 1.1. Different heterogeneous nanostructured materials based on structural complexity ^[20].

In this thesis, the fabrications and characterizations of the composite nano-architecture materials involving metal atom cluster and oxides to form the multi-functional nanocomposites have been focused. The cluster molecules containing three or more metal atoms which are connected by direct metal-metal bond linking with non-metal atoms as inner ligands (face-capping position) and apical ligands (terminal position), were firstly named as “metal atom clusters” by F.A. Cotton (1964)^[21]. They exhibit interesting photochemical and redox properties that are allocable in variety of fields, such as energy, photo catalyst or biotechnology. Transition octahedral metal clusters have been synthesized, processed and characterized based on solid chemistry, and solution chemistry and then incorporating with other support materials by the solution and electrochemical methods.

1.2. A new class of nanomaterials based on metal atom clusters

1.2.1. Metal atom cluster

The definition of metal atom cluster which has been known as “a finite group of metal atoms that are held together mainly, or at least to a significant extent, by bonds directly between the metal atoms, even though some non-metal atoms may also be intimately associated with the cluster”, was firstly given by F. A. Cotton (1964) ^[21]. Some typical cluster units are shown **Figure 1.2**. F. A. Cotton suggested that the interaction of the d orbitals of all six metal centers leads to a large number of highly delocalized bonding and antibonding MO's. As the result, the photochemical properties of the metal atom clusters originate from the electron transitions in essential d orbitals. The discovery of the $A_xM_6Q_8$ (Q = chalcogen, A = cation) cheverel phase by a group at Rennes University in 1971 was the starting point for a new research in chemistry, dealing with M_6 (M = Nb, Ta, Mo, W and Re) halides and chalcohalide cluster prepared via solid state routes at high temperature (1000°C – 1200°C)^[22]. Basically, the metallic

core is covalently bonded to faced-capping or edge-bridged ligands (L^i , where i stands for inner) and stabilized by terminal ligands (L^a , where a stands for apical), yielding a so-called cluster unit, as presented in **Figure 1.2**. These species, which can be discrete or condensed by either ligands or metals, constitute the basic building blocks of a wide range of inorganic, hybrid organic-inorganic, and supported materials and nanomaterials that can be prepared by either solid-state or solution chemistry^[23]. Metallic core of metal atom cluster could be made of alkali metal, alkaline-earth metal, group III (a) and IV (a) metal, and transition metal ^[24]. Based on the relative radius of the atomic (n+1) s and n s orbitals, the excitation energy data of transition-metal atoms was calculated from experimental value by numerical Hatree-Fock methods ^[25]. M. D. Morse et al. suggested that the 3d and 4d orbitals of the transition metal molecules considerably contract as the nuclear charge increase through the chemical bonding between them ^[25]. Physical properties of the transition metal atom cluster, such as, ionization potential, electron affinity, magnetic moment, electric polarizability, etc., originating from the atomic structure, have been understood by solid-state quantum chemistry ^[24]. The quantum chemistry including the qualitative explanation of the electronic structure has been used to reveal the properties of relatively stable molecules with well-defined bonds, and predict the behaviors of unusual small molecular systems. The relation between electronic structure, atomic structure, and magnetism of transition-element clusters based on Ni, Fe, Nb, Ti, Vd and Cr metals have been reviewed by J. A. Alonso ^[26]. Two types of the oscillation, which amplitude decays for increasing N, related to the filling of these delocalized electronic shells and linking to purely geometrical effects.

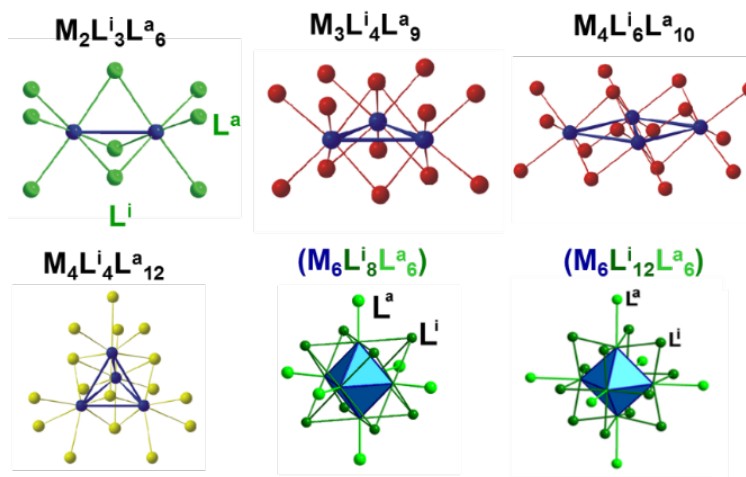


Figure 1.2. Scheme illustrations of clusters units with linear, triangular, tetrahedral and octahedral. The metallic core is presented in blue and non-metal ligands in green, red and yellow.

1.2.2. Octahedral metal cluster

Octahedral cluster complexes of transition metals which are associated with halogen or chalcogen inner ligands to form edge-bridged $\{M_6(\mu_2-X)_{12}\}$ or face-capped $\{M_6(\mu_3-X)_8\}$ cluster cores have been the focus of the studies for a long time (**Fig. 1.3**) ^[27, 28]. The $[M_6(\mu_3-X)_8L^a_6]$ ($M = Mo, W, Re; L = \text{halogen}$,

chalcogen or functional groups; L^i = face-capping inner ligand; L^a = terminal apical ligand) face-capped cluster unit is more chemically stable than the $[M_6(\mu_2-X)_{12}L^a_6]$ ($M = Nb, Ta$) edge-bridged one. Such face-capped $[M_6(\mu_3-X)_8L^a_6]$ clusters ($M = Re, L^i = S, L^a = Se$ or $Te; M = Mo$ or $W, L^i = L^a = Cl, Br, I$) exhibit photoluminescence properties characterized by a multicomponent emission from the red to infrared region with a continuous excitation window from ultraviolet (UV) to visible as well as photocatalytic activity ^[29, 30]. Transition-metal atom clusters basing on the octahedron, molybdenum halides ($Mo_6X_8L^a_6; L^i = \text{halides}; L^a = OH, H_2O$ or halides, cyanide, phosphine, isothiocyanate, etc.) ^[31, 32] and rhenium chalcogen ($Re_6Q^i_8L^a_6; Q = S, Se, Te; L^a = \text{halides, cyanide, phosphine, isothiocyanate, etc.}$) ^[33], have attracted the focus due to prominent characteristics as photochemical and photophysical properties ^[34, 35], luminescent property ^[36], redox transformation ^[37] and possibility to incorporate with functionalized copolymer or inorganic support materials. The advances in the engineering of molecular assemblies and nanomaterials based on octahedral Re_6 metal atom clusters have been reported ^[38]. The unique intrinsic structural and physicochemical properties (photoluminescence, redox and generation of singlet oxygen) ^[39] have been generated at the nanometric scale and potentially functionalized in hybrid organic–inorganic materials and supramolecular frameworks ^[38]. Therefore, the interunit connectivity of the octahedral Mo_6 and Re_6 chalcogenides ($M_6L_{14}; L$: ligand) was reduced to 2D, 1D and finally 0D compounds in order to create the nano-crystals that give access to a large variety of hybrid organic/inorganic cluster materials ^[22, 40]. The promises of the Mo_6 and Re_6 octahedral cluster in the biotechnology have also been studied by the investigation of the cell uptake and toxicity in the corporation with the organic-inorganic hybrid materials ^[41-43]. The intrinsic properties of the clusters and thus their physical properties could be changed by the nature and number of metal atoms accompanying with the inner or apical ligands and affected by the number of valence electrons on a cluster unit ^[38]. For instance, the progressively shift from a dielectric characteristic in cluster-based halides to semiconducting and superconducting characteristics in the cluster-based chalcogenides could be decided by the electron transport properties via metal-ligand bonds ^[44].

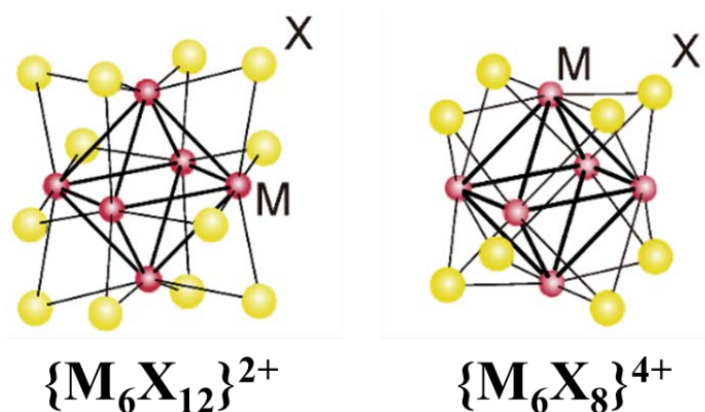


Figure 1.3. Two basic structures of halide clusters. Halogen π -donor ligands coordinate in two modes as inner ligands: 12 halogen ligands in a μ_2 -fashion in $\{M_6X_{12}\}^{2+}$, and eight halogen ligands in a μ_3 -fashion in $\{M_6X_8\}^{4+}$ ^[28].

Octahedral Molybdenum cluster $[\text{Mo}_6(\mu_3\text{-X})_8\text{L}^a_6]$

New families of ternary molybdenum (II) chlorides with octahedral Mo_6 clusters synthesized by solid chemistry at high temperature were also performed by a group at University of Rennes-1 in 1986 [44, 45]. The $[\text{Mo}_6(\mu_3\text{-X})_8\text{L}^a_6]$ cluster (X = halogen) is the most chemically-stable cluster unit that drastically limits the reduction the luminescent properties by changing the valence electron concentration ($\text{VEC}=24$) [46-49]. The $[\text{Mo}_6\text{X}^i_8\text{X}^a_6]^{2-}$ cluster units, based on the family $\{\text{Mo}_6\text{X}^i_8\}^{4+}$ core ($\text{X}^i=\text{Br}, \text{Cl}, \text{I}$ at face-capping inner position) capped by 6 halogens or functional groups at the terminal apical position ($\text{X}^a=\text{Br}, \text{Cl}, \text{I}, \text{OH}, \text{H}_2\text{O}, \text{CF}_3\text{COOH}$, etc.) [50], have recently been studied in the applications of pH-sensor [51], singlet oxygen sensitization [52], photocatalytic reaction [53, 54], solar cell [30, 55, 56] or biotechnology [52, 57-62] (**Fig. 1.4**). In order to extend the ability in preparing Mo_6 cluster-based hybrid materials and enhance the photonic and optoelectronic properties, the basic $\text{Cs}_2\text{Mo}_6\text{X}^i_8\text{X}^a_6$ metal cluster compound has been synthesized by changing cationic metathesis $((n\text{-C}_4\text{H}_9)_4\text{N}^{[13]}$ and BEDO-TTF [63]) via solution chemistry or replacing the apical ligands with functional groups (PhCN [63], N_3 [64], $\text{SC}_6\text{F}_4\text{H}$ [65] or $\text{C}_n\text{F}_{2n+1}\text{COO}$ [66]). The molecular nature of the metal cluster compounds proceeds the incorporation with different types of the matrices to prepare nanocomposites. The interest in the preparation of transparent thin films from hybrid nanocomposites based on metal atom clusters has also increased [62, 67]. The $((n\text{-C}_4\text{H}_9)_4\text{N})_2\text{Mo}_6\text{Br}_{14}\text{@ZnO}$ cluster compound [68] or $\text{Cs}_2\text{Mo}_6\text{X}^i_8\text{X}^a_6\text{@SiO}_2$ phosphor nanoparticles have been fabricated by the water-in-oil micro emulsion method or by solution chemistry, respectively [57, 69, 70]. Grafting the Mo_6 clusters on semiconducting surfaces via organic linkers to create the original molecular junctions and diodes has been attempted by S. Cordier et al. [71]. Photoelectric hybrid materials have been created by directly polymerizing methyl methacrylate and urethane monomers with metal clusters [72-74]. The graphene-functionalized metal cluster has been studied in the photocatalysis and energy fields [54, 75]. However, most of the solution chemistry methods have been used to prepare these nanocomposite materials as powders or bulk materials. Consequently, the studies of the fabrication of thin films composed of metal clusters are still limited [70, 74, 75].

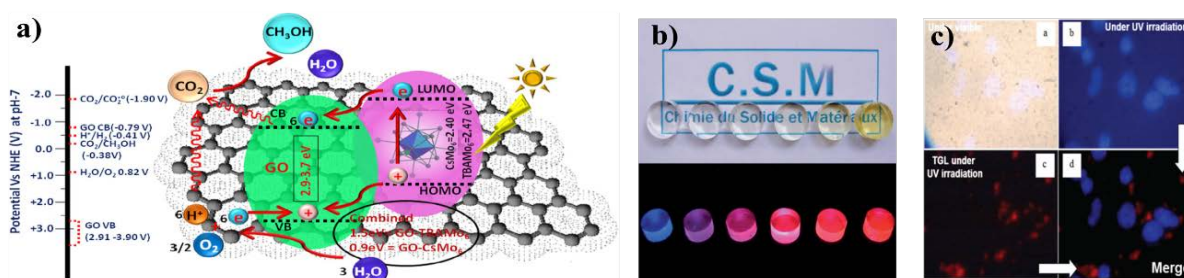


Figure 1.4. a) Plausible mechanism of photoreduction of CO_2 into methanol catalyzed by GO-hexamolybdenum composite [54], b) Photographs of the Mo_6 -PMMA hybrid copolymer pellets under visible (top) and UV light (bottom); $\lambda_{\text{ex}}=365$ nm; cluster concentrations range is from 0 to 0.36 wt % from left to right [72], c) Images of the $\text{Cs}_2\text{Mo}_6\text{I}_8(\text{C}_2\text{F}_5\text{COO})_6\text{@SiO}_2$ nanostructured particles internalized by cancer cells using different modes of the time-gated luminescence microscope, under excitation at 365 nm [76].

In this thesis, the octahedral halide molybdenum clusters with excellent luminescent characteristic are selected to fabricate their nanocomposites supported with organic and inorganic materials that includes: $\text{Cs}_2\text{Mo}_6\text{Br}_{14}$, $((n\text{-C}_4\text{H}_9)_4\text{N})_2\text{Mo}_6\text{Br}_{14}$, $(\text{NH}_4)_2\text{Mo}_6\text{Br}_{14}$, $(\text{NH}_4)_2\text{Mo}_6\text{Br}_8(\text{SCN})_6$, $\text{Cs}_2\text{Mo}_6\text{I}_{14}$, $\text{Cs}_2\text{Mo}_6\text{I}_8(\text{OCOC}_2\text{F}_5)_6$, $\text{TBA}_2\text{Mo}_6\text{Cl}_{14}$, and $\text{Cs}_2\text{Mo}_6\text{Cl}_{14}$ cluster precursors.

Octahedral tantalum cluster ($[\text{Ta}_6(\mu_2\text{-X})^i_{12}\text{L}^a_6]$)

The $[\text{M}_6(\mu_2\text{-X})^i_{12}\text{L}^a_6]$ octahedral cluster derived from the $\{\text{M}_6(\mu_2\text{-X})^i_{12}\}^{n+}$ ($\text{M} = \text{Ta}$ and Nb , $\text{X} = \text{halogen}$, $n = 2, 3, 4$) metallic cluster core has been generally known as strong oxidizing and reducing agents [77-80]. B. Peric et al. and J. Sinzig et al. suggested that the $[\text{M}_6(\mu_2\text{-X})^i_{12}\text{L}^a_6]$ clusters with fifteen electrons per cluster belong to an unusual class of materials that have one unpaired electron delocalized over whole metal-cluster units that can generate interesting magnetic properties [81, 82]. The photolytic property of the $\{\text{Ta}_6\text{L}^i_{12}\}^{2+}$ tantalum cluster in aqueous acidic solution has been reported to understand the photochemistry mechanism during the study on the reversible multi electron photo-redox reaction [83, 84]. Hydrated hexanuclear metal cluster halides $\{(\text{M}_6\text{X}^i_{12})\text{X}^a_2(\text{H}_2\text{O})^a_4\} \cdot n\text{H}_2\text{O}$ ($\text{M} = \text{Nb}, \text{Ta}$; $\text{X} = \text{Cl}, \text{Br}$), usually formulated as $\text{M}_6\text{X}_{14} \cdot 8\text{H}_2\text{O}$, are representatives of a particular class of coordination compounds that are based on $\{\text{M}_6\text{X}^i_{12}\}^{n+}$ cluster units as central cations [85, 86]. A few applications of the $(\text{Ta}_6\text{X}^i_{12})^{n+}$ ($n = 2, 3, 4$) have been reported for the use in bio-macromolecular crystallographic phase determination [87, 88] or the reaction of tantalum hexanuclear halide clusters with cadmium(II) halides, diamagnetic and paramagnetic clusters for catalysts at high temperature [28] and semiconducting properties [89]. Recently, UV and IR blocking electrochromic devices based on the $\{\text{Ta}_6\text{Br}_{12}^i\text{Br}_6^a\}^{4+}$ transparent tantalum cluster for smart window have been developed by the researcher group at the university of Rennes-1 with the positive results [90]. The (poly vinyl pyrrolidone) polymer matrix has been processed to reduce the oxidation from green-colored reduced $\{\text{Ta}_6\text{Br}_{12}\}^{2+}$ species to brown-colored oxidized $\{\text{Ta}_6\text{Br}_{12}\}^{3+/4+}$ species accompanying with the addition of Br_2 leading to the control of their solution color by dip coating (**Fig. 1.5**). The results showed that the tantalum cluster films exhibited high transparency, switchable strong color from emerald-green to brown and modulated light absorption in the red-NIR region [90].

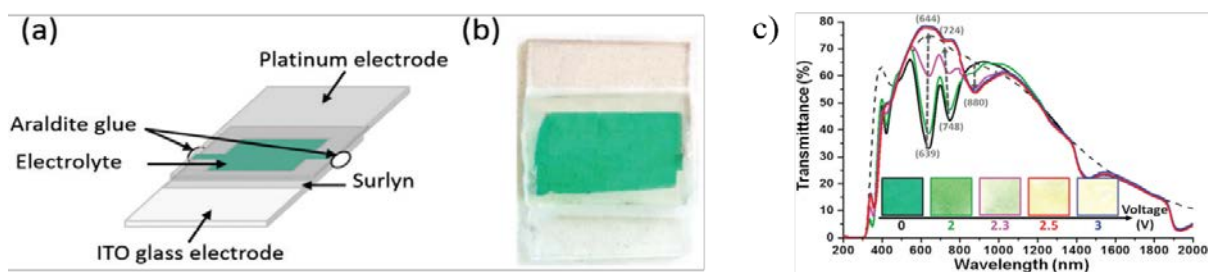


Figure 1.5. a) Scheme of the Ta_6 electrochromic cell architecture, b) photograph of the cell and c) UV-vis-NIR spectra and photographs of the Ta_6 electrochromic cell under voltage applied between ITO-coated glass and Pt electrodes. The dashed line corresponds to the empty cell (without Ta_6 aqueous solution) [90].

In this thesis, the $\{\text{Ta}_6\text{Br}_{12}\}^{2+}$ octahedral cluster has continually studied to figure out the simple way for fabricating the thin, transparent, homogenous and strong UV-NIR adsorbing film, moreover, the improvement of the oxidation stabilization of the green $\{\text{Ta}_6\text{Br}_{12}\}^{2+}$ species in the matrix film was also investigated.

1.2.3. Three band model – the reason of redox, spectroscopic, and photophysical characteristics of the octahedral cluster

In order to understand the mechanism of the electronic transfer in quenching process, the electronic spectroscopy and photophysics of d^4 cluster have been reported by Thomas C. Zietlow et al.⁹¹. The electronic structural analogies between $(d^4)_2 \{\text{M}_2\text{X}_8\}^{4-}$ and $(d^4)_6 [\text{M}_6\text{X}_8\text{X}_6]^{2-}$ ($\text{M} = \text{Mo}, \text{W}; \text{X} = \text{Cl}, \text{Br}, \text{I}$) clusters are resulted:

- Metal-localized δ -type orbitals play an important role in the ground state and the lowest excited states of each complex. All evidence suggests that the splitting between the emissive $\delta\delta^*$ singlet and the $\delta\delta^*$ triplet excited states of $\{\text{M}_2\text{X}_8\}^{4-}$ and related species is greater than 1 eV, whereas the ~ 2 eV emissive excited state of $[\text{M}_6\text{X}_8\text{X}_6]^{2-}$ is a spin triplet. All four d electrons on each metal in the $[\text{M}_6\text{X}_8\text{X}_6]^{2-}$ clusters are involved in metal-metal bonding.
- In these clusters, the HOMO is built by overlapping d_{xy} functions on adjacent metal atoms (**Fig. 1.6**). Because this "cis" overlap is much greater than the face-to-face δ overlap in the quadruple bonded dimers, the energy gap between the lowest triplet excited state and the ground state of an M_6 cluster is expected to be fairly large (~ 2 eV).

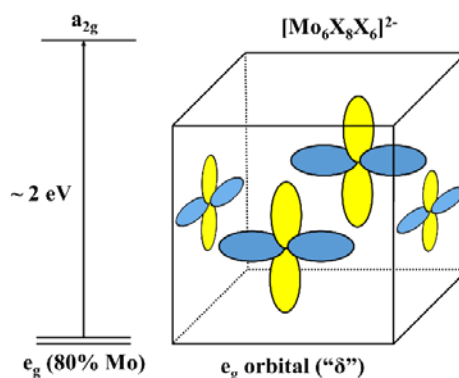


Figure 1.6. HOMO-LUMO splitting for $[\text{M}_6\text{X}_8\text{X}_6]^{2-}$ cluster. The ground state is $(e_g)_4^{91}$.

In the molybdenum series, the intense bands in the near UV are red-shifted upon exchange of chloride ligands for bromides (or bromides for iodides), clearly implying that these bands are due to ligand-to-metal charge transfer (LMCT) transitions. However, the emission spectra of these Mo clusters are insensitive to the halide ligand, suggesting that the emissive excited state is metal-localized, which is expected by analogy to the dimer photophysics.

In 1986, the theory of a pattern for the electric structure of $\text{M}_6\text{L}_8\text{L}_6$ cluster compound was firstly revealed by D. Certain et al based on tight-binding band-structure calculations and extended Hückel

method ⁴⁵. In chevrel phases, the fermi-level area of has been studied in term of band structure and density of electronic states: chalcogen-chalcogen repulsions are regularly minimized to create the ligand crystalline field containing a $\text{Mo}_6\text{L}_8\text{L}_6$ octahedron and perform the band structure frame.

It can be seen that in the band structure of PbMo_6S_8 cluster (**Fig. 1.7 left**), from bottom to top, a single narrow 3p S band according to a weaker S-S intercluster interaction, a 12d Mo band is partially filled with 22 electrons in PbMo_6S_8 case and an empty 18d Mo band.

In the same way, this structure is also included in $\text{Mo}_6\text{S}_6\text{Br}_2$ cluster whose main difference with the PbMo_6S_8 is the substitution of S by Br in 2c position of R3-crystallographic group (**Fig. 1.7 right**). Depending only on different stoichiometry or the different splitting of orbitals in ligands and metal, the value of the Fermi level is shifted at higher value.

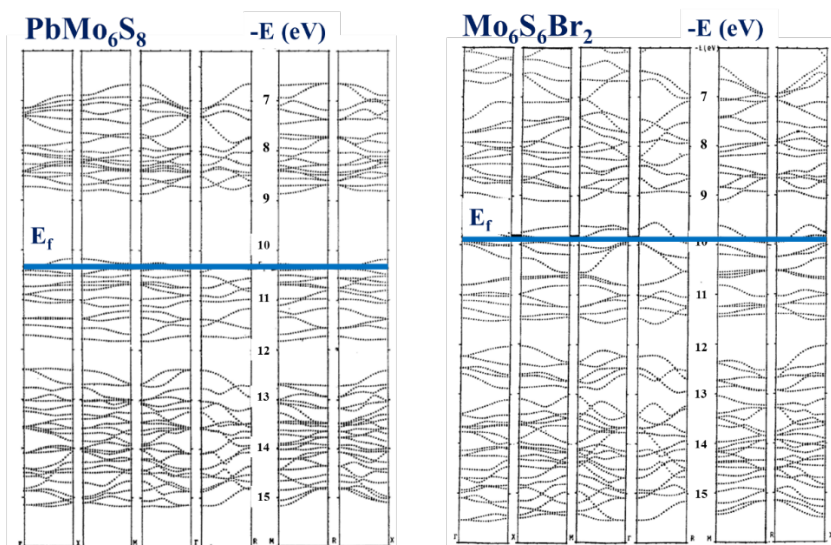


Figure 1.7. The band structure of PbMo_6S_8 and $\text{Mo}_6\text{S}_6\text{Br}_2$ clusters ⁴⁵.

In the case of Mo_6S_8 cluster, the band-structure frame gives rise a 20 electron filling of the 12d Mo band. However, for PbMo_6S_8 , Pb gives 2 electrons to fulfill 22 electron totally in 12 d Mo band. In chevrel phases, it should be noticed that S_8 band structure is very flat accordingly with the minimization of S-S intercluster repulsion. Therefore, in PbMo_6S_8 band structure, S_8 bands are nearly undisturbed by the d orbitals of Mo_6 cluster when Mo_6 band structure is splitted by ligand crystalline field.

In summary, the ligand will create the different crystal field that defines the band structure and density of electronic states of the Mo_6 cluster and counter cation will maximize the electron in 12 d band to change the photophysical property of the cluster.

Many $\text{M}_6\text{L}_6\text{L}_8$ materials, in which Mo atoms have been replaced by Re, Rh, Ru and other ones and ligands are halogens or a chalcogen-halogenid mixture, have also been made. The interest of this various stoichiometry lies in the possibility of making the Fermi level to fluctuate. Partial (d Mo, p L) and total densities have been computed and recognized three groups of bands in $\text{PbMo}_6\text{Se}_8\text{Cl}_6$ cluster (**Fig. 1.8**). From bottom to up: (i) The first group which is mainly made of 3 p Cl and Se with a tiny metallic

contribution, is lied between -13 and -16.5 eV. The weak mixture of p orbitals of ligand and d metallic orbital is caused by geometrical consideration: ligand-ligand repulsion prior to form than metal-ligand intercluster interaction, (ii) The second group is mainly composed of 12d Mo orbitals between – 10.5 and - 12 eV and (iii) The third group which is separated from the previous one by a gap (-6.5 and -9.5), is mainly made of 18d Mo orbitals. The gap width is about 1 eV.

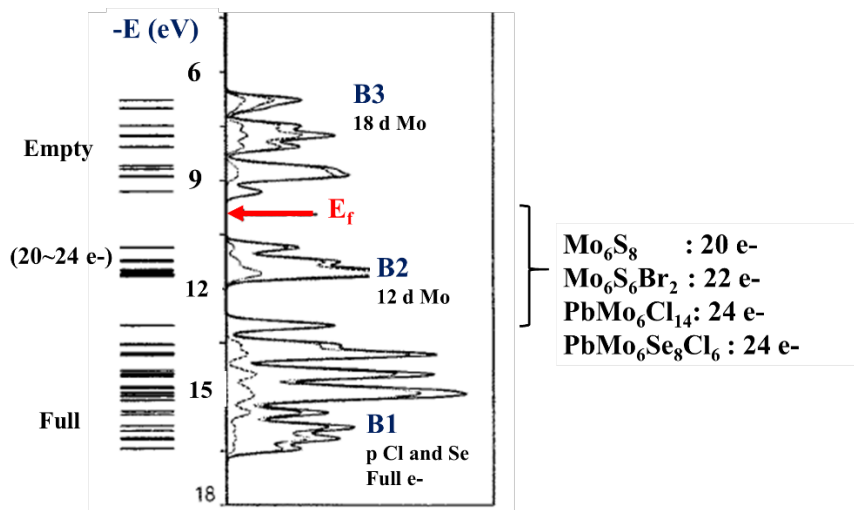


Figure 1.8. Energy levels and convoluted density of states of $\text{PbMo}_6\text{Se}_8\text{Cl}_6$ (partial p L DOS in dotted line, partial d M DOS in dashed line, total DOS in continuous line) ⁴⁵.

From the spitting of the band of electron states of the Mo cluster in $\text{PbMo}_6\text{Se}_8\text{Cl}_6$ clusters, three band model theory including the Fermi level position in the middle of the gap between B2 and B3 area (d Mo orbital) has been aimed by D. Certain and R. Lissillour (France). The frame of density of states is separated with three band groups (**Fig. 1.9**): B1 band is essentially composed of p ligand orbitals; B2 and B3 band composed of d M metallic orbitals with B2 made of 12d M levels and B3 made of 18d M levels. This splitting of d-like metal level can be related to the global geometry. For the reason, d metallic atomic orbitals may be splitted with a ratio of 3/2 by a cubic field caused from ligand crystalline field.

Depend on the nature of ligands and counter cations, the number of electron in 12d M levels will be in the range from 20 to 24 in valance electron orbitals. For example, the 12d M band of the Mo_6S_8 cluster is filled with 20 electrons, $\text{Mo}_6\text{S}_6\text{Br}_2$ with 22 and $\text{PbMo}_6\text{Cl}_{14}$ or $\text{PbMo}_6\text{Se}_8\text{Cl}_6$ with 24 electrons (i.e. completely full).

If B2 band is full (24 electrons), the concerned compound is an insulator or a semiconductor depending on the B2-B3 gap width. On the other hand, if B2 band is partially filled with less than 24 electrons, the compound should be a metal. Moreover, in the case of $\text{PbMo}_6\text{Cl}_{14}$, 12d band of the $\text{Mo}_6\text{Cl}_{14}$ cluster only contains 22 electrons and other electrons from Pb cation. For the result, the insert cation supply the charge on Mo_6 cluster that allows the Fermi level to be on a maximum of density of state closed with superconducting properties.

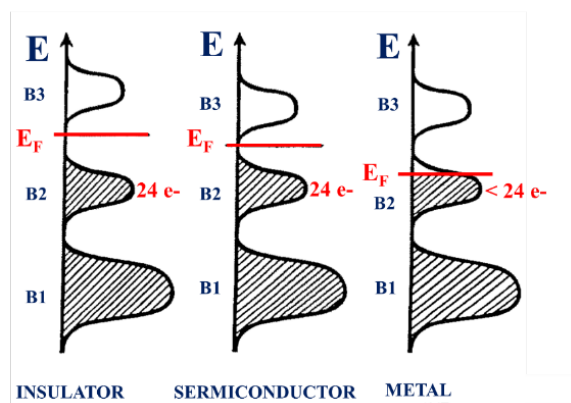


Figure 1.9. Three band model ⁴⁵.

In order to verify lattice and valence electronic structures of crystalline octahedral molybdenum halide clusters-based compounds, $\text{Cs}_2[\text{Mo}_6\text{X}_{14}]$ ($\text{X} = \text{Cl}, \text{Br}, \text{I}$), Saito et al. has applied the density functional theory calculations ⁹². **Figure 1.10 (left)** presents the energy dispersion of the valence p-orbitals of X^{a} , obviously changed with X ($\text{X} = \text{Cl}, \text{Br}, \text{I}$). That causes the population of X p orbitals within valence band maximum (VBM) increased with the atomic number of X . The valence band structures of $\text{Cs}_2[\text{Mo}_6\text{X}_{14}]$ varied with X were obtained using the density functional theory (DFT) functional after structural optimization (**Fig. 1.10 right**). Authors suggested that the Mo 4d states were dominantly found around VBM, while the valence p-orbitals of X were distributed in the relatively deeper parts of the valence band. In particular, the valence p-states of X^{i} were located in deeper parts of the valence band compared to those of X^{a} . Moreover, the s-orbitals of X in the semicore region ($> 9 \text{ eV}$) showed similar behavior: the s states of X^{i} were deeper than those of X^{a} . These results indicate that the chemical states of total electron are made of the distribution of partial atomic orbitals.

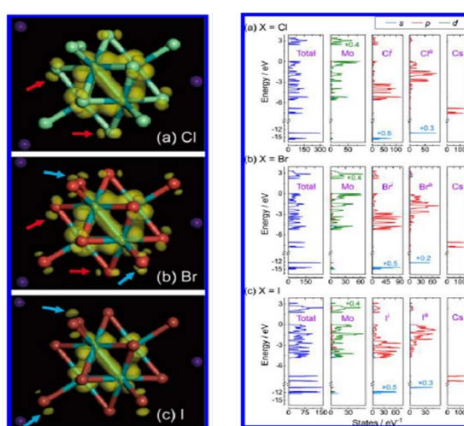


Figure 1.10. Electron orbital distribution of the highest occupied orbital in $\text{Cs}_2[\text{Mo}_6\text{X}_{14}]$ for (a) $\text{X} = \text{Cl}$, (b) $\text{X} = \text{Br}$, and (c) $\text{X} = \text{I}$. The yellow clouds indicate isosurfaces normalized at $0.08 \text{ e}/\text{\AA}^3$, and the red and blue arrows indicate the clouds representing the contributions of X^{i} and X^{a} , respectively (left) and density of states (PDOS) of $\text{Cs}_2[\text{Mo}_6\text{X}_{14}]$: (a) $\text{X} = \text{Cl}$, (b) $\text{X} = \text{Br}$, and (c) $\text{X} = \text{I}$ (right)⁹².

From the density of states (DOS), Saito et al. also suggested the gap energy of the $\text{Cs}_2[\text{Mo}_6\text{Cl}_{14}]$ cluster by density functional theory (DFT) calculations (**Fig. 1.11**). The energy band gap deduced from the E–k plot was 2.46–2.48 eV, which is slightly smaller than the experimentally determined optical band gap⁹³.

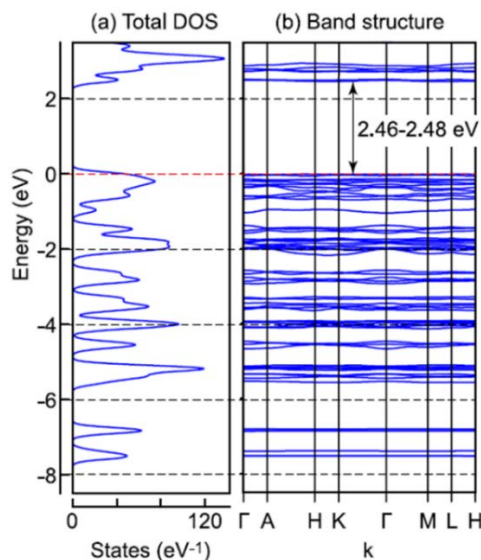


Figure 1.11. a) Density of states and b) band dispersion in $\text{Cs}_2[\text{Mo}_6\text{Cl}_8\text{Cl}_6]$ with P_{31c} symmetry⁹³.

The redox, spectroscopic, and photophysical characteristics of a series of $[\{\text{Mo}_6\text{X}_8^i\}\text{X}_6^a]^{2-}$ ($X = \text{Cl}, \text{Br},$ or I) octahedral hexamolybdenum (II) clusters have reported by Soichiro Akagi et al. group⁹⁴. They suggested that: (i) all of the $[\text{Mo}_6\text{X}_8^i\text{X}_6^a]^{2-}$ clusters show intense and long-lived phosphorescence in both CH_3CN and crystalline phases at 298 K, (ii) The emission quantum yields (Φ_{emission}) increase in the sequences $\text{X}^i = \text{Cl} < \text{Br} < \text{I}$ and $\text{X}^a = \text{I} < \text{Br} < \text{Cl}$ for given X^i and X^a , respectively, and (iii) The emission lifetimes (τ_{emission}) of the clusters also increase in the sequence $\text{X}^a = \text{I} < \text{Br} < \text{Cl}$ for given $\{\text{Mo}_6\text{X}_8^i\}^{4+}$ -core clusters. Arbitrary combinations of X^i and X^a in $[\text{Mo}_6\text{X}_8^i\text{X}_6^a]^{2-}$ could tune τ_{emission} and Φ_{emission} in the ranges of 85–300 μs and 0.09–0.47, respectively.

Both capping (X^i) and terminal ligand (X^a) effects on the photophysical properties of the clusters are discussed on the basis of the energy gap (i.e., emission energy) dependence of the nonradiative decay rate constant.

In order to understand the evidence of dual emission, K. Costuas et al. has studied the combined theoretical time-resolved photoluminescence investigations of $[\text{Mo}_6\text{Br}_8^i\text{Br}_6^a]^{2-}$ metal cluster units²⁹.

Figure 1.12 illustrates that the large energy difference between absorption and emission observed experimentally is thus a consequence of important stabilizations of the emissive triplet excited states upon geometrical relaxation. Emission indeed occurs from those geometrical arrangements. This also implies that the emission from a triplet state T_y can be lower in energy than the one of the lower lying triplet state T_1 since (i) the geometrical relaxation can be more important in T_y than in T_1 and (ii) the singlet-state energy to be considered is the one at the relaxed triplet geometry.

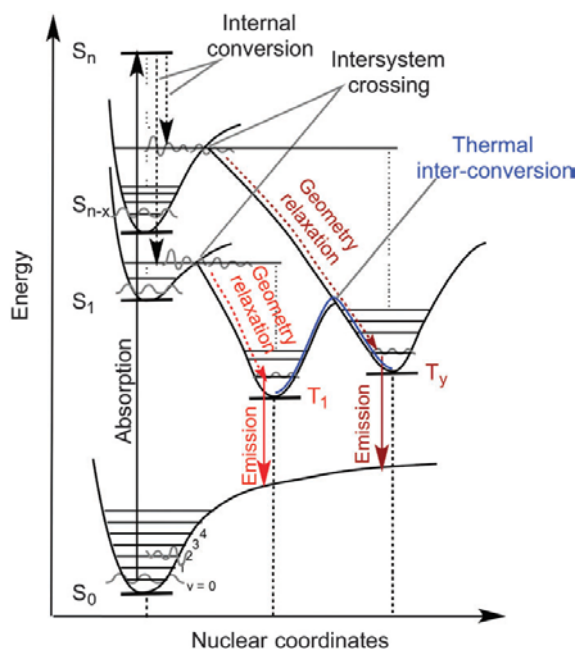


Figure 1.12. Schematic Jablonski-type diagram of de-excitation via two paths leading to the emission from T_1 and any emissive T of higher energy labeled T_y with a possible thermal inter conversion ²⁹.

In summary, they suggested the NIR-luminescence of $[Mo_6Br_8Br^a_6]^{2-}$ metal cluster is due to at least two emission states: (i) the non-radiative de-excitation by the elongation of one Mo–Mo bond ($\sim 0.3\text{--}0.4$ eV) and (ii) the geometrical relaxation of the triplet state by the outstretching of an apex away from the square plane of the Mo_6 octahedron.

The modification of the local environment of the cluster (geometrical constraints, electrostatic external field) or changing the excitation procedure (time of irradiation, irradiation wavelength, temperature), one can access different excited states. It has to be emphasized that the environment of the cluster unit has an influence on the relaxation process. This contribution to the comprehension of the de-excitation/emission processes of $[Mo_6Br_8Br^a_6]^{2-}$ containing systems provides new tools to design target (hybrid) materials notably by constraining the relaxation of the excited states.

1.3. Methodology - electrophoretic deposition process

Numerous chemical solution deposition (CSD) techniques have been used to functionalize the surfaces of a variety of materials for fabricating the nano/micrometer-thick films ^[95]. Among them, the electrophoretic deposition (EPD) process has been widely used as one of the significantly advantage coating methods; for instance, the thin film-coating capability on complex-shaped conductive substrates ^[96] and the requirement of the suspensions containing charged particles, i.e., conductive polymers ^[97], organic, inorganic, or organic–inorganic composites ^[98, 99]. Up to now, because of the simple apparatus setup, short preparation time and easy control of the film thickness, EPD has widely been applied to

prepare film coatings as the most popular electrochemical methods.

As the fundamental steps during the EPD process, two phenomena have been recognized that includes (i) the electrophoresis of charged particles moving toward the electrode under an electric field, and (ii) the deposition of the particles on the electrode surface by coagulation. The deposition mechanisms of the EPD process have been figured out through many experiments on variously matrix materials [100-108]. Parameters related to the suspension (particle size, dielectric constant of liquid, conductivity, viscosity, zeta potential and stability) and parameters related to the EPD process (effect of deposition, applied voltage, concentration of solid in suspension and conductivity of substrate) have noticeably investigated [103]. Jonathan J. Van Tassel et al. has suggested several mechanisms of the deposition during electrophoretic deposition process; densification, direct electrostatic force, electroosmotic, ion depletion enhanced electrostatic, salting out, charge reduction/neutralization, squeezing out, bridging flocculation, desorption of neutral/charged polymer and polyelectrolyte neutralization [104]. In the real suspension, several mechanisms could occur at the same time. Y. Fukada et al. suggested the mechanism during EPD process including main steps: particle charge neutralization, electrochemical coagulation of particles, flocculation by particle accumulation and electrical double layer (EDL) distortion and thinning (Fig. 1.13) [102].

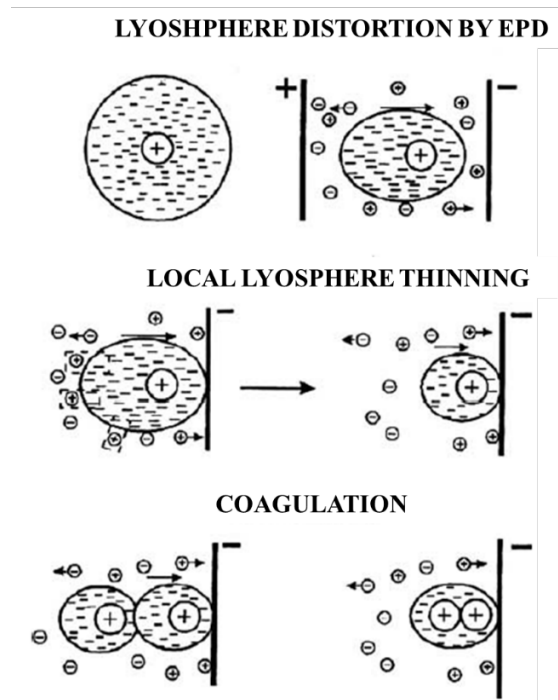


Figure 1. 13. Schematic of the deposition mechanism by lysosphere distortion and thinning [102].

The application of the EPD process have been widely used in assembly of nanoscale particles into nanostructures and micro patterned thin, near shape manufacturing of complex-shaped glasses and ceramics, solid oxide fuel cell (SOFC) fabrication, laminated materials, functionally graded materials, Hybrid materials, fiber reinforced ceramic matrix composites films, etc., [103]. The fabrications of thin films based on the materials of hydroxyapatite [109, 110], SiO₂ [111], carbon nanotube [112-114], graphene [115],

Al_2O_3 [116], TiO_2 [117-119], ZnO [120, 121], forsterite [122], metal–organic frameworks (MOFs) [123, 124], ligand covered metal particles [125] and fluorescent Cu or Au sheet for light-emitting diode [126] by the EPD process, have achieved the elucidation of interesting deposition characteristics. Depending on the advantages of the EPD process, in the first time, it is applied to fabricate the thin film containing of the charged octahedral metal clusters.

1.4. Objective of the thesis

The possibility of the application can be further extended by supporting the metal clusters on substrate materials, improving the stability and handling of the metal clusters. In the case of supported metal clusters, the functional properties may be changed due to the electronic interactions via the chemical bonding with the ligands and support materials. The objective of this study is fabrication and characterization of new nanocomposite materials built up from transition metal cluster and inorganic matrix for industrial applications.

According to recent reports, the good transparent optical films based on the $[\text{Mo}_6\text{Br}_8(\text{OCOC}_2\text{F}_5)_6]^{2-}$ cluster units and zinc oxide with polyvinylpyrrolidone (PVP) [67] and the $\{\text{Ta}_6\text{Br}_{12}\}^{2+}$ cluster in PVP polymer matrix [90] have been successfully fabricated on normal glasses by dip coating. However, one strong restriction of this method is the requirement of a high concentration of the polymer addition in order to stabilize the Mo_6 clusters on the glass surface. In order to overcome these problems, our study investigated the applicability and processability of the EPD process for obtaining transparent, homogeneous, and thin octahedral Mo_6 and Ta_6 cluster films by optimizing (i) the dispersion medium of the Mo_6 and Ta_6 cluster precursors or suspension parameter (pH, concentration, zeta potential, conductivity, etc.) and (ii) the parameters of EPD process (deposition time, applied voltage, distance between electrodes, etc.). In this study, we did succeed to fabricate and characterize the thin, transparent and homogeneous films with retaining the original optical property of the Mo_6 and Ta_6 octahedral clusters by using the electrophoretic deposition (EPD). The strong advantage of the EPD process is that we can easily fabricate pure cluster films containing no counter cations at room temperatures, creating a new cluster network exhibiting prominent luminescent stabilization. The new crystallographic network of the cluster unit is expected to form on the support materials that bring out the enhanced optical properties. Moreover, we also introduced the clusters into inorganic (silica) or organic matrix (polymer) materials. The supporting materials play an important role as sustainable framework to immobilize and stabilize the octahedral clusters at the nanometric scale that gives excellent optical properties.

Reference

1. D. O. Akinyele, and R. K. Rayudu. Review of energy storage technologies for sustainable power networks. *Sus. Ener.Tech. and Assess.*, 8, 74-91, 2014.
2. X. Luo, J. Wang, M. Dooner, and J. Clarke. Overview of current development in electrical energy

storage technologies and the application potential in power system operation. *App.Ener.*, 137, 511-536, 2015.

3. T. Kousksou, P. Bruel, A. Jamil, T. ElRhafiki, and Y. Zeraouli, Energy storage: Applications and challenges. *Solar Ener. Mater. & Solar Cells*, 120, 59-80, 2014.

4. M. W. Ahmada, M. Moursheda, D. Mundowb, M. Sisinnic, and Y. Rezguia. Building energy metering and environmental monitoring – A state-of-the-art review and directions for future research. *Ener. and Build.*, 120, 85-102, 2016.

5. A. C. Menezes, A. Cripps, R. A. Buswell, J. Wright, and D. Bouchlaghem. Estimating the energy consumption and power demand of small power equipment in office buildings. *Ener. and Build.*, 75, 199-209, 2014.

6. M. S. Gul, and S. Patidar. Understanding the energy consumption and occupancy of a multi-purpose academic building. *Ener. and Build.*, 87, 155-165, 2015.

7. R. Baetens, B. P. Jelle, and A. Gustavsen. Properties, requirements and possibilities of smart windows for dynamic daylight and solar energy control in buildings: A state-of-the-art review. *Solar Ener. Mat. & Solar Cells*, 94, 87-105, 2010.

8. C. G. Granqvist. Electrochromics for smart windows: Oxide-based thin films and devices. *Thin Solid Films*, 564, 1-38, 2014.

9. B. P. Jelle, C. Breivik, and H. D. Røkenes. Building integrated photovoltaic products: A state-of-the-art review and future research opportunities. *Solar Ener. Mat. & Solar Cells*, 100, 69-96, 2012.

10. B. P. Jelle. Solar radiation glazing factors for window panes, glass structures and electrochromic windows in buildings - Measurement and calculation. *Solar Ener. Mat. & Solar Cells*, 116, 291-323, 2013.

11. C. Baldassarri, A. Shehabi, F. Asdrubali, and E. Masanet. Energy and emissions analysis of next generation electrochromic devices. *Solar Ener. Mat. and Solar Cells*, 156, 170-181, 2016.

12. G. Gorgolis, and D. Karamanis. Solar energy materials for glazing technologies. *Solar Ener. Mat. & Solar Cells*, 144, 559-578, 2016.

13. K. Kirakci, S. Cordier and C. Perrin. Synthesis and properties of charge-transfer solids with cluster units $[Mo_6X_{14}]^{2-}$ (X = Br, I). *Z. Anorg. Allg. Chem.*, 631, 411-416, 2005.

14. T. K. N. Nguyen, F. Grasset, B. Dierre, C. Matsunaga, S. Cordier, P. Lemoine, N. Ohashi, and T. Uchikoshi. Fabrication of transparent thin film of octahedral molybdenum metal clusters by electrophoretic deposition. *ECS J. Solid State Sci. and Tech.*, 5, 178-186, 2016.

15. P. Rochaa, A. Siddiquia, and M. Stadler. Improving energy efficiency via smart building energy management systems: A comparison with policy measures. *Ener. and Build.*, 88, 203-213, 2015.

16. Y. Cao, J. H. Dou, N. Zhao, S. Zhang, Y. Q. Zheng, J. P. Zhang, J. Y. Wang, J. Pei, and Y. Wang. Highly efficient NIR-II photothermal conversion based on an organic conjugated polymer. *Chem. Mater.*, 29, 718-725, 2017.

17. S. Schiavoni, F. D. Alessandrea, F. Bianchia, and F. Asdrubalia. Insulation materials for the building sector: A review and comparative analysis. *Renewable and Sustainable Energy Reviews*, 988-

1011, 2016.

18. C. G. Granqvist. Recent progress in thermochromics and electrochromics: A brief survey. *Thin Solid Films*, 614, 90-96, 2016.
19. C.G. Granqvista, A. Azensb, P. Heszlerc, L.B. Kishd, and L.Osterlunde. Nanomaterials for benign indoor environments: Electrochromics for “smart windows”, sensors for air quality, and photo-catalysts for air cleaning. *Solar Ener. Mat. & Solar Cells*, 91, 355-365, 2007.
20. R. Liu, J. Duaya and S. B. Lee. Heterogeneous nanostructured electrode materials for electrochemical energy storage. *Chem. Commun.*, 47, 1384-1404, 2011.
21. F. A. Cotton. Metal Atom Clusters in Oxide Systems. *Inorg. Chem.*, 3, 1217-1220, 1964.
22. A. Perrin, and C. Perrin. The molybdenum and rhenium octahedral cluster chalcogenides in solid state chemistry: From condensed to discrete cluster units. *Comptes Rendus Chimie*, 15, 815-836, 2012.
23. S. Cordier, F. Dorson, F. Grasset, Y. Molard, B. Fabre, H. Haneda, T. Sasaki, M. Mortier, S. A. Girard, and C. Perrin. Novel nanomaterials based on inorganic molybdenum octahedral clusters. *J. Clust. Sci.*, 20, 9-21, 2009.
24. J. Koutecky, and P. Fantucci. Theoretical aspects of metal atom clusters. *Chem. Rev.*, 66, 539-587, 1986.
25. M. D. Morse. Clusters of transition-metal atoms. *Chem. Rev.*, 86, 1049-1109, 1986.
26. J. A. Alonso. Electronic and atomic structure, and magnetism of transition-metal clusters. *Chem. Rev.*, 100, 637-677, 2000.
27. N. G. Naumov, K. A. Brylev, Y. V. Mironov, S. Cordier, and V. E. Fedorov. Octahedral clusters with mixed inner ligand environment: Self-assembly, modification and isomerism. *J. Struct. Chem.*, 55, 1371-1389, 2014.
28. S. Kamiguchi, S. Nagashima and T. Chihara. Characterization of catalytically active octahedral metal halide cluster complexes. *Metals*, 4, 84-107, 2014.
29. K. Costuas, A. Garreau, A. Bulou, B. Fontaine, J. Cuny, R. Gautier, M. Mortier, Y. Molard, J. L. Duvail, E. Faulques and S. Cordier. Combined theoretical and time-resolved photoluminescence investigations of $[\text{Mo}_6\text{Br}_8^i\text{Br}_6^a]$ metal cluster units: evidence of dual emission. *Phys. Chem. Chem. Phys.*, 17, 28574-28585, 2015.
30. Y. Zhao, and R. R. Lunt. Transparent luminescent solar concentrators for large-area solar windows enabled by massive stokes-shift nanocluster phosphors. *Adv. Ener. Mat.*, 3, 1143-1148, 2013.
31. X. Zarate, E. Schott, L. A. Soto, and R. R. Tagle. A family of octahedral molybdenum cluster complexes $[\text{Mo}_6\text{Cl}_8(\text{H}_2\text{O})_n(\text{OH})_{6-n}]^{n-2}$ with $n = 0-6$ as a pH-sensors: A theoretical study. *Chem. Phys. Lett.*, 567, 39-42, 2013.
32. S. Cordier, N. G. Naumov, D. Salloum, F. Paul, and C. Perrin. Synthesis and characterization of mo_6 chalcobromides and cyano-substituted compounds built from a novel $[(\text{Mo}_6\text{Br}_6^i\text{Y}^i_2)\text{L}^a_6]^{n-}$ discrete cluster unit (Y^i) S or Se and L^a) Br or CN). *Inorg. Chem.*, 43, 219-226, 2004.
33. K. A. Brylev, Y. V. Mironov, S. S. Yarovoi, N. G. Naumov, V. E. Fedorov, S. J. Kim, N. Kitamura, Y. Kuwahara, K. Yamada, S. Ishizaka, and Y. Sasaki. A family of octahedral rhenium cluster complexes

- [Re₆Q₈(H₂O)_n(OH)_{6-n}]ⁿ⁻⁴ (Q = S, Se; n = 0-6): structural and pH-dependent spectroscopic studies. *Inorg. Chem.*, 46, 7414-7422, 2007.
34. P. C. Ford, and A. Vogler. Photochemical and photophysical properties of tetranuclear and hexanuclear clusters of metals with d¹⁰ and s² electronic configurations. *Acc. Chem. Res.*, 26, 220-226, 1993.
35. T. G. Gray, C. M. Rudzinski, E. E. Meyer, R. H. Holm, and D. G. Nocera. Spectroscopic and photophysical properties of hexanuclear Rhenium(III) chalcogenide clusters. *J. Am. Chem. Soc.*, 125, 4755-4770, 2003.
36. L. F. Szczepura, J. A. Edwards, and D. L. Cedeno. Luminescent properties of hexanuclear molybdenum(II) chloride clusters containing thiolate ligands. *J. Clust. Sci.*, 20, 105-112, 2009.
37. T. Yoshimura, Z. N. Chen, A. Itasaka, M. Abe, Y. Sasaki, S. Ishizaka, and N. Kitamura. Preparation, structures, and redox and emission characteristics of the isothiocyanate complexes of Hexarhenium(iii) clusters [Re₆(μ₃-E)₈(NCS)₆]⁴⁻ (E = S, Se). *Inorg. Chem.*, 42, 4857-4863, 2003.
38. S. Cordier, Y. Molard, K. A. Brylev, Y. V. Mironov, F. Grasset, B. Fabre, and N. G. Naumov. Advances in the engineering of near infrared emitting liquid crystals and copolymers, extended porous frameworks, theranostic tools and molecular junctions using tailored Re₆ cluster building blocks. *J. Clust. Sci.*, 26, 53-81, 2015.
39. A. D. Fuhrmann, A. Seyboldt, A. Schank, G. Zitzer, B. Speiser, D. Enseling, T. Jüstel, and H. J. Meyer. Luminescence quenching of ligand-substituted molybdenum and tungsten halide clusters by oxygen and their oxidation electrochemistry. *Eur. J. Inorg. Chem.*, 37, 4259-4266, 2017.
40. A. A. Krasilnikova, M. A. Shestopalova, K. A. Brylev, A. Kirilova, O. P. Khripko, K. E. Zubareva, Y. I. Khripko, V. T. Podorognay, L. V. Shestopalova, V. E. Fedorova, and Y. V. Mironova. Prospects of molybdenum and rhenium octahedral cluster complexes as X-ray contrast agents. *J. Inorg. Biochem.*, 144, 13-17, 2015.
41. S. J. Choi, K. A. Brylev, J. Z. Xu, Y. V. Mironov, V. E. Fedorov, Y. S. Sohn, S. J. Kim, and J. H. Choy. Cellular uptake and cytotoxicity of octahedral rhenium cluster complexes. *J. Inorg. Biochem.*, 102, 1991-1996, 2008.
42. T. Aubert, F. C. Hurtado, M. A. Esnault, C. Neaime, D. L. Chauvel, S. Jeanne, P. Pellen, C. Roiland, L. Le Polles, N. Saito, K. Kimoto, H. Haneda, N. Ohashi, F. Grasset, and S. Cordier. Extended investigations on luminescent Cs₂[Mo₆Br₁₄]@SiO₂ nanoparticles: physico-structural characterizations and toxicity studies. *J. Phys. Chem. C*, 117, 20154-20163, 2013.
43. L. A. Soto, and R. R. Tagle. A theoretical study of the binding of [Re₆Se₈(OH)₂(H₂O)₄] rhenium clusters to DNA purine base guanine. *Materials*, 8, 3938-3944, 2015.
44. M. Potel, C. Perrin, A. Perrin and M. Sergent. New families of ternary molybdenum (II) chlorides with octahedral Mo₆ clusters. *Mat. Res. Bull.*, 21, 1239-1245, 1986.
45. D. Certain, and R. Lissillour. The Three-Band Model. A pattern for the electronic structure of M₆L₈L₆ cluster compounds. *Z. Phys. D - Atoms, Mol. and Clus.*, 3, 411-420, 1986.
46. K. Kirakci, S. Cordier, and C. Perrin. Synthesis and Characterization of Cs₂Mo₆X₁₄ (X = Br or I)

Hexamolybdenum cluster halides: efficient Mo₆ cluster precursors for solution chemistry syntheses. *Z. Anorg. Allg. Chem.*, 631, 411-416, 2005.

47. P. Kumar, S. Kumar, S. Cordier, S. Paofai, R. Boukherroub and S. L. Jain. Photoreduction of CO₂ to methanol with hexanuclear molybdenum [Mo₆Br₁₄]²⁻ cluster units under visible light irradiation. *RSC Adv*, 4, 10420–10423, 2014.

48. G. Saito, H. Hosoda, Y. Yoshida, J. Hagiwara, K. Nishimura, H. Yamochi, A. Otsuka, T. Hiramatsu, Y. Shimazaki, K. Kirakci, S. Cordier, and C. Perrin. Synthesis and properties of charge-transfer solids with cluster units [Mo₆X₁₄]²⁻ (X = Br, I). *J. Mater. Chem.*, 22, 19774-19791, 2012.

49. J. Cuny, S. Cordier, C. Perrin, C. J. Pickard, L. Delevoye, J. Trébosc, Z. Gan, L. Le Pollès, and R. Gautier. ⁹⁵Mo solid-state nuclear magnetic resonance spectroscopy and quantum simulations: synergetic tools for the study of molybdenum cluster materials. *Inorg. Chem.*, 52, 617–627, 2013.

50. S. Cordier, K. Kirakci, D. Mery, C. Perrin, and D. Astruc. Mo₆X₈ⁱ nanocluster cores (X: Br, I): From inorganic solid state compounds to hybrids. *Inorganica Chimica Acta*. 359, 1705-1709, 2006.

51. X. Zarate, E. Schott, L. A. Soto, and R. R. Tagle. A family of octahedral molybdenum cluster complexes [Mo₆Cl₈(H₂O)_n(OH)_{6-n}]ⁿ⁻² with n = 0–6 as a pH-sensors: A theoretical study. *Chem. Phys. Lett.*, 567, 39-42, 2013.

52. K. Kirakci, P. Kubát, K. Fejfarová, J. Martinčík, M. Nikl, and K. Lang. X-ray inducible luminescence and singlet oxygen sensitization by an octahedral molybdenum cluster compound: A New Class of Nanoscintillators. *Inorg. Chem*, 55, 803–809, 2016.

53. S. Cordier, F. Grasset, R. Boukherroub, N. Saito, H. Haneda, Y. Molard, S. Ravaine, M. Mortier, M. Amela-Cortes and N. Ohashi. Inorganic molybdenum octahedral nanosized cluster units, versatile functional building block for nanoarchitectonics. *J. Inorg. Organomet. Polym.*, 25, 189-204, 2015.

54. P. Kumar, H. P. Mungse, S. Cordier, R. Boukherrou, O. P. Khatri, and S. L. Jain. Hexamolybdenum clusters supported on graphene oxide: visible-light induced photocatalytic reduction of carbon dioxide into methanol. *Carbon*, 94, 6491 -100, 2015.

55. A. Renaud, F. Grasset, B. Dierre, T. Uchikoshi, N. Ohashi, T. Takei, A. Planchat, L. Cario, S. Jobic, F. Odobel, and S. Cordier. Inorganic molybdenum clusters as light-harvester in all inorganic solar cells: a proof of concept. *Chem. Sel.*, 1, 2280-2289, 2016.

56. P. S. Kuttipillai, Y. Zhao, C. J. Traverse, R. J. Staples, B. G. Levine, and R. R. Lunt. Phosphorescent nanocluster light-emitting diodes. *Adv. Mater.*, 28, 320-326, 2016.

57. T. Aubert, F. C. Hurtado, M. A. Esnault, C. Neaime, D. L. Chauvel, S. Jeanne, P. Pellen, C. Roiland, L. L. Polles, N. Saito, K. Kimoto, H. Haneda, N. Ohashi, F. Grasset and S. Cordier. Extended investigations on luminescent Cs₂[Mo₆Br₁₄]@SiO₂ nanoparticles: physico-structural characterizations and toxicity studies. *J. Phys. Chem. C*, 117, 20154–20163, 2013.

58. A. O. Solovieva, Y. A. Vorotnikov, K. E. Trifonova, O. A. Efremova, A. A. Krasilnikova, K. A. Brylev, E. V. Vorontsova, P. A. Avrorov, L. V. Shestopalova, A. F. Poveschenko, Y. V. Mironov and M. A. Shestopalov. Cellular internalisation, bioimaging and dark and photodynamic cytotoxicity of silica nanoparticles doped by {Mo₆I₈}⁴⁺ metal clusters. *J. Mater. Chem. B*, 4, 4839-4846, 2016.

59. C. Neaime, M. Amela-Cortes, F. Grasset, Y. Molard, S. Cordier, B. Dierre, M. Mortier, T. Takei, H. Haneda, M. Verelst, and S. Lechevallier. Time-gated luminescence bioimaging with new luminescent nanocolloids based on $[\text{Mo}_6\text{I}_8(\text{C}_2\text{F}_5\text{COO})_6]^{2-}$ metal atom clusters. *Phys. Chem. Chem. Phys.*, 18, 30166-30173, 2016.
60. F. C. Hurtado, M. D. Lozano-Baena, C. Neaime, A. Burel, S. Jeanne, P. Pellen-Mussi, S. Cordier and F. Grasset. Studies on plant cell toxicity of luminescent silica nanoparticles ($\text{Cs}_2[\text{Mo}_6\text{Br}_{14}]\text{@SiO}_2$) and its constitutive components. *J. Nanopart. Res.*, 18, 69-84, 2016.
61. A. Beltran, M. Mikhailov, M. N. Sokolov, V. Perez-Laguna, A. Rezusta, M. J. Revillo and F. Galindo. A photobleaching resistant polymer supported hexanuclear molybdenum iodide cluster for photocatalytic oxygenations and photodynamic inactivation of *Staphylococcus aureus*. *J. Mater. Chem. B*, 4, 5975-5979, 2016.
62. T. Aubert, N. Nerambourg, N. Saito, H. Haneda, N. Ohashi, M. Mortier, S. Cordier, and F. Grasset. Tunable visible emission of luminescent hybrid nanoparticles incorporating two complementary luminophores: zno nanocrystals and $[\text{Mo}_6\text{Br}_{14}]^{2-}$ nanosized cluster units. *Part. Part. Syst. Charact.*, 30, 90-95, 2013.
63. K. Kirakcia, H. Hosoda, S. Cordier, C. Perrin, and G. Saito. A hybrid material based on $[\text{Mo}_6\text{Br}_{14}]^{(2-)}$ inorganic cluster units and $[\text{BEDO-TTF}]^{(+)}$ organic monocationic radicals: Synthesis, structure and properties of $(\text{BEDO-TTF})^{(2)}\text{Mo}_6\text{Br}_{14}(\text{PhCN})$. *J. Solid State Chem.*, 179, 3628-3635, 2006.
64. A. Barrasa, S. Cordier, and R. Boukherrouba. Fast photocatalytic degradation of rhodamine B over $[\text{Mo}_6\text{Br}_8(\text{N}_3)_6]^{2-}$ cluster units under sun light irradiation. *App. Cat. B: Envi.* 123-124, 1- 8, 2012.
65. M. N. Sokolov, M. A. Mikhailov, A. V. Virovets, K. A. Brylev, R. A. Bredikhin, A. M. Maksimov, V. E. Platonov, and V. P. Fedina. Synthesis, structure, and luminescence of the octahedral molybdenum cluster $[\text{Mo}_6\text{I}_8(\text{SC}_6\text{F}_4\text{H})_6]^{2-}$. *Rus. Chem. Bull., Inter. Ed.* 62, 1764-1767, 2013.
66. M. Prévôt, M. A. Cortes, S. K. Manna, R. Lefort, S. Cordier, H. Folliot, L. Dupont, and Y. Molard. Design and integration in electro-optic devices of highly efficient and robust red-nir phosphorescent nematic hybrid liquid crystals containing $[\text{Mo}_6\text{I}_8(\text{OCOC}_n\text{F}_{2n+1})_6]^{2-}$ ($n = 1, 2, 3$). *Adv. Funct. Mater.*, 25, 4966-4975, 2015.
67. T. G. Truong, B. Dierre, F. Grasset, N. Saito, N. Saito, T. K. N. Nguyen, K. Takahashi, T. Uchikoshi, M. Amela-Cortes, Y. Molard, S. Cordier and N. Ohashi. Visible tunable lighting system based on polymer composites embedding ZnO and metallic clusters: from colloids to thin films. *Sci. Technol. Adv. Mater.*, 17, 443-453. 2016.
68. F. Grasset, Y. Molard, S. Cordier, F. Dorson, M. Mortier, C. Perrin, M. G. Viry, T. Sasaki, and H. Haneda. When “metal atom clusters” meet zno nanocrystals: $\text{A}((-\text{C}_4\text{H}_9)_4\text{N})_2\text{Mo}_6\text{Br}_{14}\text{@ZnO}$ hybrid. *Adv. Mater.*, 20, 1710-1715, 2008.
69. F. Grasset, F. Dorson, S. Cordier, Y. Molard, C. Perrin, A. M. Marie, T. Sasaki, H. Haneda, Y. Bando, and M. Mortier. Water-in-oil microemulsion preparation and characterization of $\text{Cs}_2[\text{Mo}_6\text{X}_{14}]\text{@SiO}_2$ phosphor nanoparticles based on transition metal clusters ($\text{X}=\text{Cl}, \text{Br}, \text{and I}$). *Adv. Mater.*, 20, 143-148, 2008.

70. J. F. Dechezelles, T. Aubert, F. Grasset, S. Cordier, C. Barthou, C. Schwob, A. Maitre, R. A. L. Valle'e, H. Cramaild and C. Ravaine. Fine tuning of emission through the engineering of colloidal crystals. *Phys. Chem. Chem. Phys.*, 12, 11993-11999, 2010.
71. S. Cordier, B. Fabre, Y. Molard, A. B. Fadjie-Djomkam, P. Turban, S. Tricot, S. Ababou-Girard and C. Godet. Elaboration, characterizations, and energetics of robust Mo₆ cluster-terminated silicon-bound molecular junctions. *J. Phys. Chem. C*, 120, 2324–2334, 2016.
72. Y. Molard, C. Labbé, J. Cardin, and S. Cordier. Sensitization of Er³⁺ infrared photoluminescence embedded in a hybrid organic-inorganic copolymer containing octahedral molybdenum clusters. *Adv. Funct. Mater.*, 23, 4757-4869, 2013.
73. M. A. Cortes, A. Garreau, S. Cordier, E. Faulques, J. L. Duvaillb and Y. Molard, Deep red luminescent hybrid copolymer materials with high transition metal cluster content. *J. Mater. Chem. C*, 2, 1545-1552, 2014.
74. M. A. Cortes, S. Paofai, S. Cordier, H. Folliot and Y. Molard. Tuned Red NIR phosphorescence of polyurethane hybrid composites embedding metallic nanoclusters for oxygen sensing. *Chem. Commun.*, 51,189-204, 2015.
75. A. Barras, M. R. Das, R. R. Devarapallic, M. V. Shelkec, S. Cordier, S. Szuneritsa, and R. Boukherrouba. One-pot synthesis of gold nanoparticle/molybdenum cluster/graphene oxide nanocomposite and its photocatalytic activity. *App. Cat. B: Envi.*, 130-131, 270- 276, 2013.
76. C. Neaime, M. Amela-Cortes, F. Grasset, Y. Molard, S. Cordier, B. Dierre, M. Mortier, T. Takei, K. Takahashi, H. Haneda, M. Verelstf and S. Lechevallier. Time-gated luminescence bioimaging with new luminescent nanocolloids based on [Mo₆I₈(C₂F₅COO)₆]²⁻ metal atom clusters. *Phys. Chem. Chem. Phys.*, 18, 30166-30173, 2016.
77. J. H. Espenson, and R. J. Kinkey. A kinetic study of the oxidation of the tantalum cluster ion [Ta₆Br₁₂]²⁺ by Chromium (VI)a. *Inorg. Chem.*, 10, 376-378, 1971.
78. J. H. Espenson. A kinetic study of the two-stage oxidation of the tantalum halide cluster ion (Ta₆Br₁₂)²⁺ Vanadium (V)'. *Inorg. Chem.*, 7, 631-635, 1971.
79. B. G. Hughes, J. L. Meyer, P. B. Fleming, and R. E. Mccarley. Chemistry of polynuclear metal halides. 111. synthesis of some niobium and tantalum [M₆X₁₂]²⁺ cluster derivatives. *Inorg. Chem.*, 9, 1343-1346, 1970.
80. W. N. Hansen, and R. A. Osteryoung. Oxidation of tantalum cluster ions. *J. Am.Chem. Soc.*, 88, 1063-1064, 1966.
81. B. Peric, S. Cordier, J. Cuny, R. Gautier, T. Guizouarn, and P. Planinic. High-temperature experimental and theoretical study of magnetic interactions in diamond and pseudo-diamond frameworks built up from hexanuclear tantalum clusters. *J. Chem. Eur.*, 17, 6263 – 6271, 2011.
82. J. Sinzig, L. J. de Jongh, A. Ceriotti, R. della Pergola, G. Longoni, M. Stener, K. Albert, and N. Rösch. Molecular magnetic quantum dots in multivalent metal cluster compounds. *Phys. Rev. Let.*, 81, 3211-3214,1998.
83. A. Vogler, And H. Kunkely. Photolysis of the tantalum cluster {Ta₆L₁₂}²⁺ in aqueous acidic

- solution. *Inorg. Chem.*, 23, 1360-1363, 1984.
84. N. E. Cooke, T. Kuwana, and J. Espension. Electrochemistry of tantalum bromide cluster compound. *Inorg. Chem.*, 5, 1081-1083, 1971.
85. F. W. Koknat, J. A. Parsons, and A. Vongvusharintra. Metal cluster halide complexes. i. efficient synthesis of hydrated hexanuclear niobium and tantalum cluster halides $M_6X_{14} \cdot 8H_2O$. *Inorg. Chem.* 13, 1699-1702, 1974.
86. U. Beck, A. Simon, S. Sirac, and N. BrnEevik. Crystal Structures of trans- $[Ta_6C_{12}(OH)_4(H_2O)_2] \cdot 10 H_2O$ and $(NMe_4)_2[Ta_6Cl_{12}(OH)_6] \cdot 21H_2O$. *Z. anorg. allg. Chem.*, 623, 59-64, 1997.
87. D. N. T. Hay, and L. Messerle. Low-temperature, high yield synthesis, and convenient isolation of the high-electron-density cluster compound $Ta_6Br_{14} \cdot 8H_2O$ for use in biomacromolecular crystallographic phase determination. *J. Struc. Biol.*, 139, 147-151, 2002.
88. J. Knaeblein, T. Neuefein, F. Schneider, A. Bergner, A. Messerschmidt, J. Loewe, B. Steipe and R. Huber. $\{Ta_6Br_{12}\}^{2+}$, a tool for phase determination of large biological assemblies by x-ray crystallography. *J. Mol. Biol.*, 270, 1-7, 1997.
89. M. Vojnovic, N. Brnicevic, I. Basic, R. Trojko, M. Miljak, and I. D. Desnica-Frankovic. Reactions of niobium and tantalum hexanuclear halide clusters with cadmium (II) halides, diamagnetic and paramagnetic clusters with semiconducting properties. *Mat. Res. Bull.*, 36, 211-225, 2001.
90. A. Renaud, M. Wilmet, T. G. Truong, M. Seze, P. Lemoine, N. Dumait, W. Chen, N. Saito, T. Ohsawa, T. Uchikoshi, N. Ohashi, S. Cordier and F. Grasset. Transparent tantalum cluster-based UV and IR blocking electrochromic devices. *J. Mater. Chem. C*, 5, 8160-8168, 2017.
91. T. C. Zietlow, M. D. Hopkins, H. B. Gray. Electronic spectroscopy and photophysics of d^4 clusters. *J. Solid State Chem.*, 57, 112-119, 1985.
92. N. Saito, S. Cordier, P. Lemoine, T. Ohsawa, Y. Wada, F. Grasset, S. J. Cross, and N. Ohashi. Lattice and valence electronic structures of crystalline octahedral molybdenum halide clusters-based compounds, $Cs_2[Mo_6X_{14}]$ ($X = Cl, Br, I$), studied by density functional theory calculations. *Inorg. Chem.*, 56, 6234-6243, 2017.
93. N. Saito, Y. Wada, P. Lemoine, S. Cordier, F. Grasset, T. Ohsawa, N. Saito, J. S. Cross, and N. Ohashi. Theoretical and experimental determination of the crystal structures of cesium-molybdenum chloride. *Jap. J. App. Phys.*, 55, 1-8, 2016.
94. S. Akagi, S. Fujii and N. Kitamura. A study on the redox, spectroscopic, and photophysical characteristics of a series of octahedral hexamolybdenum (II) clusters: $[\{Mo_6X_8\}Y_6]^{2-}$ ($X, Y = Cl, Br, or I$), *Dalton Trans.*, DOI: 10.1039/C7DT04485B, 2017.
95. T. Schneller, R. Waser, M. Kosec, and D. Payne. Chemical solution deposition of functional oxide thin films. *Spr. Sci. & Busi. Media: Aachen*, 233-319, 2014.
96. J. Tabellion, and R. Clasen. Electrophoretic deposition from aqueous suspensions for near-shape manufacturing of advanced ceramics and glasses-applications. *J. Mater. Sci.*, 39, 803-811, 2004.
97. A. Boccaccini, C. Peters, J. Roether, D. Eifler, S. Misra, and S. Minay. Electrophoretic deposition

of polyetheretherketone (PEEK) and PEEK/Bioglass coatings on NiTi shape memory alloy wires. *J. Mater. Sci.*, 41, 8152–8159, 2006.

98. T. Yoshioka, A. Chávez-Valdez, J. Roether, D. Schubert, and A. Boccaccini. AC electrophoretic deposition of organic–inorganic composite coatings. *J. Col. and Interf. Sci.*, 392, 167–171, 2013.

99. X. Guo, X. Li, H. Li, D. Zhang, C. Lai, and W. Li. A comprehensive investigation on the electrophoretic deposition (EPD) of Nano-Al/Ni energetic composite coatings for the combustion application. *Surf. & Coat. Tech.* 265, 83-91, 2015.

100. N. Koura, T. Tsukamoto, Hiromasa and T. Hotta, Preparation of various oxide films by an electrophoretic deposition method: A study of the mechanism. *Jpn. J. Appl. Phys.*, 34,1643-1647, 1995.

101. P. Sarkar, and P. S. Nicholson. Electrophoretic deposition (EPD): mechanisms, kinetics, and application to ceramics. *J. Am. Ceramic. Soc.*, 79, 1987-2002, 1996.

102. Y. Fukada, N. Nagarajan, W. Mekky, Y. Bao, H. Kim, and P. S. Nicholson. Electrophoretic deposition—mechanisms, myths and materials. *J. Mat. Sci.*, 39, 787- 801, 2004.

103. L. Besra, and M. Liu. A review on fundamentals and applications of electrophoretic deposition (EPD). *Prog. in Mat. Sci.*, 52, 1-61, 2007.

104. J. J. V. Tassela, and C. A. Randall. Mechanisms of electrophoretic deposition. *Key Eng. Mat.*, 314, 167-174, 2006.

105. I. Corni, M. P. Ryan and A. R. Boccaccini. Electrophoretic deposition: From traditional ceramics to nanotechnology. *J. Eu. Cer. Soc.*, 28, 1353-1367, 2008.

106. M. Ammam. Electrophoretic deposition under modulated electric fields: a review. *RSC Adv.*, 2, 7633-7646, 2012.

107. A. C. Valdez, and A. R. Boccaccini. Innovations in electrophoretic deposition: Alternating current and pulsed direct current methods. *Electrochimica Acta*, 65, 70- 89, 2012.

108. F. Keller, H. Nirschl, W. Dörfler and E. Woldt. Efficient numerical simulation and optimization in electrophoretic deposition processes. *J. Eu. Cer.Soc.*, 35, 2619-2630, 2015.

109. I. Zhitomirsky, and L. Galor. Electrophoretic deposition of hydroxyapatite. *J. Mat. Sci.: Mat. in Med.*, 8, 213-219, 1997.

110. M. Wei, A. J. Ruys, B. K. Milthorpe, and C. C. Sorrell. Solution ripening of hydroxyapatite nanoparticles: Effects on electrophoretic deposition. *J. Biomed. Mater. Res.*, 45, 11-19, 1999.

111. M. Holgado, F. G. Santamari, A. Blanco, M. Ibisate, A. Cintas, H. Miguez, C. J. Serna, C. Molpeceres, J. Requena, A. Mifsud, F. Meseguer and C. Lo´pez. Electrophoretic deposition to control artificial opal growth. *Langmuir*, 15, 4701-4704, 1999.

112. B. Gao, G. Z. Yue, Q. Qiu, Y. Cheng, H. Shimoda, L. Fleming, and O. Zhou, Fabrication and electron field emission properties of carbon nanotube films by electrophoretic deposition. *Adv. Mater.*, 13, 1770-1773, 2001.

113. A. R. Boccaccini, J. Cho, J. A. Roether, B. J. C. Thomas, E. J. Minay, and M. S. P. Shaffer. Electrophoretic deposition of carbon nanotubes. *Carbon 94*, 44, 3149-3160, 2006.

114. J. Choa, K. Konopkab, K. Rozniatowskib, E. G. Lecinac, M. S. P. Shaffer, and A. R. Boccaccinia.

Characterisation of carbon nanotube films deposited by electrophoretic deposition. *Carbon* 94, 47, 58 - 67, 2009.

115. Z. S. Wu, S. Pei, W. Ren, D. Tang, L. Gao, B. Liu, F. Li, C. Liu, and H. M. Cheng. Field emission of single-layer graphene films prepared by electrophoretic deposition. *Adv. Mater.*, 21, 1756-1760, 2009.

116. G. Anne, K. Vanmeensel, J. Vleugels, and O. Van der Biest. Influence of the suspension composition on the electric field and deposition rate during electrophoretic deposition. *Col. and Surf. A: Physicochem. Eng.*, 245, 35-39, 2004.

117. S. Dor, S. Rühle, A. Ofir, M. Adler, L. Grinis, and A. Zaban. The influence of suspension composition and deposition mode on the electrophoretic deposition of TiO₂ nanoparticle agglomerates. *Col. and Surf. A: Physicochem. and Eng. Aspects*, 342, 70-75, 2009.

118. D. Hanaor, M. Michelazzi, P. Veronesi, C. Leonelli, M. Romagnoli, and C. Sorrella. Anodic aqueous electrophoretic deposition of titanium dioxide using carboxylic acids as dispersing agents. *J. Eu. Cer. Soc.*, 31, 1041-1047, 2011.

119. R. Kawakami, T. Yuasa, K. Ito, Y. Sato, Y. Mori, M. Adachi and S. Yoshikado. Evaluation of TiO₂ nanoparticle thin films prepared by electrophoresis deposition. *J. Aus. Cer. Soc.*, 48, 236 – 243, 2012.

120. L. A. Ma, and T. L. Guo. Morphology control and improved field emission properties of ZnO tetrapod films deposited by electrophoretic deposition. *Cer. Inter.* 39, 6923-6929, 2013.

121. Y. Huang, D. K. Sarkar, and X. G. Chen. Superhydrophobic nanostructured ZnO thin films on aluminum alloy substrates by electrophoretic deposition process. *App. Surf. Sci.*, 327, 327-334, 2015.

122. S. N. Hosseini, H. SalimiJazi, and M. H. Fathi. Novel electrophoretic deposited nanostructured forsterite coating on 316L stainless steel implants for biocompatibility improvement. *Mat. Let.*, 143, 16-19, 2015.

123. H. Zhu, H. Liu, I. Zhitomirsky, and S. Zhu. Preparation of metal–organic framework films by electrophoretic deposition method. *Mat. Let.*, 142, 19-22, 2015.

124. I. Hod, W. Bury, D. M. Karlin, P. Deria, C. W. Kung, M. J. Katz, M. So, B. Klahr, D. Jin, Y. W. Chung, T. W. Odom, O. K. Farha, and J. T. Hupp. Directed growth of electroactive metal-organic framework thin films using electrophoretic deposition. *Adv. Mater.*, 26, 6295–6300, 2014.

125. C. Streicha, S. Koenena, M. Lelleb, K. Penevab, and S. Barcikowskia. Influence of ligands in metal nanoparticle electrophoresis for the fabrication of biofunctional coatings. *App. Sur. Sci.*, 348, 92-99, 2015.

126. J. Liu, Z. Wu, T. Li, D. Zhou, K. Zhang, Y. Sheng, J. Cui, H. Zhang and B. Yanga. Electrophoretic deposition of fluorescent Cu and Au sheets for light-emitting diodes. *Nanoscale*, 8, 395–402, 2016.

Chapter 2

Electrophoretic deposition of Octahedral Molybdenum Metal Clusters

Chapter 2

Electrophoretic deposition of Octahedral Molybdenum Metal Clusters

The surface of glass is often coated for intrinsic reasons (safety, convenience or better stability) or specific functionalization (ultraviolet or heat protection), water-repellent coating, shatter protection, easy-to-clean and self-cleaning coatings [1-4]. As a method for these applications, electrophoretic deposition (EPD) would be an attractive process for preparing transparent, smooth and thickness-controlled thin coating [5-7]. In this work, for the first time, the EPD process was used to fabricate the Mo₆ metal cluster thin films based the Cs₂Mo₆Br₁₄ and ((n-C₄H₉)₄N)₂Mo₆Br₁₄ precursors.

2.1. Fabrication of the metal cluster and methodology

2.1.1. Fabrication of the hexamolybdenum clusters

Reagent grade chemicals, acetone (99.5 %), methyl ethyl ketone (99%), acetyl acetone (99%), 1-propanol (99.5%) and ethanol (99.5 %), were used without purification. The Cs₂Mo₆Br₁₄ (**CMBP**) cluster compound was synthesized by the reaction between stoichiometric amounts of CsBr and MoBr₂ in a quartz ampoule at high temperature while the ((n-C₄H₉)₄N)₂Mo₆Br₁₄ powder (**TMBP**) was prepared from **CMBP** and TBABr agents by solution chemistry [8, 9].

The MoBr₂ powder was synthesized by solid chemistry at high temperature in N₂ medium. The Mo powder (> 99.99%) was reacted with Br₂ gas in N₂ medium (140 mmHg) at 720°C for 24 hours. Then, the process was stopped to reduce the N₂ gas speed to 120 mmHg. The reaction was continued at 710°C for 24 hours. The synthesized MoBr₂ powder with the productivity of about 75% was collected for next synthesis steps (**Fig. 2.1a**).

The Cs₂Mo₆Br₁₄ cluster was created from the reaction of CsBr (99.9 %) and MoBr₂ powder in Ar medium at 800°C for 3 days by solid chemistry. The temperature program was set up for three steps i) heating to 800°C at scan rate of 1°/min, ii) annealing at 800°C for 2880 min, iii) freezing down to 80°C at scan rate of 0.5°/min. The purification of the Cs₂Mo₆Br₁₄ cluster in acetone by stirring for several days, collecting the transparent solution, and evaporating by hot water to collect the dark yellow-colored powder (**Fig.2.1b**).

The ((n-C₄H₉)₄N)₂Mo₆Br₁₄ cluster was synthesized from the Cs₂Mo₆Br₁₄ cluster by solution chemistry at room temperature. Firstly, Cs₂Mo₆Br₁₄ cluster compound was dissolved in the solution containing distilled water and ethanol (1:1), and HBr (48%) at the pH of 2. The suspension was agitated for 24 hours at room temperature and then collected the transparent cluster solution. Afterward, the (n-C₄H₉)₄N)Br (98%) was slowly introduced in the Cs₂Mo₆Br₁₄ cluster solution and continually stirred for 24 hours at room temperature. The collected solid was purified by H₂O: EtOH (1:1) solution by three times, then dissolved in acetone to obtain the transparent solution. The collected transparent solution was evaporated to obtain the light yellow-colored powder (**Fig. 2.1c**).

The Cs₂Mo₆Br₁₄ and ((n-C₄H₉)₄N)₂Mo₆Br₁₄ clusters were characterized the single crystal X-ray

diffraction. They crystallize in the P31c space group (Nr. 163) with the following lattice parameters: $a = 10.1925(1) \text{ \AA}$, $c = 15.0690(3) \text{ \AA}$, $Z = 2$ [8].

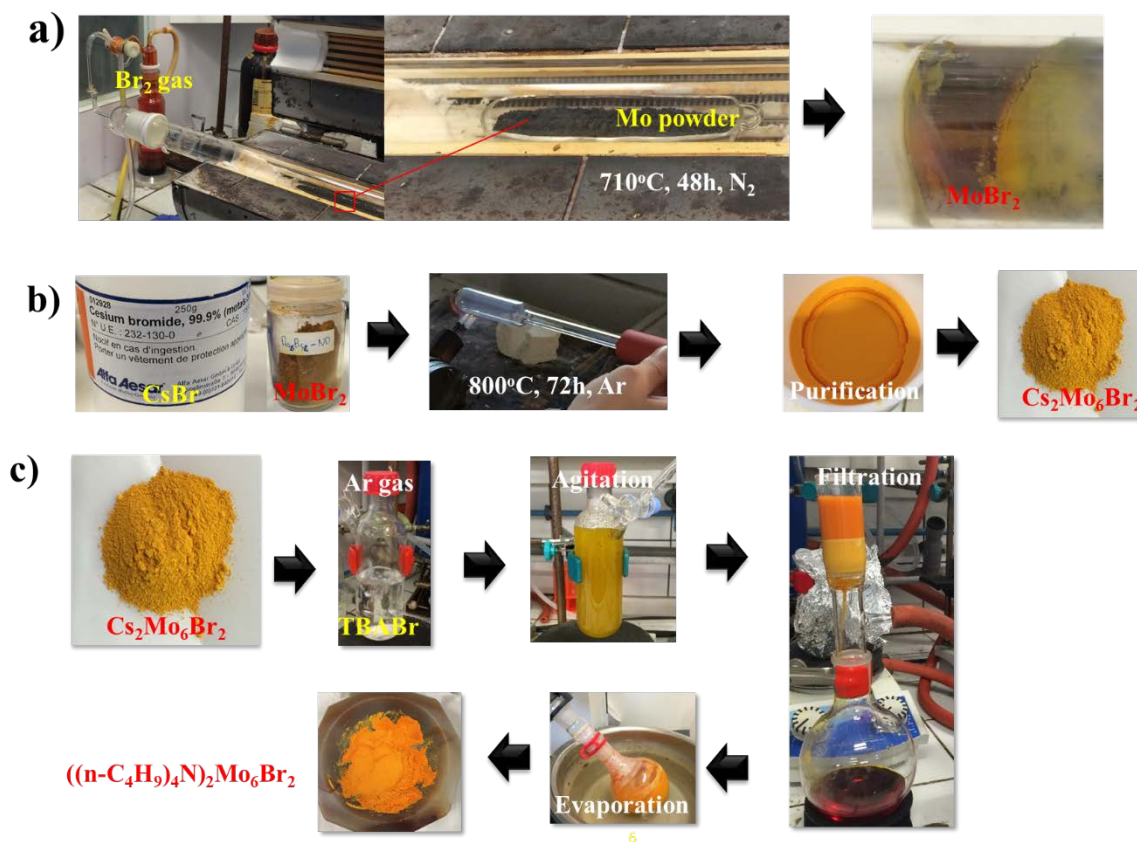


Figure 2.1. The synthesis schemes of: a) MoBr₂ powder, b) the Cs₂Mo₆Br₁₄ cluster and ((n-C₄H₉)₄N)₂Mo₆Br₁₄ cluster.

2.1.2. The EPD system

The sourcemeter (Keithley Model 2400, Ohio, USA) was connected to a stainless steel cathode and ITO glass ($1 \times 1.5 \text{ cm}^2$) (Geomatec Co., Ltd., Tokyo, Japan; $6.15\text{--}7.27 \text{ } \Omega/\text{sq}$) anodic substrate (**Fig. 2.2**). The distance between the electrodes were optimized for the Mo₆ cluster slurry systems. Before applying the EPD process, the ITO glass substrates with a surface area of $1.0 \times 2.5 \text{ cm}^2$ were washed by detergent, then acetone for 30 minutes by sonication. Anodic EPD system including a pair of electrodes, which includes a stainless steel sheet ($4 \times 1 \text{ cm}^2$) as the cathode and ITO glass ($1.0 \times 2.5 \text{ cm}^2$) as the anode, was connected to a DC generator. The EPD process was carried out in the constant voltage mode of 5–50 V during the deposition time within 80 s. During the voltage application, counter cations and [Mo₆Br₁₄]²⁻ anions were deposited on the stainless steel cathode and ITO glass anode, respectively. The area of the cluster-deposited ITO glass was approximately $1.0 \times 1.5 \text{ cm}^2$. The applied voltages and deposition time of the EPD were separately optimized. The prepared Mo₆ cluster thin films were slowly dried in air and

used for characterization of the properties.

2.2. Characterization techniques of the EPD suspension and the Mo₆ film

2.2.1. Suspension

The zeta potential and electric conductivity of the suspensions were measured by a zeta-potential analyzer (Malvern Instrument, Ltd., Zetasizer Nano Z).

The particle size of the cluster in an MEK suspension was measured by a dynamic light scattering (DLS) technique using a Nano Q V2.5.9.0 analyzer (Cordouan Technologies) at the wavelength of 657 nm.

2.2.2. Morphology of thin film

The thickness of the Mo₆ cluster thin films was measured using a color 3D laser microscope (Keyence VK 9700) equipped with a 408-nm violet laser.

The surface morphology of the films and the components of Mo, Br and Cs elements were identified by field-emission secondary electron microscopy (FE-SEM), (S4800, Hitachi High-Technologies Corp.) at 10 kV and an X-ray fluorescence (XRF) measurement (ZSX Primus II, Rigaku Corp.), respectively.

2.2.3. Chemical characterization

The crystallographic structure of the precursor and films was determined by XRD (SmartLab, RIGAKU, 40 kV and 30 mA) in the 2 θ angle range from 5° to 55° and at the scan speed of 1°/min with Cu K α radiation ($\lambda = 1.54 \text{ \AA}$).

The chemical state and composition were verified by coupling several techniques, such as FTIR (Thermoscientific Nicolet 4700) in the wavenumber range from 4000 to 400 cm⁻¹ and XRF measurement (EZS Primus II, Rigaku).

XPS spectra of the powder and film were measured by a PHI Quantera SXM (ULVAC-PHI) using Al K α radiation at 20 kV and 5 mA, neutralization by Ar⁺, pass energy of 55 eV and the take-off angle of 45°.

High resolution observation of the cluster-deposited films was performed by a TEM (JEOL JEM 2100F) equipped with an EDS analysis device. The cluster powder was collected from thin film on ITO coated-glass and dissolved suspension was sonicated to obtain the homogeneous.

The structural identification of the films was determined by XRD (SmartLab, RIGAKU, Tokyo, Japan, 40 kV and 30 mA) in the 2 θ angle range from 5° to 35° at the scan speed of 1°/min using Cu K α radiation ($\lambda = 1.54 \text{ \AA}$).

2.2.4. Optical characterization

Optical absorbance of the Mo₆ cluster films was measured by UV-Vis-NIR spectroscopy (V570, Jasco Corp.) in the wavelength range of 220 to 2000 nm at the scan rate of 400 nm/s.

The emission spectra of the cluster films were obtained by high performance fluorescence spectroscopy (FL) (FP8500, Jasco Corp.) connected to a xenon lamp at the scan rate of 500 nm/s. A micro photoluminescence (PL) system (LabRam HR, Horiba Corp.) with a 325-nm He-Cd laser system was used to record the emission peak in the wavelength range of 350 nm and 1000 nm and the photoluminescent (PL) profile during the irradiation for 600 s.

2.3. The thin, homogeneous and transparent Mo₆ film by EPD process

To achieve a homogeneous microstructure, the metal clusters have to be dissolved in a solvent to prepare a uniform solution. We selected several appropriate dispersing media to obtain a stable and transparent suspension for the Cs₂Mo₆Br₁₄ cluster compound. The Mo₆ clusters were fixed as a thin layer on the ITO-coated glass (anode) by the EPD process, then the applied voltage and deposition time parameters were optimized. Finally, the Mo₆ cluster thin films were fully characterized the morphology, structure and optical properties.

2.3.1. Preparation of the Mo₆ cluster solution and fabrication of the thin films by electrophoretic deposition (EPD)

The distilled water, ethanol, 1-propanol, acetone, MEK or acetyl acetone solutions were selected as the dispersing media of the as-synthesized Cs₂Mo₆Br₁₄ cluster nanoparticles at the concentration of 5g per liter. In the case of ethanol, adding a little amount of water was necessary to prepare the transparent cluster solution (**Fig. 2.2**). All the solutions were magnetically stirred; suspensions from distilled water and 1-propanol were stirred for 24 hours and from acetyl acetone for 6 hours to obtain the stabilization, while others for 10 min. The suspensions were recorded the pH value at room temperature. Afterwards, the zeta potential and conductivity of the Mo₆ cluster suspensions were necessary to measure by a zeta-potential analyzer. The “operational pH”, which was measured by a pH meter (TOA Corp., HM-14P) calibrated for an aqueous solvent should be different from the real p_{aH} in nonaqueous solvents, was used in this study for the sake of convenience ^[10].

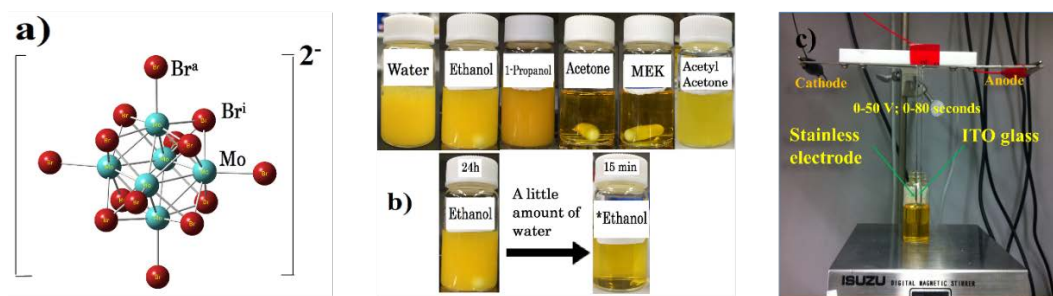


Figure 2.2. a) Scheme of the octahedral structure of $[\text{Mo}_6\text{Br}_8\text{Br}_6]^{2-}$ metal cluster; b) slurries of $\text{Cs}_2\text{Mo}_6\text{Br}_{14}$ clusters dissolved in distilled water, ethanol, 1-propanol, acetone, MEK and acetylacetone b) Schematic representation of anodic EPD for preparing Mo_6 cluster functional thin film.

Anodic EPD systems including a pair of electrodes, which include a stainless steel sheet ($4 \times 1 \text{ cm}^2$) as the cathode and ITO glass ($1.0 \times 2.5 \text{ cm}^2$) as the anode, were connected to a DC generator (Keithley Instruments, Inc., SourceMeter Model 2400) (**Fig. 2.1b**). The EPD was carried out in the constant voltage mode of 5–50 V during the deposition time within 80 s. The area of the cluster-deposited ITO glass was approximately $1.0 \times 1.5 \text{ cm}^2$. The applied voltages and deposition time of the EPD were separately optimized for each different solvent. The deposit weight was determined by subtracting the weight of the ITO glass before and after the EPD. The prepared Mo_6 cluster thin films were slowly dried in air and used for characterization of the properties.

2.3.2. Characterization of the suspension, the Mo_6 film and optical properties

Zeta potential and conductivity

Figure 2.3 shows the electric conductivity and zeta potential of the $\text{Cs}_2\text{Mo}_6\text{Br}_{14}$ cluster solutions. All the solutions showed a negative zeta potential probably due to the existence of the agglomeration, but partially-dissociated $[\text{Mo}_6\text{Br}_{14}]^{2-}$ units. In the cases of acetone, MEK, acetyl acetone and ethanol, fully transparent $\text{Cs}_2\text{Mo}_6\text{Br}_{14}$ cluster solutions were obtained after stirring, suggesting the dissociation and homogeneous dispersion of the $\text{Cs}_2\text{Mo}_6\text{Br}_{14}$ cluster compound as Cs^+ cations and $[\text{Mo}_6\text{Br}_{14}]^{2-}$ anions in the solvents. The difference in the electric conductivity was another important factor reflecting the degree of the dissociation of the $\text{Cs}_2\text{Mo}_6\text{Br}_{14}$ clusters into Cs^+ ions and $[\text{Mo}_6\text{Br}_{14}]^{2-}$ cluster units. It was observed that the electric conductivity of the solution in distilled water reached the highest value (0.895 mS/cm) when the absolute value of the zeta potential was the lowest (-5.42 mV). It is probable that the Cs^+ cations with a small size, dissociated from the $\text{Cs}_2\text{Mo}_6\text{Br}_{14}$ cluster compound, significantly dispersed in water creating a high conductivity in the solution. Consequently, the high mobility of Cs^+ free ions in water may be the dominant carriers in the solution under the applied electric field, which may reduce the movement of the $[\text{Mo}_6\text{Br}_{14}]^{2-}$ anionic clusters [11]. The 1-propanol solution has a low conductivity (0.022 mS/cm), which could reduce the mobility of the ions under the applied voltages and thus prevent the $[\text{Mo}_6\text{Br}_{14}]^{2-}$ anions from obtaining the necessary electrophoretic mobility to move toward the anode. Suitable values of the electric conductivity (0.26 - 0.47 mS/cm) and zeta potential (-

10.6 to -25.3 mV) were obtained for the acetone, MEK, ethanol and acetyl acetone solutions.

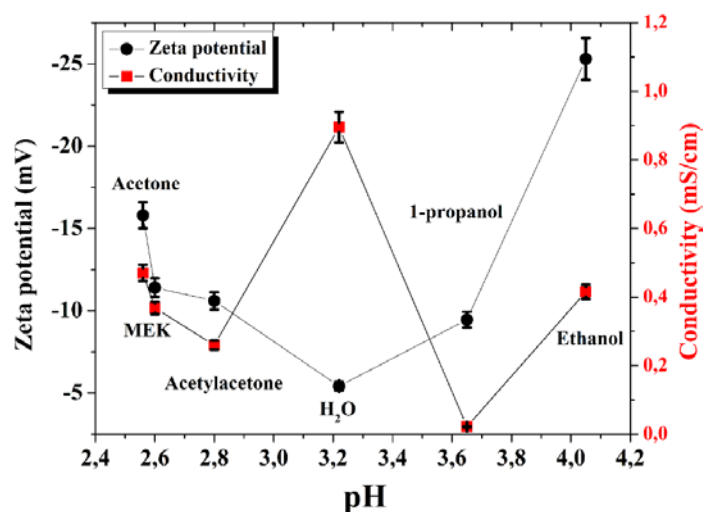


Figure 2.3. Relation of zeta potential and conductivity versus pH of the $\text{Cs}_2\text{Mo}_6\text{Br}_{14}$ solutions from different solvents.

Since all the solutions have negative zeta potential values, the anodic EPD process was applied to all the $\text{Cs}_2\text{Mo}_6\text{Br}_{14}$ solutions. **Figure 2.4** shows the films obtained from the different solutions under visible and 324 nm light. Yellow thin films were obtained from the acetone, MEK, acetyl acetone, and ethanol solutions by the anodic EPD process. The yellow films exhibited photoluminescence with a red color during the irradiation of 324-nm wavelength light. This clearly visible red luminescence to the naked eye was a simple first proof of the successful deposition of the $[\text{Mo}_6\text{Br}_{14}]^{2-}$ cluster unit on the ITO glass surfaces.



Figure 2.4. The Mo_6 cluster thin films deposited from (left to right) water, ethanol, 1-propanol, acetone and MEK solutions at 15 V for 20 s and from acetyl acetone solution at 50 V for 40 s (upper), respectively. Image of the luminescence of the cluster thin films irradiated at 324 nm wavelength (under).

Figures 2.5a and 2.5b show the relation of the initial current density and the total deposited weight versus applied voltage (5 V-50 V) during the deposition for 30 s for all the solutions, respectively. When the applied voltage increased, ions in the solution quickly moved between the two electrodes, and consequently, the current density increased (**Fig. 2.5a**). The fastest rate was observed for water solution,

while the slowest rate was in the 1- propanol solution, and similar increasing trends for the other solvents. The deposited weight of the films from the water, 1-propanol and acetyl acetone solutions hardly changed while maintaining the amount lower than 0.5 mg/cm^2 even by increasing the applied voltages to 50 V (**Fig. 2.5b**). According to Hamaker's mass balance law, the deposition yield of charged particles should be proportional to the applied electric field strength and the current should be proportional to the applied voltage ^[12]. The results observed for the films from the MEK, ethanol and acetone solutions were relatively consistent with this law in the range of applied voltages lower than 30 V. However, the deposited weight of the films from the ethanol, acetone, and MEK solutions once reached the maximum at 1.59 mg/cm^2 (25 V), 1.62 mg/cm^2 (25 V) and 2.47 mg/cm^2 (30 V), respectively, and then gradually decreased. In general, a high applied voltage increases the migration of the particles to the electrode, and consequently, increase the amount of deposit on the electrode. Accumulation of the clusters on a substrate is achieved by interaction between the clusters and the electrode surface. If the velocity of the clusters to the electrode is too fast, there will not be enough time to make them lose their negative charge by interacting with the substrate; they could be repelled due to the counter force between the clusters on the electrode surface. In addition, at a high velocity, the movement of the particles to the electrode may be disturbed and the collision between the particles when moving may occur, restricting the deposition of the particles closely packed on the electrode ^[13]. As a result, the amount of deposit on the films decreased with an applied voltage higher than 30 V. As an exception, the deposited cluster amount was 0.65 mg/cm^2 at 50 V which was more than twice the value at the lower voltages (0.24 mg/cm^2) in the case of the acetyl acetone solution. For this reason, the applied voltage of 50 V was selected to investigate the deposition property only for the acetyl acetone solution. Fifteen V was selected for the films prepared from the other solutions due to most of them obtaining a relative homogeneity over the entire ITO surface. At an applied voltage higher than 15 V, the cluster films started to appear as a U-shaped line at the edge of the ITO surface. The selection of the applied voltage for the films depended on the stabilization and homogeneity of the films.

Figures 2.5c and 2.5d show the relation of the current density and deposit weight versus the deposition time. With the increasing deposition time, the current density decreased and the deposit amount sharply increased at the early stage of the deposition (**Fig. 2.5c**). This behavior was recognized in the first 40 s since there was coagulation between the clusters. However, detachment and removal of the deposited cluster agglomerates were visibly recognized in the beaker during the EPD after 40 s. This trend was remarkable in the water solution. The maximum deposition weight were similarly recorded for the films prepared from the MEK (2.25 mg/cm^2), acetone (1.65 mg/cm^2) and ethanol (1.85 mg/cm^2) solutions in 40 s at 15 V (**Fig. 2.5d**). Although the film from the acetyl acetone solution was still formed at 50 V, the deposition weight was not very much at the highest value (1.12 mg/cm^2). The deposition amount of the clusters in the water and 1-propanol solutions was very small and the maximum value was not clearly observed. During the EPD process, the applied potential is reduced by potential drops at the electrodes (electrode potential) and in the suspension ^[12]. Though the potential applied between the two electrodes is maintained constant, the effective potential applied to the suspension decreases due to the

ohmic loss by the deposition layer on the electrode [13, 14], causing a decrease in the electrophoretic mobility and pressing force of the charged species onto the counter electrode. Following the scaling theory [15], if no electrochemical interaction occurs, the particle charge would be balanced with the charge of the electrode. Estrelia-Lopez et al. have suggested that the particles are immobilized on the electrode by interacting with irreversible ions produced from the electrical reaction and dipole interaction [16]. In the case of the $[\text{Mo}_6\text{Br}_{14}]^{2-}$ anions, during the EPD process, the small cluster groups (100 nm) of the first layers are immobilized by balancing the charge with the H_3O^+ cations and the charge on the electrode, along with a dipole interaction in the electric field. Between the clusters, there exist van der Waals interactions between the halogen ligands. On the other hand, cations could diffuse into the still negatively charged cluster deposit to balance the charge and produce an ion interaction. In addition, Bohmer interpreted that the aggregation decreased if the ion strength increased [17]. At the longer deposition time, when the distance between the large negative cluster particles is shorter than the diameter of the cluster particle, an electrostatic repulsion between the clusters will be generated. In summary, there are three possible reasons for breaking up the cluster layers at a long deposit time: i) the field strength decreases because the cluster layers acting as a resistance, ii) the electrostatic repulsion increases between the large negative particles, and iii) the ion interaction strength increases because the free cations that diffused in the outside cluster layer increased.

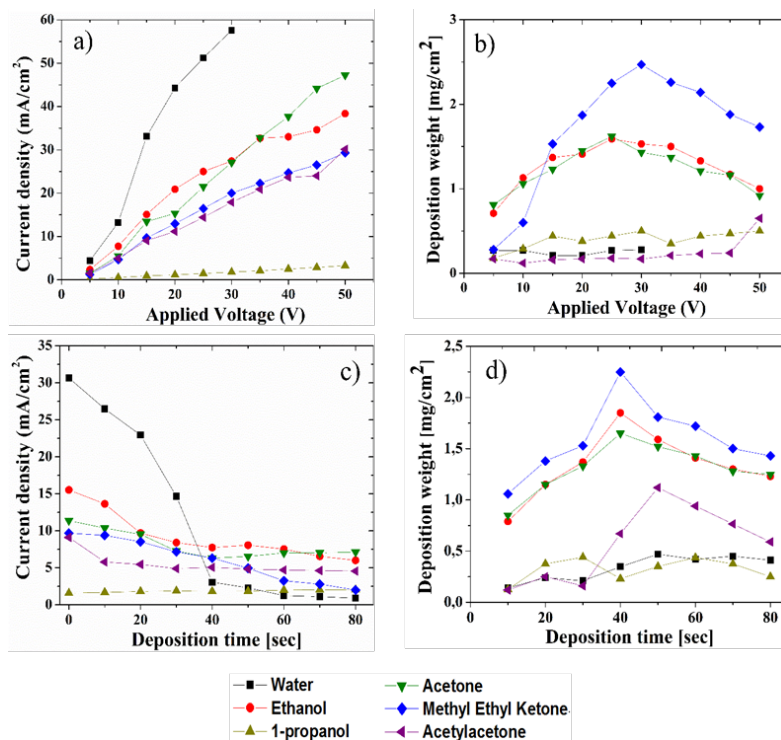


Figure 2.5. The dependence of a) current density at 0 s and b) deposition amount for 30 s on applied voltage; c) current density and d) amount of deposition on deposition time of the Mo_6 cluster films prepared from the ethanol, water, MEK, acetone, and 1-propanol solutions at 15 V and from acetyl acetone solution at 50 V.

By considering the results of the zeta potential, conductivity, current density and deposition amount during the EPD process, especially in terms of the stabilization of the solutions and the uniformity of the films, the optimized applied voltage and deposition time were determined at 15 V between 10 and 30 s for the acetone, MEK and ethanol solutions and at 50 V for 40 s for the acetyl acetone solution. The $\text{Cs}_2\text{Mo}_6\text{Br}_{14}$ suspensions in MEK, ethanol, acetone and acetyl acetone solutions seem relevant for the fabrication of a homogeneous film during the EPD process.

Morphology and structure

The film parameters using the optimized parameters were characterized by the thickness measurement, morphology observation, Br/Mo atomic ratio measurement and XRD analysis of the crystallographic parameters. **Figure 2.6** shows the surface images of the fabricated layers on the ITO glass observed by FE-SEM. It could be seen that the Mo_6 cluster films prepared from the water and 1-propanol solutions have small grains of cluster crystals with the size about 5 μm and are embedded on the surface of the ITO glass. The film prepared from the 1-propanol solution has a higher density and smaller grain size than that from the water solution. Cluster nanoparticles were very easily dissolved in the acetone, ethanol, MEK, and acetyl acetone solutions; consequently, the deposit surfaces showed smooth and homogeneous morphology and no presence of any cluster crystals under the observation at 500 and 10,000 magnifications. However, some of the thin films, especially in the case of ethanol, were cracked and peeled off from the substrates after drying in air.

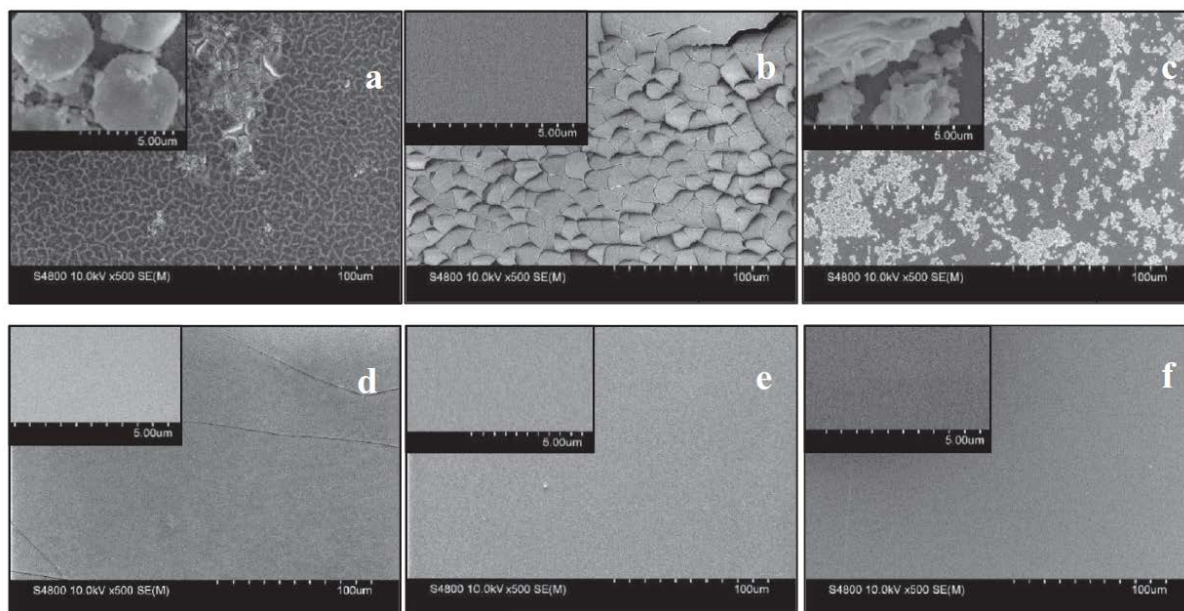


Figure 2.6. FE-SEM morphology on the surface of the Mo_6 cluster films prepared from a) distilled water; b) ethanol; c) 1-propanol; d) acetone; e) MEK solutions at 15 V for 20 s; and f) acetyl acetone solution at 40 V for 10 s, with 500 and 10,000 magnifications.

The thickness of the thin films prepared from the different solvents was measured by color 3D laser microscopy at a high resolution. The results are shown in **Table 2.1**. For the ethanol, acetone and MEK solutions, the thickness of about 1 μm was attained in the first 10 s and it increased to 2 μm when the deposition time was 20 s. In contrast, the thickness of the film from the acetyl acetone solution was very thin ($0.76 \pm 0.04 \mu\text{m}$) even though the EPD was performed at a high applied voltage (50 V) and for a longer deposition time (40 s). When acetyl acetone was used as the dispersion medium, the thickness of the deposited layer was the thinnest although the obtained suspension was stable. The low conductivity of the suspension in the acetyl acetone could be the reason for this behavior. The suitable thickness of the cluster film could be regulated by altering the deposition time and applied voltage during the EPD process.

Table 2.1. Thickness and Br/Mo atomic ratio of the Mo_6 cluster films prepared from different solvents.

Sample	Thickness (μm)	Br/Mo atomic ratio
$\text{Cs}_2\text{Mo}_6\text{Br}_{14}$	-	2.20 (theoretical)
Water 20s	N/A	N/A
1-Propanol 20s	N/A	N/A
AA(40s, 50V)	0.76 ± 0.04	3.41
Ethanol 10s	0.82 ± 0.07	2.96
Ethanol 20s	2.00 ± 0.14	1.74
Acetone 10s	0.86 ± 0.13	2.09
Acetone 20s	1.76 ± 0.09	1.92
MEK 10s	1.12 ± 0.08	2.73
MEK 20s	1.85 ± 0.17	2.26
MEK30s	2.11 ± 0.09	2.18

Pure Mo_6 bromide cluster films, which have not been yet reported in the literature to the best of our knowledge, were successfully fabricated using the EPD process. The results of XRF measurements indicated that no Cs elements are present in the deposited film. Interestingly, the atomic ratio of Br/Mo of the powder measured by XRF was not significantly different from those of the theoretical index while the ratios of Br/Mo in the thin films fabricated in 10 s were higher than the theoretical ratio of the $\text{Cs}_2\text{Mo}_6\text{Br}_{14}$ powder. This implies that Br rich layers were prepared on the ITO glass in the first 10 s of the EPD process. The Br^- anion would originate from the $\text{Cs}_2\text{Mo}_6\text{Br}_{14}$ cluster compound during the dissolving, stirring and deposition in the solvents. The solvent could partially dissociate the $\text{Cs}_2\text{Mo}_6\text{Br}_{14}$ cluster compound and separate the Br^- ions out of the apical ligand positions of the octahedral blocks, reducing the negative charge on the surface of the $\text{Cs}_2\text{Mo}_6\text{Br}_{14}$ cluster nanoparticles. This reaction might

be accelerated by the applied electric field. For the 20 s deposition time, the Br/Mo atomic ratios of the films prepared from the acetone (1.92) and ethanol (1.74) solutions were remarkably lower than those of the original Cs₂Mo₆Br₁₄ powder (2.20), while it reached a stable value for the films from the MEK solution (2.26 at 20 s and 2.18 at 30 s). In solution, the compound is fully dissociated into the Cs⁺ cations and [Mo₆Brⁱ₈Br^a₆]²⁻ anions; however, it is known that [Mo₆Brⁱ₈Br^a₆]²⁻ can react with solvent to form species like [Mo₆Brⁱ₈Br^a₅(solvent)^a]¹⁻ and one Br⁻, or [Mo₆Brⁱ₈Br^a₄(solvent)₂]⁰ and two Br⁻ ions. It has also been reported that the apical Br atoms of the Mo₆ clusters are easily replaced by H₂O or OH⁻ molecules to form the compound of Mo₆Brⁱ₈Br^a₄(H₂O)₂ or [Mo₆Brⁱ₈Br^a_{6-x}(OH)_x]²⁻,^[18, 19] respectively. The decrease in the Br/Mo ratio reduces with the increasing deposit time means that the structure of the octahedral clusters is continually transferred at different deposition times under the impact of the electric field. In addition, during the EPD process, dissociated Cs⁺ cations migrate to the cathode and deposit there, while the electrolysis of water molecules takes place at the anode to generate "H⁺" cations, combining with H₂O molecules to produce H₃O⁺ cations. These H₃O⁺ cations would neutralize the negative charge of the Mo₆ clusters leading to deposition on the surface of the ITO glass substrate. The framework of the Mo₆ octahedral clusters depends on the ratio and classification of anions and counter cations. Based on these hypotheses, a general formulation of the cluster particles inside layer could be tentatively estimated as [H₃O⁺]_{6+x+2}[Br⁻]_{6+x} [(Mo₆Brⁱ₈Br^a_{6-x}(OH)_x]²⁻. For example, the Br/Mo ratio of the film prepared from acetyl acetone is 3.41, which is close to twenty Br atoms corresponding to six Mo atoms, thus the formation of the octahedral cluster structure could be suggested to be [H₃O⁺]₈[(Br)₆(Mo₆Br₁₄)²⁻] or [H₃O⁺]₁₄[(Br)₁₂(Mo₆Br₈(OH)₆)²⁻] with x = 0 or 6. The formation of the Mo₆ cluster will be specifically demonstrated in a future investigation.

Figure 2. 7 shows XRD patterns of the ITO glass, Cs₂Mo₆Br₁₄ powder and thin films prepared by the EPD from the ethanol, acetone, and MEK solutions at 15 V for 20 s, and from the acetyl acetone solution at 50 V for 40 s. Diffraction peaks of the Cs₂Mo₆Br₁₄ powder are obvious and the signal to noise ratio is strong, while the peaks are unclear and broad for the deposited films. The broadening of the diffraction peaks around the 2θ angles of 11° and 31°, observed on the patterns of the Mo₆ cluster films prepared from the acetone, MEK, acetyl acetone and ethanol solutions, is probably due to the smaller crystallite sizes in the films compared to powder but are also strongly influenced by the thickness of the films and local distortion of the crystal structure from the ITO interface. The dissolution of the Cs₂Mo₆Br₁₄ powder, the cationic metathesis and the solvation implies a packing arrangement of cluster units in the deposited films different from that observed in the Cs₂Mo₆Br₁₄ powders. It could be suggested that the original frameworks of the Mo₆ cluster were modified in the film deposited on the ITO glass by substituting the counter cations as already discussed. The stability of the octahedral structure of the Mo₆ clusters in a solvent was very important regarding the prominent luminescent property. Therefore, MEK would be the most suitable solvent for dissolving the Cs₂Mo₆Br₁₄ cluster compound and maintaining the stability and transparency of the solution during the EPD process.

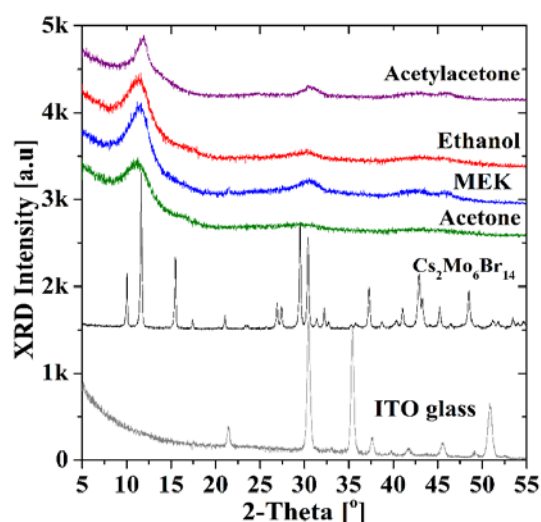


Figure 2. 7. X-ray diffraction diagram of ITO glass, the $\text{Cs}_2\text{Mo}_6\text{Br}_{14}$ powder and the thin films prepared by the EPD from ethanol, acetone, MEK solutions at 15 V for 20 s and acetyl acetone solution at 50 V for 40 s.

Optical properties

The homogeneity, transmittance and optical properties of the Mo_6 cluster thin films were clearly confirmed by UV-Vis spectroscopy. **Figure 2.8** shows the UV-Vis spectra measured for the ITO-coated glass, the cluster solution dissolved in the MEK solution, and the films fabricated from the different solutions. As illustrated in the UV-Vis absorption spectra, the films prepared from the water and 1-propanol solutions showed similar profiles to the ITO-coated glass; the adsorption edge wavelength is 375 nm (**Fig. 2.8b**). On the other hand, two strong adsorption peaks at 330 nm and 382 nm were recognized for the $\text{Cs}_2\text{Mo}_6\text{Br}_{14}$ clusters dissolved in the MEK solution (**Fig. 2.8a**), while the light absorptions at the wavelengths lower than 580 nm were recorded for the films from the ethanol, acetone, MEK and acetyl acetone solutions (**Figs. 2.8b, c, d, and e**). The UV-Vis absorption spectra of the Mo_6 cluster films were the combination of the absorption by the $[\text{Mo}_6\text{Br}_{14}]^{2-}$ clusters and that of the ITO glass. Not only the transparent property, but also the extended absorption wavelength in the visible light range for the cluster functionalized ITO surface would be another positive characteristic of the film as a band pass filter. A significant feature in the UV-Vis absorption spectra of the thin films is the existence of several peaks with different absorption bands in the range from 580 nm to 2000 nm. The appearance of these peaks originated from the interference phenomena of the incident and reflected lights by the cluster film overlapping with the attenuation peak due to the absorption by the ITO in the wavelength range higher than 580 nm. Therefore, many new strong absorption peaks appeared with gradually increasing intensities. When a film has a good transparency, the interference reflection regularly appears in the absorption spectrum. The interference peaks appeared in the film deposited from the MEK solution for 10 to 30 s (**Fig. 2.8c**), from the ethanol solution for 10 s (**Fig. 2.8e**) and from the acetyl acetone solution for 40 s (**Fig. 2.8b**), showing the homogeneous property of these films while the interference peaks did not appear for the film from the acetone solution (**Fig. 2.8d**). The number and

position of the interference peaks depend on the thickness of the transparent Mo₆ cluster film. Four peaks appeared for the film from the acetyl acetone solution (0.76 μm thick) the same as the film from the ethanol solution (0.82 μm), but the number of peaks increased in the film from the MEK solution deposited in 30 s (2.11 μm).

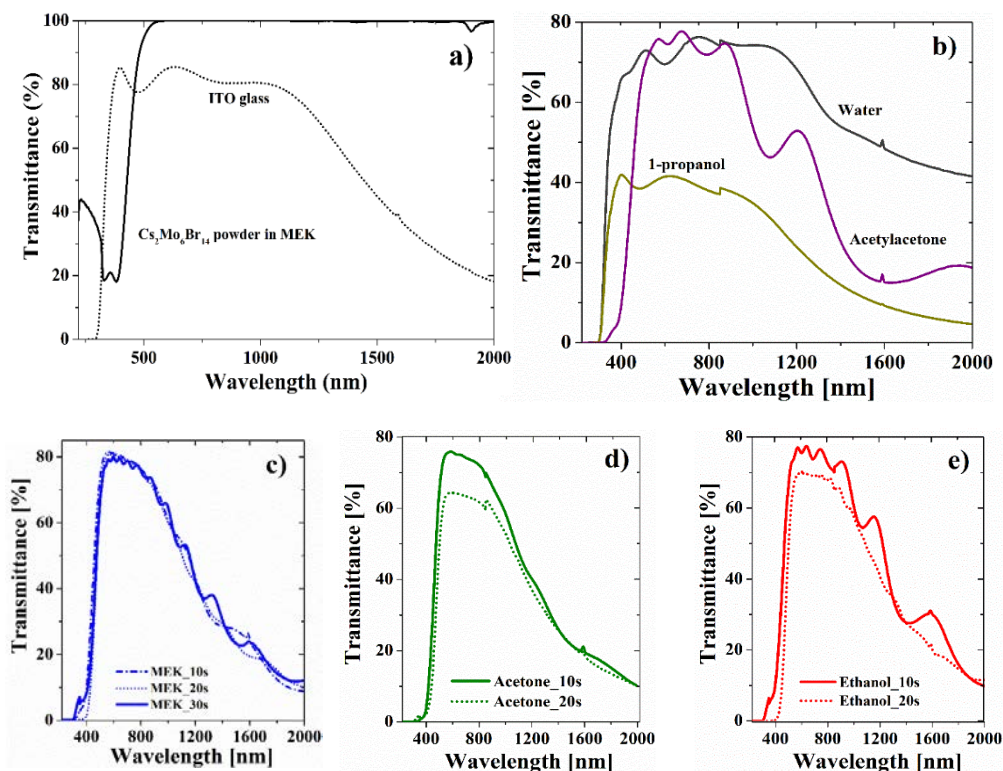


Figure 2.8. UV-Vis transmission spectra of a) ITO glass, Cs₂Mo₆Br₁₄ powder dissolved in MEK solution, Mo₆ cluster films prepared from b) distilled water, 1-propanol and acetyl acetone, c) MEK, d) acetone, and e) ethanol solutions. The Mo₆ film from the acetyl acetone solution was prepared by the EPD at 50 V for 40 s while the films from the other solutions were prepared at 15 V for 20 s.

The photoluminescence excitation (PLE) is another important property to characterize the Mo₆ cluster films prepared on ITO glasses by the EPD process. The PLE spectra of the Cs₂Mo₆Br₁₄ powder and the Mo₆ cluster films under a xenon lamp are shown in **Figure 2.9**. In the excitation spectra of the Cs₂Mo₆Br₁₄ powder shown in **Figure 2.9a**, excitation peaks sharply appear at 370 nm, low at 275 nm and broad at around 430 nm and 480 nm. Most of the cluster thin films exhibited peaks at the wavelengths of 275 nm, 370 nm and 430 nm, like the cluster powder, except for the film from acetone which did not show any clear peaks. It was also predicted that the high symmetry of the [Mo₆Br₁₄]²⁻ clusters was partially broken because of the prominent solubility in acetone. **Figures 2.9b and 2.9c** show emission spectra monitored in the range from 500 nm to 850 nm when the films were excited at the 275 nm and 370 nm wavelengths, respectively. Except for the film from the acetone solution with a significantly low intensity, the other films showed large, broad emission peaks in the visible light range (685 nm - 700 nm). The peak position was at 680 nm for the Cs₂Mo₆Br₁₄ powder, at 685 nm for the film

from the MEK solution and at 690 nm for the film from the acetyl acetone solution, with relatively strong intensity. As a result, the MEK and acetyl acetone solutions would be good dispersing media for the $\text{Cs}_2\text{Mo}_6\text{Br}_{14}$ cluster nanoparticles to maintain their PL property. The change in the PL excitation and emission spectra could be explained by i) change in the ligands environment, and ii) a higher symmetry of the cluster unit in the starting compound and after deposition [20].

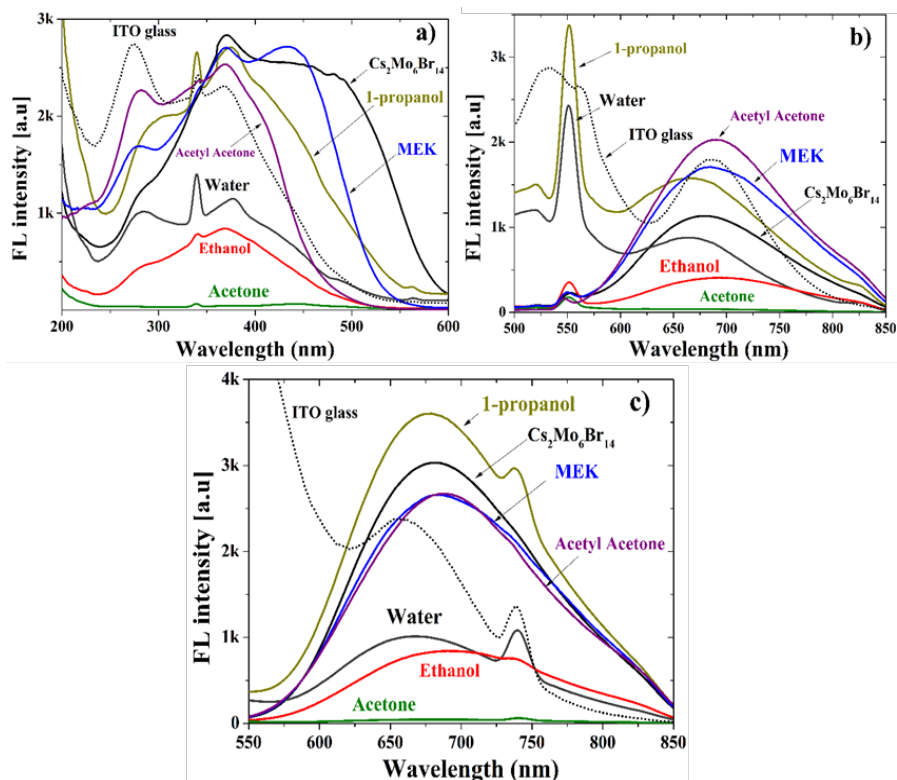


Figure 2.9. a) Photoluminescent excitation (PLE) spectrum monitored at 680 nm; b) Emission spectra excited at 275 nm and c) Emission spectra excited at 370 nm of ITO glass, $\text{Cs}_2\text{Mo}_6\text{Br}_{14}$ powder, Mo_6 cluster films prepared from water, 1-propanol, ethanol, acetone and MEK solutions at 15 V for 20 s and from acetyl acetone solution at 50 V for 40 s.

The PL property and optical stabilization of the Mo_6 cluster thin films under continuous irradiation by a 325 nm laser for 600 s are shown in **Figure 2.10**. All the films display strong emissions in the range from 550 to 1000 nm, which is characteristic of the $\text{Cs}_2\text{Mo}_6\text{Br}_{14}$ cluster. In **Figure 2.10a**, it seems that two main emission peaks appeared at 757 nm and 761 nm for the films prepared from the ethanol solution (0.82 μm thick), at 707 nm and 757 nm for the films from the acetyl acetone solution (0.76 μm), and at 720 nm and 776 nm for the films from the MEK solution (1.12 μm). When increasing the thickness of the film to 2 μm , one abroad peak appeared for the films from the ethanol solution (753 nm) and acetone solution (723 nm) with a reduced emission intensity. Emission for the films from the MEK solution included several peaks overlapped at 680, 725, 782 and 858 nm for a film having a 1.82 μm thickness and at 680, 716, 768, 825 and 916 nm for the film having a 2.11 μm thickness. The

appearance of new emission peaks for the homogeneous and thicker films prepared from the MEK solution means a change in the electron excited states of the deposited layer from the as-synthesized powder. It has been proved that the luminescence of the $[\text{Mo}_6\text{Br}_8\text{Br}^a_6]^{2-}$ cluster unit is a multicomponent emission that results from four possible excited states that differ from each other by their geometry. Thus each phenomenon that changes the geometry of the units (counter cations, solvation effects, defects...) implies modifications of the shape of the photoluminescence spectra [20]. The intensity of the PL spectra decreased with time during the continuous irradiation of the 325 nm laser on the deposited films as shown in **Figure 2.10b**. The PL intensity of the film from the ethanol solution deposited for 10 s strongly decreased (23.9 %) in the first 120 s and was 43.6 % in 600 s of the irradiation. A similar decreasing trend occurred in the film deposited in 20 s from the ethanol solution. The PL intensity reduced 50.5 % in 600 s for the film from the acetyl acetone solution (15 V and 40 s), while there was no obvious change for the film deposited for 10 s and 20 s from the acetone solution. Similarly, the film deposited for 10, 20 and 30 s from the MEK solution reduced 35.7 %, 31.7 % and 27.2 % in the 600 s irradiated time, respectively. The PL emission of the film from the MEK solution was more stable than those of the other films at a similar thickness and the emission stabilization was improved corresponding to the increase in the thickness. The appearance of the new peaks and the attenuation of the PL intensity will be related to the impurity states, defects, and/or change in the local cluster geometry which might be introduced during the dissolution and deposition of the clusters. The pathways of the valence electrons are metal-metal charge transfer and metal-ligand-metal charge transition through the localized orbital of the metallic core and ligands [20, 21]. The localized orbitals may stably store the valence electrons. When the amount of the Mo_6 clusters on the ITO glass increases, it achieves a close-packed assembly of the localized orbitals between the Mo_6 clusters. It is necessary to determine the origin of this excellent behavior of the Mo_6 clusters in the future.

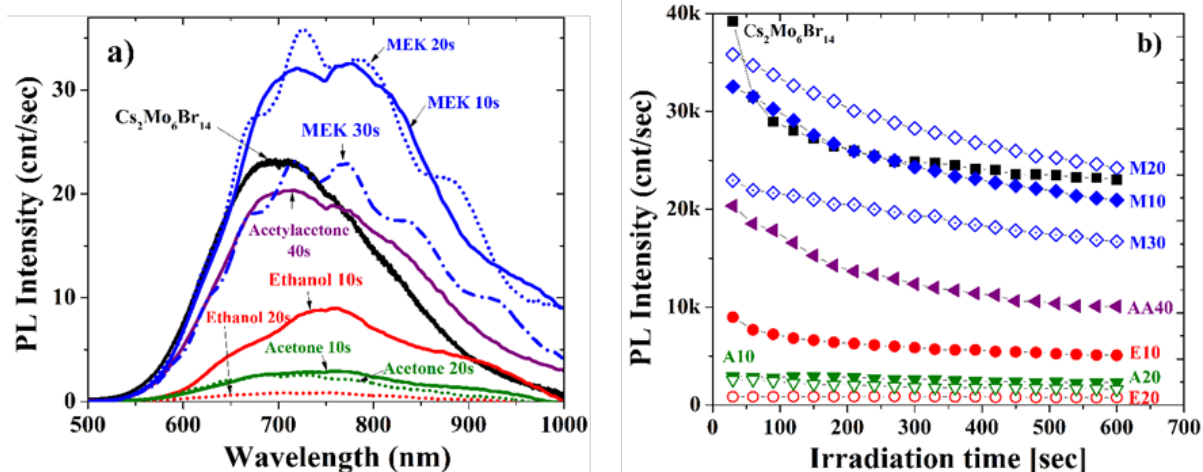


Figure 2.10. a) Photoluminescence spectroscopy at 325 nm by excitation laser and b) emitting stabilization of the Mo_6 cluster thin films at different emissions by irradiation at 325 nm laser light for 600 s. The films prepared from the ethanol (E10, E20), acetone (A10, A20) and MEK (M10, M20, M30) solutions fabricated at 15 V for 10, 20 and 30 s, and from acetyl acetone (AA40) solution fabricated at 50 V for 40 s.

2.3.3. Conclusions

The MEK and acetyl acetone solutions strongly dissolve the $\text{Cs}_2\text{Mo}_6\text{Br}_{14}$ cluster compound to obtain well dispersed colloid suspensions of Cs^+ and the $[\text{Mo}_6\text{Br}_8^i\text{Br}_6^a]^{2-}$ cluster unit which can remain stable during the following EPD process. Homogeneous and smooth deposited layers of Mo_6 clusters containing no Cs^+ cations were successfully obtained for the first time after optimizing the applied voltage and deposition time. Furthermore, the Mo_6 thin films prepared from the MEK and acetyl acetone solutions presented a strong UV-Vis absorption (less than 580 nm) with many absorption peaks from 500 nm to 2000 nm. They also exhibited a strong transparency and phosphorescent emission when excited at the wavelengths of 275 nm and 370 nm. The PL intensity of the films prepared from the MEK solution was improved with the increasing thickness of the film. The Mo_6 cluster films fabricated by the EPD still retained the prominent emission properties of the raw material. The deposition mechanism of the Mo_6 clusters on the ITO glass by the EPD and specific Mo_6 octahedral structure will be further explored in the future. The molybdenum octahedral cluster film on the ITO glass due to the prominent transmittance and luminescence will have a significant effect on the field of optical materials for LED or solar cell devices [22, 23].

2.4. Formation mechanism of transparent Mo_6 metal atom cluster film prepared by electrophoretic Deposition

From the results of the previous report, Methyl Ethyl Ketone (MEK) was evidenced as the stably dispersing medium in order to remain the original luminescent characterization of the $\text{Cs}_2\text{Mo}_6\text{Br}_{14}$ cluster precursors [24]. In this work, we used $\text{TBA}_2\text{Mo}_6\text{Br}_{14}$ (TBA = Tetra Butyl Ammonium, $((\text{n-C}_4\text{H}_9)_4\text{N})$) and $\text{Cs}_2\text{Mo}_6\text{Br}_{14}$ as the raw materials. The main objectives are to (i) select the best cluster precursor in order to obtain good quality Mo_6 cluster films and (ii) evaluate the stability of the $\text{Cs}_2\text{Mo}_6\text{Br}_{14}$ and $\text{TBA}_2\text{Mo}_6\text{Br}_{14}$ cluster compounds in Methyl Ethyl Ketone (MEK). Indeed, in MEK solution, the Br^- ligands may be partially replaced and released out of the octahedral cluster during the dissolving and depositing procedures. The deposition mechanism to fabricate a transparent Mo_6 cluster film by the EPD process and the structure of the obtained film were studied for the first time as far as we know by using complementary tools and techniques.

2.4.1. Preparation suspensions and the Mo_6 cluster films by EPD process

The $\text{Cs}_2\text{Mo}_6\text{Br}_{14}$ powder (*CMBP*) and $((\text{n-C}_4\text{H}_9)_4\text{N})_2\text{Mo}_6\text{Br}_{14}$ (*TMBP*) suspensions were similarly prepared in 2.1.1 part, separately dissolved in reagent grade methyl ethyl ketone (MEK) at the concentration of 5g/L with agitating by a magnetic stirrer for 20 minutes. The *CMBP* and *TMBP* cluster-containing suspensions in the MEK solvent presented an electric conductivity of approximately 0.3 mS/cm and a negative zeta potential in the range of 20 and 25 mV as listed in **Table 2.2**. These values

are slightly different compared to those in our previous study. It is related to the stirring time, which was optimized in order to achieve a good colloidal liquid and a thick film by the EPD. The dissolution of *TMBP* in MEK is quicker than for *CMBP* due to the better compatibility of the TBA⁺ cation in an organic solvent. Nevertheless, the hydrodynamic diameters of the *CMBP* and *TMBP* clusters in the MEK solution (1g/L) obtained by DLS were in the same range of 11±1 and 13±1 nm, respectively. It could correspond to an aggregate of less than 1000 [Mo₆Br₈Br^a]₆²⁻ cluster units [25].

Table 2.2. Physical properties of the *CMBP* and *TMBP* cluster suspensions in MEK solutions.

Suspension (5g/L in MEK)	Conductivity (mS/cm)	Zeta potential (mV)	DLS Particle size (nm) (1g/L in MEK)
CMBP	0.33±0.01	-21.0±1.2	11±1
TMBP	0.30±0.03	-26.4±1.7	13±1

Based on our previous study [24], the voltage from 7.5 to 25 V and deposition time up to 40 s were applied by the EPD process. The best quality Mo₆ films containing the **CMBF** and **TMBF** precursors were obtained by applying voltages at 13 and 17 V, respectively. The Mo₆ cluster-based films deposited on the ITO glass substrates were characterized after drying in air for 24 h.

2.4.2. Formation mechanism of transparent Mo₆ metal atom cluster film

In order to discuss the deposition process, the chemical composition and structure were analyzed for the **CMBF** and **TMBF** films prepared at different voltages and deposition times. The Br/Mo atomic ratios evaluated by XRF of the Mo₆ cluster-based films obtained by the EPD process as a function of the deposition time and applied voltage are shown in **Figure 2.11**. At 13V, which was used for the **CMBF**, was applied to **TMBF**, a good homogeneity was not obtained because the film was easily broken by the re-dissolution in the MEK solution after stopping the applied voltage. The Br/Mo atomic ratios as a function of the deposition time were determined at 13 V for **CMBF** and 17 V for **TMBF**, which are the optimal voltages to attain the best uniformity in the films, respectively, for those as a function of the applied voltage at 10s for both **CMBF** and **TMBF**.

The atomic ratios of the Br and Mo atoms were estimated to be 2.20 (±0.11) and 2.25 (±0.13) for the *CMBP* and *TMBP*, respectively, which were in fairly good agreement with the theoretical value of 2.33 (14 Br atoms/6 Mo atoms). In addition, the Cs⁺ atom was detected in *CMBP* solution, but it was not possible to measure any signal showing the existence of Cs atoms in all of the **CMBF** films, suggesting the absence of the Cs⁺ cations in the electrodeposited films.

The curves in **Figure 2.11a** show a decrease in the Br/Mo atomic ratio of the films from 7.2 (±0.3) (**TMBF**) or 4.9 (±0.2) (**CMBF**) to 2.8 (±0.2) in the first 10s when the applied voltage increased from 7.5 to 25V. These values are much higher than the theoretical value (2.33) and the experimental values determined for *CMBP* and *TMBP*, suggesting that the Br-atom rich Mo₆ cluster layers are preferentially deposited on the ITO-coated glass for the first 10s, especially at the low applied voltages.

In a similar way, the Br/Mo atomic ratio decreases to the theoretical index (2.33) for the higher deposition time (at a fixed applied voltage) and reaches the theoretical value after 30s (**TMBF**) or 40s (**CMBF**) of the deposition (**Fig. 2.11b**). These data also indicate that a Br-rich layer containing Mo₆-clusters is deposited during the first seconds of the EPD process, followed by the deposition of the Mo₆-cluster units. One explanation of these two steps during the deposition process can be expressed as follows: During the dissolution process, the free Br⁻ anions are generated by the substitution of the solvent molecules to form [Mo₆Br₈Br^a_{6-x}(solvent)^a_x]^{x-2} cluster units, then move toward the electrode faster than the bigger [Mo₆Br₈Br^a_{6-x}(solvent)^a_x]^{x-2} cluster units under the impact of an electric field. Considering the Br/Mo atomic ratio of **CMBF** and **TMBF** versus the applied voltage and deposition time, the EPD parameters were selected to obtain the Mo₆-cluster films with a Br/Mo atomic ratio close to the theoretical one (2.33); i.e., the deposition time was longer than 20s, and the voltage fixed at 13V for **CMBF** and 17V for **TMBF**.

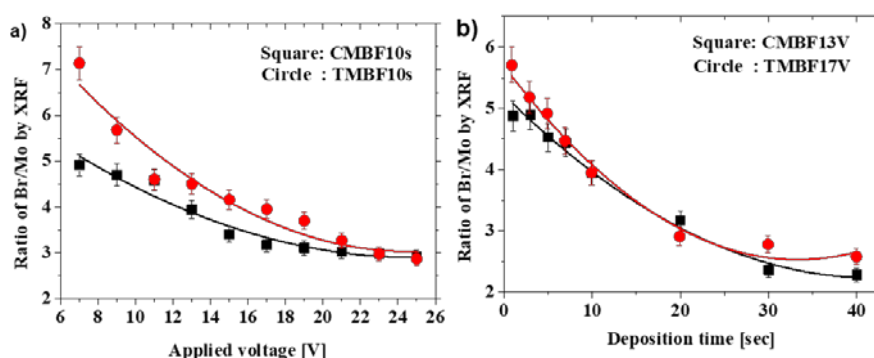


Figure 2.11. The Br/Mo atomic ratio in the **CMBF** and **TMBF** films as a function of (a) the applied voltage for a deposition time of 10s, and (b) the deposition time for an applied voltage of 13V and 17V, respectively.

The thickness of the Mo₆ cluster films prepared from the **CMBP** and **TBMP** suspensions in the MEK solution at the different deposition times of 10, 20, 30 and 40 seconds was measured using a color 3D microscope as presented in **Table 2.3**. The average values were recorded at least on three samples and three positions on each films. It can be seen that **CMBF** reached a maximum thickness of 1.89 ± 0.08 μm for the deposition time of 40 s (applied electric field of 13 V), while **TMBF** presented a maximum thickness of 1.68 ± 0.07 after 30 s of the deposition. For higher deposition at 40 s, the thickness of the **TMBF** sample decreased. Such phenomena was previously reported for **CMBF** [24] and was explained by the fact that the deposited Mo₆ film on the ITO glass with a high thickness plays the role as a resistance layer and then reduces the influence of the electric field on the movement of further cluster particles. Moreover, the diffusion of cations to the outside cluster layer will break up the balance of anion cluster particles with the charge on the electrode. Consequently, the Mo₆ cluster units will be released out of the layer by the re-dissolution in the MEK solution after 40 s for the **TMBF** film. Considering these results, the use of **CMBP** for fabricating the Mo₆ cluster thin film seems to be better

for controlling the thickness of the Mo₆ cluster-deposited films.

Table 2.3 Thickness (average) of the films deposited from the *CMBP* and *TMBP* cluster suspensions in MEK solutions for deposition times.

Deposition time (Second)	Thickness of films fabricated from MEK solution (μm)			
	Cs ₂ Mo ₆ Br ₁₄ solution (13V)		(TBA) ₂ Mo ₆ Br ₁₄ solution (17V)	
10	CMBF10s	0.81 ± 0.03	TMBF10s	0.49 ± 0.05
20	CMBF20s	1.05 ± 0.09	TMBF20s	1.23 ± 0.09
30	CMBF30s	1.54 ± 0.09	TMBF30s	1.68 ± 0.07
40	CMBF40s	1.89 ± 0.08	TMBF40s	1.29 ± 0.12

The surface morphology of the Mo₆ cluster films was characterized by SEM on the 20s deposition time samples. The SEM images of the **CMBF20s** and **TMBF20s** films show the evidence of homogeneous and flat morphology area of the film even at low magnifications of 1000 and 50000 times (**Fig. 2.12a**). However, the surface of the film seems not to be stable under high vacuum because many hairline cracks with 500 nm widths were observed. Such cracks are probably generated on the smooth surface of the films by the quick evaporation of the absorbed water molecules or residual solvent, especially during the evacuation in the SEM chamber. The cross-sectional SEM images of the high resolution images of the **CMBF20s** and **TMBF20s** films shown in **Figure 2.12b** exhibit a layered structure formed on the glass matrix, the ITO layer (0.2 μm) and the Mo₆-cluster layer (~1.2 μm). These values are in good agreement with the color 3D microscope results. A larger view of the cross-section of the **CMBF40s** film confirmed the homogeneity of the deposition process and also the thickness could reach 2 μm as shown in **Figure 2.12c** at 40s.

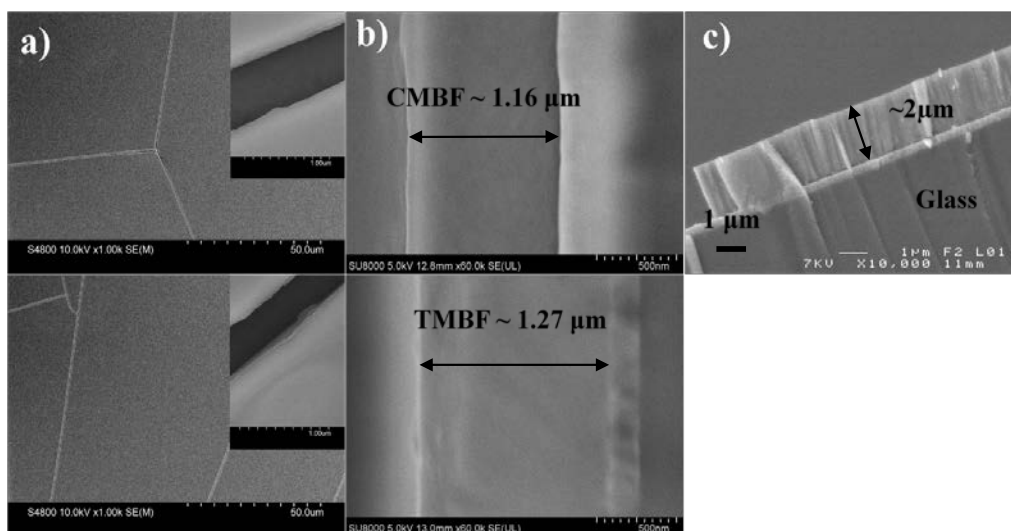


Figure 2.12. The FE-SEM images of a) the surface and b) the cross-section of the Mo₆ cluster films fabricated by EPD: **CMBF20s** at 13 V (top) and **TMBF20s** at 17 V (bottom). c) FE-SEM image of the cross-section of the **CMBF40s** film.

The recognition of the chemical vibrations in *CMBP*, *TMBP*, and the Mo₆ cluster films (*CMBF30s* and *TMBF30s*) by FTIR spectroscopy is shown in **Figure 2.13**. In the case of the *TMBF30s* film, the disappearance of the butyl vibrational band (from 1500 to 750 cm⁻¹) and C-H stretch vibrational band (from 2900 to 2800 cm⁻¹) is clearly observed, which supports the hypothesis of the separation of the TBA⁺ ions and [Mo₆Br₈Br^a_{6-x}L^a_x]^{x-2} cluster units during the EPD process. The intensity of O-H vibrational band in the wavenumber range between 3600 cm⁻¹ (ν₃) and 3200 cm⁻¹ sharply increases, continuously including a stretching vibration (ν₃) at 3600 cm⁻¹, a stretching vibration (ν₁) at 3450 cm⁻¹ and an overtone of the bending vibration (2ν₂) at 3250 cm⁻¹. The *TMBF30s* and *CMBF30s* films have similar FTIR spectra consisting of the asymmetric O-H stretch vibrational band (2ν₂) at 3250 cm⁻¹, combined bending modes (ν₂) and vibrations (ν_L) of the H-O-H mode at 2304 cm⁻¹, and the H-O-H bending mode at 1589 cm⁻¹, 1400 cm⁻¹ (ν₂) and 792 cm⁻¹ (ν_L)^[26]. The band assigned to O-H of the H-O-H stretch vibration (ν₃) at 3527 cm⁻¹ in the *CMBP* sample, representing the adsorbed free H₂O molecules, shifted to the O-H of the H-O-H stretch vibration (2ν₂) at 3250 cm⁻¹ in the *CMBF30s* film, the signal of the hydrogen bond^[18-19]. For this reason, we assumed that the Br apical ligands were exchanged by the H₂O molecules or OH⁻ groups, consequently, new hydrogen bonds were formed in the Mo₆ cluster film prepared by the EPD process. In addition, the obvious increase in the intensity of the O-H vibrational band in the FTIR spectrum originated from the increase of the H₃O⁺ cation absorption in the film, which would be generated on the surface of the ITO glass anode by the oxidization reaction of the H₂O molecules contaminated in the suspension in order to neutralize the negative charges of the [Mo₆Br₈Br^a_{6-x}L^a_x]^{x-2} cluster molecules^[24].

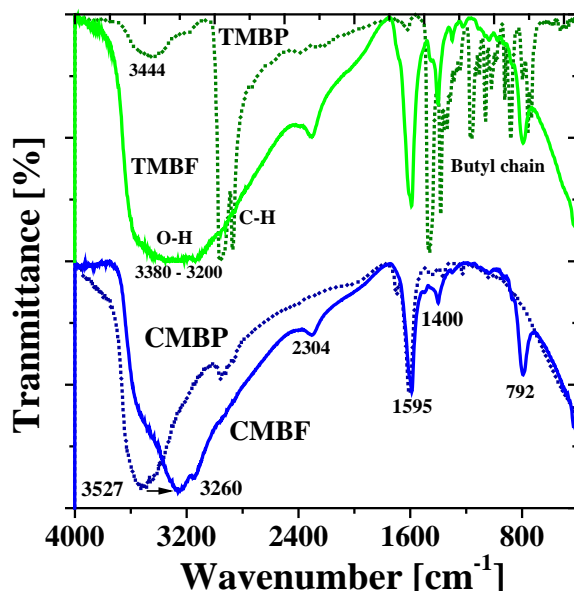


Figure 2.13. The FT-IR spectra of *CMBP*, *TMBP*, *CMBF* and *TMBF* samples.

The Br/Mo atomic ratio of the *CMBF* (4.9±0.2) after the first 10 seconds is lower than that of the *TMBF* (7.2±0.3) at 7.5 V (**Fig. 2.11a**), which suggests that the Br apical ligands of *CMBP* are less

labile than *TMBP* probably due to a limited exchange by the H₂O molecules or OH⁻ groups in the MEK solution. Thus, the *CMBP* suspension was selected as the precursor solution to prepare the Mo₆ cluster film (**CMBF30s**) that was investigated for the chemical elements through the XPS and EDX measurements. In order to elucidate the difference in the structure and chemical components of the [Mo₆Br₈Br^a_{6-x}L^a_x]^{x-2} cluster unit, the XPS spectra of the O 1s (**Fig. 2.14a**), Cs 3d and 4d (**Fig. 2.14b**), Mo 3d (**Fig. 2.14c**) and Br 3d region (**Fig. 2.14 d, e and f**) of the Cs₂Mo₆Br₁₄ powder (*CMBP*) and the Mo₆ film (**CMBF30s**) were recorded and analyzed. The atomic ratio results are also presented in **Table 2.4**.

Table 2.4. The percentage of the component elements in the *CMBP* and the CMBF30s films prepared at 13 V estimated by the peak analysis of the XPS measurements.

Element	O 1s	C 1s	Mo 3d	Cs 4d	Br 3d	Cs: Mo: Br (Wt.% at.)
CMBP	4.9%	22.3%	20.2%	5%	47.6%	1.5: 6.0: 14.1
CMBF30s	13.7 %	37.2%	16.1%	-	32.5%	0: 6.0: 12.1

The XPS spectra of O 1s evidences a peak at 533.2 eV for both samples (**Fig. 2.14a**), which is assigned to either H₂O molecule or OH⁻ group. However, the intensity of the signal of O 1s atoms in the **CMBF30s** film is higher than that in *CMBP*. This result supports the substitution of apical Br atoms by H₂O molecules or OH⁻ groups during the dissolution process and the absorption of the H₃O⁺ cations during the deposition on an ITO glass. The XPS spectra of Cs 4d evidences the peaks at 738 eV (3d_{3/2}), 724 eV (3d_{5/2}), 76.1 eV (4d_{3/2}) and 78.4 eV (4d_{5/2}) only for the *CMBP* sample (**Fig. 2.14b**), confirming (i) the presence of Cs atoms as counter cation in the precursor and (ii) the absence of Cs atoms in the film after the EPD process. The Mo 3d XPS spectra show equivalent peak intensity at 229.5 (3d_{5/2}) and 233 eV (3d_{3/2}) for both the *CMBP* and **CMBF30s** samples (**Fig. 2.14c**). Consistently with the XRF and EDS results, it confirms the presence of octahedral Mo₆ clusters in the film after the deposition.

The peaks in the Br 3d region of the *CMBP* and **CMBF30s** samples have relatively similar values (**Fig. 2.14d**). The peaks at 70.4 eV and 68.5 eV are assigned to the inner Br atoms and terminal apical Br atoms, respectively. While the peak intensities corresponding to the inner Br atoms of the *CMBP* and **CMBF30s** samples are equivalents, those of the Br atoms at the face-capping apical position are clearly different, as confirmed by their deconvolutions (**Fig. 2.14e and 2.14f**). Indeed, a reduction of the Br 3d_{5/2} peak intensity at 68.5 eV of apical Br atoms is clearly observed for the **CMBF30s** sample. Similar feature was also observed for the Mo₆ clusters immobilized on graphene oxide [19]. It can be interpreted as a new valence linking between the Mo₆ octahedral clusters and OH⁻ functional groups by the removal of apical Br atoms from the cluster unit.

The atomic ratio of *CMBP* sample estimated from XPS spectra of Br 3d and Mo 3d is 14.1/6 (≈ 2.35). This value is very close to the theoretical index (2.33), while that in the **CMBF30s** sample is lower: 12.1/6 (≈ 2). It indicates that in average each octahedral [Mo₆Br₈Br^a₆]²⁻ cluster unit deposited in the film lost 2 Br atoms (**Table 2.4**). This ratio is inferior to that obtained from the XRF measurements (Fig.

1), probably due to the free Br⁻ anions lost during the preparation of the XPS measurement. Consequently, only the Br atoms directly linking with the Mo₆ clusters are then detected by XPS.

From XPS and FTIR analyses, it could be concluded that the dissolution in the MEK solvent and the EPD process induces the substitution of two Br apical ligands from the [Mo₆Brⁱ₈Br^a₆]²⁻ cluster units, which are replaced by two OH⁻ groups or H₂O molecules originated from the solvent to form either [Mo₆Brⁱ₈Br^a_{6-x}(OH)^a_x]²⁻ or [Mo₆Brⁱ₈Br^a₄(H₂O)^a₂] cluster units. Both of them are known to exhibit a stable octahedral structure [18, 19].

The chemical analysis, shape and size diameter of the first deposited cluster units inside the EPD film (**CMBF30s**) were clearly characterized by the TEM-EDX and STEM images (**Fig. 2.15**). The EDX-TEM mapping (**Fig. 2.15a**) shows homogenous distribution of Br and Mo atoms, while the presence of Cs atoms is not significantly recognized. The later point supports the absence of Cs atoms previously suggested by XRF and XPS analyses. The TEM images indicate that the **CMBF30s** sample consists of many crystallized nanoparticles of average diameter about 6 nm, homogeneously distributed near the substrate (**Fig. 2.15b and 2.15c**). Considering that a single cluster unit presents an average volume of 1.2 nm³ [25], it can be deduced that a nanoparticle of 6 nm diameter is formed by less than 90 [Mo₆Brⁱ₈Br^a_{6-x}(OH)^a_x]²⁻ or [Mo₆Brⁱ₈Br^a₄(H₂O)^a₂] cluster units, the number of cluster units per nanoparticle being dependent on the cluster unit density. Considering that in MEK solution, the cluster units are linked together by hydrogen bonds, it leads to the formation of bigger negative charged spherical particles, which are accumulated on the electrode surface through the effective impact of the electric field to form the multilayers. Therefore, the structure in the first 100 nm layer is proposed to be an arrangement of [Mo₆Brⁱ₈Br^a_{6-x}(OH)^a_x]²⁻ and [Mo₆Brⁱ₈Br^a₄(H₂O)^a₂] spherical nanoparticles of 6 nm diameter. Consequently, the micron-sized layer is formed by the closed-pack stacking of different types of the species: (H₃O)⁺ cations, free Br⁻ anions, spherical nanoparticles containing a large number of [Mo₆Brⁱ₈Br^a_{6-x}(OH)^a_x]²⁻ and [Mo₆Brⁱ₈Br^a₄(H₂O)^a₂] cluster units.

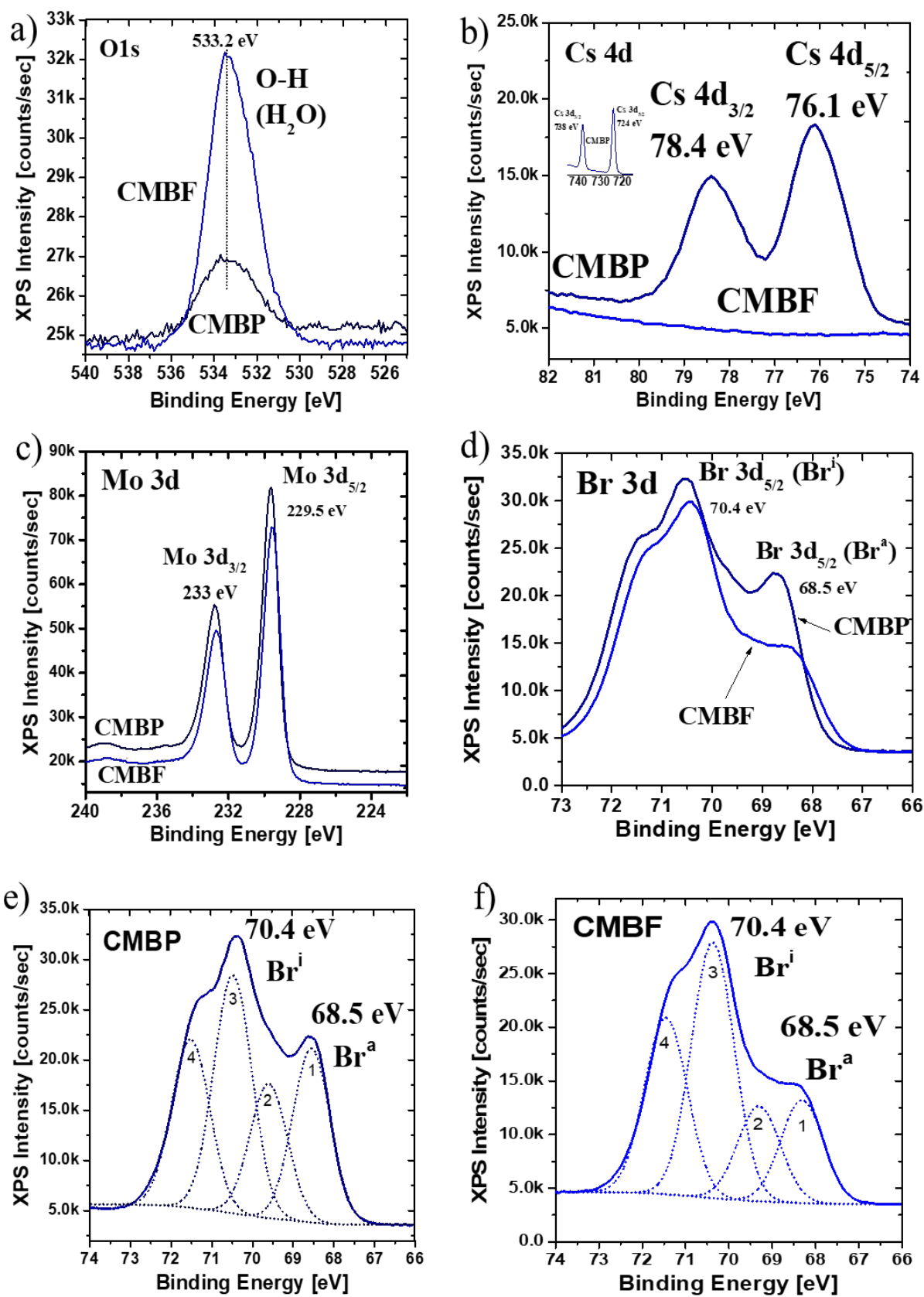


Figure 2.14. The XPS spectra of O 1s (a), Cs 3d and 4d (b), Mo 3d (c), and Br 3d region (d), deconvolution spectra of Br 3d region of *CMBP* (e) and deconvolution spectra of Br 3d of *CMBF* (f).

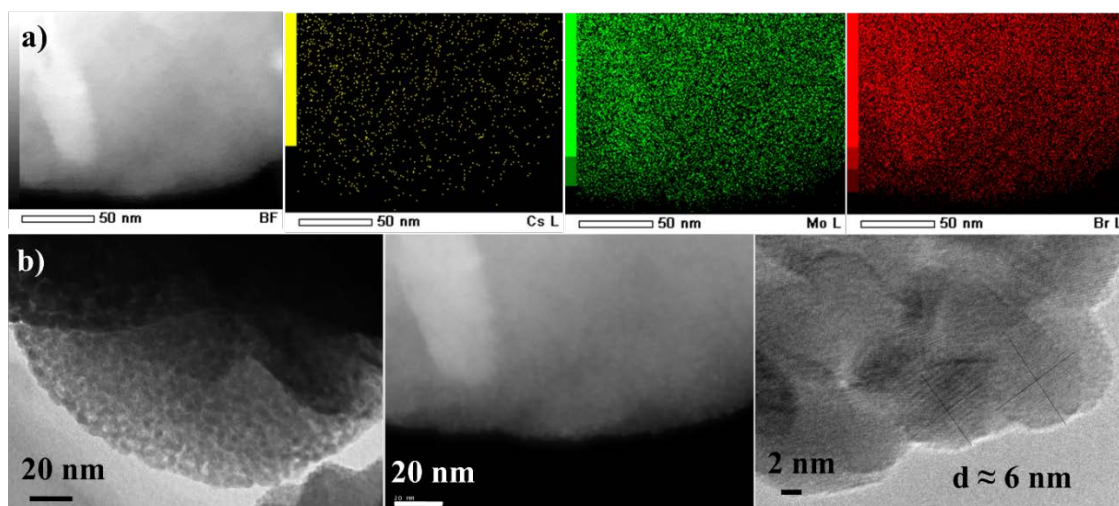


Figure 2.15. a) The EDX-TEM mapping of Cs, Mo and Br elements and b) TEM image (left) and STEM mode image (right) of the Mo_6 cluster nanoparticles from film by EPD. c) Spherical Mo_6 cluster nanoparticles included in the **CMBF30s**.

Based on the variation in the Br/Mo atomic ratios as a function of the applied voltage and deposition time and the modifications of the chemical linking observed by FTIR, XPS and TEM, we propose the following mechanism for the fabrication of the Mo_6 cluster film by the EPD process. In the first seconds of the EPD process, high mobile Br^- anions (originated from OH^- to Br^- substitution in MEK solution) move toward the ITO glass anode in the electric field to form a Br^- rich sublayer. The $[\text{Mo}_6\text{Br}_i^i\text{Br}_6-i-x(\text{OH})_x]^{2-}$ cluster units neutralized by H_3O^+ cations move towards the ITO glass and form $(\text{H}_3\text{O})_2[\text{Mo}_6\text{Br}_i^i\text{Br}_4(\text{OH})_2]$ assemblies. Due to lower pH close to the electrode, these later are quickly protonated to form $[\text{Mo}_6\text{Br}_i^i\text{Br}_4(\text{H}_2\text{O})_2]$ neutral cluster units. Some the $[\text{Mo}_6\text{Br}_i^i\text{Br}_4(\text{H}_2\text{O})_2]$ and $(\text{H}_3\text{O})_2[\text{Mo}_6\text{Br}_i^i\text{Br}_4(\text{OH})_2]$ cluster units interact together by hydrogen bonds to form approximately 6-nm size nanoparticles. The outer layers would mostly contain the $(\text{H}_3\text{O})_2[\text{Mo}_6\text{Br}_i^i\text{Br}_4(\text{OH})_2]$ cluster units which are simply packed by the EPD process (high velocity and collision of clusters). In summary, the Mo_6 film is a nanocomposite material with a multilayer structure made by the stacking of Br^- anions, $[\text{Mo}_6\text{Br}_i^i\text{Br}_4(\text{H}_2\text{O})_2]$ and $(\text{H}_3\text{O})_2[\text{Mo}_6\text{Br}_i^i\text{Br}_4(\text{OH})_2]$ cluster units. A schematic representation is shown in **Figure 2.16**. It is important to note that in the proposed model, the nature of the cations, namely Cs^+ or TBA^+ , of the initial powder precursors does not seem to play a key role at the surface of the electrode. These cations seem to play only an important role in the dissolution of metal cluster in the solvent, and consequently, on the rate of the deposition and thickness.

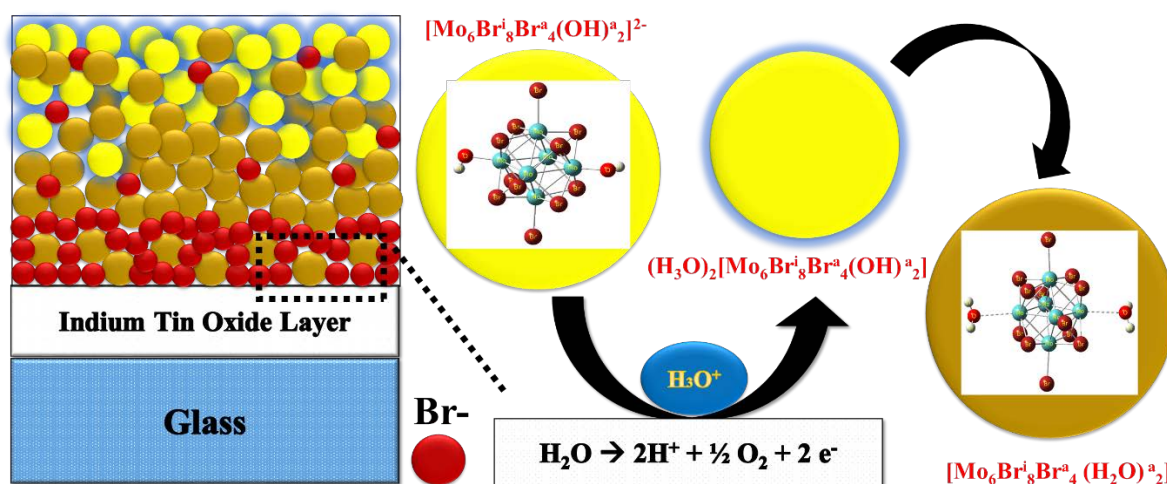


Figure 2.16. Schematic representation of the multilayered structure of Mo₆ cluster thin film

2.4.3. Conclusions

This study describes on the preparation, and chemical, structural and optical analyses of smooth Mo₆ cluster-based films deposited by the EPD process from the Cs₂Mo₆Br₁₄ and (TBA)₂Mo₆Br₁₄ cluster compounds in the MEK solution. The combination of X-ray analyses, electron microscopy and optical characterizations allow us to propose for the first time a mechanism for the multilayer structure deposition process of the metal atom clusters. The deposition of a Br-rich layer during the first seconds of the EPD process is proved through the determination of the Br/Mo atomic ratio in relation to the deposition time and applied voltages. Moreover, three important points should be pointed out: (i) the exchange of 2 Br apical ligands by OH⁻ or H₂O, (ii) the existence of two kinds of clusters in the Mo₆ film, i.e., [Mo₆Br₈Br₄(H₂O)₂] and [Mo₆Br₈Br₄(OH)₂]²⁻ paired with two (H₃O)⁺, and (iii) the exchange of Cs⁺ and TBA⁺ cations by H₃O⁺ in order to keep a neutral charge. Finally, the films present a high transmittance in the visible range and strong absorption in UV and NIR ranges.

References

1. J. R. Jones. Review of bioactive glass: From Hench to hybrids. *Acta Biomaterialia*, **9**, 4457-4486, 2013.
2. X. Zhao, Q. Zhao, J. Yu and B. Liu. Development of multifunctional photoactive self-cleaning glasses. *J. Non-Crystalline Solids*, **354**, 1424-1430, 2008.
3. K. Guan. Relationship between photocatalytic activity, hydrophilicity and self-cleaning effect of TiO₂/SiO₂ films. *Surf. Coat. Tech.*, **191**, 155-160, 2005.
4. T. Watanabe, A. Nakajima, R. Wang, M. Minabe, S. Koizumi, A. Fujishima, and K. Hashimoto. Photocatalytic activity and photoinduced hydrophilicity of titanium dioxide coated glass. *Thin Solid Films*, **351**, 260-263, 1999.
5. L. Besra and M. Liu. A review on fundamentals and applications of electrophoretic deposition (EPD). *Prog. Mat. Sci.*, **52**, 1-61, 2007.

6. I. Corni, M. P. Ryan, and A. R. Boccaccini. Electrophoretic deposition: From traditional ceramics to nanotechnology. *J. Eur. Ceram. Soc.* **28**, 1353-1367, 2008.
7. A. C. Valdez and A. R. Boccaccini. Innovations in electrophoretic deposition: Alternating current and pulsed direct current methods. *Electrochimica Acta*, **65**, 70- 89, 2012.
8. K. Kirakci, S. Cordier and C. Perrin. Synthesis and properties of charge-transfer solids with cluster units $[\text{Mo}_6\text{X}_{14}]^{2-}$ (X = Br, I). *Z. Anorg. Allg. Chem.*, 631, 41-46, 2005.
9. G. Saito, H. Hosoda, Y. Yoshida, J. Hagiwara, K. Nishimura, H. Yamochi, A. Otsuka, T. Hiramatsu, Y. Shimazaki, K. Kirakci, S. Cordier, and C. Perrin. Synthesis and properties of charge-transfer solids with cluster units $[\text{Mo}_6\text{X}_{14}]^{2-}$ (X = Br, I). *J. Mater. Chem.*, 22, 19774-19791, 2012.
10. T. Uchikoshi, and Y. Sakka. Phosphate esters as dispersants for the cathodic electrophoretic deposition of alumina suspensions. *J. Am. Ceram. Soc.*, 91, 1923-1936, 2008.
11. M. Ammam. Electrophoretic deposition under modulated electric fields: a review. *RSC Advances*, 2, 7633-7646, 2012.
12. G. Anne, K. Vanmeensel, J. Vleugels, and O. Van der Biest. Influence of the suspension composition on the electric field and deposition rate during electrophoretic deposition. *Col. and Sur. A: Physicochem. Eng.*, 245, 35-39, 2004.
13. L. Besra, and M. Liu. A review on fundamentals and applications of electrophoretic deposition (EPD). *Progress in Mat. Sci.*, 52, 1-61, 2007.
14. P. Sarkar, and P. S. Nicholson. Electrophoretic deposition (EPD): mechanisms, kinetics, and application to ceramics. *J. Am. Ceramic. Soc.*, 79, 1987-2002, 1996.
15. W. D. Ristenpart, I. A. Aksay, and D. A. Saville. Assembly of colloidal aggregates by electrohydrodynamic flow: Kinetic experiments and scaling analysis. *Phys. Rev. E*, 69, 7, 2004.
16. Y. Solomentsev, M. Bohmer, and J. L. Anderson. Particle clustering and pattern formation during electrophoretic deposition: a hydrodynamic model. *Langmuir*, 13, 6058-6068, 1997.
17. M. Bohmer. In situ observation of 2-Dimensional clustering during electrophoretic deposition. *Langmuir*, 12, 5747-5750, 1996.
18. L. J. Guggenberger, and W. Sleight. Structural and bonding characterizations of molybdenum dibromide, $\text{Mo}_6\text{Br}_{12}\cdot 2\text{H}_2\text{O}$. *Minor. Chem.*, 8, 2041-2049, 1969.
19. Y. Q. Zheng, Y. Grin and H. G. Schnering. Crystal structure of molybdenum (II) bromide, $\text{Mo}_6\text{Br}_{12}$. *Z. Kristallogr. NCS*, 213, 469-470, 1998.
20. K. Costuas, A. Garreau, A. Bulou, B. Fontaine, J. Cuny, R. Gautier, M. Mortier, Y. Molard, J. L. Duvail, E. Faulques and S. Cordier. Combined theoretical and time-resolved photoluminescence investigations of $[\text{Mo}_6\text{Br}_8^i\text{Br}_6^a]$ metal cluster units: evidence of dual emission. *Phys. Chem. Chem. Phys.*, 17, 28574-28585, 2015.
21. X. Zarate, E. Schott, L. A. Soto, and R. Ramirez-Tagle. A family of octahedral molybdenum cluster complexes $[\text{Mo}_6\text{Cl}_8(\text{H}_2\text{O})_n(\text{OH})_{6-n}]^{n-2}$ with $n = 0-6$ as a pH-sensors: A theoretical study. *Chem. Phys. Let.*, 567, 39-42, 2013.

22. P. S. Kuttipillai, Y. Zhao, C. J. Traverse, R. J. Staples, B. G. Levine and R. R. Lunt. Phosphorescent nanocluster light-emitting diodes. *Adv. Mater.*, 28, 320–326, 2016.
23. M. A. Cortes, S. Paofai, S. Cordier, H. Folliot and Y. Molard. Tuned Red NIR phosphorescence of polyurethane hybrid composites embedding metallic nanoclusters for oxygen sensing. *Chem. Commun.*, 51, 189-204, 2015.
24. T. K. N. Nguyen, F. Grasset, B. Dierre, C. Matsunaga, S. Cordier, P. Lemoine, N. Ohashi and T. Uchikoshi. Fabrication of transparent thin film of octahedral molybdenum metal clusters by electrophoretic deposition. *ECS J. Solid. State. Sci. and Technol.*, 5, 178-186, (2016).
25. S. A. Bataineh, L. G. Britcher and H. J. Griesser. XPS characterization of the surface immobilization of antibacterial furanones. *Surf. Sci.*, 600, 952–962, 2006.
26. Y. Li, H. Chen, L. Y. Voo, J. Ji, G. Zhang, G. Zhang, F. Zhang and X. Fan. Synthesis of partially hydrogenated graphene and brominated graphene. *J. Mater. Chem.*, 22, 15021-15024, 2012.
27. T. K. N. Nguyen, B. Dierre, F. Grasset, A. Renaud, S. Cordier, P. Lemoine, N. Ohashi, T. Uchikoshi. Formation mechanism of transparent Mo₆ metal atom cluster film prepared by electrophoretic deposition. *J. Electrochem. Soc.*, 164, 412–418, 2017.
28. S. Seethapathy, and T. Górecki. Applications of polydimethylsiloxane in analytical chemistry: A review. *Anal. Chim. Acta*, 750, 48–62. 2012.
29. D. Zhu, S. H. Wang, and X. Zhou. Recent progress in fabrication and application of polydimethylsiloxane sponges. *J. Mater. Chem. A*, 5, 16467–16497, 2017.
30. K. Kirakci, S. Cordier, and C. Perrin. Synthesis and characterization of Cs₂Mo₆X₁₄ (X = Br or I) hexamolybdenum cluster halides: Efficient Mo₆ cluster precursors for solution chemistry syntheses. *Z. Anorg. Allg. Chem.*, 631, 411–416, 2005.
31. N. Saito, S. Cordier, P. Lemoine, T. Ohsawa, Y. Wada, F. Grasset, S. J. Cross, and N. Ohashi. Lattice and valence electronic structures of crystalline octahedral molybdenum halide clusters-based compounds, Cs₂[Mo₆X₁₄] (X = Cl, Br, I), studied by density functional theory calculations. *Inorg. Chem.*, 56, 6234–6243, 2017.
32. A. M. Engwall, Z. Rao, and E. Chason. Origins of residual stress in thin films: Interaction between microstructure and growth kinetics. *Mater. Des.*, 110, 616–623, 2016.
33. M. Ghidelli, M. Sebastiani, C. Collet, and R. Guillemet. Determination of the elastic moduli and residual stresses of freestanding Au-TiW bilayer thin films by nano indentation. *Mater. Des.*, 106, 436–445, 2016.
34. M. Cypryk, and Y. Apeloig. Mechanism of the Acid-Catalyzed Si–O bond cleavage in siloxanes and siloxanols: A theoretical study. *Organometallics*, 21, 2165–2175, 2002.
35. T. K. N. Nguyen, B. Dierre, F. Grasset, N. Dumait, S. Cordier, P. Lemoine, A. Renaud, H. Fudouzi, N. Ohashi and T. Uchikoshi. Electrophoretic coating of octahedral molybdenum metal clusters for UV/NIR light screening, *Coatings*, 7, 114-127, 2017.

Chapter 3

Stabilization of the hexamolybdenum cluster by incorporation with polymer

Chapter 3

Stabilization of the hexamolybdenum cluster by incorporation with polymer

3.1. Stabilization of the Mo₆ cluster film by top coating with poly dimethyl siloxane (PDMS)

The strong advantage of the EPD process is to easily fabricate the pure Mo₆ cluster films containing no counter cations at room temperature, creating a new Mo₆ cluster network exhibiting prominent luminescent stabilization ^[1, 2]. Though the deposition process seemed to be fairly good, the Mo₆ film were obviously cracked within a short time during the evaporation of the solvent. Considering the achievements of polydimethylsiloxanes (PDMS) in the studies of many application areas ^[3, 4], the PDMS coating was carried out as a post-treatment of the Mo₆ cluster films after the EPD process. The protective mechanism of the PDMS in the Mo₆ cluster film has also been suggested by the crosslinking reaction between the apical ligands of the Mo₆ cluster and the PDMS fluid with low viscosity during the slow evaporation. Actually, when the Mo₆ film is thin, it can be significantly stabilized by the hydrogen bonds generated by OH groups on the ITO-coated glass and OH or H₂O groups on the Mo₆ cluster, but the optical efficiency is limited due to low Mo₆ cluster concentration. This has been proved for a Br-rich cluster layer formed at the initial deposition stage in the previous report ^[2]. Therefore, it is necessary to fabricate thick and stable Mo₆ cluster film, which is sustainable under ambient condition in order to extend the application of the Mo₆ cluster on the window for cutting UV/NIR light. The key work is to figure out a simple and effective coating process to protect the original octahedral cluster structure as well as the optical property of the Mo₆ film that is crucial to apply at the industry level.

3.1.1. Preparation of the suspension and fabrication of film by EPD

Preparation of the EPD suspension

The Cs₂Mo₆Br₁₄ cluster precursor was added to reagent grade MEK (99%, Nacalai Tesque, Inc., Kyoto, Japan) at a concentration of 5 g/L, then stirred until obtaining a transparent yellow suspension, similarly with **2.1.1** part ^[1]. The zeta potential and electronic conductivity of the prepared Cs₂Mo₆Br₁₄ cluster suspension were measured by a zeta-potential analyzer, which were about $-(10 \pm 2)$ mV and (0.32 ± 0.70) mS/cm, respectively. The EPD system was set up as shown in **Figure 2.1b**. The Mo₆ nanoclusters were deposited on the ITO-coated glass (1×1.5 cm²) at the applied voltages from 10 to 16 V for 60 s.

Hydrophilization of the ITO Glass

The Mo₆ cluster film prepared by the EPD process showed a good transmittance, homogeneity and smooth surface (**Fig. 3.1a**). However, the surface of the Mo₆ film was easy to break into flakes originating from its edge after drying in the air for 4 days at room temperature (**Fig. 3.1b**). In order to improve the interaction between the Mo₆ film and the ITO surface, a hydrophilic plasma treatment of the ITO surface was performed by a plasma ion bombarder (PIB-10) with a discharge current of 10 mA

and a processing time of 3 min (**Fig. 3.1c**). The hydrophilized ITO glasses showed much better adhesion of the Mo₆ film after the EPD (**Fig. 3.1d**), but the film still cracked after 9 days.

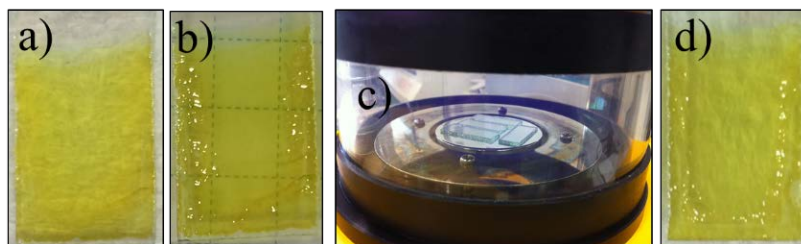


Figure 3.1 Photographs showing the influence of hydrophilic plasma treatment of the indium tin oxide (ITO) surface on the adhesion of the Mo₆ cluster films: (a) Mo₆ film on the untreated ITO glass just after the EPD (similar image are obtained on plasma-treated ITO glass); (b) after 4 days; (c) the plasma treatment of the ITO glass and (d) Mo₆ film on the plasma-treated ITO glass after 9 days.

PDMS coating on the Mo₆ Film

Several kinds of PDMS commercially labeled as KF-96L-nCS (n = kinetic viscosities; 1.5, 2, 5, 10, 20, and 100; CS = centistokes) were used for the post-surface-coating treatment. The viscosity of the PDMS fluids depends on the molecular weight and they contain no solvent. The PDMS with the volume of 0.5 mL was immediately dropped on the surface of the deposited Mo₆ cluster film after the EPD process. In order to apply a similar drying condition, all the PDMS-coated films were dried at 40 °C for 7 days in oven. Moreover, the waiting time to drop the PDMS fluid was investigated in order to obtain good quality film.

3.1.2. Optimization of the PDMS coating condition on the Mo₆ film

The Mo₆ films prepared by the EPD process at 15 V for 30 s were coated by the PDMS fluids on the surface without any treatment after drying for 10 min. Photos of the PDMS-coated Mo₆ films on the ITO glass with and without hydrophilization are shown in **Figure 3.2**. Only the Mo₆ films deposited on the hydrophilized ITO glass followed by coating with the KF-96L-1.5CS and KF-96L-2CS exhibited insignificant cracking. Most of the other films strongly cracked during drying. Even though, the PDMS-coated films were dried at 40 °C for 7 days, the PDMS fluids containing the viscosity higher than two centistokes still existed on the surface of the film accompanying with many flakes that completely separated from the ITO surface. The problems exhibited that the viscosity of the PDMS fluid decided the drying process. The films coated with low-viscosity PDMS fluids obtained volatilized appearance, but the surface of the Mo₆ film was not stable. For this result, the optimal time to coat the PDMS fluid after the EPD process was investigated.

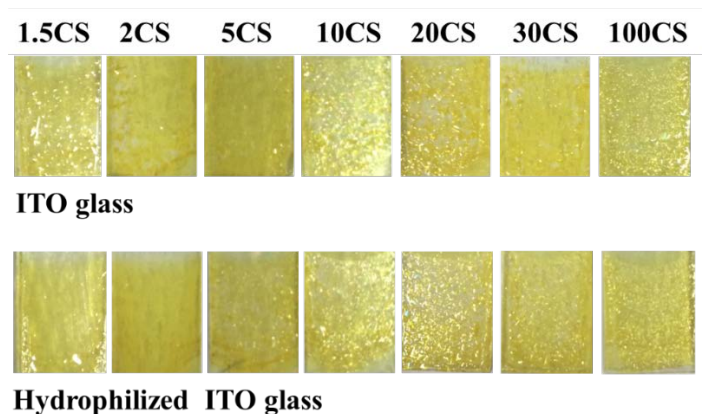


Figure 3.2. The Mo_6 film deposited on the ITO glass at 15 V for 30 s with or without hydrophilization followed by coating with polydimethylsiloxanes (PDMS) of KF-96L-1.5CS, KF-96L-2CS, KF-96L-5CS, KF-96L-10CS, KF-96L-20CS, KF-96L-30CS, and KF-96L-100CS.

Based on these results, KF-96L-1.5CS and KF-96L-2CS were selected to investigate the optimal conditions for the coating because they were dried completely. The Mo_6 film deposited at 15 V for 30 s on the hydrophilized ITO glass were coated with KF-96L-1.5CS or KF-96L-2CS for 0, 30, 60, 90, 120, 150 or 180 min after finishing the EPD (**Fig. 3.3**). The evaporation speed of the PDMS fluid during drying affects the stabilization of the Mo_6 film. In order to minimize the residual stress during the evaporation, all the films were slowly dried at room temperature for 24 h. The results based on the visual observation of the photos shown in **Figure 3.3** indicated that 90 min after the EPD was the best amount of time to perform the PDMS coating on the surface of the Mo_6 cluster film for obtaining the highest stability. The Mo_6 cluster film deposited on the hydrophilized ITO glass followed by the PDMS coating 90 min after the EPD exhibited no cracks or no spalling even after 6 months.

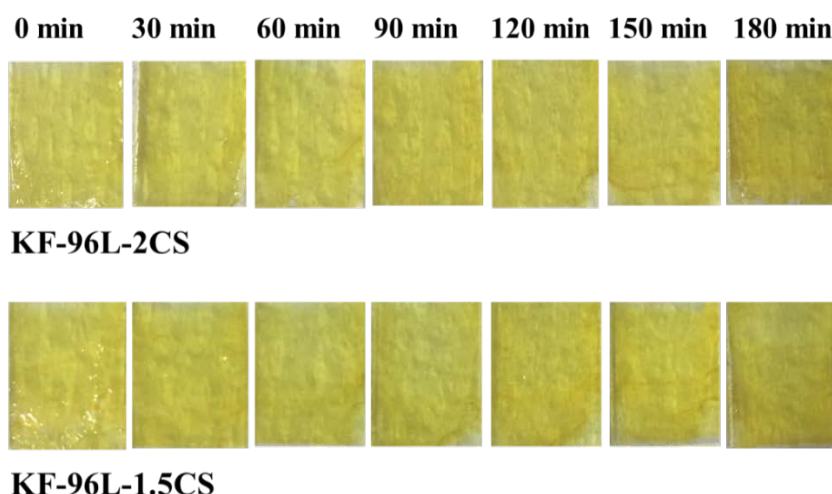


Figure 3.3. The deposited Mo_6 cluster film at 15 V for 30 s followed by coating the PDMS (KF-96L) with the kinetic viscosity of 1.5 and 2 centistokes after the different drying times. The photographs of these samples were taken after exposure to the open air for 4 days at room temperature.

3.1.3. Characterization of the PDMS-coated Mo₆ cluster film

The surface appearances of the Mo₆ film, Mo₆ film_1.5CS, and Mo₆ film_2CS samples observed by the color 3D laser microscope and FE-SEM after drying for similar time of 24 h at room temperature are shown in **Figure 3.4**. It should be noted that the SEM observation was conducted in a high vacuum. The yellow Mo₆ films seem to be stable despite the appearance of a few hairline cracks in the color 3D laser microscopy images. The stabilization of the films was enhanced after the hydrophilization of the ITO surface. It could be explained that the interaction between the hydrophilic functional groups on the ITO surface and the apical ligands of the octahedral Mo₆ cluster units was slightly improved (**Fig. 3.4 b and c**), but the PDMS coating has effectively stabilized the Mo₆ cluster film on the ITO glass surface for a long time. The existence of bubble contamination is recognized by the circular signs on the surface of the Mo₆ film_2CS (**Fig. 3.4c** (upper)). This problem is not realized in the KF-96L-1.5CS-coated Mo₆ film. The KF-96L-2CS has higher viscosity that properly reduce the volatile property at room temperature. This phenomenon was also observed in the Mo₆ films coated by the PDMS fluids with a kinetic viscosity higher than 2 cSt (**Fig. 3.2**) even dried at 40 °C for 7 days. As displayed in **Figure 3.4** (lower), the Mo₆ film without PDMS appears to have a number of crack lines, and pieces of the film seem to be separated from the surface of the ITO glass in a high vacuum. In the case of the two PDMS-coated Mo₆ films, a few crack lines were presented, but the deposited film strongly adhered to the surface of the ITO glass.

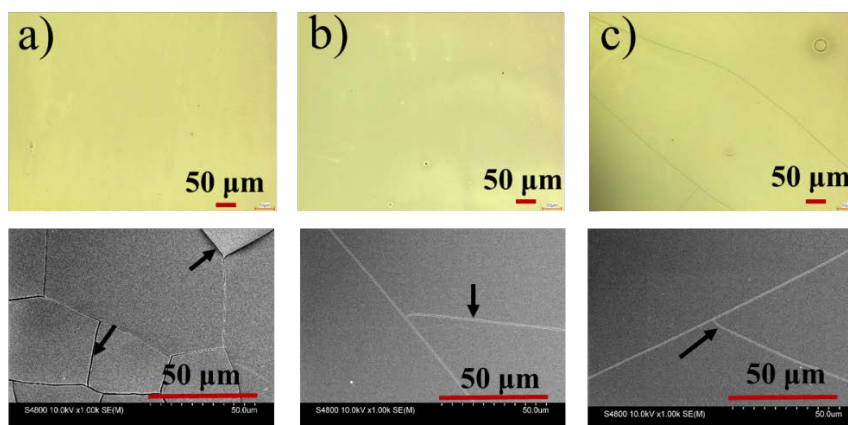


Figure 3.4. The surface appearance observed by a color 3D microscope (upper) and FE-SEM (lower): (a) Mo₆ film; (b) Mo₆ film_1.5CS; (c) Mo₆ film_2CS.

The Br/Mo atomic ratios of the Mo₆ precursors, Mo₆ film, Mo₆ film_1.5CS, and Mo₆ film_2CS, measured by an EDX measurement are presented in **Table 3.1**. These ratios were similar in the coated and un-coated films, which were slightly lower than the ratio of the Cs₂Mo₆B₈L₆^a cluster precursor. It can be explained that, on average, one (theoretical index Br/Mo ratio, R = 2.33) apical Br atom is replaced by solvent molecule or an OH⁻ group originating from the solvents or water involved in the MEK or PDMS during the dissolution. It should be mentioned that the Cs⁺ cations were not detected in

all the Mo₆ films without or with the PDMS probably due to the migration of the dissociated Cs⁺ toward the cathode, the counter electrode, during the EPD. This phenomenon has been similarly demonstrated in a previous study^[1]. Based on this result, the chemical structure of the Mo₆ film would be [Mo₆Br₃Br_{6-x}(solvent)_x]^{a-x-2} in the case of the Br ligands replaced by solvent or [Mo₆Br₃Br_{6-x}(OH)_x]^{a-2-} in the case of the Br ligands replaced by the OH⁻ groups, or [Mo₆Br₃Br_{5-x}(OH)_x(solvent)_a]^{a-1-} in the case of the Br ligands replaced by solvent and OH⁻ groups^[1]. Moreover, in the anodic EPD process, the Mo₆ cluster units are necessary to have negative charges in order to move toward the anode. It is suggested that the [Mo₆Br₃Br_{6-x}(OH)_x]^{a-2-} cluster units prior to depositing on the ITO glass are neutralized by the H₃O⁺ cations, which are generated from the oxidizing reaction of the H₂O molecules with the surface of the anode. Moreover, a previous study reported that the Mo₆Br₃Br₄·2H₂O cluster units are relatively stable in the solution^[5]. The prediction of the transformation from the (H₃O)₂ [Mo₆Br₃Br_{6-x}(OH)_x]^a cluster units to the Mo₆Br₃Br₄·2H₂O cluster units will be carefully demonstrated in a separate publication^[2].

Table 3.1. The Br/Mo atomic ratio and the thickness of the Mo₆ precursor and the deposited Mo₆ film at 15 V for 30 s evaluated by EDX measurement.

Samples	Br/Mo atomic ratio (atom % _{Br} /atom % _{Mo}) Theoretical index of 2.33 (14Br/6Mo)	Thickness (μm)
Mo ₆ precursor	2.29	–
Mo ₆ film	2.20	1.53 ± 0.09
Mo ₆ film_1.5CS	2.21	1.49 ± 0.07
Mo ₆ film_2CS	2.17	1.54 ± 0.08

Most importantly, the PDMS coating on the surface of the Mo₆ cluster film does not significantly affect the thickness of the original Mo₆ film. At the beginning of the investigation, it can be seen that the PDMS coated Mo₆ film still retains its thickness and the Br/Mo atomic ratio of the original Mo₆ cluster deposited film, suggesting the penetration of the PDMS into the cluster layer.

The XRD patterns of the bare ITO glass, the Cs₂Mo₆Br₃Br₆^a cluster precursor, the Mo₆ film without and with the PDMS coating are shown in **Figure 3.5**. The curve of the Cs₂Mo₆Br₃Br₆^a cluster precursor reveals a good crystallinity with a high intensity of the peaks in the 2θ range of 5°–35°. The crystallographic structure belonging to the space group of P3c has been reported for the Cs₂Mo₆Br₁₄ cluster precursor^[5]. The assignment for the plane in the Cs₂Mo₆Br₁₄ cluster structure that has been confirmed by Saito et al.^[7] is presented in **Figure 3.5**. The XRD patterns of the Mo₆ film after the EPD retain essentially broad peaks at the 2θ angles of 11° (101) and 30° (114 and 300) without and with the PDMS coating. The grain size calculated from the Scherrer equation at 2θ angle of 11° (101) in the Mo₆ cluster film is approximately 4 nm. The 6-nm cluster nanoparticles was also evidenced by STEM measurement in previous work^[2]. Therefore, the broad peaks normally originate from the frameworks of the crystals consisting of by [Mo₆Br₃Br₆]^{a-2-} cluster units on a nanometer scale, which means the crystal networks of the Cs₂Mo₆Br₃Br₆^a clusters are rearranged to form new 3D networks due to the

disappearance of the Cs⁺ cations. Interestingly, the existence of the PDMS does not have a significant influence on the available crystal networks in the Mo₆ film.

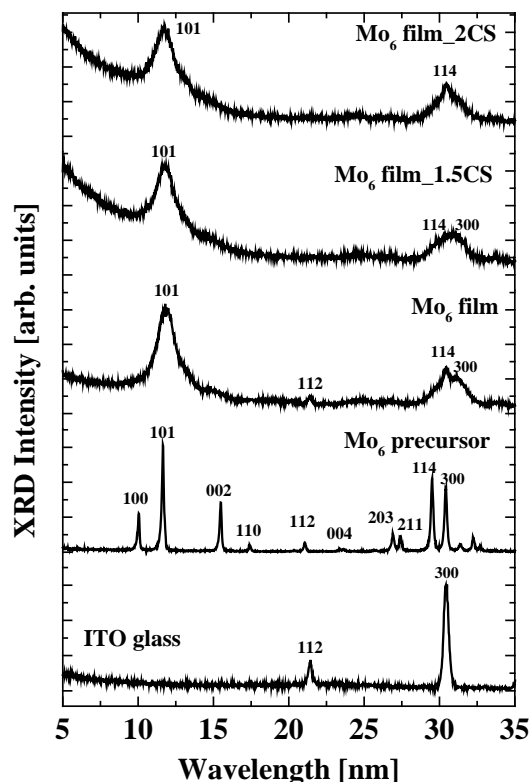


Figure 3.5. The XRD patterns of the ITO glass, the Mo₆ precursor, and the EPD deposits: Mo₆ film; Mo₆ film_1.5CS; and Mo₆ film_2CS samples. There is no (a), (b) and (c) in the figure, please check and confirm.

The FTIR spectra of the Mo₆ film, Mo₆ film_1.5CS, Mo₆ film_2CS samples are presented in **Figure 3.6**. All spectra similarly display the absorption band of O–H stretching vibration in the wavenumber range from 3600 to 3200 cm⁻¹, simultaneously, the H–O–H bending mode at 1590, 1400 and 794 cm⁻¹ ascribed to the free H₂O molecules and hydrogen bond [2]. These absorption bands originates from O–H groups linking with the Mo₆ cluster as apical ligands and the H₃O⁺ cations absorbing on the surface of the Mo₆ clusters in order to neutralize the negative charge. However, the absorption intensity of O–H stretching vibration at 3550 cm⁻¹, indicating free H₂O molecules visibly reduces in the curve of the PDMS-coated Mo₆ films. Interestingly, the PDMS fluids (1.5 and 2 CS) are volatile during drying the film, but the absorption of Si–O bonds is clearly exhibited as the vibrational band at 1080 cm⁻¹. The intensity of Si–O stretching vibration improved when coated with the PDMS owning higher viscosity. Normally, PDMS fluids with low viscosity are almost volatile at room temperature. It can be explained that the PDMS fluid remained in the Mo₆ film after finishing the dry process with a strong interaction by hydrogen bonds or chemical linking with the O–H group or H₂O molecules of the Mo₆ cluster film that forms a new crosslinking network.

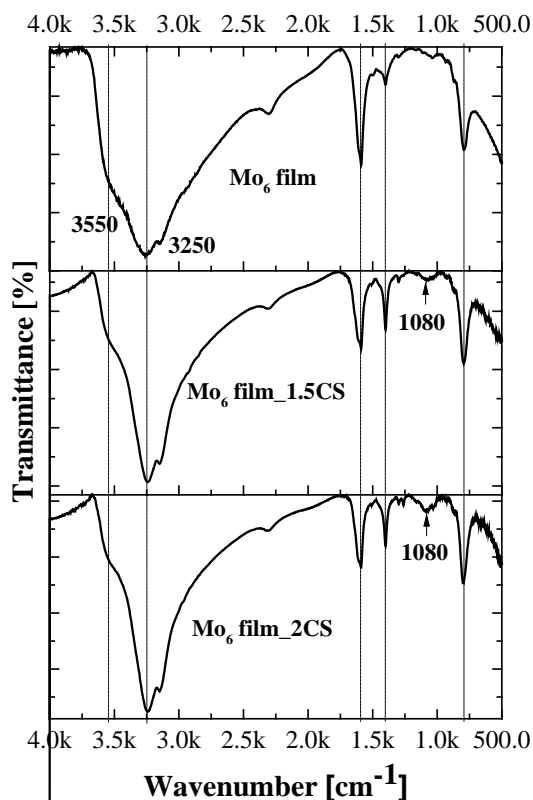


Figure 3.6. The FT-IR spectrum of the Mo₆ film, Mo₆ film_1.5CS, Mo₆ film_2CS samples.

3.1.4. Coating mechanism of PDMS on the Mo₆ cluster film

Some reasons have been suggested to explain the separation of the Mo₆ layers from the ITO glass. The cracking phenomena of the Mo₆ film started to be recognized after 4 days of the dry process at the ambient conditions. The stabilization of the Mo₆ film was partially limited because the evaporation of acetone will create a residual stress, which break the hydrogen bonding between the cluster nanoparticles containing the Mo₆Br₈ⁱBr₄^a·2H₂O and (H₃O)₂ [Mo₆Br₈ⁱBr₄^a (OH)₂^a] cluster units [1] and volume shrinking in the Mo₆ cluster network^[8, 9]. The cracking point is grown from the tiny grain boundary, which is generated by the separation of the cluster phase and solvent phase.

The PDMS effectively stabilized the morphology of the Mo₆ film for a long time under an ambient condition. Indeed, the protective mechanism of the PDMS on the surface of the Mo₆ film have been discussed. In the previous work [1], the main components existing in the Mo₆ film were Mo₆Br₈ⁱBr₄^a·2H₂O and (H₃O)₂ [Mo₆Br₈ⁱBr₄^a (OH)₂^a] cluster units that were linked together by hydrogen bonds. Normally, the outside layers of the Mo₆ film mainly contain counter cations as H₃O⁺ to neutralize the [Mo₆Br₈ⁱBr₄^a (OH)₂^a]²⁻ anion. The Mo₆ cluster nanoparticle has functional groups such as H₂O molecule, OH and H₃O⁺ acid group on the surface. During the 90 min after the EPD, most of the acetone solvent would vaporize, but free water still remains in the deposit layer; 90 min would thus be the best timing for the PDMS coating followed by the penetration of the PDMS macromolecules through the grain boundaries of the nanoclusters network. In the acidic condition containing many H₃O⁺ cations absorbed on the

surface of the cluster nanoparticles, the Si–O–Si bonds of the PDMS will be broken by H₂O molecules with Brønsted acid catalyst (H⁺). The cleavage of the Si–O bonds in siloxane have also been proved in a previous report [10]. Namely, the protective mechanism of the PDMS can be explained as shown in **Figure 3.7**: a) in the acid medium, O atom of the ≡Si₁–O–Si₂≡ bond protonated by H⁺ cation creates the electrophile Si₁ atom and ≡Si₂OH and electrophile Si₁ atom coupled with free H₂O molecule to form ≡Si₁–(OH₂)⁺; b) the ≡Si₁–(OH₂)⁺ continually reacts with OH groups of the Mo₆ clusters to form ≡Si₁OH and Mo₆ cluster–H₂O; c) the ≡SiOH crosslinks with OH groups of the Mo₆ cluster; d) the hydrogen bond is formed from the ≡SiOH group and the OH or H₂O groups of the Mo₆ cluster accompanying with covalent formed from ≡SiOH group with OH group of the Mo₆ cluster. The new crosslinking network is generated by the short PDMS circuits acting as the bridges between the Mo₆ cluster nanoparticles by covalent and hydrogen bonds. In summary, the crosslinking network prevents the penetration of ambient H₂O and oxygen molecules simultaneously reduces the phase separation at the nanocluster grain boundary and, consequently, improves the stabilization of the Mo₆ network for a long time. This mechanism has been published by author in Coating journal [11].

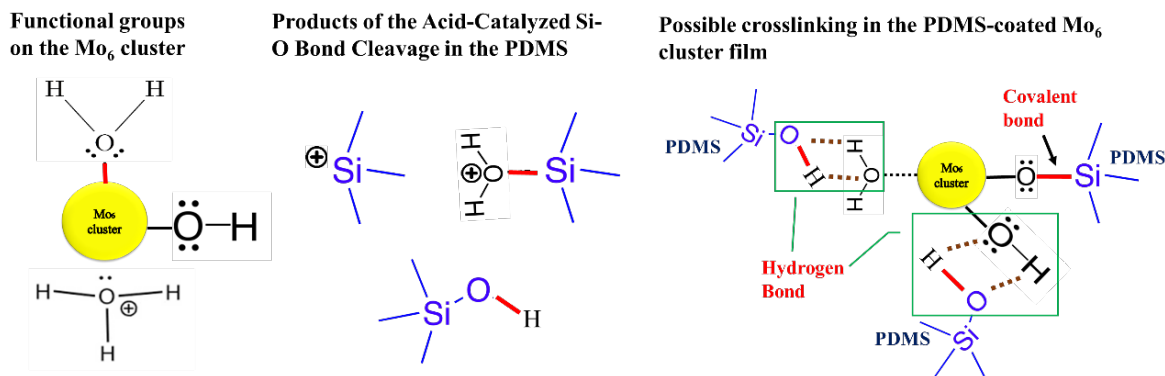


Figure 3.7. The possible crosslinking mechanism of the PDMS fluid and the Mo₆ cluster nanoparticles under the existence of Brønsted acid catalyst.

3.1.5. Optical property of the PDMS-coated Mo₆ cluster film

UV-Vis absorption is one of the important technique used to evaluate the influence of the PDMS on the Mo₆ film. The absorbance of the Mo₆ precursor in the MEK solution and the transmittance of the ITO glass, Mo₆ film, Mo₆ film_1.5CS, and Mo₆ film_2CS samples are presented in **Figure 3.8**. The impressive phenomenon in the UV-Vis-NIR transmittance of the film is the appearance of many peaks in the wavelength range from 600 to 2000 nm that does not exist in the spectra of the ITO glass. The interference of the incident and reflected lights by the Mo₆ film would give the typical interference pattern [1]. The Mo₆ precursor strongly absorbs light in the wavelength range of 300 and 500 nm, while the ITO glass absorbs light at wavelengths under 400 nm and NIR higher than 1100 nm. The transmission curves of the Mo₆ film, Mo₆ film_1.5CS and Mo₆ film_2CS samples display strong absorptions in the wavelength range under 580 nm, which is shifted to about a 40 nm higher wavelength

compared to the absorption curve of the Mo₆ precursor. This interesting result includes both the absorption by the ITO glass and the Mo₆ clusters in the UV-Vis range. Based on these results, it could be suggested that the new cluster network was formed during the EPD process, which is realized in the XRD pattern, caused the different light absorption of the valance electrons in the energy band gap of the Mo₆ cluster units. The increase of the absorption in the wavelength of visible light would be an advantage for use in UV-Vis light trapping devices. In addition, the absorption intensity in the NIR range of the Mo₆ film is stronger than that of the ITO glass, even if the absorption by the Mo₆ cluster precursor does not exist in this range. It can therefore be said that the Mo₆ cluster film plays an important role in enhancing and retaining the incident light on the surface of the ITO glass by diffraction and reflection between the ITO layers and the top of the Mo₆ film. In summary, the use of the PDMS fluid does not change the optical properties of the Mo₆ film.

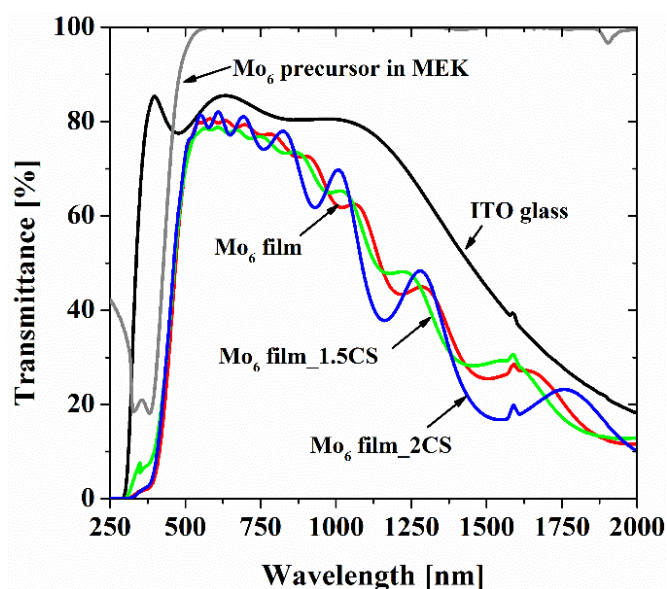


Figure 3.8. The UV-Vis absorption spectra of ITO glass and the Mo₆ precursor, Mo₆ film, Mo₆ film_1.5CS, and Mo₆ film_2CS samples.

3.1.6. Conclusions

The stabilization of the Mo₆ cluster thin film was improved by the hydrophilization of the surface of the ITO glass and the use of PDMS as a top-coating agent on the surface of the Mo₆ film. The effectiveness of the hydrophilization enhances the good interaction between the first layer of the Mo₆ clusters and ITO layers, while the PDMS prevents the penetration of air and moisture. The results of the study indicated that the thickness, the Br/Mo atomic ratio, surface morphology, crystallographic pattern, chemical linking, and UV-Vis absorption of the Mo₆ film with the PDMS coating were not significantly changed by the PDMS coating. In addition, the KF-96L-1.5CS is the best PDMS because its evaporation is completely on the surface of the Mo₆ film in a short time at room temperature. This combination helps the Mo₆ film retain its stabilization for more than 6 months under ambient conditions.

In addition, the protective mechanism of the PDMS fluid towards the Mo₆ film have been discussed by creating a new crosslinking network during the drying process at the ambient condition. The results of this study will be used in an investigation in order to develop an application of the Mo₆ film for a UV-Vis and NIR light trapping window.

3.2. Stabilization of the Mo₆ cluster film by directly fabrication with ketone polymer by EPD process

Some advantages of the use of polymers have been studied to retain long-life time luminescence, acting as the agents preventing quenching in open air and enhancing the thermal resistant of the octahedral molybdenum clusters. Photosensitive SU8 resist polymer for sensor [12], polystyrene for photocatalytic oxygenations [13], silica nanoparticles for time-gate luminescence bioimaging [14], β-Cyclodextrin polymer for biological application [15], polyurethane for oxygen sensor [16] or graphene for photocatalytic reduction [17, 18] have been reported.

Among those polymers, poly (methyl methacrylate) has been attracted a huge attention of the studies to fabricate luminescent hybrid materials because of the chemical and thermal stabilities, excellent biocompatibility and prominent transparency in the UV-NIR absorption range [19, 20]. In order to obtain homogeneous and transparent characteristics, the luminescent PMMA hybrids containing the Mo₆ clusters were directly synthesized by polymerization process between polymerizable organic counter cation of the cluster and vinyl acrylate monomers [21-24]. From the polymerized luminescent copolymer hybrids, several technologies have been used to mold the shape of materials such as microfibers prepared by electrospinning technology [21] or pellet [23]. In order to extend the application of the luminescent hybrid in the building field, thin films coated on glass have been carried out by using dip coating [25]. However, the thickness, transparency and optical properties of the film are limited by loading a high concentration of polymer matrix.

With the expectation to prepare a new functional material for the building application, in this study, the Cs₂[Mo₆I₈(OCOC₂F₅)₆] octahedral cluster (CMIF) as an excellent luminescent agent was selected to incorporate with the poly (methyl methacrylate) (PMMA) and cellulose acetate phthalate (CAP) matrix. The nanocomposites were deposited on indium tin oxide-coated glass (ITO-glass) by the electrophoretic deposition (EPD) process, a popular solution chemistry process used in the laboratory and industry scales with the bulk efficiency [26, 27]. The EPD process has been successfully applied to prepare the pure Mo₆ thin film based on the [Mo₆Br₈Br₆]ⁿ⁻ cluster precursor with excellent optical properties [7, 28] but it is not practical to deposit the pure [Mo₆I₈(OCOC₂F₅)₆]ⁿ⁻ cluster. Therefore, the polymers have crucially been used as dispersing medium to improve the film formation by the EPD process and prevent the quenching by protecting the apical ligands of the nanocluster from the air. The PMMA and CAP [29] possesses excellent mechanical strength that is a good property required for the fabrication of the UV-NIR adsorbing film on window. K. Kirakci et al. have reported that the (nBu₄N)₂[Mo₆I₁₄] exhibits the UV-Vis absorption stronger than (nBu₄N)₂[Mo₆I₈(CF₃CO₂)₆], followed

by the emission at longer wavelength with weaker emission efficiency [30]. That means the change of apical ligand also contributes to the excitation characteristic of the valance electron through the metal-ligand-metal transfer. The $\{\text{Mo}_6\text{I}_8\}^{4+}$ cluster core functionalizing with $(\text{OCOC}_2\text{F}_5)^-$ acidic groups exhibits excellent emission being studied in optic-electro device under liquid phase with high efficiency of deep red NIR luminescence [31]. The successful work is to fabricate the Mo_6 -based nanocomposite thin film (thickness of about 1.5 μm) with loading low polymer concentration, exhibiting the impressive luminescent property and relatively stability at high temperature and humidity for one month.

3.2.1. Chemicals and preparation the Mo_6 film by EPD process

Chemicals

The $\text{Cs}_2\text{Mo}_6\text{I}_8(\text{OCOC}_2\text{F}_5)_6$ (CMIF) cluster precursor was synthesized from the reaction of $\text{Cs}_2\text{Mo}_6\text{I}_8\text{I}_6$ cluster precursor [32] and $\text{Ag}(\text{OCOC}_2\text{F}_5)$ salt in acetone solution with the similar molar ratio by solution chemistry process [30]. The integrity and purity confirmed by ^{19}F nuclear magnetic resonance measurements with the presence of only two signals at $\delta = -83$ ppm and $\delta = -120$ ppm, energy-dispersive X-ray spectroscopy (EDX) and X-ray diffraction on single crystals have been reported[14]. Commercial cellulose acetate phthalate (CAP, 2534.12 g/mol, Fluka analytical Ltd.), poly (methyl methacrylate) (PMMA, 350,000 g/mol, 30,000-140,000 cm^3/g , Sigma-Aldrich company), acetone (99.5 %, Nacalai Tesque, Inc., Kyoto, Japan), methyl ethyl ketone (MEK) (99 %, Nacalai Tesque, Inc., Kyoto, Japan) were used without purification.

Preparation the Mo_6 film by EPD process

The preparation of the solution and fabrication of the Mo_6 film from the $\text{Cs}_2\text{Mo}_6\text{I}_8(\text{OCOC}_2\text{F}_5)_6$ cluster precursor were carried out in the same manner as in the previous report [28]. The $\text{Cs}_2\text{Mo}_6\text{I}_8(\text{OCOC}_2\text{F}_5)_6$ cluster was completely dissolved in Methyl Ethyl Ketone (MEK) and acetone with concentration of 5 g per litre with stirring by magnetic stirrer to prepare the homogeneous solutions. The zeta potential and conductivity of the solutions were measured by a zeta-potential analyzer (Malvern Instrument, Ltd., Zetasizer Nano Z, Malvern, UK) (Table 3.2). The Mo_6 thin film was deposited on indium tin oxide (ITO) coated glass slide as anode (Geomatec Co., Ltd. Tokyo, Japan; 6.15-7.27 Ohm/sq) with the surface area of $1.0 \times 2.5 \text{ cm}^2$ by applying an the electric field created by a Source Meter (Keithley Model 2400, Ohio, USA). Applied voltage and deposition time of the EPD process were optimized to obtain the homogeneous and transparent Mo_6 thin films.

Preparation the Mo_6 @polymer film by EPD process

The CAP and PMMA powders without purification were dissolved in acetone (50 g per litre) by agitating with a magnetic stirrer for 24 hours until obtaining the uniform dissolution. The solution of the $\text{Cs}_2\text{Mo}_6\text{I}_8(\text{OCOC}_2\text{F}_5)_6$ cluster precursor prepared in acetone (20 g per litre) was mixed with the polymer solution and continually stirred (300 rpm) for 10 min. The characterization of the solution is presented in Table 3.2. The Mo_6 @polymer films deposited on the ITO-coated glass anode were stored

at the ambient condition before characterization.

Stability of the optical properties of the Mo₆@polymer film

The Mo₆@polymer films prepared by the EPD process were dried at the ambient condition for 1 week before testing the thin film stability in a chamber (SH 641, Bench-Top Type Temperature and Humidity Chamber, Espec Ltd.). The temperature and relative humidity were fixed at 50°C and 70% RH, respectively. The nanocomposite film samples were exposed for 2 weeks and 1 month in order to observe the change of the surface morphology and optical properties of the Mo₆@polymer film. The exposed film samples collected after 2 weeks and 1 month were characterized the morphology and optical properties.

Characterization

The pocket-spectrophotometer (SEC2000 Spectra System, ALS) was used to characterize the color transformation of the Cs₂Mo₆I₈(OCOC₂F₅)₆ cluster solution during the EPD process. The in-situ electro-spectrometry data was recorded for the samples prepared at different deposition times. The morphology and thickness of the Mo₆@polymer films were measured by field-emission scanning electron microscopy (FE-SEM, Hitachi 4800). The element ratio of the cluster in nanocomposite film was measured by FE-SEM coupled with EDX analysis device. The UV-NIR absorption spectroscopy was measured by UV-Vis-NIR spectroscopy (V570, Jasco Corp.) in the wavelength range of 220 and 2000nm at the scan rate of 400 nm/s. The photoluminescence and photoluminescence excitation spectra of the nanocomposite films were measured by a high performance fluorescence spectroscope (FL) (FP8500, Jasco Corp.) connected to a xenon lamp at the scan rate of 500 nm/s. CL measurements were performed in a field emission SEM (Hitachi SU6600) equipped with a CL system (HORIBA MP32) under the pressure of 3×10⁻³ Pa at room temperature. For the CL measurements, a few milligrams of powders were deposited and hand-pressed on a carbon tape for each composition. CL spectra were obtained at room temperature by a CCD (2048 channels, HORIBA Jobin-Yvon, Spectrum One), while CL mapping was carried out with a photomultiplier (Hamamatsu Photonics, R943-02). The quantum yield was measured by an absolute PL quantum yield spectrometer C11347 (Hamamatsu Photonics) with the range of the excitation wavelength from 250 nm to 800 nm. The adhesion of the nanocomposite film was tested following the standard test method of ASTM D 3359 – 97 (test method B) by using transparent tape (Cellophane No. 252, 0.049 mm, adhesion strength of 3.1 N/10 mm, tensile strength of 36 N/10 mm, Sekisui Chemical Co., Ltd., Japan). The droplet images and adhesion testing surface were captured by the digital microscope (VHX-600, Keyence Co. Ltd.) with the magnification of 20 times.

3.2.2. EPD of Cs₂Mo₆I₈(OCOC₂F₅)₆ cluster precursor

The solutions of the Cs₂Mo₆I₈(OCOC₂F₅)₆ cluster in acetone or MEK solutions were tried to deposit on ITO-coated glass by the EPD process at 5 V for 30 s, however, no deposition film was obtained. During the EPD process, the movement of the cluster towards ITO-coated glass anode was observed,

accompanied by the color change of the cluster solution changed from yellow to green at the surface of the ITO-coated glass anode after 20 s of voltage application. The transformation of the absorbed wavelength measured by a pocket-spectrophotometer during EPD process is shown in **Figure 3.9**. The change of the absorption wavelength was recorded at different deposition times from 0 to 120 seconds at 5 V. For the first 20 s, the absorption peak shifts to higher point at the wavelength bands of 1, 2, and 3. For instance, the absorption wavelength of the band 2 increases from 410 (violet) nm to 470 (blue) after 80 s, and then saturates by 120 s. The appearance of the visible light absorption peak at 622 nm (yellow) and 700 nm (red) starts from the deposition time of 40 s and gradually increases until 120 s. The mixture of the blue (band 1, 2, 3) and yellow (band 4, 5) absorption results in the green color which corresponds to the visually observed in the cluster solution. After the suspension changed color, the particles fell down at the bottom. As the result, the Mo₆ film was not fabricated on the ITO-coated glass by the EPD process. This phenomena was not observed in the fabrication of the Mo₆ film based on Cs₂Mo₆Br₈Br₆^a cluster precursor in previous works [28], even the deposition was possible at higher voltage (25 V) for some kinds of solvents. The absorption property of the cluster originates from the [Mo₆I₈]⁴⁺ cores with VEC=24 followed by the metal to metal charge transfer (LMCT) that do not depend on the characteristic of the apical ligand separately^[6, 33]. Therefore, the development of the main absorption peak in the wavelength under 500 nm and the appearance of new absorption peaks at 622 nm (1.99 eV) and 700 nm (1.77 eV) are related to the reduction of the band gap energy of [Mo₆I₈]⁴⁺ cluster system. Normally, the [Mo₆Br₈Br₄(H₂O)₂] cluster was stabilized on the anode surface under the impact of electronic field as presenting in the previous work without the oxidization [7]. Therefore, the phenomena would be caused from the presentation of (C₂F₅COO)⁻ apical ligands liberated in the suspension during applying the voltage. It affects to the oxidation state of Mo cluster under the electric field at the surface of the anode. Under the existence of H₃O⁺ created by water electrolysis on the surface of the ITO glass, the [Mo₆I₈(OCOC₂F₅)₆]²⁻ cluster could be hydrolyzed to form the [Mo₆I₈(OCOC₂F₅)_{6-x}(OH)_x]²⁻ cluster and C₂F₅COOH acid. This reaction would cause the phenomena which was realized after 20 s by evolution of absorption spectroscopy (**Fig. 3.9**). C₂F₅COOH acid could be electrochemically oxidized by transferring radical electron toward anode and perform the free radical on C₂F₅COO^{*} group [34, 35]. This radical (C₂F₅COO^{*}) tends to receive electron from the octahedral Mo₆ cluster to come back C₂F₅COO⁻ anion state. As the result, the oxidization process of octahedral Mo₆ cluster is catalyzed by the C₂F₅COO^{*} reduction agent in order to create new oxidation state with absorbing visible light at band 4 and band 5. Interestingly, the color of the solution partially turned back to yellow color after finishing the EPD process in short waiting time. Consequently, the CMIF film was not obtained on the ITO-coated glass by the EPD process. In summary, the failure of the Mo₆ film deposition is caused by the high activity of the C₂F₅COO⁻ apical ligand under the impact of the electronic field.

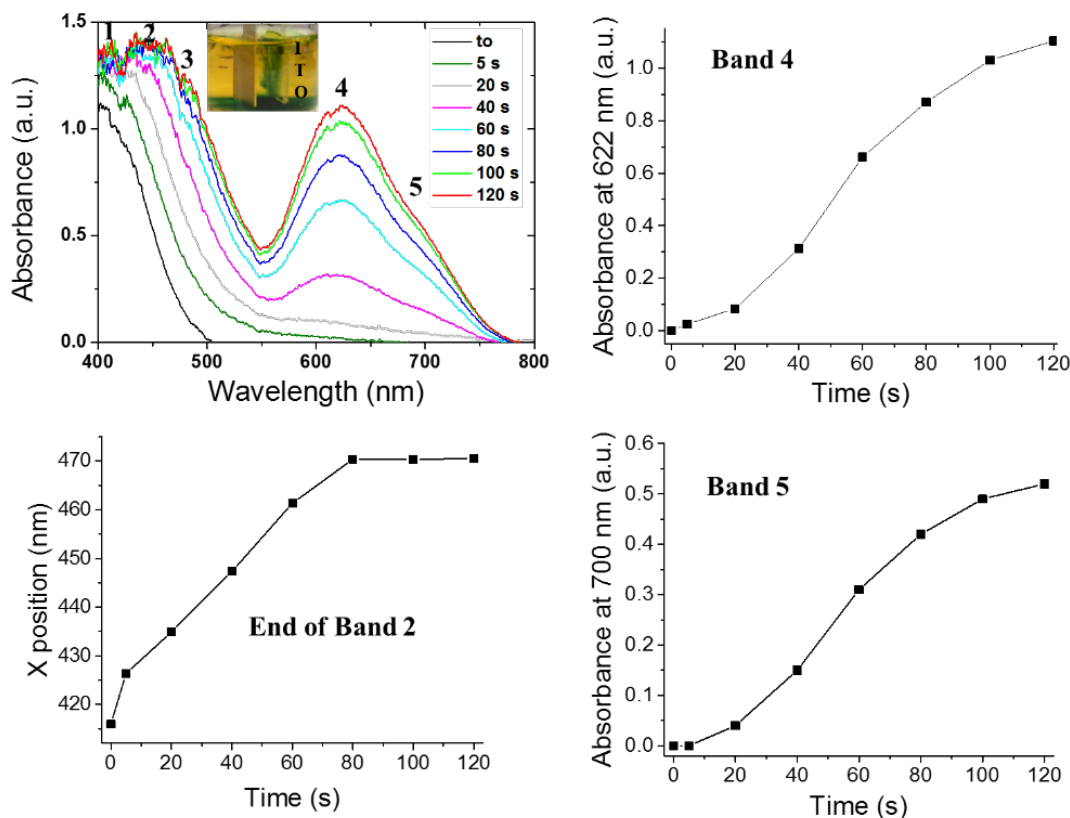


Figure 3.9. The development of UV-Vis absorption spectroscopy of the $\text{Cs}_2\text{Mo}_6\text{I}_8(\text{OCOC}_2\text{F}_5)_6$ cluster solution during the EPD process measured by the pocket-spectrophotometer.

3.2.3. EPD of Mo_6 @polymer nanocomposite

Morphology

In order to restrict the liberation of apical ligands from the octahedral Mo_6 cluster during the EPD process, CAP and PMMA polymers were used as dispersion medium as well as coating agents of the Mo_6 cluster in the solution. The $\text{Cs}_2\text{Mo}_6\text{I}_8(\text{OCOC}_2\text{F}_5)_6$ cluster in acetone and MEK solutions exhibits high negative zeta potential and high conductivity as presented in **Table 3.2**. The dissolution of the CMIF in MEK solution is limited, resulting in the electrical conductivity lower than the cluster suspensions in acetone. The electrical conductivity of CMIF@PMMA was 1.5 times higher than that of pure CMIF solution. T. Mahnaj et al. has reported that the interaction of the PMMA and propylene carbonate in inorganic acid creates proton-conducting gel-like electrolytes because PMMA can form the complexes with inorganic or organic acid by electrostatic interaction accompanied by increasing the number of free protons [36]. In the case of the nanocomposite solution, due to the formation of the complexes between $[\text{Mo}_6\text{I}_8(\text{OCOC}_2\text{F}_5)_6]^{2-}$ anion cluster and PMMA, the number of the protons liberated from acetone tend to freely move in the suspension. The more protons are free, the higher the electrical conductivity is. The electrical conductivity of the CAP-based nanocomposite gel is similar to that of the CMIF solution. The value of the electrical conductivity of the nanocomposite suspension is efficient for the EPD process.

Table 3.2. The physical properties of the CMIF cluster (20 g/lit), CMIF @PMMA (50 g/lit), and CMIF @CAP (50 g/lit) suspensions.

Solution	Zeta potential (mV)	Conductivity ($10^{-3} \times \text{mS/cm}$)
CMIF (MEK)	-31.2± 1.5	299 ± 5
CMIF (Acetone)	-39.5± 2.5	400 ± 30
CAP	-	32 ± 2
CMIF@CAP	-	451 ± 21
PMMA	-	5 ± 1
CMIF@PMMA	-	611 ± 17

Though the zeta potential of the nanocomposite suspension could not be measured with precise parameters, the deposition of the suspension on the anode was observed, showing the positive charge of the nanocomposite. The outermost surface and cross sectional images of the nanocomposite films are shown in **Figure 3.10**. All the nanocomposite films are transparent and relatively stable after the deposition process. It was observed that CAP polymer particles with visible size in the range from 10 to 100 nm still existed in the surface of the CMIF@CAP film while the signals from CAP was not detected in the CMIF@PMMA film. The solubility of the polymer in acetone also affects the homogeneity of the nanocomposite films. The recognized thickness increases corresponding to the increase of the applied voltage; 0.9 μm for CMIF@CAP 11 at 1 V, 1.1 μm for CMIF@CAP 21 at 2 V, 1.2 μm for CMIF@PMMA 21 at 2 V and 1.4 μm for CMIF@PMMA 31 at 3 V. The PMMA possesses the molecular weight of 135,000 g/mol, therefore, it needed higher voltage to form similar color films compared with CAP. The fabrication of good quality films at low voltage is one of the desirable characteristics. The applied voltage parameters were optimized at 2 V at the maximum for CMIF@CAP solution and 3 V for CMIF@PMMA solution because the green color start to appear at the maximum optimal voltage and, consequently, the photoluminescence of the nanocomposite film is reduced (not show here). Considering this result, the PMMA having higher molecular weight than CAP needs stronger electric field to move in the solution.

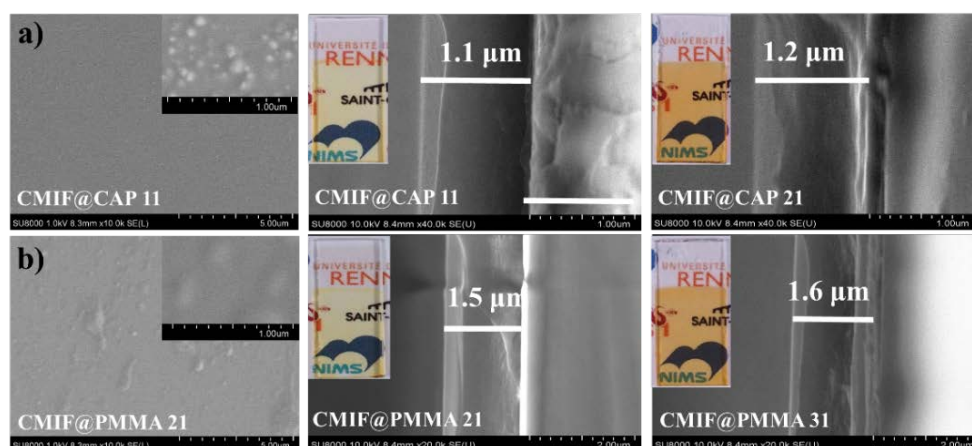


Figure 3.10. SEM images including the surface morphology and cross section of the nanocomposite films at different EPD parameters: a) CMIF with CAP and b) CMIF with PMMA.

The element concentrations of the CMIF cluster from powder to nanocomposite were measured by EDX analyzer (**Table 3.3**). The results show that the ratio of the Mo and I atoms always keeps the values which are close to the theoretical index. Even though the nanocomposite film deposited on an anode, the Cs⁺ counter cations are detected in the film. The concentration of Cs⁺ cations decreases corresponding to the increase of the applied voltage. At higher applied voltage, the tendency to dissociate the cation and anion is enhanced. On the similar way, the number of F ions from the apical ligand seems to increase up to 2 ions at higher applied voltage. The high negative charge on the surface of the CMIF cluster was confirmed from the zeta potential value (~ -40 mV) that is suggested to decide the total charge of the nanocomposite particles. The chains of polymer will stretch out during dissolving into the solvent. On the circuits of the polymer exhibit positive electrostatics originated from carbonyl groups of the acetate. The electrostatic interaction of the polymer with negative cluster nanoparticle and the formation of the complexes with acidic apical ligands occurs, followed by the cluster coating with the layers of polymer to form the nanocomposite particles. During the EPD process, low applied voltage will limit the separation of acidic apical ligands from the cluster, however, it is insufficient to create a force to completely separate the anion and cation which will be able to move to the electrodes. For this result, the Cs⁺ cation is found in the film.

Table 3.3. The element concentration of the CMIF in polymer matrixes after the EPD process.

Sample	Cs	Mo	I	F
CMIF (theoretical index)	2	6	8	30
CMIF powder	2	6	8.9	28
CMIF@CAP11 (1 V, 1 min)	1.3	6	7	40
CMIF@CAP21 (2V, 1 min)	0.8	6	7.5	20
CMIF@PMMA21 (2V, 1 min)	1.4	6	7	40
CMIF@PMMA31 (3V, 1 min)	0.9	6	7	22

Optical property

Figure 3.11a presents the absorbance of CMIF, CMIF@PMMA and CMIF@CAP in acetone solution. All the solutions give similar absorption peak at the wavelength of 330 nm and shoulder peak at 400 nm in the UV range. The CAP polymer shows a weak absorption peak at the wavelength of 328 nm. This absorption originates from the acetate phthalate group anchored on cellulose circuit. The Mo₆@polymer yellow thin films fabricated at low voltages (1 V for CMIF@CAP and 2 V for CMIF@PMMA) obtain the transmittance of about 80% being similar to that of ITO glass including the adsorption characteristic of the CMIF precursor (**Fig. 3.11b**). When the applied voltage increases, the transmittance of the brown films insignificantly reduces followed by the appearance of wavy line in the NIR wavelength. This phenomena is similar to the case of the Mo₆ film fabricated from Cs₂Mo₆Br₈Br₈^a cluster precursor in our previous work ^[1]. This phenomena originated from the interference of the incident light and diffraction light between the top of the Mo₆ film and the top of the ITO layer. The absorption of the UV light of the nanocomposite film depends on the Mo₆-based octahedral structural

cluster units. As the result, the homogeneous and transparent nanocomposite films containing the Mo₆ octahedral cluster were easily obtained by the EPD process.

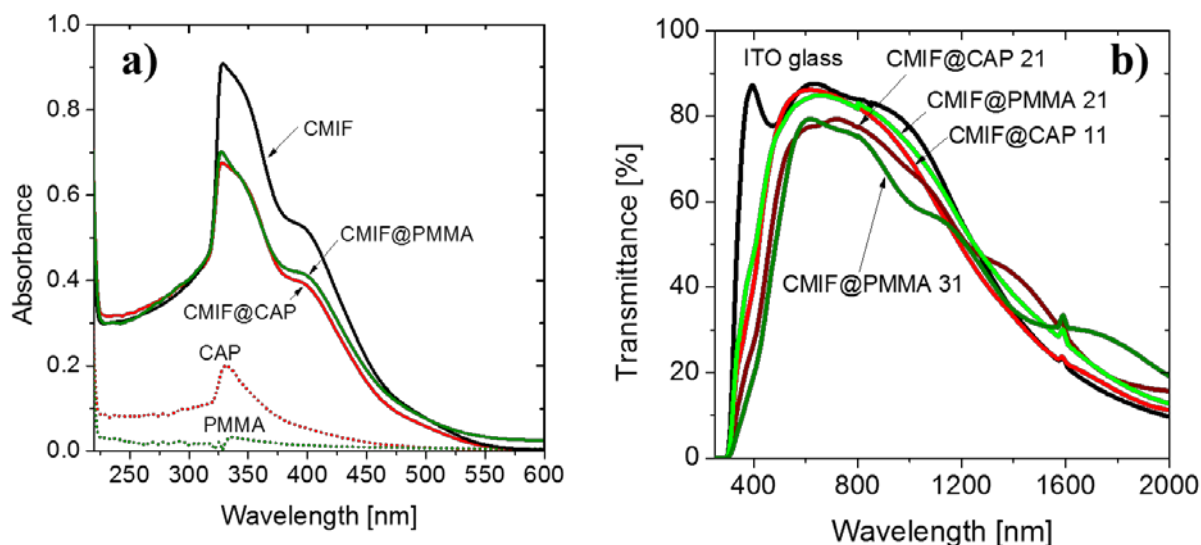


Figure 3.11. a) The absorbance of the Mo₆ cluster precursor and Mo₆@polymer in acetone and b) the transmittance of the Mo₆ and the nanocomposite thin film.

The photoluminescence of the cluster strongly depends on the {Mo₆I₈}⁴⁺ core and slightly depends on the apical ligands^[32]. The difference of the PL excitation spectra of CMIF and its nanocomposites is presented in **Figure 3.12** under strong excitation with the wavelength of 275 nm and the wavelength range between 300 nm and 400 nm (UV range). The photoluminescence curves of CMIF^[33] (**Fig. 3.12b**) and their nanocomposite films (**Fig. 3.12c**) present the obvious emission in the visible and deep near infrared wavelength of 600 nm and 800 nm with a narrow blue-shifted peak at 660 nm. With the increase of excitation wavelength, the photoluminescence intensity decreases and disappears at the excitation wavelength of 450 nm. No significant difference of PL spectra is realized, which means that the incorporation of the Mo cluster and polymer by the EPD does not affect to the optical characteristic of the cluster. Good dispersion and compatibility of the cluster in the polymer matrix approve the prominent optical property of the nanocomposite films.

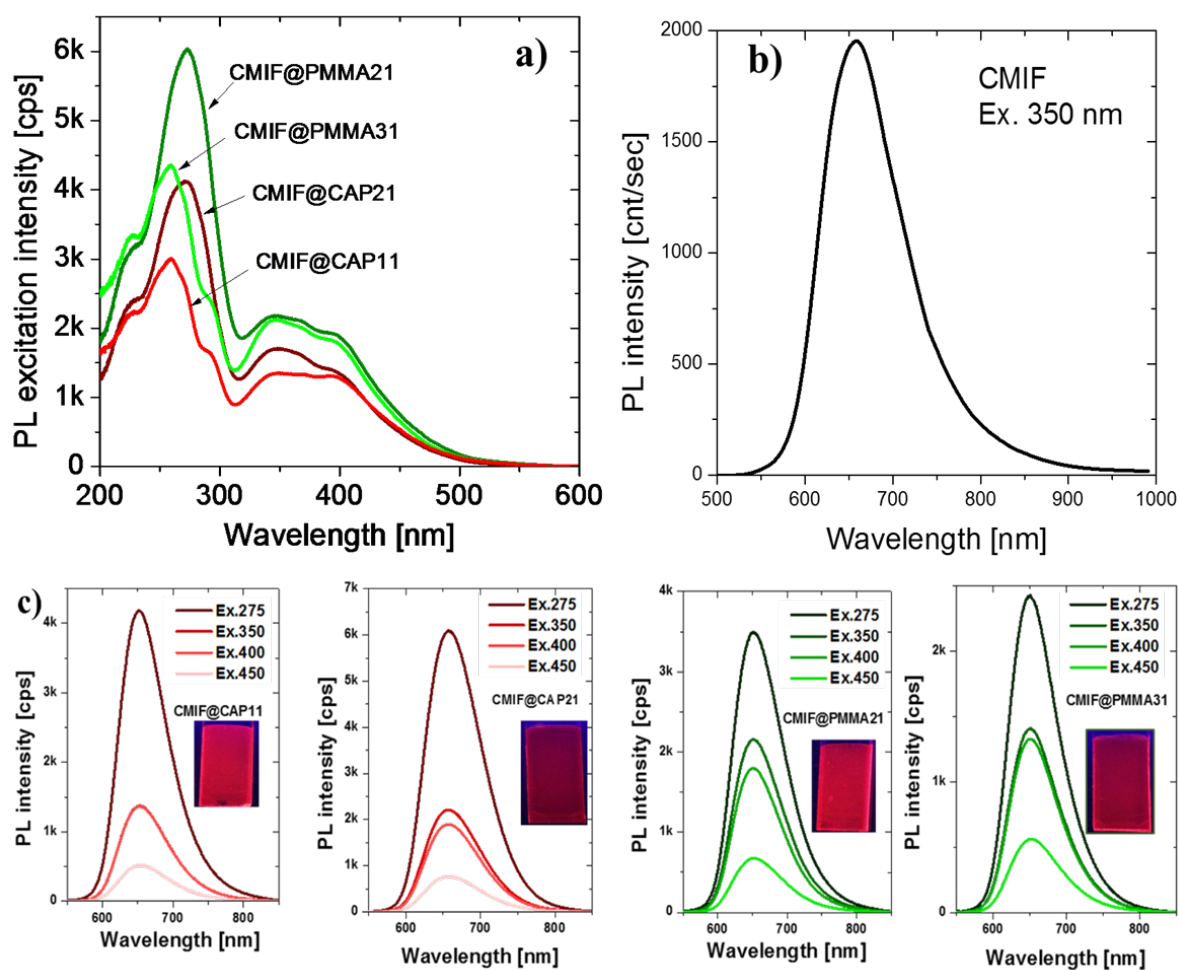


Figure 3.12. a) Photoluminescence excitation spectroscopy and b) photoluminescence spectroscopy of the Mo_6 cluster and c) fluorescence spectroscopy of the Mo_6 based nanocomposite thin films by Xenon lamp and the photoluminescence photos under 324 nm UV light.

For the same $\{\text{Mo}_6\text{L}_8\}^{4+}$ core, the cathodoluminescence is sensitive with the nature of the apical ligand. In order to realize the different interaction of apical ligand and polymer, cathodoluminescence spectroscopy of the CMIF precursor (1), CMIF@CAP (2) and CMIF @ PMMA (3) nanocomposite thin films was performed. The results are shown in **Figure 3.13a**. The CL curves of the CMIF precursor present a narrow blue-shifted band in the visible light range between 600 and 800 nm with maximum wavelength at 655 nm. This result was also reported in a previous work ^[33]. Similarly, the CL curves of the CMIF@CAP and CMIF@PMMA films exhibit a peak at the wavelength of 674 nm and 664 nm, respectively. A shift of the peak to higher wavelength in the nanocomposite film suggests that the apical ligand is influenced by the interaction with polymer matrix via the functional groups. The CAP polymer containing many hydroxyl groups would interact with $[\text{C}_2\text{F}_5\text{COO}]^-$ groups of the CMIF cluster via hydrogen bonds and Van-der Waals interactions. Consequently, the 20 nm peak-shift in the emission band was clearly recognized in the CMIF@CAP film.

To investigate the stability of optical property under the irradiation of electron beam, the CL decays of

the CMIF precursor (1), CMIF@CAP (2) and CMIF @ PMMA (3) nanocomposite thin films were compared in **Figure 3.13b**. The CL value of CMIF cluster suddenly decreases to zero after the first 80 s of irradiation by electron beam while it is approximately 300 s for the CMIF@PMMA and CMIF@CAP nanocomposite films. This result gives out the efficiency in using the polymer in order to improve of the luminescent stability of the Mo₆ cluster. This phenomenon was created by the excited electron at the triplet (T₁) and singlet (S₁) states recombining with the hole on the ground state (S₀). The luminescence of the {Mo₆I₈}⁴⁺ core is quenched because the excited electrons transfers to other molecules which contacts with {Mo₆I₈}⁴⁺ core. From the CL intensity of the Mo₆ cluster with different apical ligands, the {C₂F₅COO}⁻ apical ligands showed the strongest decay [33]. Under the irradiation of electron beam, the {Mo₆I₈}²⁻ core and C=O group of apical ligand are simultaneously excited to form the {Mo₆I₈}^{2-*} cluster and C=O* group. The absorption of the energy of the C=O group of apical ligand significantly enhance the total luminescence intensity of the [Mo₆I₈(C₂F₅COO)₆]²⁻ clusters, resulting the strongest luminescence compared with cluster linking with halogen ligand [33]. The excited electron on the cluster and carbonyl group is quickly quenched by free oxygen molecules to form singlet oxygen (O₁) and cause the loss of luminescence. When the cluster is blended with polymer, a number of carbonyl groups on PMMA and CAP would be excited at the same time with the Mo₆ clusters. The interaction of the excited carbonyl in polymer with O₂ molecules will reduce the quenching of the Mo₆ cluster by O₂ molecules.

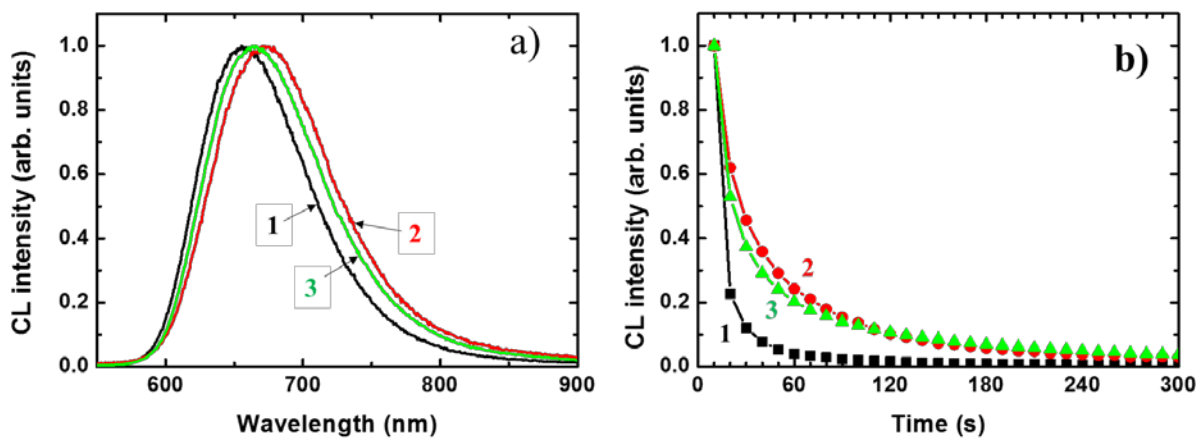


Figure 3.13. a) Cathodoluminescence spectroscopy (CL) and b) stabilization of CL under continual irradiation for 300 s. (1: CMIF, 2: CMIF@CAP, 3: CMIF@PMMA)

The quantum yield of the CMIF is recognized the loss of the emission efficiency corresponding to the increase of the excitation wavelength (**Fig. 3.14**). The quantum yield of the CMIF@PMMA and CMIF@CAP films prepared at different voltages suddenly decreases at the excitation wavelength of 300 nm and increases again to exhibit a peak at 400 nm. The incorporation with polymer causes the decrease of the emission efficiency of the Mo₆ cluster exception the CMIF@CAP11. The value of quantum yield depends on the ratio of emission energy and absorption energy. For instance, the emission value generated by CMIF cluster is constant, which means the decrease of the quantum yield

corresponding to the increase the absorption energy. The additional absorption energy is caused by the functional groups containing the π linking on the polymer chain. The second suggestion is to reduce the recognition of the emission light sign due to the scattering of the emission light by the crystallinity part of the polymer chain. However the quantum yield value of the CMIF@PMMA in the excitation wavelength range between 300 and 600 nm is lower than that of CMIF@CAP for all the different voltages due to the higher molecular weight as same as the inferior crystallinity of the PMMA. Interestingly, the CMIF@CAP film prepared at 1 V archives similar quantum yield to that of CMIF. At the excitation wavelength of 400 nm, we can see the quantum yield obtains with the deposition voltage at 1V (~15%) as same as with CMIF precursor. When the voltage is increased to 2 V, the quantum yield decreases to about 6% and it further decreases to 4% at 3 V deposition voltage. The decrease of the emission suggests that the chemical ingredients of the apical ligands of the $[\text{Mo}_6\text{I}_8(\text{OCOC}_2\text{F}_5)_6]^{2-}$ octahedral cluster are changed during applying the electric field. The electric field still influences to the chemical structure of the octahedron at high temperature even though the polymer is used to stabilize the cluster on the surface of the ITO-coated glass.

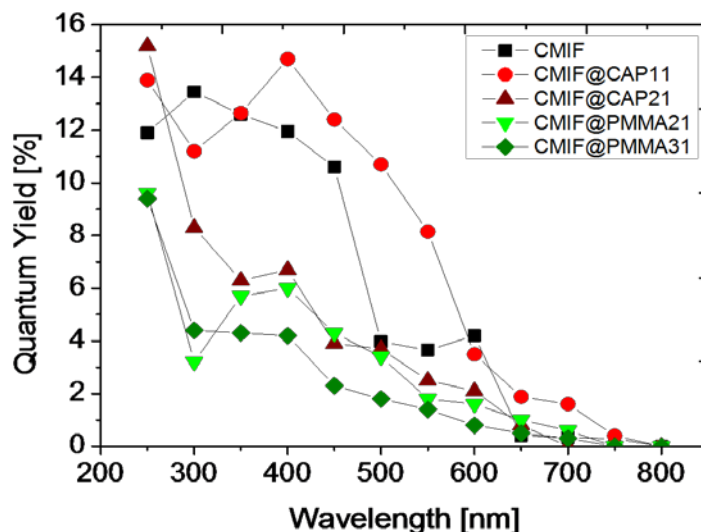


Figure 3.14. The quantum yield of the nanocomposite films prepared at different deposition voltages.

Stability of mechanical and optical properties of the Mo_6 @polymer film

Figure 3.15a shows the result of adhesion test of the nanocomposite films prepared by the EPD process. It can be seen that no peeling-off occurs by the tape test. These results show that the nanocomposite film is mechanically stabilized on the surface of ITO-coated glass. The convenience of the EPD process is easy fabrication of thin films, in this case about $1.5 \mu\text{m}$ thick, on flexible conductive substrates. The stable film based on polymer not only immobilize the Mo_6 cluster but also enhance the mechanical strength of the film that enables to extend the application field of the luminescent film. The hydrophobicity of the Mo_6 cluster-based luminescent films without and with exposing to the atmosphere of 70% RH at 50°C for 2 and 4 weeks were investigated by measuring the contact angle of a water droplet on the surface. **Figure 3.15b** presents the contact angles of the films without exposing at

different deposition voltages. In general, the contact angle of the CMIF@CAP film shows at 65° while the CMIF@PMMA film at 85° , indicating hydrophilic characteristic of the film. As it is known, CAP polymer contains a lot of hydroxyl groups on the polymer chains that causes the low hydrophilic property for the CAP-based film. However, the deposition films also adsorb large amount of water molecules during the EPD process in the solvent. The original characteristic of the Mo_6 -based film is hydrophilic and this property is enhanced after exposing to the atmosphere of 70% RH humidity corresponding to the decrease of the contact angle. At 50°C , the polymer chains may be elongated by absorption of the thermal energy, causing the local reduction in crystallinity. Most the films show the decrease of the contact angle after the exposure for 2 weeks (**Fig. 3.15c**) and for 4 weeks (**Fig. 3.15d**). Summarily, the water proof characteristic could be improved by covering the top coat layer if it is used in further future application.

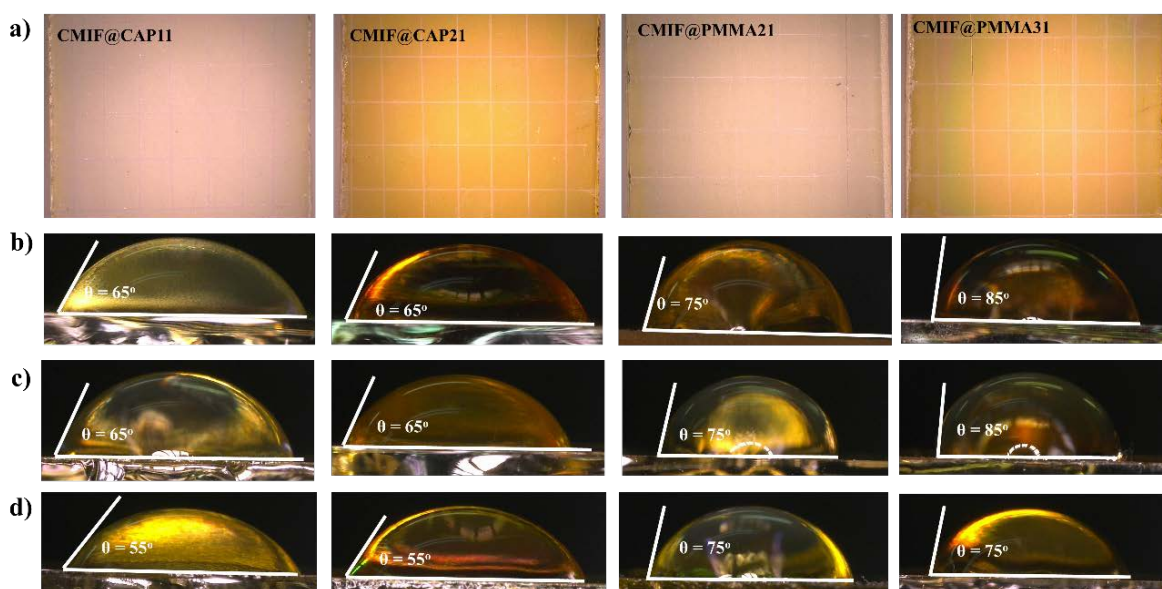


Figure 3.15. The photos of the Mo_6 @polymer based films: a) outer surface after testing adhesion by tape, b) contact angle after prepared by EPD process, c) contact angle after exposing at 50°C and RH70% for 2 weeks, and d) contact angle after exposing at 50°C and RH70% for 4 weeks.

In order to evaluate the effect of carbonyl groups in polymer on the optical of the Mo_6 cluster, the CMIF, CMIF@PMMA and CMIF@CAP were continually irradiated for 10 minute under 325 laser (**Fig. 3.16**). In the previous report, the PMMA was irradiated with the laser of 266 nm to generate the radicals such as CHO, $\cdot\text{CH}_3\text{CO}$, CH_3 , and COOCH_3 [37]. After excitation, the decay of excited carbonyl ($\text{C}=\text{O}^*$) to the ground state occurs in the wavelength between 380 nm and 450 nm [38]. The relatively similar photon energy is also recognized in the photoluminescence spectroscopy of the Mo_6 cluster-based nanocomposite films. The photoluminescence spectroscopy of the CMIF@CAP film includes an emission peak originated from Mo_6 cluster at 668 nm and an emitting peak originated from acetate phthalate at 460 nm in the first irradiation. The same phenomena is observed for the CMIF@PMMA

film after the second irradiation (60 s). Both the nanocomposite films reached the maximum emitting intensity of carbonyl group after 150 s irradiation corresponding to decrease photoluminescence intensity of the Mo_6 cluster about 67% for CMIF@CAP film and 62% for CMIF@PMMA film after 300 s. The emission characteristic and optical stability of the films depend on the irradiation source. The radicals are strongly generated from the carbonyl group on the polymer followed by the destruction of the polymer circuits by the laser irradiation. This phenomena does not occur under the electron beam or the UV light from Xenon lamp.

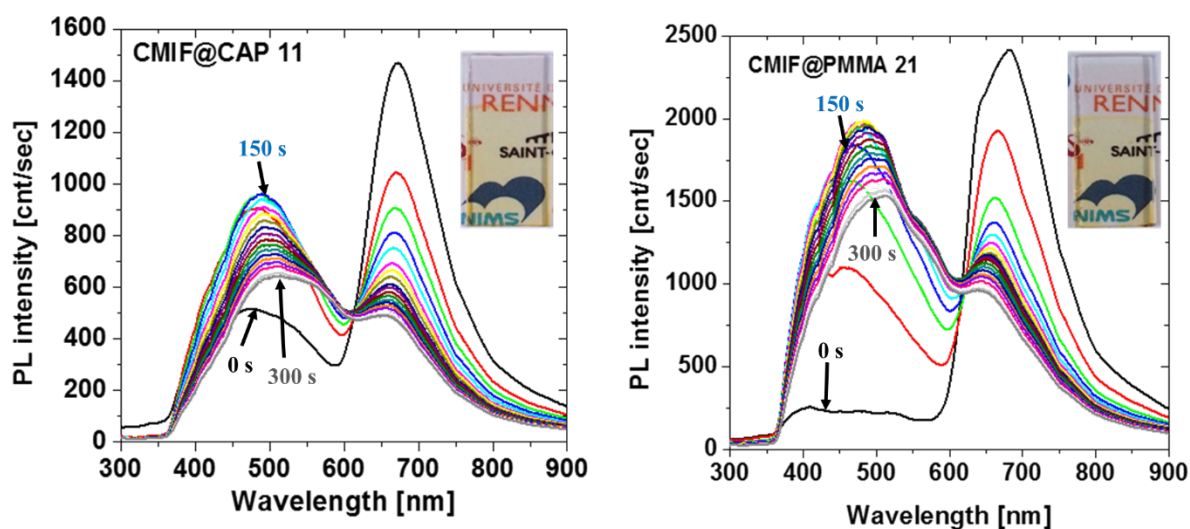


Figure 3.16. The change in the photoluminescence of the nanocomposite film under continual He-Cd laser irradiation for 300 s.

In the wavelength of the UV light range, the nanocomposite films after continually exposing under high temperature and humidity for one month have a tendency to increase the average value of the quantum yield in the excitation wavelength in the range between 300 nm and 400 nm (**Fig. 3.17**). In the case of the deposition at low voltage, the quantum yield value is proportional to the increase of the excitation wavelength following the linear fitting. The polynomial fit is obtained for the films prepared at high voltage. The increase of the quantum yield of the films agrees with the enhancement of the emission light from the cluster dispersing in polymer matrix. The polymer could be aged during heating at 50°C and humidity absorption for PMMA and CAP polymers that changes the crystallinity of the polymer chains. Consequently, the scattering of the emission light is reduced and the sign of emission light in detector is increased. The improved quantum yield is a good tendency for increase the application ability of the film material. Therefore, the mechanical property of the luminescent nanocomposite film should be further studied in further investigation.

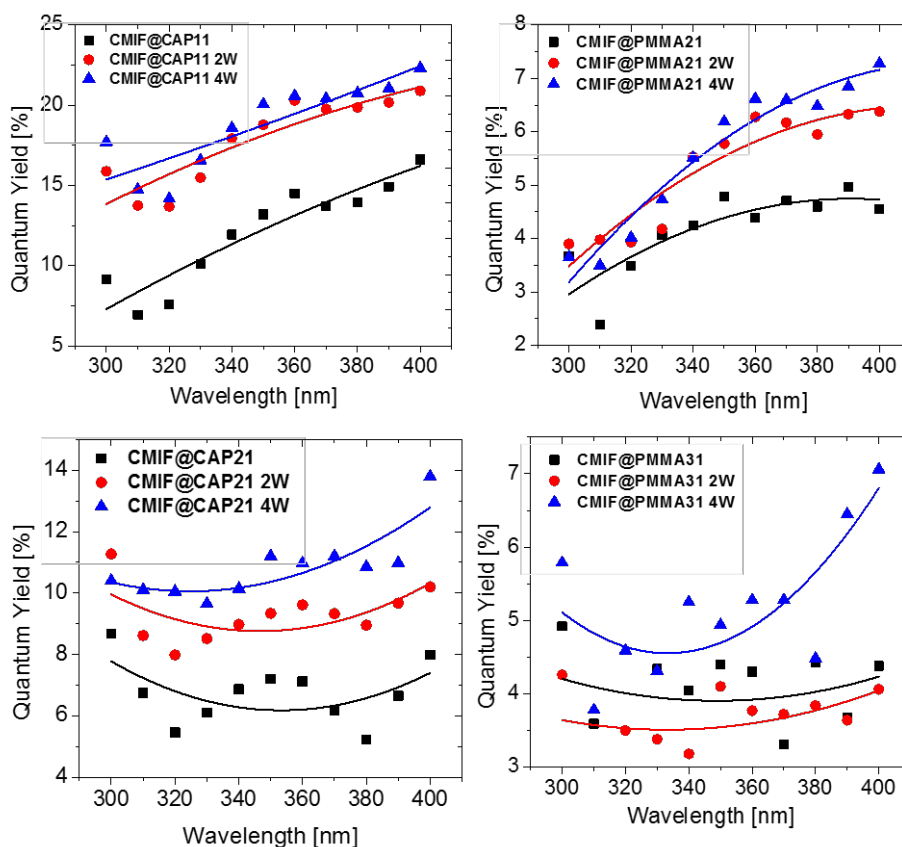


Figure 3.17. The behaviors of the quantum yield of the nanocomposite films without and with exposing at the 70%RH and 50°C for 2 weeks and 4 weeks.

3.2.4. Conclusions

In order to promote the applicable ability of the photoluminescence of the $[\text{Mo}_6\text{I}_8(\text{OCOC}_2\text{F}_5)_6]^{n-}$ octahedral cluster, the stabilization of the cluster by incorporating with the support materials was studied. The fabrication of the Mo_6 cluster-based nanocomposite film was performed by the electrophoretic deposition process on the ITO-coated glass. In this study, two kinds of the polymers exhibiting high transparent (poly methyl methacrylate) and biocompatible (cellulose acetate phthalate) characteristics were separately used as the dispersing medium to immobile and protect the Mo_6 cluster during the EPD process. With the thickness of about 1.5 μm , the nanocomposite film exhibited the excellent photoluminescence accompanying the strong absorption in the ultra-visible and near-infrared range. The quantum yield insignificantly reduced for the film prepared at low deposition voltage (1 V). Good adhesion and hydrophobic properties of the film were fairly obtained while the reduction of the photoluminescence during continually irradiated by 325 nm laser was recognized. Correspondingly, the emission from the functional groups of the polymer appeared at the wavelength of 480 nm when increasing the irradiation time. The polymer can protect the cluster during the EPD process but the protection from the weather condition is insignificant. However, as the result of the study, a new method to prepare Mo_6 -based nanocomposite thin film on a conductive substrate has been elucidated for energy saving application by performing at low voltage.

References

1. T. K. N. Nguyen, F. Grasset, B. Dierre, C. Matsunaga, S. Cordier, P. Lemoine, N. Ohashi and T. Uchikoshi. Fabrication of transparent thin film of octahedral molybdenum metal clusters by electrophoretic deposition. *ECS J. Solid. State. Sci. and Technol.*, 5, 178-186, 2016.
2. T. K. N. Nguyen, B. Dierre, F. Grasset, A. Renaud, S. Cordier, P. Lemoine, N. Ohashi, and T. Uchikoshi. Formation mechanism of transparent Mo₆ metal atom cluster film prepared by electrophoretic deposition. *J. Electrochem. Soc.*, 164, 412–418, 2017.
3. S. Seethapathy, and T. Górecki. Applications of polydimethylsiloxane in analytical chemistry: A review. *Anal. Chim. Acta*, 750, 48–62, 2012.
4. D. Zhu, S. H. Wang, and X. Zhou. Recent progress in fabrication and application of polydimethylsiloxane sponges. *J. Mater. Chem. A*, 5, 16467–16497, 2017.
5. L. J. Guggenberger, and W. Sleight. Structural and bonding characterizations of molybdenum dibromide, Mo₆Br₁₂·2H₂O. *Minor. Chem.*, 8, 2041-2049, 1969.
6. K. Kirakci, S. Cordier, and C. Perrin. Synthesis and characterization of Cs₂Mo₆X₁₄ (X = Br or I) hexamolybdenum cluster halides: Efficient Mo₆ cluster precursors for solution chemistry syntheses. *Z. Anorg. Allg. Chem.*, 631, 411–416, 2005.
7. N. Saito, S. Cordier, P. Lemoine, T. Ohsawa, Y. Wada, F. Grasset, S. J. Cross, and N. Ohashi. Lattice and valence electronic structures of crystalline octahedral molybdenum halide clusters-based compounds, Cs₂[Mo₆X₁₄] (X = Cl, Br, I), studied by density functional theory calculations. *Inorg. Chem.*, 56, 6234–6243, 2017.
8. A. M. Engwall, Z. Rao, and E. Chason. Origins of residual stress in thin films: Interaction between microstructure and growth kinetics. *Mater. Des.*, 110, 616–623, 2016.
9. M. Ghidelli, M. Sebastiani, C. Collet, and R. Guillemet. Determination of the elastic moduli and residual stresses of freestanding Au-TiW bilayer thin films by nanoindentation. *Mater. Des.*, 106, 436–445, 2016.
10. M. Cypryk, and Y. Apeloig. Mechanism of the Acid-Catalyzed Si–O bond cleavage in siloxanes and siloxanols: A theoretical study. *Organometallics*, 21, 2165–2175, 2002.
11. T. K. N. Nguyen, B. Dierre, F. Grasset, N. Dumait, S. Cordier, P. Lemoine, A. Renaud, H. Fudouzi, N. Ohashi and T. Uchikoshi. Electrophoretic coating of octahedral molybdenum metal clusters for UV/NIR light screening, *Coatings*, 7, 114-127, 2017.
12. J. Bignon, N. Huby, M. Amela-Cortes, Y. Molard, A. Garreau, S. Cordier, B. Bêche and J. L. Duvail. Efficient active wave guiding properties of Mo₆ nano-cluster-doped polymer nanotubes. *Nanotechnology*, 27, 255201-255207, 2016.
13. A. Beltran, M. Mikhailov, M. N. Sokolov, V. Perez-Laguna, A. Rezusta, M. Jose Revillod and F. Galindo. A photobleaching resistant polymer supported hexanuclear molybdenum iodide cluster for photocatalytic oxygenations and photodynamic inactivation of *Staphylococcus aureus*. *J. Mater. Chem. B*, 4, 5975-5979, 2016.
14. C. Neaime, M. Amela-Cortes, F. Grasset, Y. Molard, S. Cordier, B. Dierre, M. Mortier, T. Takei, K.

- Takahashi, H. Haneda, M. Verelstf and S. Lechevallier. Time-gated luminescence bioimaging with new luminescent nanocolloids based on $[\text{Mo}_6\text{I}_8(\text{C}_2\text{F}_5\text{COO})_6]^{2-}$ metal atom clusters. *Phys. Chem. Chem. Phys.*, 18, 30166-30173, 2016.
15. K. Kirakci, V. Sícha, J. Holub, P. Kubát, and K. Lang. Luminescent hydrogel particles prepared by self-assembly of β -Cyclodextrin polymer and octahedral molybdenum cluster complexes. *Inorg. Chem.*, 53, 13012–13018, 2014.
16. M. A. Cortes, S. Paofai, S. Cordier, H. Folliotc and Y. Molard. Tuned red NIR phosphorescence of polyurethane hybrid composites embedding metallic nanoclusters for oxygen sensing. *Chem. Commun.*, 51, 8177-8180, 2015.
17. P. Kumar, H. P. Mungse, S. Cordier, R. Boukherroub, O. P. Khatri, and S. L. Jain. Hexamolybdenum clusters supported on graphene oxide: visible-light induced photocatalytic reduction of carbon dioxide into methanol. *Carbon*, 94, 91-100, 2015.
18. M. Feliz, M. Puche, P. Atienzar, P. Concepcion, S. Cordier and Y.Molard. In situ generation of active molybdenum octahedral clusters for photocatalytic hydrogen production from water. *Chem. Sus. Chem.*, 9, 1963 – 1971, 2016.
19. F. Meinardi, A. Colombo, K. A. Velizhanin, R. Simonutti, M. Lorenzon, L. Beverina, R. Viswanatha, V. I. Klimov and S. Brovelli. Large-area luminescent solar concentrators based on ‘Stokes-shift-engineered’ nanocrystals in a mass-polymerized PMMA matrix. *Nature photonics*, 8, 392-399, 2014.
20. F. C. Hurtado, M. D. Lozano-Baena, C. Neaime, A. Burel, S. Jeanne, P. P. Mussi, S. Cordier, and F. Grasset. Studies on plant cell toxicity of luminescent silica nanoparticles ($\text{Cs}_2[\text{Mo}_6\text{Br}_{14}]\text{@SiO}_2$) and its constitutive components. *J. Nanopart. Res.*, 18-69, 2016.
21. O. A. Efremova, K. A. Brylev, Y. A. Vorotnikov, L. Vejsadova, M.A. Shestopalov, G. F. Chimonides, P. Mikes, P.D. Topham, S. J. Kim, N. Kitamura and A. J. Sutherland. Photoluminescent materials based on PMMA and a highly-emissive octahedral molybdenum metal cluster complex. *J. Mater. Chem. C*, 4, 497-503, 2016.
22. Y. Molard, C. Labbé, J. Cardin, and S. Cordier. Sensitization of Er^{3+} infrared photoluminescence embedded in a hybrid organic-inorganic copolymer containing octahedral molybdenum clusters. *Adv. Funct. Mater.*, 23, 4821–4825, 2013.
23. M. A.Cortes, A. Garreau, S. L. Duvaillb and Y. Molard. Deep red luminescent hybrid copolymer materials with high transition metal cluster content. *J. Mater. Chem. C*, 2, 1545-1552, 2014.
24. N. Saito, P. Lemoine, N. Dumait, M. A. Cortes, S. Paofai, T. Roisnel, V. Nassif, F. Grasset, Y. Wada, N. Ohashi and S. Cordier. From $\text{Cs}_2\text{Mo}_6\text{Cl}_{14}$ to $\text{Cs}_2\text{Mo}_6\text{Cl}_{14}\cdot\text{H}_2\text{O}$ and vice versa: crystal chemistry investigations. *J. Clust. Sci.*, 28, 773–798, 2017.
25. T. G. Truong, B. Dierre, F. Grasset, N. Saito, N. Saito, T. K. N. Nguyen, K. Takahashi, T. Uchikoshi, M. Amela-Cortes, Y. Molard, S. Cordier and N. Ohashi. Visible tunable lighting system based on polymer composites embedding ZnO and metallic clusters: from colloids to thin films. *Sci. Technol. Adv. Mater.*, 17, 443–453, 2016.
26. N. Saito, Y. Wada, P. Lemoine, S. Cordier, F. Grasset, T. Ohsawa, N. Saito, J. S. Cross, and N.

- Ohashi. Theoretical and experimental determination of the crystal structures of cesium–molybdenum chloride. *Jap. J. App. Phys.*, 55, 1-8, 2016.
27. W. D. Hewett, J. H. Newton, and W. Weltner. Absorption spectra of molybdenum oxide molecules and molybdenum atoms in neon and argon matrices at 4 K. *J. Phys. Chem.*, 79, 2640-2649, 1975.
28. S. Yang, W. Li, B. Cao, H. Zeng, and W. Cai. Origin of blue emission from silicon nanoparticles: direct transition and interface recombination. *J. Phys. Chem. C*, 115, 21056-21062, 2011.
29. Y. Zeng, C. Fan, D. D. Do, and D. Nicholson. Evaporation from an ink-bottle pore: mechanisms of adsorption and desorption. *Eng. Chem. Res.*, 53, 15467–15474, 2014.
30. K. Kirakci, P. Kubát, M. Dusek, K. Fejfarová, V. Sícha, J. Mosinger, and K. Lang. A highly luminescent hexanuclear molybdenum cluster–apromising candidate toward photoactive materials. *Eur. J. Inorg. Chem.*, 2012, 3107-3111, 2012.
31. M. Prévôt, M. A. Cortes, S. K. Manna, R. Lefort, S. Cordier, H. Folliot, L. Dupont, and Y. Molard. Design and integration in electro-optic devices of highly efficient and robust red-NIR phosphorescent nematic hybrid liquid crystals containing $[\text{Mo}_6\text{I}_8(\text{OCOC}_n\text{F}_{2n+1})_6]^{2-}$ ($n = 1, 2, 3$). *Adv. Funct. Mater.*, 25, 4966-4975, 2015.
32. Y. Zhao, C. Riemersma, F. Pietra, R. Koole, C. M. Donega, and A. Meijerink. High-temperature luminescence quenching of colloidal quantum dots. *ACS Nano*, 6, 9058-9067, 2012.
33. B. Dierre, K. Costuas, N. Dumait, S. Paofai, M. Amela-Cortes, Y. Molard, F. Grasset, Y. Cho, K. Takahashi, N. Ohashi, T. Uchikoshi and S. Cordier. Mo_6 cluster-based compounds for energy conversion applications: comparative study of photoluminescence and cathodoluminescence. *Sci. Technol. Adv. Mater.*, 18, 458-466, 2017.
34. H. Chang Kim, H. G. Hong, C. Yoon, H. Choi, I. S. Ahn, D. C. Lee, Y. J. Kim, and K. Lee. Fabrication of high quantum yield quantum dot/polymer films by enhancing dispersion of quantum dots using silica particles. *J. Colloid and Interface Sci.*, 393, 74-79, 2013.
35. S. Liang, K. Shephard, D. T. Piercea and J. X. Zhao. Effects of a nanoscale silica matrix on the fluorescence quantum yield of encapsulated dye molecules. *Nanoscale*, 5, 9365-9373, 2013.
36. T. Mahnaj, S. U. Ahmed, and F. M. Plakogiannis. Characterization of ethyl cellulose polymer. *Pharm. Dev. Technol.*, 18, 982-989, 2013.
37. X. Min, M. Fang, Z. Huang, Y. Liu, Y. Huang, R. Wen, T. Qian, and X. Wu. Enhanced thermal properties of novel shape-stabilized PEG composite phase change materials with radial mesoporous silica sphere for thermal energy storage. *Scientific Reports*, 5, 1-11, 2015.
38. R. Mitran, D. Berger, C. Munteanu, and C. Matei. Evaluation of different mesoporous silica supports for energy storage in shape-stabilized phase change materials with dual thermal responses. *J. Phys. Chem. C*, 119, 15177–15184, 2015.

Chapter 4

Fabrication and characterization of the Mo₆-incorporated hollow silica nanoparticles

Chapter 4

Fabrication and characterization of the Mo₆-incorporated hollow silica nanoparticles

Silica has been a good encapsulant candidate to prepare bio-compatible functional nanocomposite for medical applications such as drug delivery, cancer diagnosis^[1,2] or biomedical imaging and theranostics^[3] due to its stability, biocompatibility and easy functionalization on the silica surface by active or functional groups. In addition, mesoporous silica nanoparticle is one of the interesting materials for the thermal insulating applications^[4] because these heat conducting mechanisms of the mesoporous spaces on the wall of the silica and big hollow of the silica nanoparticles were prominently studied on^[5,6]. The introductions of the phase change materials (PCMs) for new heat insulation material, such as, the lauric acid^[4], n-pentadecane^[7], PEG^[8], paraffin wax^[9] or KNO₃ and Al₂O₃^[10] in the pores of the silica have been the focus of the current studies. Interestingly, the hollow silica nanoparticle was introduced into transparent and chemically stable polymers such as polyethersulfone^[11] or polyurethane^[12], in order to prepare transparent thermal insulation materials by means of the sol-gel or W/O emulsion process. Most of the materials incorporated with silica play a role as heat absorbing component based on the heat conducting mechanism by vibrating the molecules accompanying with radiation in the pores. Ernawati et al. has used hollow silica directly blending with polyethersulfone to prepare the thermal insulation film with low thermal conductivity of 0.03 W.m.K-1^[11]. Fujimoto et.al also reported the hollow silica@polyurethane (1:1) insulation film by sol-gel process which resulted the decrease of the temperature of 20°K (0.029 W/mK) after characterization following the thermal conductivity of 0.18 W/mK for polyurethane, 1.180 W/mK for silica and 0.024 W/mK for air^[12]. It was suggested that the heat diffused into the nano spaces of the hollow the silica shells.

As we know, the octahedral molybdenum clusters strongly exhibits not only UV absorption under 400 nm but also luminescence emission in the wavelength range of 600 nm and 800 nm, being attracted the current focuses in UV blocking device and luminescent material^[13,14]. The extension of the application of luminescent cluster precursor has been attempted by incorporating with polyurethane (PU) by direct polymerization for oxygen sensor^[15], hybrid liquid crystals for electro-optic devices^[16] or biocompatible silica nanoparticles for time-gated luminescence bio-imaging by water-in-oil (W/O) micro-emulsion process^[17].

In this study, the Cs₂Mo₆Cl₈Cl₆^a and Cs₂Mo₆I₈(OCOC₂F₅)₆^a luminescent cluster precursors were selected to prepare the nanocomposite based on pseudocube hollow silica nanoparticles (HSNs) by vacuum impregnation process (VIP). The great characteristic of VIP in preparing the nanocomposite is not dependent on the morphology and shape of the porosities of the material, moreover, the impregnation is applicable to various encapsulant under the impact of gas pressure. The expectations in the incorporation of the Mo₆ cluster with the silica nanoparticles are (i) to prepare the luminescent silica nanoparticle based on emitting characteristic of the Mo₆ cluster for luminescent applicable materials, and (ii) to create the nanocomposite material with shielding irradiation of heat based on mesoporous

silica nanoparticles combining with UV blocking characteristic of the Mo_6 cluster for insulation material application.

The $\text{Cs}_2\text{Mo}_6\text{Cl}_8\text{Cl}^a_6$ and $\text{Cs}_2\text{Mo}_6\text{I}_8(\text{OCOC}_2\text{F}_5)_6$ cluster precursors which exhibit impressive luminescence, were dissolved in acetone, and then introduced into the HSNs by the VIP accompanying with heating. Thermal stability of the cluster@HSNs nanocomposites were then characterized. The results of the UV-Vis absorption and photoluminescence showed that the optical properties of the cluster@HSNs nanocomposites still retained after annealing up to 200°C . This results is so impressive in comparison with other previous reports: Zhao et. al. has concluded that the CdSe core_shell quantum dots in PMMA matrix lost photoluminescence at the temperature higher than 100°C [18]. Even the perovskite quantum dots coated with silica by in situ synthesis exhibited the optical stability under 125°C [19].

4.1. Fabrication and characterization of the Mo_6 @HSNs nanocomposite

4.1.1. Characteristic of materials

The $\text{Cs}_2\text{Mo}_6\text{Cl}_8\text{Cl}^a_6$ (CMC) precursor cluster was synthesized by the following procedure: i) $\text{NaMo}_6\text{Cl}_{13}$ octahedral cluster was synthesized from MoCl_2 and NaCl salts by the solid chemistry technique, ii) $(\text{H}_3\text{O})_2\text{Mo}_6\text{Cl}_{14}$ cluster was prepared from the $\text{NaMo}_6\text{Cl}_{13}$ clusters and HCl solution by the solution chemistry process, iii) $\text{Cs}_2\text{Mo}_6\text{Cl}_{14}$ cluster was synthesized from the derivation of the $(\text{H}_3\text{O})_2\text{Mo}_6\text{Cl}_{14}$ clusters and CsCl_2 salt by the solution chemistry process [20]. Similarly, the $\text{Cs}_2\text{Mo}_6\text{I}_8(\text{OCOC}_2\text{F}_5)_6$ (CMIF) precursor cluster was synthesized from reaction of the $\text{Cs}_2\text{Mo}_6\text{I}_8\text{I}^a_6$, which was synthesized from the MoI_2 and CsI_2 salts by the solid chemistry process [13], with the $\text{Ag}(\text{OCOC}_2\text{F}_5)$ salts by the solution chemistry process in the acetone solution.

The pseudocube hollow silica nanoparticles (HSNs, SiliNax SP-PN(b)), supplied from Nittestu Mining Co., Ltd, were synthesized from calcium carbonate as an inorganic template [21]. The pore channel size (~ 5 nm) and BET surface area (~ 300 $\text{m}^2\cdot\text{g}^{-1}$) of the HSNs were characterized from the N_2 adsorption or desorption isotherm measurement at 77 K (BELSORP-maxII, Microtrac BEL Corp.) as presented in **Figure 4.1**. Considering the particle size of the HSNs, the surface area of 300 $\text{m}^2\cdot\text{g}^{-1}$ should be the sum of the outer and inner surfaces of the HSNs that indicates the HSNs exhibiting open channels, the size of which is about 5 nm.

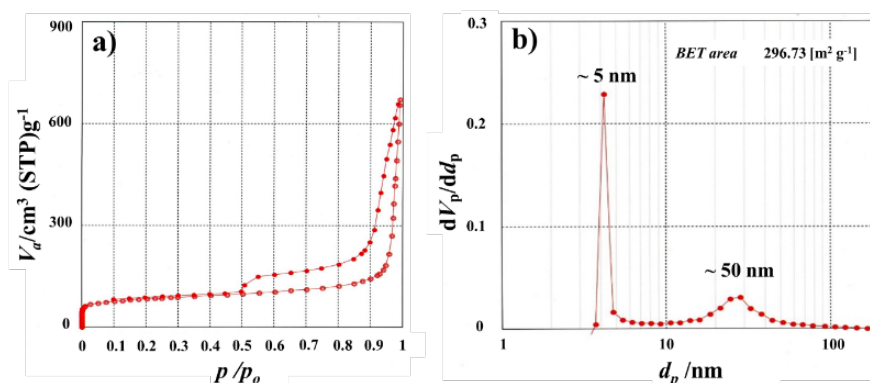


Figure 4.1. a) N_2 adsorption/desorption isotherm (at 77K) and b) Pore size distribution calculated from N_2 desorption isotherm of the HSNs.

4.1.2. Preparation of suspensions and vacuum impregnation process

The cluster precursor (2 g/L) and HSNs (70 g/L) were separately dissolved in reagent grade acetone (99.5 %, Nacalai Tesque, Inc., Kyoto, Japan) by agitating with a stirrer for 10 min to obtain homogeneous solutions before mixing together. The CMC@HSNs and CMIF@HSNs nanocomposite solutions were placed in a vacuum chamber connected to a diaphragm pump creating the pressure of 0.1 Mpa (DAU-Z0, Ulvac Kiko, Inc) (**Fig. 4.2a**). After the solution was completely impregnated (**Fig. 4.2b**) and evaporated in the VIP system for 6 hours, the nanocomposite was dried at 60°C until no change of the weight (**Fig. 4.2c**). The same procedure was repeated twice or more. The obtained nanocomposite powder was washed in pure acetone, centrifuged, and then dried at 60°C for three times until the washing solution becomes colorless. The cluster precursors and their nanocomposites were annealed at different temperatures as 100°C, 150°C, 200°C, 250°C, and 300°C for 30 min in air before the characterizations.

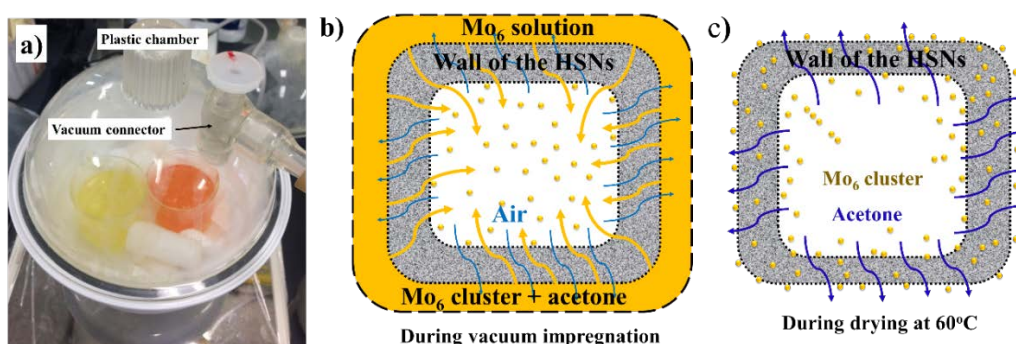


Figure 4.2. The schematic illustration showing the experimental setup: a) VIP system containing the Mo_6 cluster precursor in acetone solution, b) the possible movement of the gas and Mo_6 clusters during VIP, c) the possible porosity structure of the HSNs deposited the Mo_6 clusters after impregnating and drying.

4.2. Characteristic of the Mo₆-incorporated silica nanoparticle

4.2.1. Morphology and chemical property

In the first time, vacuum impregnation process (VIP) was used to introduce the Mo₆ cluster precursors into silica nanocomposite at the ambient condition. Many nano-channels in the shell of the HSNs are higher than 5 nm that is a good pathway to put in the nanocluster under the impact of low air pressure (0.1 MPa). The selection of a suitable solvent to disperse the impregnation components is also important because the cluster precursors need to be well-dispersed in nanometer scale meanwhile the solvent does not interact with functional groups on the silica or physical interaction with the HSNs. These conditions assure that the replacement of the air in the HSNs with the cluster solution smoothly occurred via the pore channel. For this reason, acetone was a good solvent to dissolve the cluster precursors and disperse the HSNs. The drying process at 60°C was combined with the impregnation process that accelerates the evaporation of the solvent followed by the coagulation of the clusters which were trapped in the HSNs. Completely replacing the solvent by air improves the efficiency to introduce the number of the clusters in the next VIP procedure.

In order to consider the efficiency of the VIP method in the incorporation of the cluster and silica, a simple experiment was carried out to prepare a nanocomposite of CMIF@HSNs without VIP. The CMIF and HSNs were mixed by continually agitating for 6 hours, and then washing coupled with centrifuging 3 times in acetone. The obtained results is shown in **Figure 4.3**. The nanocomposite has no change color, consequently, photoluminescence does not appear while yellow nanocomposite is archived by the VIP method. With the VIP method, the CMIF cluster strongly tends to fill the pores on the outside wall of the HSNs. This suggestion is proven in the reflection spectroscopy (**Fig. 4.3**). The HSNs presents the strong reflection in the UV-Vis range while the nanocomposite without the VIP method lightly enhances the reflectance in the UV range (dot line). The nanocomposite by the VIP presents the weak reflectance with improving the absorption in the UV-Vis range between 200 nm and 600 nm followed by the impressive absorption of the Mo₆ cluster in the Mo₆@HSNs nanocomposite. This result proves that the Mo₆ clusters is obviously trapped on the porous wall of the HSNs.

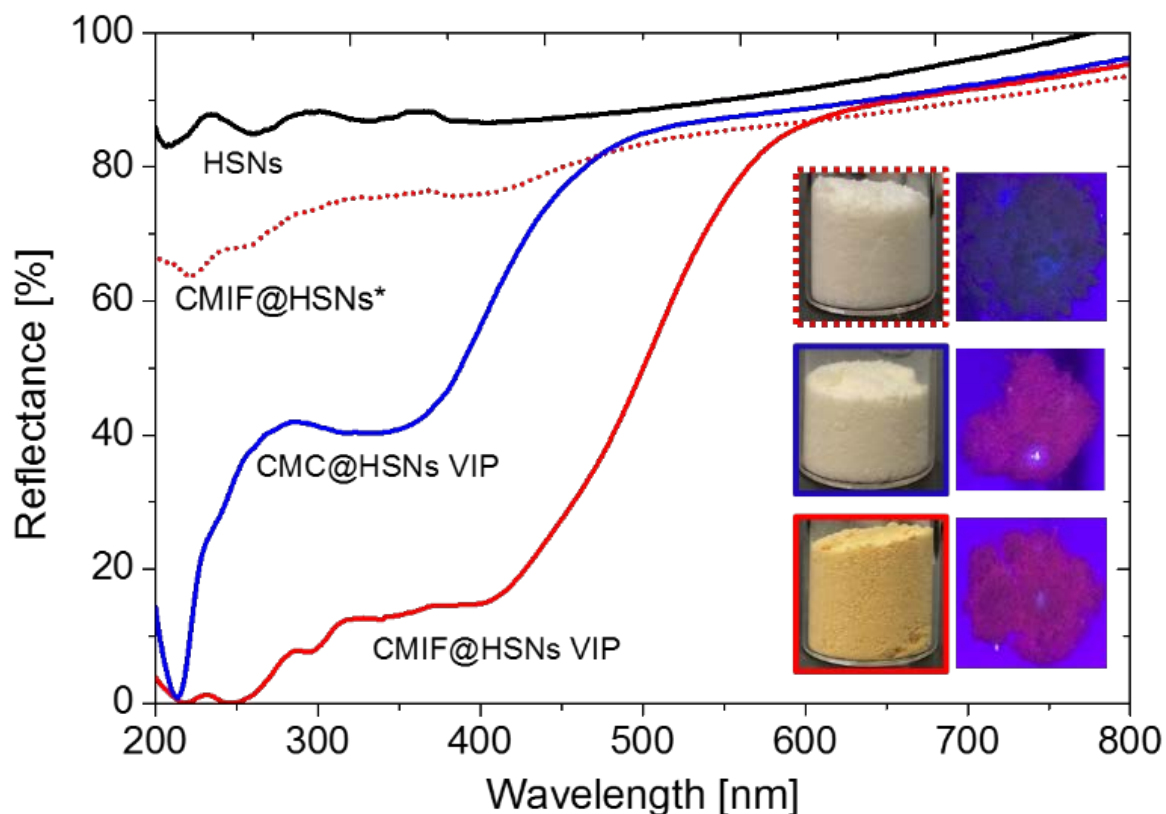


Figure 4.3. The reflection of HSNs and nanocomposite in the UV-Vis light range. CMIF@HSN* was prepared by mixing cluster and silica in acetone for 6 hours without vacuum impregnation process.

The observations by TEM and STEM measurements coupled with an EDX analysis device were performed to recognize the existence of the Mo_6 cluster in the HSNs following outside the wall and inside the hollow of the HSNs. The pseudocube shape of the HSNs having internal cavity which size is about 50 nm is recognized by TEM with the wall thickness of about 10 nm (**Fig. 4.4a**). The sign of black dots of about 2 nm inside the internal cavity of the HSNs in **Figure 4.4b** indicates the existence of CMC clusters. This results is reasonable because the channel in the shell of the HSNs is determined about 5 nm (**Fig. 4.1**). In the case of the CMIF@HSNs, the STEM images give out the clear white dots which indicate to the Mo_6 clusters not only inside the HSNs but also on the outer surface of the shell of the HSNs (**Fig. 4.4c**). It seem to be predicted that only Mo_6 cluster at nanometer scale which possesses strong interaction with the HSNs is immobilized on outside and inside walls of the silica shell after the washing and centrifuging finish totally. No appearance of the bulk crystals of free Mo_6 cluster in SEM images and the colorless washing solutions of the nanocomposites also support this results. The element analysis performed by STEM-EDS mapping shown in **Figure 4.4d**. Cs, Mo and Cl atoms exhibited the existence of the clusters on the wall of the HSNs, however, the concentration is not significant compared with Si and O atoms.

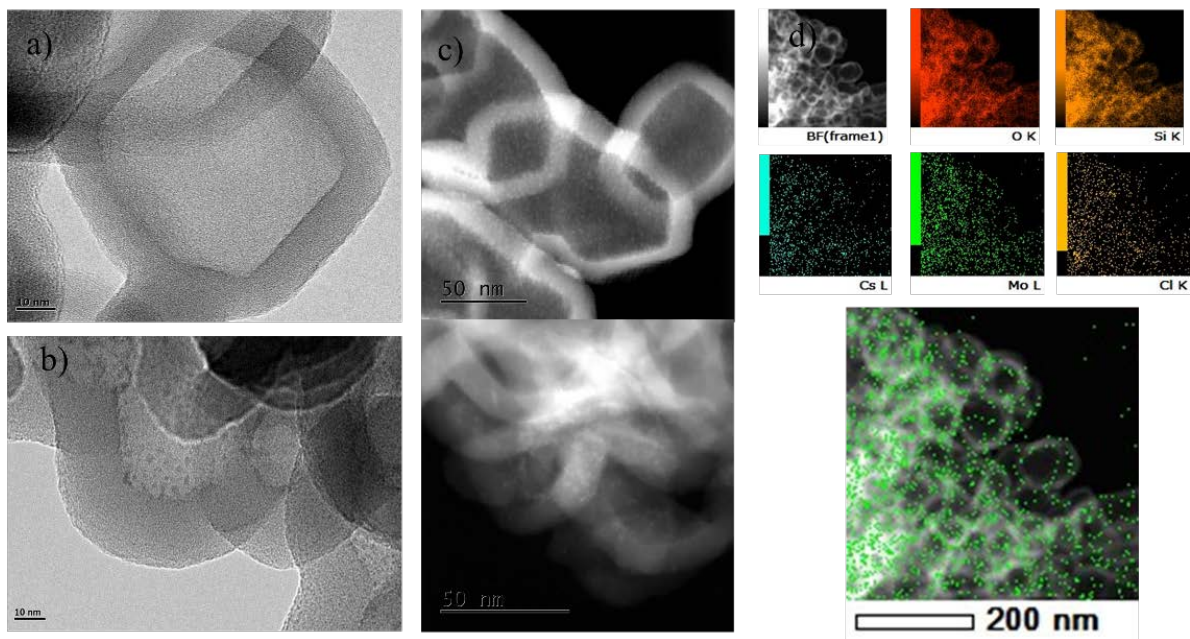


Figure 4.4. a) TEM image of the HSNs, b) TEM image of CMC@HSNs nanocomposite, c) STEM image of CMIF@HSNs nanoparticles, d) STEM-EDS image of CMC@HSNs nanocomposite.

4.2.2. The thermal stability of the Mo_6 -incorporated silica nanoparticle

In order to confirm the influence of the cluster solution on the morphology and shape of the pseudocube HSNs during the solvent treatment of the VIP method, the FE-SEM observation of the CMC, CMIF, CMC@HSNs, CMIF@HSNs powders without and with annealing at 300°C were performed. The observed images are shown in **Figure 4.5**. Normally, the CMC and CMIF cluster precursors exhibit the condensed crystals with bulk sizes (**Fig. 4.5a and 4.5b**). The pseudocube shape of the HSNs still remains the perfect state after treating with the acetone solution during VIP for 18 hours. They have no sign of the metal cluster crystals outside the wall of the HSNs or between the bulk powder (**Fig. 4.5c and d**). It is known that the CMIF cluster strongly associates in acetone solution to break the agglomerated block shown in **Figure 4.5a**. In addition, the acetone solution seem to be the best choice to prepare the nanocomposite because it does not create the hydrogen bonds with the hydroxyl groups on the wall of the HSNs. It is evidenced that the cluster@HSNs powder retains the stable shell morphology even annealing at 300°C. From this result, the existence of the clusters inside or outside the wall of the silica nanoparticles has no influence to the decomposition of the HSNs at high temperature (**Fig. 4.5e and 4.5f**).

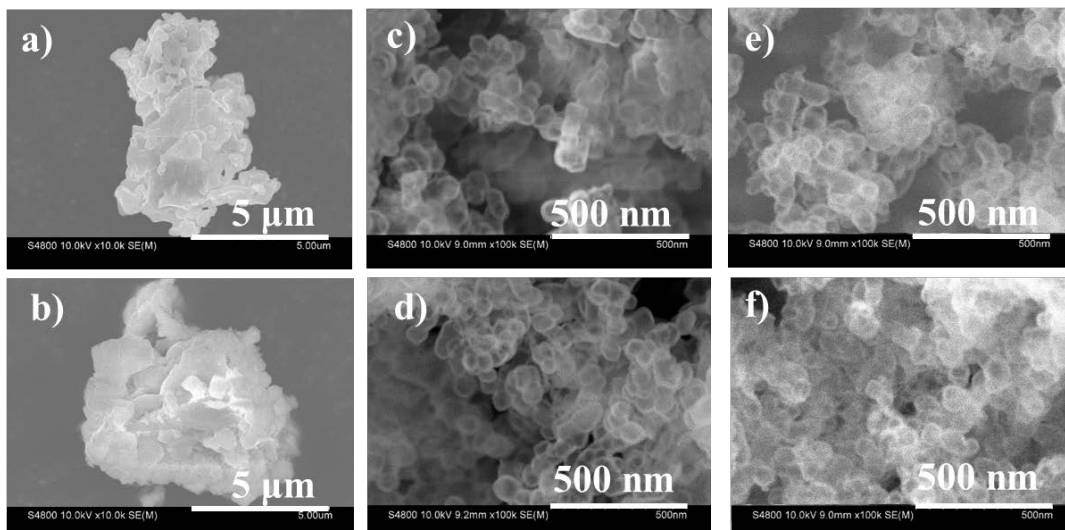


Figure 4.5. FE-SEM image of: a) CMC cluster precursor, b) CMIF cluster precursor, c) CMC@HSNs nanocomposite, d) CMIF@HSNs nanocomposite, e) CMC@HSNs nanoparticles annealed at 300°C, f) CMIF@HSNs nanoparticles annealed at 300°C. Samples were annealed for 30 minutes.

The atomic ratios of the cluster and cluster@HSNs powders with and without annealing at 300°C were measured by an FE-SEM coupled with an EDS analyzer presented in **Table 4.1**. The ratios of Cs, Mo, Cl, I and F atoms of the CMC and CMIF cluster precursors are close to the theoretical index.

In the case of CMC cluster precursor, two Cl ions at the terminal apical positions are partially replaced by the H₂O molecules, which has been evidenced in a previous report [22]. At 300°C, the increase of the concentration of oxygen ions is significantly recognized meanwhile the Cl ion disappears in the CMC cluster precursor. It can be suggested that the Mo atom is oxidized in the air at high temperature. After introducing the CMC cluster into the HSNs, the concentration of Cs atoms visibly increases because the Cs cations are properly absorbed on the surface of the HSNs to neutralize the negative charges of silica [23]. The CMC cluster losses four Cl ions to form the $[\text{Mo}_6\text{Cl}_8\text{Cl}_2(\text{H}_2\text{O})_4]^{2+}$ cluster and then it is immobilized on the silica surface by electrostatic interaction. The Cl atoms is not also recognized in the nanocomposite after annealing at 300°C.

In the case of the CMIF cluster precursor, the inner and apical atoms exhibit a little difference from the theoretical index because the exchange reaction between I⁻ anion and (OCOC₂F₅)⁻ anion is not completely performed. The CsI chemical is suggested to stay in the cluster product after purifying. At 300°C, the value of I atoms strongly decreases meanwhile that of O atoms visibly increases and F atom is not detected. In the case of the CMIF@HSNs, the value of Cs atoms slightly increases and that of F atom decreases corresponding to the loss of 2 (OCOC₂F₅)⁻ groups at the terminal position. The prediction is gave out that the OH groups on the surface of the HSNs will react with nucleophilic C of the {OCOC₂F₅} group, following the mechanism of the acid-catalyzed hydrolysis of esters [24]. The hydroxonium ion is generated from the proton transformation of keto-enol tautomerism in acetone-water solution [25] or from hydroxo groups of the HSNs. The pH of the mixture solution which was

recognized about 5 also supports this suggestion. The predicted products would be C₂F₅CO-O-silica and neutral Mo₆I₈(OCOC₂F₅)₄(OH)₂ clusters. During washing with acetone solvent containing hydroxonium ion, it is predicted that C₂F₅CO-O-Silica ester linking continue hydrolyzing to form C₂F₅COOH acid and removing out of the HSNs. Only [Mo₆I₈(OCOC₂F₅)_{a-x}(OH)_x]²⁻ cluster was immobilized on the HSNs by hydrogen bond or covalent bond (Mo-O-Si) that has been suggested in a previous report [23]. The EDS analysis of CMIF@HSNs annealed at 300°C does not figure out I and F atoms in the results, corresponding to the annealing result of CMIF cluster precursor.

Table 4.1. The atomic ratio of Cs, Mo, Cl, I, F and O atoms in the Cs₂Mo₆Cl₈Cl₆^a (CMC) and Cs₂Mo₆I₈(OCOC₂F₅)₆^a (CMIF) cluster precursors measured by with EDS analyzer equipped in SEM.

Sample	Cs (at)	Mo (at)	Cl (at)	I (at)	F(at)	O (at)
CMC*	2	6	14			0
CMC	1.8	6	12.1			1.4
CMC300	2.1	6	0			15.8
CMC@HSNs	3	6	10			
CMC@HSNs 300	2.8	6	0			
CMIF*	2	6	-	8	30	12
CMIF	2.1	6	-	9.5	28	9
CMIF300	2.3	6	-	1.5	0	15.4
CMIF@HSNs	2.3	6	-	7	20	-
CMIF@HSNs 300	2.4	6	-	0	0	-

*Theoretical index was calculated basing on: the Cs₂Mo₆I₈(OCOC₂F₅)₆^a and Cs₂Mo₆Cl₈Cl₆^a formulation.

Considering the interaction between the Mo₆ cluster and the wall of the HSNs, the FTIR spectra measurement of the cluster precursors, the HSNs and the cluster@HSNs nanocomposites were performed. The vibrational signs of the chemical groups are shown in **Figure 4.6**. For the HSNs, the absorption bands of O-H stretching vibration in the wavenumber range between 3600 and 3200 cm⁻¹, H-O-H bending vibration at 1632 cm⁻¹ and Si-O-Si bending vibration in the range between 1200 and 1000 cm⁻¹ are recognized. The FTIR spectrum of the CMC cluster shows the strong and sharp absorption peaks at the wavenumber of 3500 cm⁻¹ (O-H stretching vibration) and 1608 cm⁻¹ (H-O-H bending vibration) [26]. Similarly, the FTIR spectrum of the CMIF cluster includes the absorption bands of C=O stretching vibration at 1680 cm⁻¹, C-O-C bending vibration in the range between 1300 and 1000 cm⁻¹ and C-F stretching in the range between 800 and 500 cm⁻¹. In the case of the CMC@HSNs and CMIF@HSNs nanocomposite, most of the absorption bands are similar to the FTIR spectrum of the HSNs. A little shoulder peak was observed at the wavenumber of 1680 cm⁻¹ in the spectrum of the CMIF@HSNs indicating the existence of CMIF. Both of the spectra of the nanocomposites are very similar to the spectrum of the HSNs when annealed at 300°C.

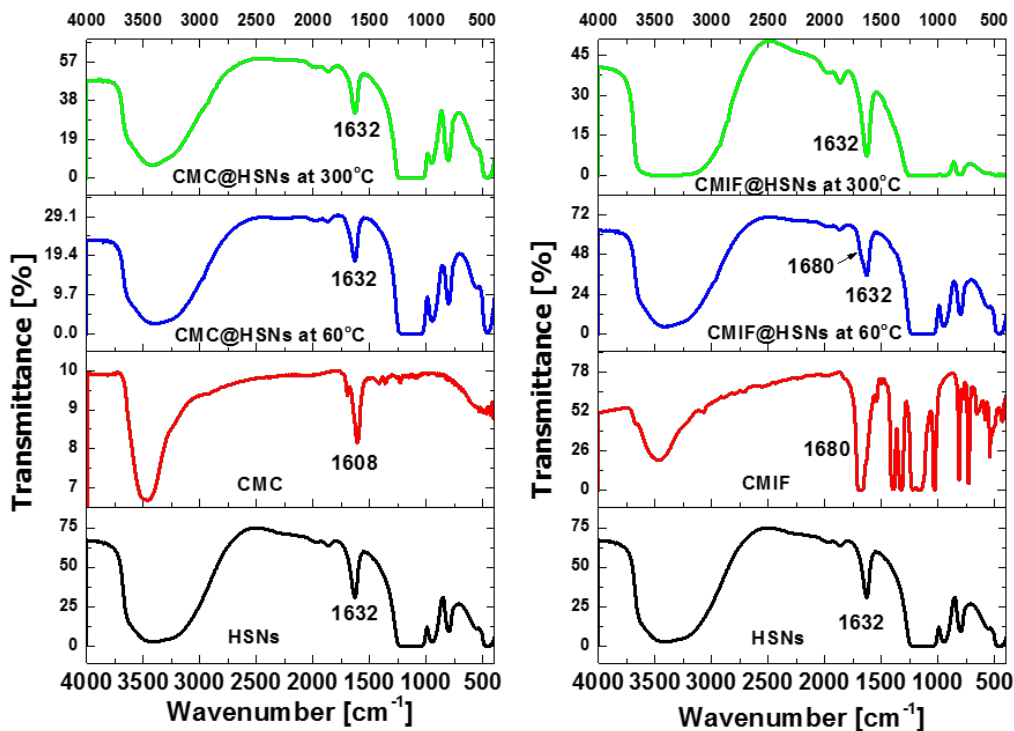


Figure 4.6. FTIR spectra of the CMC cluster precursor, HSNs nanoparticles and CMC@HSNs nanoparticles (left) and CMIF cluster precursor, HSNs nanoparticles and CMIF@HSNs nanoparticles at different annealed temperatures.

4.2.3. Optical property stabilization of the Mo₆-incorporated silica nanoparticle

In order to confirm the optical influence of the clusters on the HSNs, the measurements of photoluminescence, UV-Vis absorption and PL quantum yield were performed. The optical characteristic of the octahedral Mo₆ cluster depends on the Mo₆ octahedral structure bonding with inner halogen ligands that absorbs ultra-visible light and creates the luminescent emission in the range of visible light.

UV-Vis absorptions

The UV-Vis absorptions of the CMC, CMIF, CMC@HSNs and CMIF@HSNs with and without annealing are displayed in **Figure 4.7**. Pure HSNs was used as a reference in order to reduce the unnecessary diffraction that gives out the clear difference of the HSNs after annealing at 300°C. The HSNs 300 shows the weak absorption at the wavelength of 275 nm. The CMC cluster precursor strongly absorbs the light in the wavelength range between 200 and 600 nm with the highest intensity at 380 nm. At 250°C, CMC still retains the original absorption with the increase of the absorption in the visible-NIR range between 600 and 1000 nm, especially, a sharp peak at the wavelength of 213 nm (**Fig. 4.7a**). It is predicted that the absorption peak at the wavelength of 213 nm is assigned to the Mo-O bonding of MoO₃ oxide^[27]. At 300°C, the CMC 300 totally absorbs in the UV-Vis range. For CMC@HSNs, the

absorption peak of the CMC cluster is recognized but it shifts to lower wavelength of 360 nm accompanying with the strong increase of the absorption intensity at the wavelength of 213 nm. The similar phenomena also occur to the CMC@HSNs powder annealed at 250°C and 300°C. The curves showed the absorption peak of the CMC cluster at the wavelength of 360 nm, simultaneously, extend in the wavelength range between 200 and 340 nm.

Similarly, the absorption of the CMIF strongly presents at the wavelength of 410 nm and the absorption in the ultra-visible and visible ranges significantly increases after annealing at 250°C and 300°C (**Fig. 4.7b**). Interestingly, the incorporation of the CMIF and the HSNs generates some new absorbing peaks at the wavelength of 217, 241, 294, 380 and 400 nm. The emission of the CMIF completely disappears after annealed up to 300°C.

At high temperature, a lots of the functional OH or H₂O groups on the surface of the different HSNs will react each other that increase the siloxane bonds (O-Si-O). From the absorption curve of the HSNs at 300°C, it can be seen that the weak absorption at 300 nm indicates new Si-O bonds. When the [Mo₆X₈L^a_{6-n}(H₂O)_n]²⁻ⁿ cluster reacts with OH or H₂O groups of the HSNs, the Mo-O-Si would be created during the impregnation and drying displayed at the wavelength of 213 nm. This absorption slowly extends in the wavelength range between 200 nm and 350 nm because the oxidation reaction between Mo atom and O₂ molecules in the air enhances the Mo-O bonds [27]. From these results, the interaction between the Mo₆ cluster and the HSNs is obviously evidenced. Vorotnikov et al. have suggested some mechanisms and interactions which can occur between hydrolyzed Mo₆ cluster units and functional groups anchoring on the surface of silica nanoparticles by the W/O emulsion process. It is predicted that the hydrolysis of the Mo₆ cluster units to form aquahydroxo or hydroxo cluster unit that interact with the silica nanoparticle by hydrogen bond and covalent linking to form the compound with the general formula of [{ Mo₆X₈ } (H₂O)_{6-y-z}(OH)_y(OSi)_z]_{4-y-z} [28].

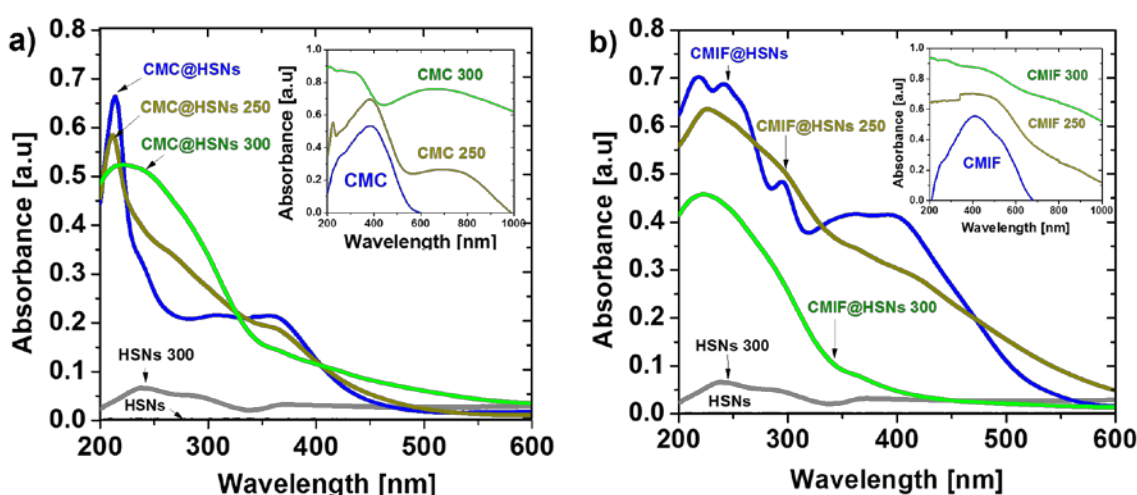


Figure 4.7. The UV-Vis absorption spectra of: a) the CMC cluster and CMC@HSNs powder without and with annealing at 250°C and 300°C, and b) the CMIF cluster and CMIF@HSNs powder without and with annealing at 250°C and 300°C.

Thermal stabilization of the luminescent Mo₆-incorporated silica nanoparticle

The stabilization of luminescent property at high temperature would expand to the applicability of the luminescent materials. The Cs₂Mo₆Cl₈Cl₆^a (CMC) and Cs₂Mo₆I₈(OCOC₂F₅)₆^a (CMIF) cluster precursors and their nanocomposites based on hollow silica nanoparticles (HSNs) (CMC@HSNs and CMIF@HSNs) were annealed at 100, 150, 200, 250 and 300°C for 30 min in air. The stabilization of luminescent property of the cluster precursors supported by the HSNs was checked under the irradiation of UV light at the wavelength of 324 nm (**Fig. 4.8**). All the powders were dried at 60°C for 24 h to evaporate acetone completely before annealing. As shown in **Figure 4.8**, the CMC and CMIF clusters emitted dark red color meanwhile the HSNs had no emission under the excitation light. Interestingly, the CMC@HSNs and CMIF@HSNs nanocomposites visibly exhibited the photoluminescence. It is noted that the residual clusters would be completely removed from the CMC@HSNs and CMIF@HSNs by washing 3 times with pure acetone until obtaining the colorless solution. Therefore, the luminescence must be originated from the cluster which is properly condensed or trapped inside or on the silica shell of the HSNs. This result evidences that the VIP method is a sufficient process to incorporate the luminescent cluster with the HSNs.

The emission light of all the powders was investigated after the annealing at different temperatures. Under the visible light, the Cs₂Mo₆Cl₈Cl₆^a cluster changes the color from yellow to green yellow at 250°C and dark blue at 300°C, similarly, from dark yellow to brown at 250°C and dark brown at 300°C for Cs₂Mo₆I₈(OCOC₂F₅)₆^a clusters (not shown here). Correspondingly, the luminescent phenomena of the clusters suddenly disappears after annealing at 300°C. The degradation of the luminescent property of the nanocomposites basically depends on the stabilization of the original clusters: the luminescent quenching in oxygen medium by annealing at 300°C. The photoluminescent images of the cluster@HSNs still retained after annealing up to 200°C and visibly started with the reduction of the red color at 250°C. Both of the clusters and their nanocomposites significantly retain the optical property up to 200°C. This characteristic potentially contributes to the applicable extension of the luminescent silica nanoparticles. The luminescent characteristic of the Mo₆ cluster originates from metal-metal bonding of Mo₆ octahedral structure linking with halogen ligands. It could be suggested that the disappearance of the luminescence corresponds to the loss of organic halogen atoms.

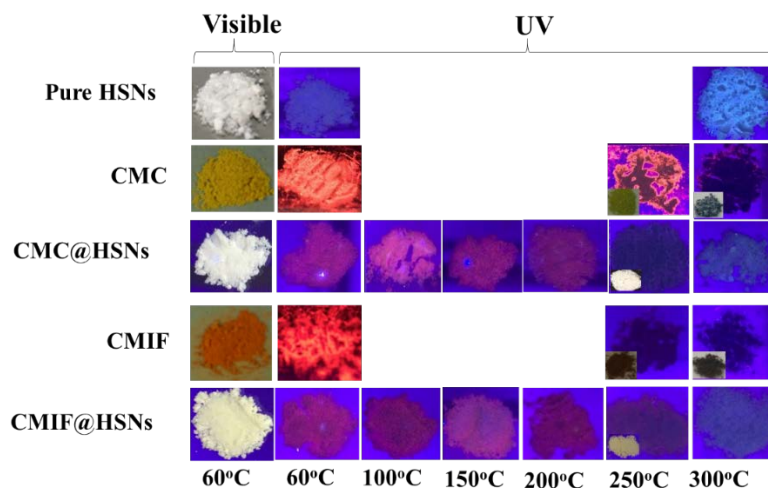


Figure 4.8. The CMC, CMIF and their nanocomposite based on the HSNs under visible light and ultra-visible light at the wavelength of 324 nm. Powders were dried at 60°C in air at least for 24h before annealed at different temperature for 30 minutes.

The photoluminescence spectra of the HSNs, CMC, CMC@HSNs, CMIF and CMIF@HSNs without and with annealing at high temperature under the irradiation of 325nm laser light are shown in **Figure 4.9a** and **b**. The HSNs powder obviously displays the emission at the wavelength of 340 nm and 360 nm while the CMC and CMIF clusters exhibit the emission in the wavelength range between 550 and 900 nm with the maximum peak at the wavelength of 700 nm and 668 nm, respectively. In the case of the Mo₆@HSNs nanocomposites, the spectra include the emission of the HSNs and CMC cluster but it exhibits a clear shift to higher wavelength from 700 nm to 730 nm and 760 nm for CMC@HSNs and from 668 to 680 nm for the CMIF@HSNs. The CMC and CMIF clusters have tendency to replace the apical halogen ligands with H₂O molecules ^[20] which create a hydrogen bonding or covalent bond with OH group of the HSNs or create new Mo-O bonding by removing the apical Cl ions ^[23]. For this result, the excited state on the orbitals of the Mo atom would be disturbed by new interaction in Mo-O-Si linking system. Both of the CMC and CMIF clusters obtain good interaction with HSNs by vacuum impregnation process combining with drying that reported the same results in the previous studies by means of the W/O micro-emulsion process ^[17, 23].

In order to support the above-mentioned stabilization mechanism of the luminescent silica nanoparticles at high temperature, annealing temperature dependences versus of the emission spectra were presented in **Figure 4.9c** and **4.9d**. For the nanocomposites, the reduction of the photoluminescence of the Mo₆ clusters accompanying the increase of the emission at the wavelength of 480 nm after annealing at 60, 100, 150, 200, and 300°C is recognized (**Fig. 4.9c** and **4.9d**). The photoluminescence of the nanocomposite originating from the Mo₆ clusters in the wavelength range between 550 and 800 nm obviously disappears at 300°C. It is suggested that the octahedral structure of the Mo₆ cluster is not retained because of the loss of the Cl ions. The EDX results also agree with this suggestion. Interestingly, the emission of the CMC@HSNs nanocomposite is significantly retained after annealing at 200°C and

the result is better than that of the CMIF@HSNs. The blue emission at the wavelength of 480 nm clearly appear after incorporating the HSNs and the Mo₆ cluster, and the intensity of the blue emission increases with annealing at higher temperatures. The blue emission from the Mo₆ cluster incorporating with the HSNs has not been explained [17, 29]. However, the blue emission originated from oxide-related defects between the surface of Si and the surrounding SiO_x layers has been reported for the 4 month-aged silicon nanoparticles [30]. An intense blue emission of tantalum doped silica glass created by the excitation and relaxes of the valence electron between an O 2p orbital (defect-related oxygen in silica) and Ta 5d⁰ energy level under UV photon has reported [31]. Moreover, the photoluminescence of the molybdenum oxide at the blue emission (390 - 470 nm) originating from Mo⁵⁺ d-d transition of distorted polyhedron (Mo-O) and the blue emission shifting to higher energy at high temperature have been reported [32]. The new Mo-O bondings formed in the cluster@HSNs nanocomposite could be the cause of the appearance of the blue emission at the wavelength of 480 nm.

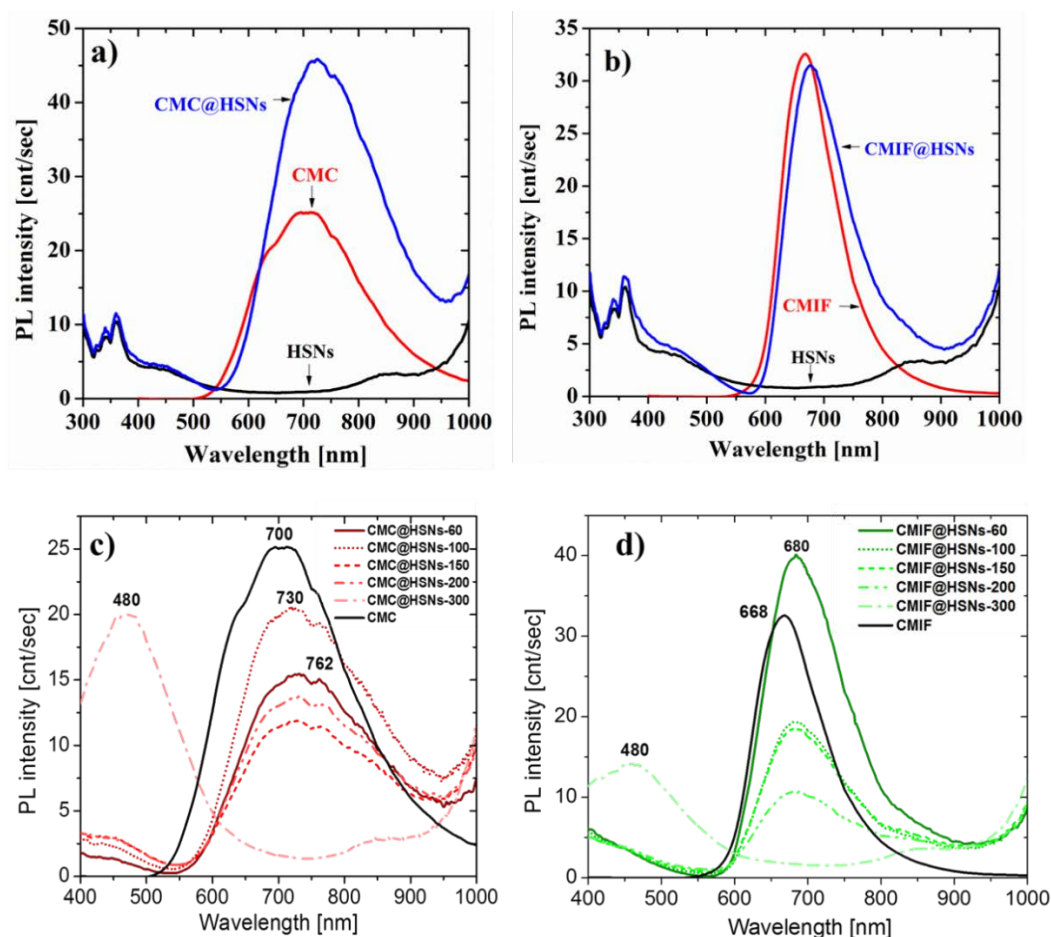


Figure 4.9. Photoluminescent spectra of: a) the CMC cluster precursor, HSNs and CMC@HSNs nanoparticles after dried at 60°C for 24h, b) the CMIF cluster precursor, HSNs and CMIF@HSNs nanoparticles after dried at 60°C for 24h, c) the HSNs and CMC@HSNs nanoparticles before and after annealed at 250°C and 300°C, d) the HSNs and CMIF@HSNs nanoparticles after annealed at 250°C and 300°C, e) the PL evolution of the HSNs after preparing by the VIP method.

The quantum yield of the Mo₆-incorporated silica nanoparticle

The PL quantum yield of the precursors, HSNs and their nanocomposites are shown in **Figure 4.10**. The Mo₆ clusters exhibit high PL quantum yield significantly: 36% for CMC and 26% for CMIF. However, the quantum yield of the Mo₆ cluster strongly decreases when it is incorporated with the HSNs. In TEM image, the Mo₆ cluster are almost condensed the inner wall of the HSNs. During the irradiation, the incident light is taken in the hollow silica nanoparticle and strong scattering of the light occurs in the pores of the silica nanoparticles, resulting the disturbance of the absorption of the emission light generated from the Mo₆ cluster [33, 34]. The effective interactions between the Mo₆ cluster and the HSNs enhance the absorption of the emission light, resulting the reduction of the detected signal. The incorporation of the CMC with the HSNs brings about better PL quantum yield than CMIF cluster precursor. This result is consistent with the PL quantum yield value of the clusters unit.

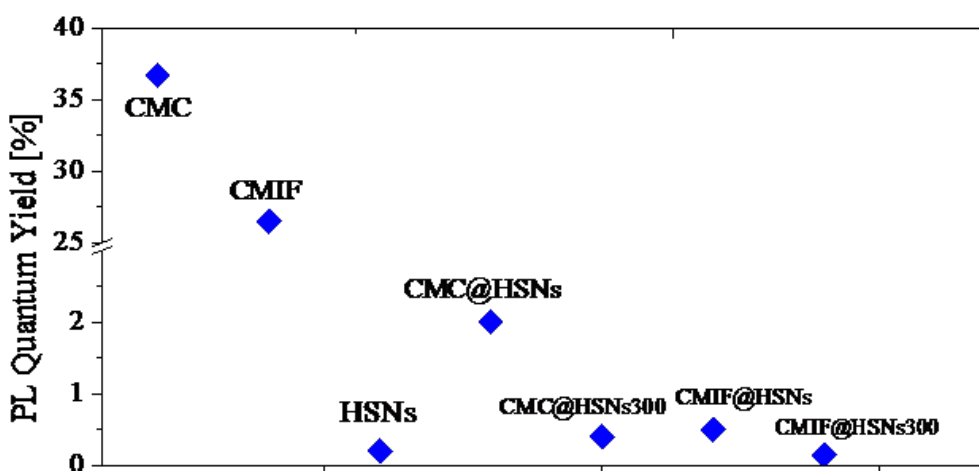


Figure 4.10. The PL quantum yield valuation of the CMC, CMIF, HSNs, CMC@HSNs and CMIF@HSNs powders.

4.2.4. Conclusions

The nanocomposites of the HSNs and the Mo₆ octahedral clusters (Cs₂Mo₆Cl₈Cl₆^a and Cs₂Mo₆I₈(OCOC₂F₅)₆) were successfully synthesized by the vacuum impregnation process (VIP) at room temperature. By STEM-EDS measurement, the existence and distribution of the Mo₆ cluster inside the pores of the HSNs shell were confirmed. The stabilization of the prominent optical property of the cluster@HSNs nanocomposite is obviously obtained even by annealing up to 200°C by UV-Vis absorption and PL spectra. The PL quantum efficiency of the CMIF@HSNs nanocomposite decreased in comparison with the cluster itself because the scattering phenomena strongly occurs in the pores of the silica wall and the top coat film.

4.3. The Mo₆@HSNs film by EPD process

Following the nature of the Mo₆ cluster precursor, the apical ligands can be replaced by the H₂O molecules or alcohol that reduces the emission effect of the clusters. For this reason, the organic solvent containing low concentration of water has been used to prepare the Mo₆-incorporated hollow silica suspension for the EPD process. Generally, the retained luminescent properties of the Mo₆ film fabricated by the EPD process has been proven in previous reports [35]. Alcohols and ketones are the popular media to disperse the deposit particles due to chemical stability, high density and low conductivity. The addition of the iodine into acetone solution improving the positive charge on the surface of the oxide particles have been reported by N. Koura et al. [36]. Some studies have used the iodine-acetone solvent for fabricating the silica and its composite film by the EPD process [37-40] while most of the studies have reported the fabrication of silica by using acid-alcohol solution as dispersing medium for emulsion process [41, 42].

In this work, in order to retain the luminescence property of the Mo₆ cluster, the Mo₆@HSNs suspension was prepared by dissolving into the iodine additional acetone solution with polyethyleneimine (PEI) for improving the charge on the Mo₆@HSNs particles. The results show that the Mo₆@HSNs film was successfully fabricated by the EPD process in the iodine-acetone solution on indium tin oxide (ITO) glass and fluorine tin oxide (FTO) glass. The characteristics of the Mo₆@HSNs film were investigated.

4.3.1. Preparation of suspension and setup of EPD

Firstly, acetone, H₂O and PEI were mixed at the different ratios presented in **Table 4.2** by agitating with stirrer and ultra-sonication for 15 min. Then, the HSNs nanoparticles, CMIF @HSNs and CMC@HSNs were separately added in the solution and agitated for 5 min or more. The pH of the suspension was about 10 for every solution. The suspension was titrated by I₂ solution to reduce the pH value lower than 3. The additional concentration of I₂ molecules depends on the nature of the silica and its nanocomposite. The zeta potential and electric conductivity of the suspensions were measured by a zeta-potential analyzer (Malvern Instrument, Ltd., Zetasizer Nano Z). The particle size of the Mo₆@HSNs suspension was measured by a dynamic light scattering (DLS) technique (Nikkiso Co., Ltd.).

Table 4.2. The ratio of the chemical components in the suspension for EPD process

Suspension	HSNs mg	Acetone ml	H ₂ O ml	PEI mg	I ₂ (1% in acetone) for pH~2.3 ml
HSNs	100	10	1	5	1.4
CMIF@HSNs	100	10	1	5	1.8
CMC@HSNs	100	10	1	5	1.7

The Mo₆@HSNs film was fabricated on ITO glass and FTO glass as cathode from three kinds of suspensions. The EPD process was similarly set up as shown in the **Figure 2.1**. In the acidic medium containing PEI polymer, the positive charges on the surface of the silica nanoparticles is recorded by zeta sizer measurement and the value depends on the additional concentration of I₂ solution. For this reason, the fabrication of the films was performed by cathodic EPD process. In order to reduce the oxidation of the ITO or FTO glass used as cathode, the voltage was applied from 1 V to 10 V for 10 min maximally. The Mo₆@HSNs film prepared on ITO or FTO glass were dried at ambient condition before the characterizations.

4.3.2. Optimization of the Mo₆@HSNs suspensions for EPD process

The suspensions of the HSNs, CMIF@HSNs and CMC@HSNs nanoparticles in PEI-acetone solution were titrated by I₂ solution (1% in acetone). The titration results are shown in **Figure 4.11a**. A part of the generated protons adsorb on the surface of the HSNs and interacting with amine groups of PEI meanwhile others freely mobilize in the suspension that is recorded by pH measurement. The same protons are generated for the same concentration of I₂ molecules in acetone medium. At the same concentration of I₂ added, pH value of the HSNs suspension is lower or number of the free protons higher than other Mo₆@HSNs suspensions. For this result, the incorporation of the Mo₆ cluster on the surface of the HSNs improve the adsorption of the protons that gives high pH value. The combination of the PEI layers outside the HSNs in acetone gives the positive charge at the initial condition. However, the zeta potential is inversely proportional with the concentration of I₂ added as presented in **Figure 4.11b**. The zeta potential is relatively stable for the CMC@HSNs suspension in the range between 15 mV and 20 mV corresponding to the increase of the protons. The CMIF@HSNs suspension reaches the value saturated at the concentration of I₂ at 30 mg/ml with 8 mV while the behavior of the HSNs nanoparticle is so different with others corresponding to the sudden decrease and saturating at 2 mV (20 mg/ml I₂). Generally, a number of additional PEI will cover on the surface of the HSNs and link the nanoparticles together. At the point of the concentration of I₂ is zero, the zeta potential is determined by positive charge of PEI coupling with protons generated from iodine-acetone solution. When I₂ molecules is added to the suspension, protons and iodine anion were released at the same time through a keto-enol reaction following the catalytic action of a coexisting acid or base [36]. Protons will continually adsorb on the surface of the silica nanoparticle and neutralize the hydroxyl groups on pure HSNs and amine groups on PEI. For this reason, iodine anion (I⁻) as counter anion combining with proton will occupy outside layers and make a light reversion of the zeta potential on the surface of the HSNs at that time. Moreover, at high pH, the particle size decreases that reduce the double layer thickness as well as decrease the repulsive force between the particles. This phenomena has also been realized in a previous report [39]. The strong proton absorption of the Mo₆@HSNs at the initial stage results the poor proton absorption during arising pH by adding I₂ solution. The saturating absorption of new protons as well as neutralization by I⁻ counter anions is recognized for the Mo₆@HSNs suspension

corresponding to the slow zeta potential reversion. The surface of the CMIF@HSNs seem to adsorb the proton better than the CMC@HSNs due to the ester group on the Mo_6 cluster ($OCOC_2F_5$). At the concentration of I_2 at 30 mg/ml, the absorption is saturated. Even the surface of the HSNs positively charged with PEI, the addition of I_2 in the acetone solution is necessary due to enhance the electrostatic repulse force that prevents the agglomeration and improves the suspension stability with small particle size. The same tendency of the electric conductivity for all suspensions is showed in **Figure 4.11c**. This conductivity mostly depends on the mobilization of the ions generated by the reaction between iodine and acetone molecules. Consequently, the same concentration of I_2 molecules will create the same amount of protons and iodine anion (I^-).

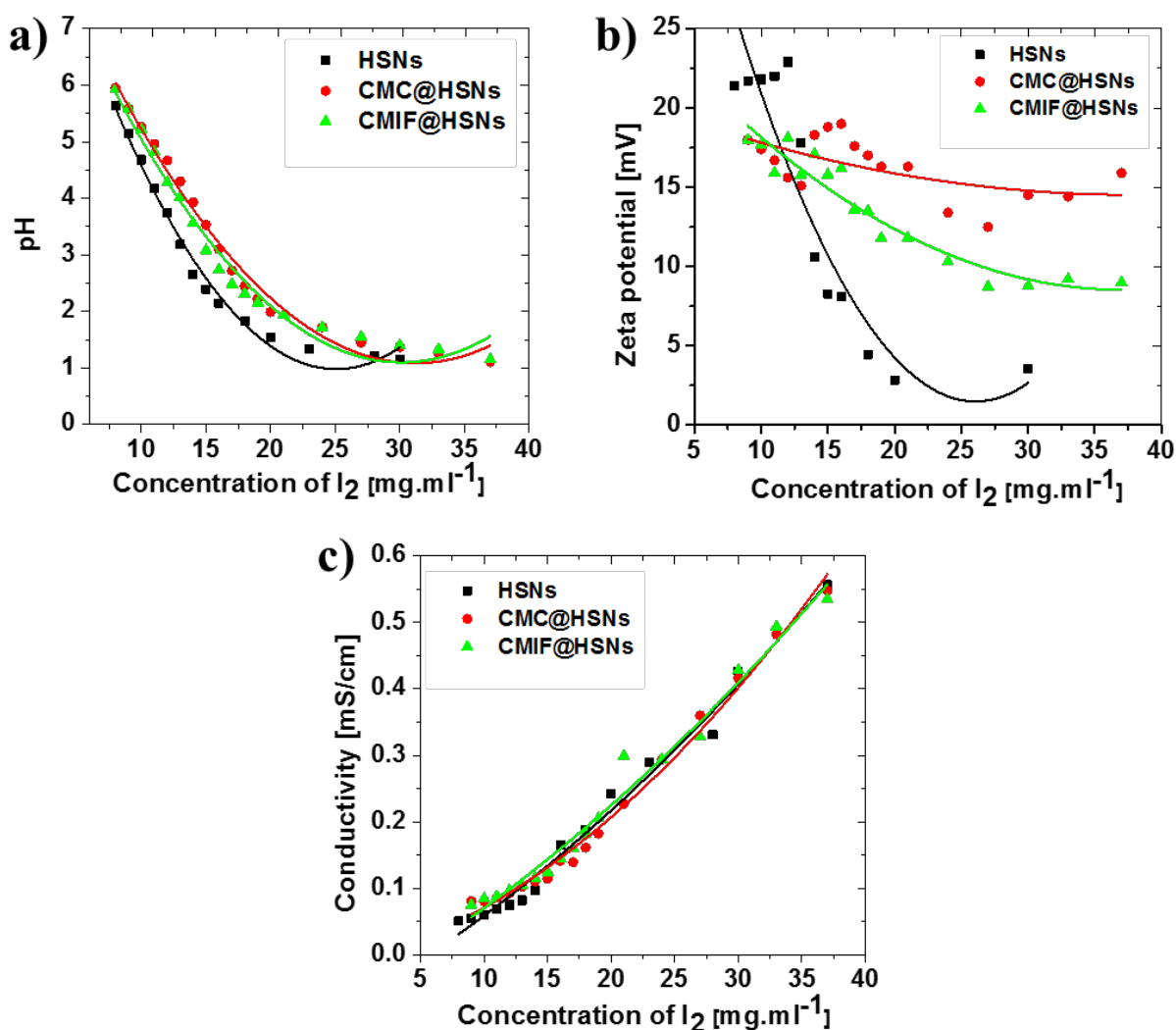


Figure 4.11. a) The change of the pH, b) zeta potential, and c) electric conductivity with the amount of I_2 added.

The positive charge of the silica nanoparticles was performed by adsorbing the protons on the surface through the interaction with hydroxyl groups and amine groups of PEI. The concentration of the PEI

possibly controls the number of absorbing protons. To improve the positive charged surface and reduce the local coagulation of the silica nanoparticles, the optimization of a mount of the added PEI has firstly been investigated for the HSNs suspension versus of the particle size (**Fig. 4.12**). The concentrations of the PEI, 2%, 5% and 8%, calculated per 100 g of the HSNs were reported. The particle size of the HSNs at the different concentration of PEI shows that most of the particle size focus under 2 μm at 2% and 5% PEI and it increase to the range of 2 and 4 μm at 8% PEI. The PEI is necessary to control the positive charge and be enough to avoid the coagulation between polymer chains. For this reason, 5% PEI of 100 mg HSNs is the suitable concentration to add in the suspension.

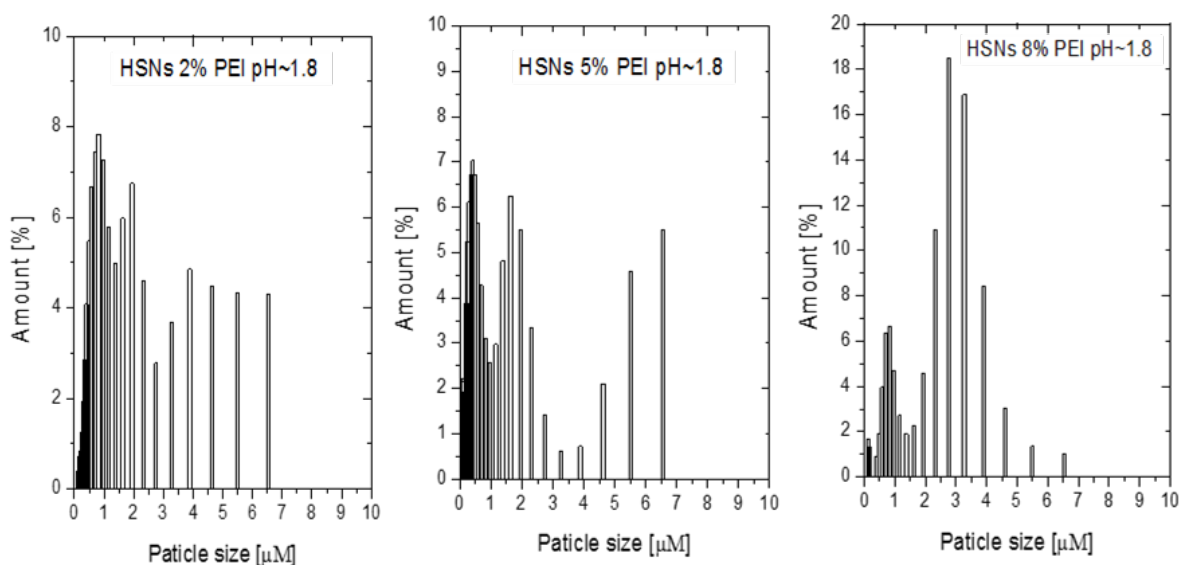


Figure 4.12. The change of the particle size of the HSNs on the concentration of PEI in the suspension.

The change of the pH value by adding I_2 also contributes to the particle size of the HSNs as presented in **Figure 4.13**. With the optimized ratio of the HSNs and PEI (100:5), the particle size of the HSNs reduce versus of the decrease of pH of the suspension. At high pH, crucial particle size in the range between 2 and 4 μm for pH of 2.7, and between 0.8 and 1.5 μm for pH of 2.3. At pH of 2.1, most of particle sizes basically concentrate on the range under 100 nm. However, the range of particle size is extended from 0 to 200 nm for pH of about 1.8. From the results, pH of 2.1 was selected to apply for the EPD suspension. The homogeneity of the particle size effect to the uniform morphology of the HSNs film. This result obtain as same as with the report of A.G. Bhosale et al. ^[39] to fabricate the ceramic film by the EPD process.

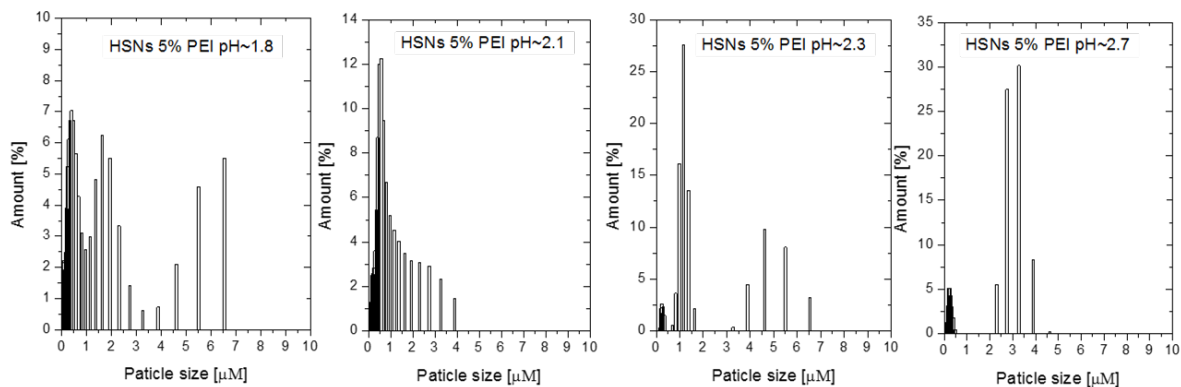


Figure 3.13. The change of the particle size of the HSNs on versus of pH value of the suspension.

In the same way, the particle size of the $\text{Mo}_6\text{@HSNs}$ suspension was investigated at different pH values (**Fig. 4.14**). Most of the particle size of the suspension at pH of 2.1 focuses on the range under 400 nm and significant amount under 100 nm. The distribution of the particle size increases to higher range for the pH value of 2.7 for two suspensions that can be seen clear in the CMC@HSNs suspension. The dissolution of the $\text{Mo}_6\text{@HSNs}$ covered by the PEI in the iodine-acetone medium is poorer than pure HSNs.

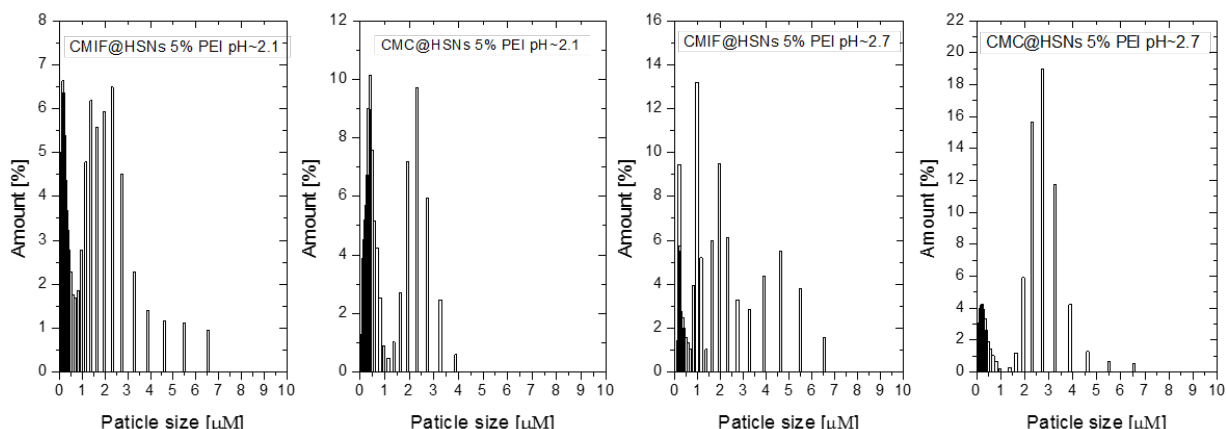


Figure 4.14. The change of the particle size of the $\text{Mo}_6\text{@HSNs}$ on versus of pH value of the suspension.

In summary, the ratio of silica nanoparticle and PEI of 100: 5 and the crucial concentration of I_2 molecules to achieve the pH of 2.1 (**Table 4.2**) were selected as essential suspension to prepare the nanocomposite films by the EPD process.

4.3.3. Characterization of the $\text{Mo}_6\text{@HSNs}$ film by the EPD

After optimizing the suspensions to achieve uniform nanoparticle size lower than 200 nm, a voltage was applied to the suspension. The HSNs and $\text{Mo}_6\text{@HSNs}$ were deposited on indium tin oxide coated glass (ITO-glass) and fluorine tin oxide coated glass (FTO-glass) by cathodic EPD process. To avoid the oxidation on the surface of ITO, the applied voltage was controlled lower than 5 V for 3 min. The

morphology of the prepared films is presented on **Figure 4.15**. At the same magnification, the porous property of the HSNs film is higher than the Mo₆@HSNs with a lots of the empty spaces on the surface. The good condense is clearly recognized in the CMIF@HSNs film than other films. The broken particles are not figured out in the SEM images at the magnification of $\times 100k$. That means the shell of the HSNs is enough hard to retain during preparing the followed by deposition by the EPD process. The existence of the PEI also prevents the destruction of the HSNs surface from the acidic medium. Relatively uniform Mo₆@HSNs film was prepared at 5 V for 3 min by cathodic EPD process.

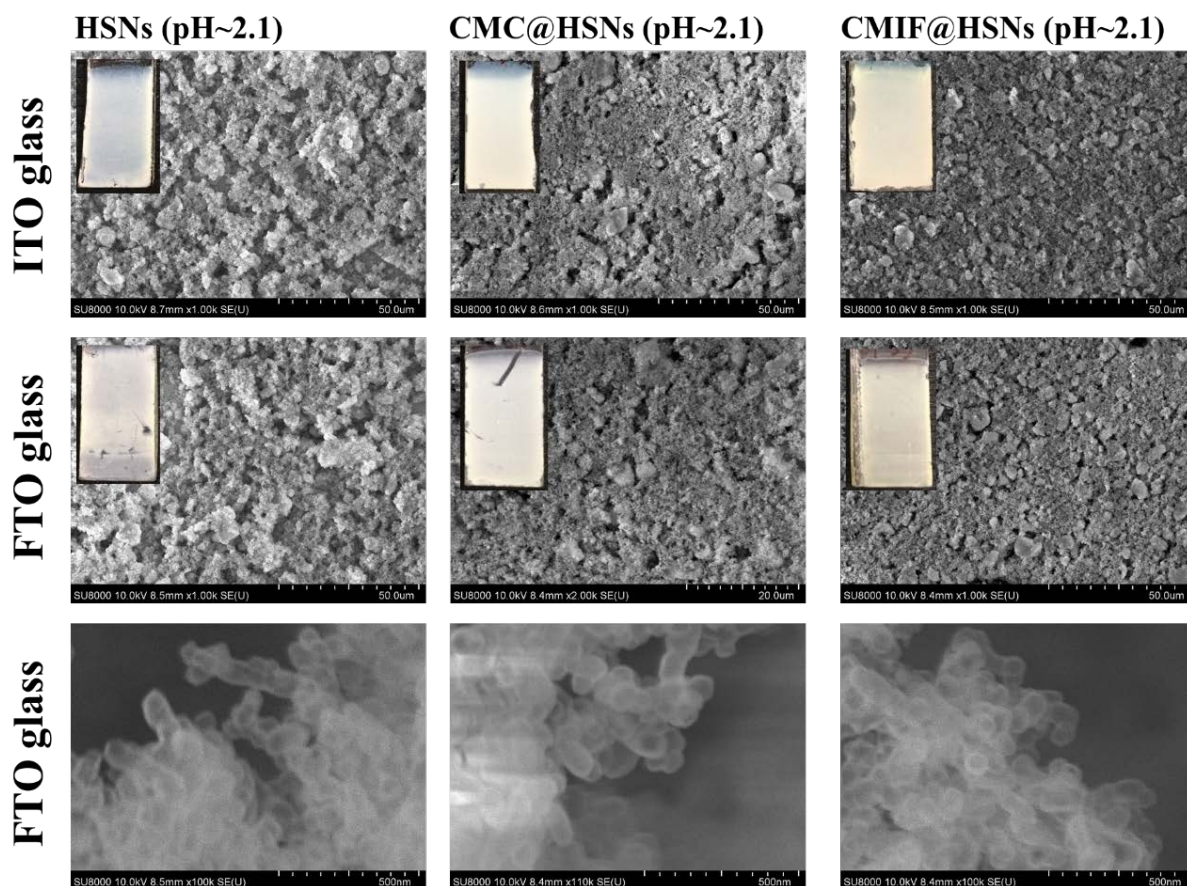


Figure. 4.15. The FE-SEM images of the HSNs, CMC@HSNs and CMIF@HSNs on the different deposition substrates.

In order to ensure the success of iodine-added acetone solution with retaining apical ligands on the Mo₆ clusters, the optical properties of the HSNs films were measured as shown in **Figure 4.16**. The reflection of the porous silica nanoparticles makes the poor transmittance for all the HSNs film (**Fig. 4.16a**). It is difficult to determine the absorption range caused from the Mo₆ clusters. In the photoluminescence emission in **Figure 4.16b**, the HSNs films on ITO or FTO coated glass appear a emission peak at 490 nm that does not exist on the curves of the pure HSNs or HSNs handled by only vacuum impregnation. The PL spectrum of ITO was also measured without any emission peaks. In connection with this phenomena, it is suggested for the emission of I, I₂ and CH₃COCH₂I chemicals ^[36] generated in the

suspension during occurring the reaction of I_2 molecules and acetone. In order to prove this prediction, some measurements of chemical position will be clarified in the further future. Even though the CMC@HSNs nanocomposite was successfully deposited on the conductive substrates by the EPD process, the emission peak created by the Mo_6 cluster was not recognized. The PL spectra of the CMC@HSNs only show an emission peak at the wavelength of 490 nm as same as the HSNs film. However, the CMIF@HSNs film shows the emission peak not only at the wavelength of 490 nm but also at 700 nm. A shift to higher wavelength is recognized for the emission peak of the Mo_6 cluster from 668 nm for precursor to 700 nm that indicates the good incorporation between the HSNs and Mo_6 @cluster by the EPD process.

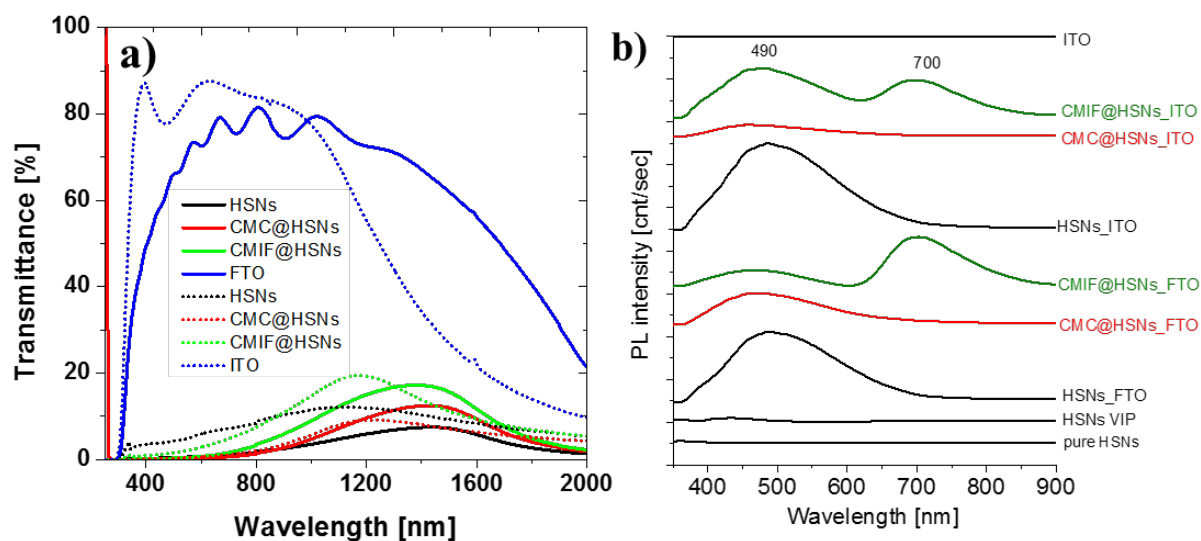


Figure 4.16. a) The UV-Vis absorption and b) the photoluminescence spectra of the HSNs, and Mo_6 @HSNs nanocomposites on the different substrates.

In summary, the selection of the EPD medium for the Mo_6 @HSNs powder is complicated, however, the nanocomposite films have successfully been fabricated by the EPD process. The use of the FTO will reduce the oxidation on the substrate during the EPD process, resulting the successful preparation of the CMIF@HSNs film with retaining the luminescence of the Mo_6 cluster by the EPD process.

4.4. Fabrication and characterization the Mo_6 @HSNs film by dip coating

4.4.1. Mechanical properties

Though the fabrication of Mo_6 @HSNs film with uniform morphology was possible by the EPD process, the stability of the film was poor with weak mechanical strength. In order to extend the application under the natural weather condition, the hydrophobic film containing the Mo_6 @HSNs would be necessary to obtain on the glass. The hydrophobic nanocomposite films (F1~F6) have been prepared by

dipping in the top coat suspension (TCS) (**Fig. 4.17**). The dipping suspension was prepared by mixing with top-coat suspension (TCS) containing nitro cellulose as an essential component and the CMIF@HSNs powder in acetone solution. The soda-lime glass is immersed in the nanocomposite suspension for 3 times or 6 times and dried at 60°C for 1 hour to form the stable CMIF@HSNs film. The Mo₆@HSNs film obtained the relative transparency depends on the transparency of the top coat film. Based on the adhesion test by the test method tape, a notch of 1 mm grid squire was cut on the films with the thickness 30 μm or less with a cutter knight to form the patterns on the surface (**Fig. 4.17**). The thickness of the 5 first films was similar. Only the film F6 with the significant thickness of 28.7 ± 4.2 μm was not stable even without and with adhesion measurement. The concentration of the suspension insignificantly affected to the thickness of the film except for the film with 6 g/litre and 6 dips. It can be seen that the film surface have no change without and with measuring the adhesion with tape, followed by 4B~5B classification of the D3359-97 ASTM standard test method. In summary, TCS is a good medium to immobile and disperse the cluster@HSNs nanoparticles and the dip coating method is a simple method to fabricate the thin film about 5 μm with high adhesion property.

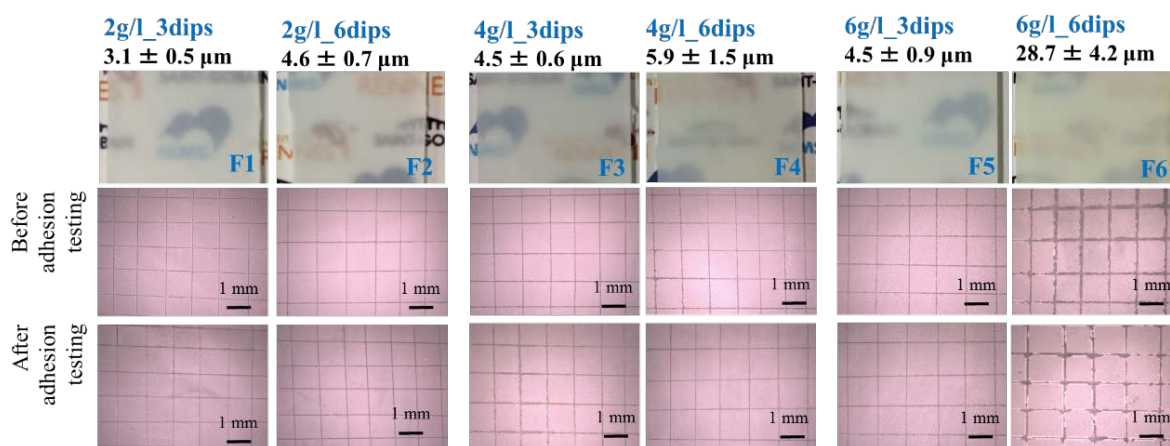


Figure 4.17. The obtained cluster@HSNs films by dipping in top coat suspension (TCS) and the photos of the films without and with measure the adhesion by transparent tape.

The morphology of TCS film (F0 with 3 dips) and the Mo₆@HSNs films (F1~F6) observed by color 3D laser microscope are shown in **Figure 4.18**. F0 film appears many of the homogenous holes on the surface due to solvent evaporation that cause the strong light scattering for the film, consequently, the film has poor transparency. Similarly, the porous morphology is recognized for most the Mo₆@HSNs films from F1 film to F6 film. However, the homogeneity of the film reduces and the size of the holes increases when increasing the number of dips. At high concentration, the surface become more roughness due to a non-uniform distribution of the Mo₆@HSNs nanoparticles in a whole of the film. The compatibility of the nanocomposite and TCS influences to the homogeneity of the obtained films. The hydrophobic characteristic of the films was determined by measuring the contact angle of a water droplet. The water droplet was captured on the surface of the film by a digital microscope to calculate

the contact angle. **Figure 4.18** shows the similar contact angles for all the films (F0~ F6). The contact angles higher than 90° indicates all the films achieve good hydrophobic properties. The existence of the Mo_6 @HSNs nanoparticles does not influence to the waterproof of the F0 film even though there are many hydroxyl groups on the surface of the HSNs nanoparticles. It is predicted that hydroxyl groups on the HSNs is blocked by the Mo_6 cluster or the ingredients of TCS. The excellent waterproof characteristic of the Mo_6 @HSNs films is one of the prominent advantages for the applications under the weather condition.

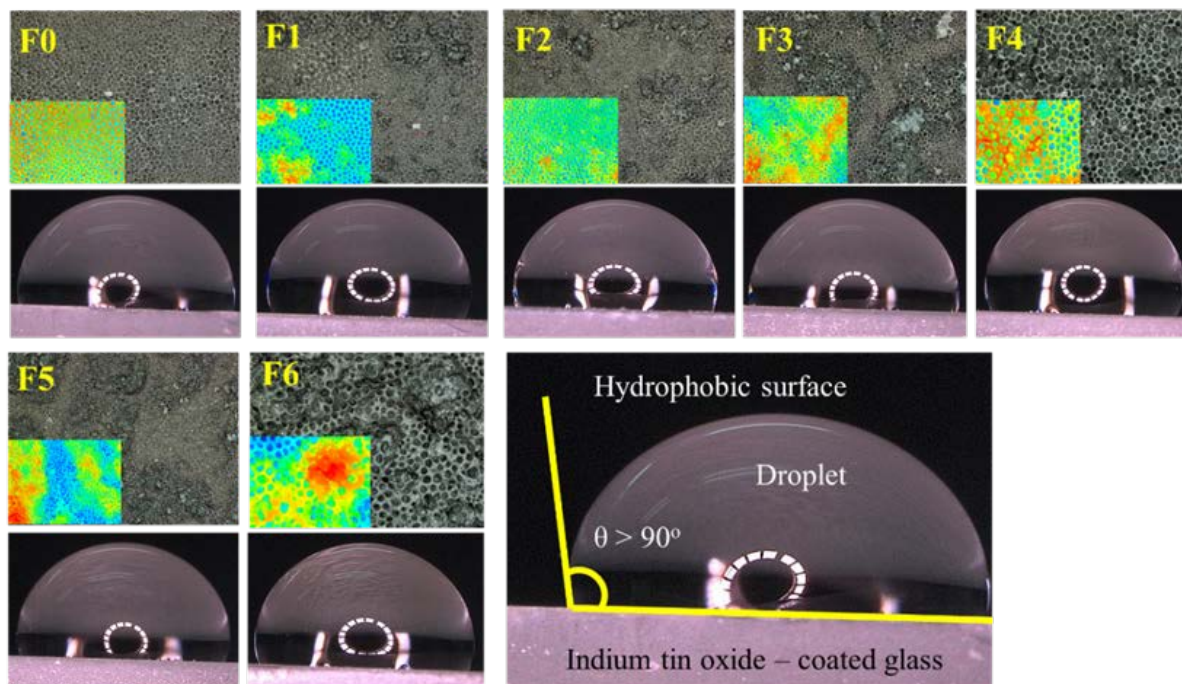


Figure 4.18. The morphology and water droplet photos of the films.

4.4.2. Optical property

The nanocomposite films show the strong photoluminescence under the 324 nm UV light presented in **Figure 4.20** (left). The strong photoluminescence obtains when increasing the thickness or concentration of the CMIF@HSNs nanocomposite in the film. The F1, F3, and F5 films exhibiting the relative thickness ($3\sim 5\ \mu\text{m}$) were selected to measure the PL quantum yield in the excitation wavelength between 300 nm and 600 nm in **Figure 4.19** (right). The CMIF precursor obtained the excellent PL quantum yield by exciting at the wavelength between 400 nm and 500 nm with a peak of about 26%. However, the quantum yield of the Mo_6 cluster significantly decrease when it is incorporated with the HSNs. The maximum quantum yield of the CMIF@HSNs powder reach at 18% by exciting at the wavelength of 420 nm. In TEM image, the Mo_6 clusters are almost condensed in the porous shell of the HSNs. During the irradiation, the CMIF@HSNs powder partially adsorbs the energy of incident light and, simultaneously causes the emission light by CMIF cluster, scattering light by silica and transmitted

light. The decrease of the quantum yield is consistent with the reduction of the emission light recorded in detector. The CMIF still retains the PL quantum yield at the excitation wavelength of 600 nm while it disappears in the CMIF@HSNs powder. The emission wavelength of the CMIF at the wavelength of 668 nm and poorly absorption of the HSNs in the visible light range give the suggestion that the emission light is scattered by the pores of the silica shell [35]. The metal cluster in the pores of the HSNs acts as an UV light absorbing agent and the heat energy transfer to the emission state. Then the HSNs will diffuse the heat caused by the UV light and reduce the emission intensity by the reflection inside the pores. Therefore, the quantum yield can be reduced by absorbing and reflecting the UV light of the mesoporous silica nanoparticles. The similar phenomena occurs to the nanocomposite film dipped with the top coat suspension. The scattering phenomena is significantly enhanced by a lot of the holes inside the nanocomposite film that cause the reduction of the total quantum yields. When the scattering in the nanocomposite film strongly occurs, the emission intensity from the CMIF is reduced. Due to this result, the porous nanocomposite film can eliminate the negative effect of the passing light on the window. The quantum yield of the CMIF@HSNs films still remains at the excitation wavelength lower than 450 nm.

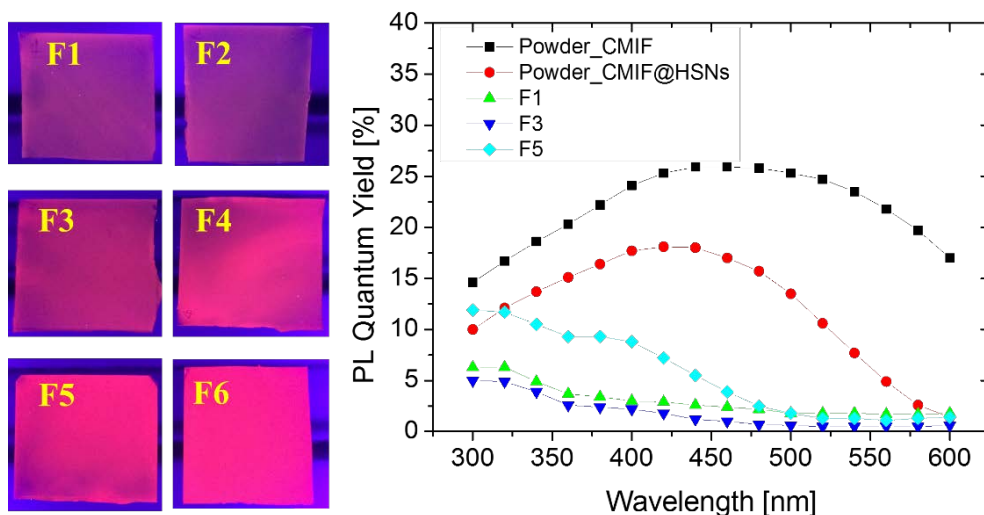


Figure 4.19. The photoluminescence photos of the CMIF@HSNs films with different concentrations and coating process excited by 324 nm UV light (left) and the PL quantum yield valuation of the CMIF, CMIF@HSNs powder and CMIF@HSNs film coated on soda lime glass.

4.5. Conclusions

The insulation characteristic of the CMIF@HSNs film caused by diffusing the heat in the porous channel of the hollow silica nanoparticles and the UV light blocking property accompanying the photoluminescence emission from the Mo₆ cluster would be a promising for a saving energy material application. The CMIF@HSNs could be a potential luminescence material when the optical property have retained after fabricating by dip coating or the EPD process.

Reference

1. W. Arap, R. Pasqualini, M. Montalti, L. Petrizza, L. Prodi, E. Rampazzo, N. Zaccheroni, and S. Marchio. Luminescent silica nanoparticles for cancer diagnosis. *Curr. Med. Chem.*, 20, 2195–2211, 2013.
2. X. Li, Q. He, and J. Shi. Global gene expression analysis of cellular death mechanisms induced by mesoporous silica nanoparticle-based drug delivery system. *ACS Nano*, 8, 1309-1320, 2014.
3. J. L. Vivero-Escoto, R. C. Huxford-Phillips, and W. Lin. Silica-based nanoprobe for biomedical imaging and theranostic applications. *Chem. Soc. Rev.*, 41, 2673-2685, 2012.
4. R. Mitran, D. Berger, C. Munteanu, and C. Matei. Evaluation of different mesoporous silica supports for energy storage in shape-stabilized phase change materials with dual thermal responses. *J. Phys. Chem. C*, 119, 15177–15184, 2015.
5. S. Cordier, K. Kirakci, D. Mery, C. Perrin, and D. Astruc. Mo₆X₈ nanocluster cores (X: Br, I): from inorganic solid state compounds to hybrids. *Inorganica Chimica Acta*, 359, 1705-1709, 2006.
6. D. Bozsaky. Application of nanotechnology-based thermal insulation materials in building construction. *Slovak Journal of Civil Engineering*, 24, 17 – 23, 2016.
7. L. Wang, P. S. Tsai, and Y. M. Yang. Preparation of silica microspheres encapsulating phase-change material by sol-gel method in O/W emulsion. *J. Microencapsul.*, 23, 3-14, 2006.
8. X. Min, M. Fang, Z. Huang, Y. Liu, Y. Huang, R. Wen, T. Qian, and X. Wu. Enhanced thermal properties of novel shape-stabilized PEG composite phase change materials with radial mesoporous silica sphere for thermal energy storage. *Scientific Reports*, 5, 1-11, 2015.
9. D. Certain, and R. Lissillour. The Three-Band Model. A pattern for the electronic structure of M₆L₈L₆ cluster compounds. *Z. Phys. D - Atoms, Molecules and Clusters*, 3, 411-420, 1986.
10. T. Hughbanks, and R. Hoffmann. Chains of trans-edge-sharing molybdenum octahedra: metal-metal bonding in extended systems. *J. Am. Chem. Soc.*, 105, 3528–3537, 1983.
11. L. Ernawati, T. Ogi, R. Balgis, K. Okuyama, M. Stucki, S. C. Hess, and W. J. Star. Hollow silica as an optically transparent and thermally insulating polymer additive. *Langmuir*, 32, 338–345, 2016.
12. M. Fuji, C. Takai, H. Watanabe, and K. Fujimoto. Improved transparent thermal insulation using nano-spaces. *Advanced Powder Technology*. 26, 857-860, 2015.
13. K. Kirakci, S. Cordier, and C. Perrin. Synthesis and characterization of Cs₂Mo₆X₁₄ (X = Br or I) hexamolybdenum cluster halides: efficient Mo₆ cluster precursors for solution chemistry syntheses. *Z. Anorg. Allg. Chem.*, 631, 411-416, 2005.
14. G. Saito, H. Hosoda, Y. Yoshida, J. Hagiwara, K. Nishimura, H. Yamochi, A. Otsuka, T. Hiramatsu, Y. Shimazaki, K. Kirakci, S. Cordier and C. Perrin. Synthesis and properties of charge-transfer solids with cluster units [Mo₆X₁₄]²⁻ (X= Br, I). *J. Mater. Chem.*, 22, 19774-19791, 2012.
15. M. A. Cortes, S. Paofai, S. Cordier, H. Folliot and Y. Molard. Tuned red NIR phosphorescence of polyurethane hybrid composites embedding metallicnanoclusters for oxygen sensing. *Chem. Commun.*, 51, 8177-8180, 2015.
16. M. Prévôt, M. A. Cortes, S. K. Manna, R. Lefort, S. Cordier, H. Folliot, L. Dupont, and Y. Molard.

Design and integration in electro-optic devices of highly efficient and robust red-nir phosphorescent nematic hybrid liquid crystals containing $[\text{Mo}_6\text{I}_8(\text{OCOC}_n\text{F}_{2n+1})_6]^{2-}$ ($n = 1, 2, 3$) Nanoclusters. *Adv. Funct. Mater.*, 25, 4966-4975, 2015.

17. C. Neaime, M. A. Cortes, F. Grasset, Y. Molard, S. Cordier, B. Dierre, M. Mortier, T. Takei, K. Takahashi, H. Haneda, M. Verelstf and S. Lechevallier. Time-gated luminescence bioimaging with new luminescent nanocolloids based on $[\text{Mo}_6\text{I}_8(\text{C}_2\text{F}_5\text{COO})_6]^{2-}$ metal atom clusters. *Phys. Chem. Chem. Phys.*, 18, 30166-30173, 2016.

18. Y. Zhao, C. Riemersma, F. Pietra, R. Koole, C. M. Donega, and A. Meijerink. High-Temperature luminescence quenching of colloidal quantum dots. *ACS Nano*, 6, 9058-9067, 2012.

19. M. Yang, H.S. Peng, F. Zeng, F. Teng, Z. Qu, D. Yang, Y. Wang, G. Chen, and D. Wang. In situ silica coating-directed synthesis of orthorhombic methylammonium lead bromide perovskite quantum dots with high stability. *J. Colloid and Interf. Sci.*, 509, 32-38, 2018.

20. N. Saito, P. Lemoine, N. Dumait, M. A. Cortes, S. Paofai, T. Roisnel, V. Nassif, F. Grasset, Y. Wada, N. Ohashi and S. Cordier. From $\text{Cs}_2\text{Mo}_6\text{Cl}_{14}$ to $\text{Cs}_2\text{Mo}_6\text{Cl}_{14}\cdot\text{H}_2\text{O}$ and vice versa: crystal chemistry investigations. *J. Clust. Sci.*, 28, 773-798, 2017.

21. M. Fuji, C. Takai, Y. Tarutani, T. Takei and M. Takahashi. Surface properties of nanosize hollow silica particles on the molecular level. *Advanced Powder Technol.*, 18, 81-91, 2007.

22. N. Saito, Y. Wada, P. Lemoine, S. Cordier, F. Grasset, T. Ohsawa, N. Saito, J. S. Cross, and N. Ohashi. Theoretical and experimental determination of the crystal structures of cesium-molybdenum chloride. *Japanese J. App. Phys.*, 55, 1-8, 2016.

23. T. Aubert, F. C. Hurtado, M. A. Esnault, C. Neaime, D. L. Chauvel, S. Jeanne, P. Pellen, C. Roiland, L. L. Polles, N. Saito, K. Kimoto, H. Haneda, N. Ohashi, F. Grasset, and S. Cordier. Extended investigations on luminescent $\text{Cs}_2[\text{Mo}_6\text{Br}_{14}]\text{@SiO}_2$ nanoparticles: physico-structural characterizations and toxicity studies. *J. Phys. Chem. C*, 117, 20154-20163, 2013.

24. I. Roberts, and H. C. Urey. The mechanisms of acid catalyzed ester hydrolysis, esterification and oxygen exchange of carboxylic acids. *J. Am. Chem. Soc.*, 61, 2584-2587, 1939.

25. C. S. Cucinotta, A. Ruini, A. Catellani, and A. Stirling. Ab initio molecular dynamics study of the keto-enol tautomerism of acetone in solution. *Chem. Phys. Chem.*, 7, 1229 - 1234, 2006.

26. T. K. N. Nguyen, B. Dierre, F. Grasset, A. Renaud, S. Cordier, P. Lemoine, N. Ohashi, and T. Uchikoshi. Formation mechanism of transparent Mo_6 metal atom cluster film prepared by electrophoretic deposition. *J. Electrochem. Soc.*, 164, 412-418, 2017.

27. W. D. Hewett, J. H. Newton, and W. Weltner. Absorption spectra of molybdenum oxide molecules and molybdenum atoms in neon and argon matrices at 4 K. *J. Phys. Chem.*, 79, 2640-2649, 1975.

28. Y. A. Vorotnikov, O. A. Efremova, N. A. Vorotnikova, K. A. Brylev, M. V. Edeleva, A. R. Tsygankova, A. I. Smolentsev, N. Kitamura, Y. V. Mironov and M. A. Shestopalov. On the synthesis and characterization of luminescent hybrid particles: Mo_6 metal cluster complex/ SiO_2 . *RSC Adv.*, 6, 43367-43375, 2016.

29. F. Grasset, F. Dorson, S. Cordier, Y. Molard, C. Perrin, A. M. Marie, T. Sasaki, H. Haneda, Y.

- Bando, and M. Mortier. Water-in-oil microemulsion preparation and characterization of Cs₂[Mo₆X₁₄]/SiO₂ phosphor nanoparticles based on transition metal clusters (X = Cl, Br, and I). *Adv. Mater.*, 20, 143-148, 2008.
30. S. Yang, W. Li, B. Cao, H. Zeng, and W. Cai. Origin of blue emission from silicon nanoparticles: direct transition and interface recombination. *J. Phys. Chem. C*, 115, 21056-21062, 2011.
 31. X. Meng, S. Murai, K. Fujita, and K. Tanaka. Intense blue emission from tantalum-doped silicate glass. *Appl. Phys. Lett.*, 89, 1-3, 2006.
 32. I. Navas, R. Vinodkumar, and V. P. M. Pillai. Self-assembly and photoluminescence of molybdenum oxide nanoparticles. *Appl. Phys. A*, 103, 373-380, 2011.
 33. H. C. Kim, H. G. Hong, C. Yoon, H. Choi, I. S. Ahn, D. C. Lee, Y. J. Kim, and K. Lee. Fabrication of high quantum yield quantum dot/polymer films by enhancing dispersion of quantum dots using silica particles. *J. Colloid and Interf. Sci.*, 393, 74-79, 2013.
 34. S. Liang, K. Shephard, D. T. Piercea and J. X. Zhao. Effects of a nanoscale silica matrix on the fluorescence quantum yield of encapsulated dye molecules. *Nanoscale*, 5, 9365-9373, 2013.
 35. T. K. N. Nguyen, F. Grasset, B. Dierre, C. Matsunaga, S. Cordier, P. Lemoine, N. Ohashi and T. Uchikoshi. Fabrication of transparent thin film of octahedral molybdenum metal clusters by electrophoretic deposition. *ECS J. Solid. State. Sci. and Technol.*, 5, 178-186, (2016).
 36. N. Koura, T. Tsukamoto, H. Shoji and T. Hotta. Preparation of various oxide films by an electrophoretic deposition method: a study of the mechanism. *Jpn. J. Appl. Phys*, 34, 1643-1647, 1995.
 37. L. Dusoulier, R. Cloots, B. Vertruyen, R. Moreno, O. B. Montes, and B. Ferrari. YBa₂Cu₃O_{7-x} dispersion in iodine acetone for electrophoretic deposition: Surface charging mechanism in a halogenated organic media. *Journal of the European Ceramic Society*, 31, 1075-1086, 2011.
 38. L. Grinis, S. Dor, A. Ofir, and A. Zaban. Electrophoretic deposition and compression of titania nanoparticle films for dye-sensitized solar cells. *J. Photochem. Photobiology A: Chem.*, 198, 52-59, 2008.
 39. A. G. Bhosale, R. Joshi, K. M. Subhedar, R. Mishra, S. H. Pawar. Acetone mediated electrophoretic deposition of nanocrystalline SDC on NiO-SDC ceramics. *J. Alloys and Compounds*, 503, 266-271, 2010.
 40. A. Chavez-Valdez, M. S. P. Shaffer, and A. R. Boccaccini. Applications of graphene electrophoretic deposition. A Review. *J. Phys. Chem. B*, 117, 1502-1515, 2013.
 41. Y. Sakka and T. Uchikoshi. Forming and microstructure control of ceramic by electrophoretic deposition (EPD). *KONA Powder and Particle Journal*, 28, 74-90, 2010.
 42. A. R. Boccaccini, J. Cho, J. A. Roether, B. J. C. Thomas, E. J. Minay, and M. S. P. Shaffer. Electrophoretic deposition of carbon nanotubes. *Carbon*, 44, 3149-3160, 2006.

Chapter 5

Fabrication of Octahedral Tantalum Cluster Film by Electrophoretic Deposition

Chapter 5

Fabrication of Octahedral Tantalum Cluster Film by Electrophoretic Deposition

The octahedral $\text{Ta}_6\text{Br}_{14}\cdot 8\text{H}_2\text{O}$ or $\{\text{Ta}_6\text{Br}_{12}(\text{H}_2\text{O})^a_6\}\text{Br}_2$ cluster, one of the popular clusters of $\{\text{M}_6\text{L}^i_{12}\text{L}^a_6\}^{n-}$ octahedron family (M= Nb, Ta; L^i = inner halogen, L^a = apical halogen or chalcogen), exhibits interesting oxido-reduction and optical properties in solution^[1, 2]. The nature of the optical absorption extending from about 250 nm to the near-infrared region are suggested to the association of d-d transitions of the cluster, corresponding to the metal-to-metal charge-transfer transition meanwhile the bands below 250 nm are believed to belong to ligand-to-metal charge-transfer transition^[3-5]. The application of the $\{\text{Ta}_6\text{Br}_{12}\}^{2+}$ cores has been potentially studied in biotechnologies^[6, 7], optical devices^[8], photovoltaic cells^[9] and UV blocking devices^[10]. With the expectation to block the UV and NIR light on low-emissivity window, the $\text{Ta}_6\text{Br}_{14}\cdot 8\text{H}_2\text{O}$ cluster thin film on ITO glass has been fabricated by the electrophoretic deposition (EPD) process, a fairly rapid and low cost two-step process well-known for ceramic shaping, conductive surface coating and easily scalable to industrial level. The interesting characteristic has been recognized that the green-colored $\{\text{Ta}_6\text{Br}_{12}\}^{2+}$ cores (adsorbing Ultra-Visible range) easily transfers to brown-colored $\{\text{Ta}_6\text{Br}_{12}\}^{3+/4+}$ cores (absorbing near-infrared range) when dissolved in different solvents. Therefore, the selection of dispersing medium and the optimization of the concentration of $\text{Ta}_6\text{Br}_{14}\cdot 8\text{H}_2\text{O}$ cluster in the solvent to obtain the green homogeneous suspension with high dissolution are one of the biggest concerns of the study. Considering the green color and good transmittance of the solution, as well as uniform surface morphology of the green-colored film at the SEM level, the ratio of H_2O and $\text{Ta}_6\text{Br}_{14}\cdot 8\text{H}_2\text{O}$ cluster at 20:1 was selected as the optimal ratio to obtain the green transparent suspension and, possibly, to fabricate the green film by the EPD process. However, the $\{\text{Ta}_6\text{Br}_{12}\}^{2+}$ green film has been essentially incorporated with polyvinylpyrrolidone (PVP) in order to improve the dispersion of the $[\text{Ta}_6\text{Br}_{12}(\text{H}_2\text{O})^a_6]\text{Br}_2$ cluster clusters inside the suspension and effectively prevent the performance of new $\{\text{Ta}_6\text{Br}_{12}\}^{3+/4+}$ clusters (brown-color) by the oxidation reactions.

5.1. Fabrication of the $\{\text{Ta}_6\text{Br}_{12}(\text{H}_2\text{O})^a_6\}\text{Br}_2$ cluster film by EPD process

5.1.1. Synthesis of the $\{\text{Ta}_6\text{Br}_{12}(\text{H}_2\text{O})^a_6\}\text{Br}_2$ cluster precursor

The $\{\text{Ta}_6\text{Br}_{12}(\text{H}_2\text{O})^a_6\}\text{Br}_2$ cluster precursor was synthesized through the following two steps: i) Preparation of $\text{K}_4\text{Ta}_6\text{Br}_{18}$ cluster precursor by solid chemistry at high temperature using the process of F. W. Koknat et al.^[1, 11] and ii) Transformation of $\{\text{Ta}_6\text{Br}_{12}(\text{H}_2\text{O})^a_6\}\text{Br}_2$ cluster precursor from the $\text{K}_4\text{Ta}_6\text{Br}_{18}$ cluster precursor by solution chemistry^[12]. Firstly, KBr (0.930 g), TaBr_5 (3.394 g) and Ta (3.176 g) was weighted in an Argon atmosphere because the compound of tantalum is sensitive to oxygen. The mixture of them was ground to obtain fine powder, and then put in a glass tube. The glass tube was sealed by fire with argon gas filled. Afterwards, the tube containing the powder was heated in

an oven under the following program: i) heating to 650°C at a rate of 1°C/min, ii) annealing at 650°C for 900 min, iii) freezing down to 80°C at a rate of 2.5 °C/min. The obtained solid ($K_4Ta_6Br_{18}$) was converted to $\{Ta_6Br^{i}_{12}(H_2O)^a_6\}Br_2$ cluster in the following route:

- The $K_4Ta_6Br_{18}$ powder (5 g) was put in a flask with 40 ml of water and Ar gas, and then continually agitated with a magnetic stirrer for 3 days at room temperature.
- 45 ml of HBr was added in the filtrated $K_4Ta_6Br_{18}$ suspension and heated to 80°C (1°/min). Other suspensions including $SnBr_2$ (0.7g) and HBr (45 ml) were agitated for about 1 hour to obtain the complete dissolution, then the mixture was filtrated to collect the homogeneous solution.
- This solution was added in the $K_4Ta_6Br_{18}$ suspension at two temperature points at 80°C and 50°C using 15 ml for each.
- The mixture was agitated for 1 hour more before cooling, filtrating and washing by HCl (37%) solution with diethyl ether to formulate the $\{Ta_6Br^{i}_{12}(H_2O)^a_6\}Br_2$ cluster with dark green color.

The obtained $\{Ta_6Br^{i}_{12}(H_2O)^a_6\}Br_2$ cluster powder was dried in a vacuum at least for 24 h before the next steps. The rod-like crystal shape and the XRD pattern of the $\{Ta_6Br^{i}_{12}(H_2O)^a_6\}Br_2$ cluster framework are shown in **Figure 5.1**. The difference of bond lengths in the clusters with $\{Ta_6Br^{i}_{12}\}^{2+}$ core species has been reported corresponding to the different ligands [11]. Most of the suggestions for the crystal pattern of the $\{Ta_6Br^{i}_{12}(H_2O)^a_6\}Br_2$ cluster frameworks are cubic lattice [13] or cubic F lattice [14].

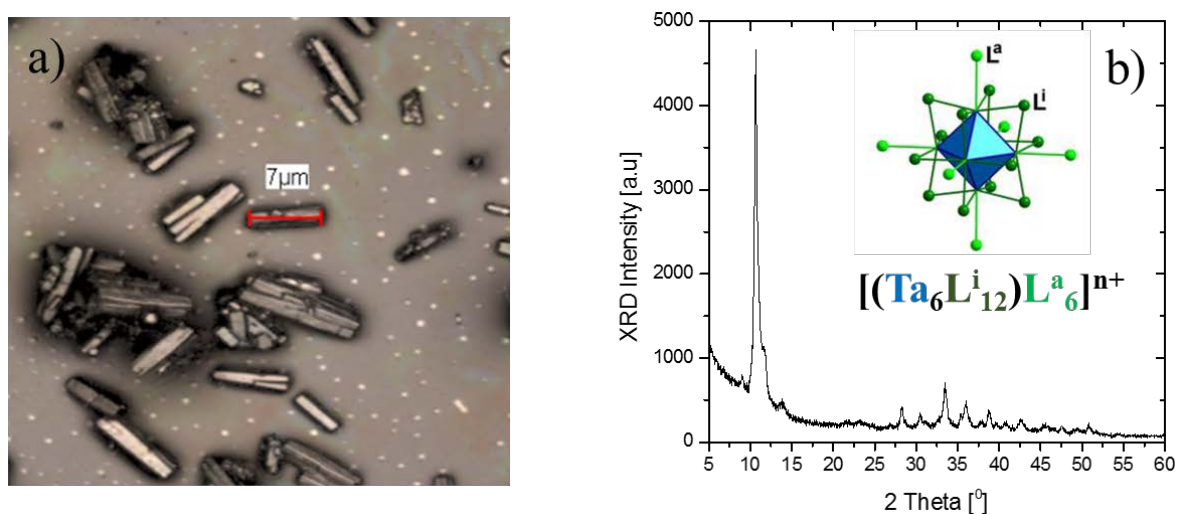


Figure 5.1. a) Rod-like crystal of the $\{Ta_6Br^{i}_{12}(H_2O)^a_6\}Br_2$ cluster observed by SEM and b) XRD pattern of the octahedral framework and scheme of the $\{Ta_6Br^{i}_{12}(H_2O)^a_6\}Br_2$ cluster.

5.1.2. Preparation of the EPD suspension

The $\{Ta_6Br_{12}(H_2O)_6\}Br_2$ cluster precursor was dissolved in different solvents, including distilled water, ethanol (99.5%), acetone (99.5 %), and methyl ethyl ketone (MEK, 99.5%), supplied from Nacalai Tesque (Inc., Kyoto, Japan), with the concentration of 1 g per litre for all. The homogeneous $\{Ta_6Br^{i}_{12}(H_2O)^a_6\}Br_2$ suspensions were obtained by sonicating the cluster in water or ethanol solutions

for 30 minutes or by agitating in acetone and MEK solutions for 3 days. All the suspensions were filtrated and collected as transparent solutions with different colors (**Fig. 5.2**). The zeta potential and electric conductivity of the solutions were measured by a zeta-potential analyzer (Malvern Instrument, Ltd., Zetasizer Nano Z, Malvern, UK) presented in **Table 5.1**.

Table 5.1. The physical parameters of the dissolution of $\{\text{Ta}_6\text{Br}^{i}_{12}(\text{H}_2\text{O})^a_6\}\text{Br}_2$ cluster particles in different solvents

Transparent Solution	Zeta potential (mV)	Conductivity 10^{-2} (mS/cm)
H₂O	6.68±0.06	9.47±0.12
Ethanol	34.5±0.31	2.61±0.03
Acetone	2.47±0.14	2.86±0.03
MEK	1.56±0.45	1.17±0.09

The suspensions with the various concentrations of the $\{\text{Ta}_6\text{Br}^{i}_{12}(\text{H}_2\text{O})^a_6\}\text{Br}_2$ cluster particles in mixture dispersing medium including water and acetone are noticed in **Table 5.2**. H0, H10, H15, H20, H25 and H50 suspensions were prepared by respectively sonicating at different time for 60, 60, 50, 40, 30 and 30 min that depend on the solubility of the $\{\text{Ta}_6\text{Br}^{i}_{12}(\text{H}_2\text{O})^a_6\}\text{Br}_2$ cluster particles in every solutions. The $\{\text{Ta}_6\text{Br}^{i}_{12}(\text{H}_2\text{O})^a_6\}\text{Br}_2$ cluster particles were quickly sonicated in water before adding acetone. The suspensions were filtrated to obtain the transparent solution containing homogeneous particles smaller than 2 μm .

Table. 5.2. The concentration of the $\{\text{Ta}_6\text{Br}^{i}_{12}(\text{H}_2\text{O})^a_6\}\text{Br}_2$ cluster particles in the dispersing medium containing water and acetone.

	Ratio of H ₂ O/Ta ₆ cluster		S1 (1 g/l)	S0.7 (0.67 g/l)
	H ₂ O (ml)	Ta ₆ cluster (g)	Acetone (ml)	Acetone (ml)
H50	0.5	0.01	10	15
H25	0.25	0.01	10	15
H20	0.2	0.01	10	15
H15	0.15	0.01	10	15
H10	0.1	0.01	10	15
H0	0	0.01	10	15

The $\{\text{Ta}_6\text{Br}^{i}_{12}(\text{H}_2\text{O})^a_6\}\text{Br}_2$ @PVP suspension was prepared from the mixture of the two main solutions: i) 10 ml the green $\{\text{Ta}_6\text{Br}^{i}_{12}(\text{H}_2\text{O})^a_6\}^{2+}$ cluster suspension of S1-H20 and ii) 5 ml the PVP solution in acetone with concentration of 2 gram per litre by sonicating and agitating. The mixture of the suspensions was agitated for 1 hour to obtain the homogeneous suspension. The zeta potential and electric conductivity were recorded at 38.37 (± 1.78) mV and 1.07 (± 0.05) mS/cm, respectively. The incorporation of the $\{\text{Ta}_6\text{Br}^{i}_{12}(\text{H}_2\text{O})^a_6\}\text{Br}_2$ cluster in PVP suspension excellently enhanced the positive

charge on the cluster particles. The EPD parameters to fabricate the green film@PVP are presented in **Table 5.3**.

Table 5.3. Optimization of the EPD parameters for the fabrication of the $\{Ta_6Br^{i}_{12}(H_2O)^a_6\}^{2+}$ cluster thin film. The concentrations of the $\{Ta_6Br^{i}_{12}(H_2O)^a_6\}Br_2$ cluster are 0.7 and 1 g/l with the different ratios of acetone and water solutions.

EPD Solution	Applied voltage (V)	Deposition time (sec)	Thin film realization
S1-H15	8, 10, 12, 15, 18, 20, 25	30	✓
		60	✓
S1-H20	8, 10, 12, 15, 18, 20, 25	30	✓
		60	✓
S1-H25	8, 10, 12, 15, 18, 20, 25	30	✓
		60	✓
S1-H50	8, 10, 12, 15, 18, 20, 25	30	✓
		60	✓
S0.7-H20	15	20	✗
		30	✗
		60	✓
		90	✓
	20	20	✗
		30	✓
		60	✓
		90	✓
S0.7-H20@PVP	25	30	✓
		60	✓
		90	✓
	30	30	✓
		60	✓
		90	✓
	35	30	✓
		60	✗
		90	✗

5.1.3. The fabrication of the green Ta₆ film by the EPD process

The EPD system was similarly setup to the scheme as shown in **Figure 2.1** with indium tin oxide-coated glass (ITO glass) as both the electrodes. The EPD parameters were investigated to fabricate the green

homogeneous $\{\text{Ta}_6\text{Br}_{12}(\text{H}_2\text{O})^a_6\}^{2+}$ cluster film based on the suspensions listed in **Table 5.2**. The optimal applied voltage and deposition time parameters were presented in **Table 5.3**. The EPD conditions under which thin film was obtained are noted by the green circles.

5.1.4. Characterization

The morphology and thickness of the Mo_6 @polymer films were characterized by field-emission scanning electron microscopy (FE-SEM, Hitachi 4800). The element ratio of the cluster films was measured using an EDX analyzer device installed in the FE-SEM. The UV-NIR absorption spectra were measured by UV-Vis-NIR spectroscopy (V570, Jasco Corp.) in the wavelength range of 220 and 2000 nm at the scan rate of 400 nm/s. The crystallographic structure of the films was determined by XRD (SmartLab, RIGAKU, 40 kV and 30 mA) in the 2θ angle range from 5° to 55° and at the scan speed of $1^\circ\text{C}/\text{min}$ with Cu K_α radiation ($\lambda = 1.54 \text{ \AA}$).

5.2. Characterization of the $\{\text{Ta}_6\text{Br}_{12}(\text{H}_2\text{O})^a_6\}^{n+}$ cluster film

5.2.1. Optimization of the $\{\text{Ta}_6\text{Br}_{12}(\text{H}_2\text{O})^a_6\}\text{Br}_2$ cluster suspension

The zeta potential of the $\{\text{Ta}_6\text{Br}_{12}(\text{H}_2\text{O})^a_6\}\text{Br}_2$ clusters in ethanol suspension showed the highest positive charge of the particles, resulting strong dissolution accompanying with emerald-green color. The same color was obtained for the aqueous suspension possessing the highest electric conductivity relatively low zeta potential. It is known that water molecules always prior to coordinate with to metal atoms of the $\{\text{Ta}_6\text{Br}_{12}(\text{H}_2\text{O})^a_6\}\text{Br}_2$ octahedron, consequently, it increases the solubility by hydration reaction of the cluster with water or ethanol solvents [2]. For this reason, the stabilization of the $\{\text{Ta}_6\text{Br}_{12}(\text{H}_2\text{O})^a_6\}^{2+}$ cation is relatively improved in water or ethanol solutions. As known, the higher the zeta potential, the stronger the repulsion, resulting the system more stable. Even though H_2O molecules can be retained on the $\{\text{Ta}_6\text{Br}_{12}\}^{2+}$ species by the hydration, low zeta potential can reduce the stabilization of the suspension. In this case, ethanol is suitable media with high zeta potential and electric conductivity to prepare stable EPD suspension.

In acetone and MEK solutions, the incomplete dissolution of the $\{\text{Ta}_6\text{Br}_{12}(\text{H}_2\text{O})^a_6\}\text{Br}_2$ clusters could occur, consequently, and two phases with red-brown solution and green solid existed after agitating for 3 days (**Fig. 5.2**). The cluster suspension prepared over period of long time also leads to the oxidation in air. The zeta potential of the obtained red-brown suspensions was slightly positive. It was probable that only a small amount of the $\{\text{Ta}_6\text{Br}_{12}(\text{H}_2\text{O})^a_6\}\text{Br}_2$ cluster precursor was able to solute in MEK solvent.

It has been reported aimed the brown color originates from the change of oxidation state from $\{\text{Ta}_6\text{Br}_{12}\}^{2+}$ to $\{\text{Ta}_6\text{Br}_{12}\}^{3+/4+}$ by reversing one electron when the cluster unit interacts with oxygen medium [15, 16]. According to Cooke et al. [15], normally, the $\{\text{Ta}_6\text{Br}_{12}\}^{4+}$ species is properly generated and $\{\text{Ta}_6\text{Br}_{12}\}^{2+}$ species is more stable due to the reproporationation reaction of the $\{\text{Ta}_6\text{Br}_{12}\}^{2+}$ species and $\{\text{Ta}_6\text{Br}_{12}\}^{4+}$ species. The oxidation by air-oxygen to transfer electron from $\{\text{Ta}_6\text{Br}_{12}\}^{2+}$ species to

$\{\text{Ta}_6\text{Br}_{12}\}^{3+}$ and further to $\{\text{Ta}_6\text{Br}_{12}\}^{4+}$ in acidic medium has also been reported by C. B. Thaxtox et al. [17]. In acetone, the protons which were generated by keto-enol tautomerism, could accelerate the oxidation reaction of the water in air-oxygen during stirring. The generated protons in MEK solution is low due to the poor solubility of the $\{\text{Ta}_6\text{Br}_{12}(\text{H}_2\text{O})^a_6\}\text{Br}_2$ cluster. In the UV absorption spectra (**Fig. 5.2**), it can be seen that all the suspensions including the $\{\text{Ta}_6\text{Br}_{12}\}^{2+}$ species and $\{\text{Ta}_6\text{Br}_{12}\}^{4+}$ species strongly absorb the UV bands under 400 nm. In addition, the absorptions are observed at the wavelength of 660 nm and 780 nm for emerald-green color in water and ethanol or 930 nm for red-brown color in acetone and MEK. These absorptions are used to confirm the existence of the $\{\text{Ta}_6\text{Br}_{12}\}^{2+}$ species and $\{\text{Ta}_6\text{Br}_{12}\}^{3+/4+}$ species.

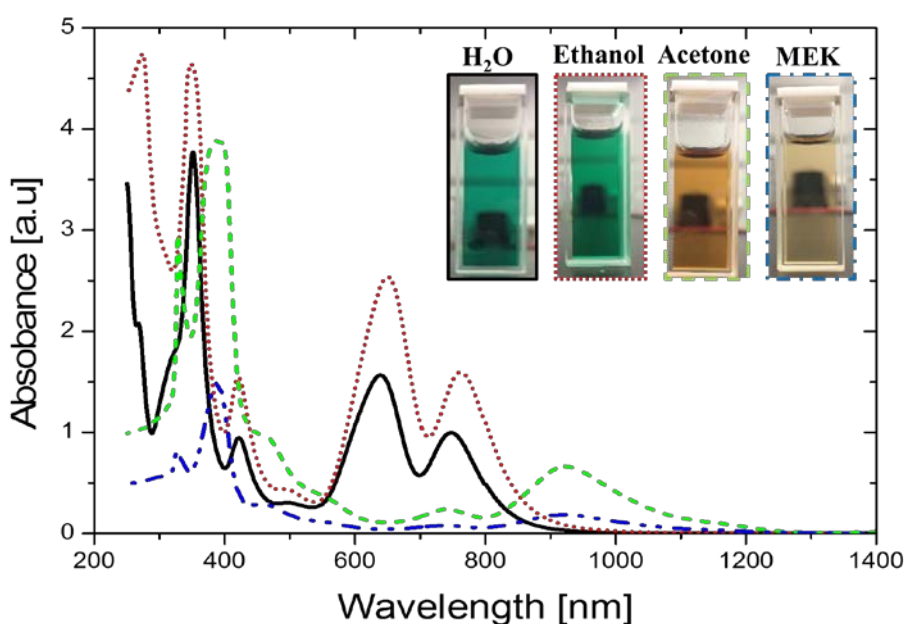


Figure. 5.2. The photos of the different colored suspensions prepared from different solvents and their optical characteristics by UV-Vis absorption spectra.

The obtained suspensions containing the $\{\text{Ta}_6\text{Br}_{12}(\text{H}_2\text{O})^a_6\}\text{Br}_2$ cluster were used to fabricate the Ta_6 film on ITO glass as the electrodes (**Fig. 5.3**) by the EPD process. It can be seen that the deposition is performed on cathode or anode depending on the nature of the dispersing medium. All the suspensions required the applied voltage at 15 V for 30 s to form the Ta_6 -cluster deposit on the ITO glass electrode. In the case of the water and ethanol solutions, only the appearance of metallic film on cathode was recognized at 15 V for 30 s even though the emerald-green color suspensions were used. However, the specific signs which are originated from the $\{\text{Ta}_6\text{Br}_{12}\}^{2+}$ core species at the wavelength of 660 nm and 780 nm confirmed by the UV-Vis absorption spectra of the solutions, have not observed in the absorption spectra for the films (deposited on cathode) even though the zeta potential was positive for both the suspensions (**Fig. 5.3a**). At high concentration of water, strong reduction of the indium tin oxide occurs to reduce electron conduction of the ITO layer, which disturbs the moving direction of the

positive $\{\text{Ta}_6\text{Br}_{12}^i(\text{H}_2\text{O})^a_6\}^{2+}$ cluster particles to cathode. In addition, the gas generated on the surface of electrode prevents the coagulation of the particles.

In the case of acetone and MEK, the brown thin deposit films were observed on the ITO-coated glass by the anodic EPD process. Interestingly, the signs of the $\{\text{Ta}_6\text{Br}_{12}\}^{3+/4+}$ cluster species are presented as shown in the blue line (**Fig. 5.3b**) with the strong absorption at the wavelength of 400 nm and 890 nm. At low pH, the conversion of $\{\text{Ta}_6\text{Br}_{12}\}^{2+}$ ($\{\text{Ta}_6\text{Br}_{12}^i(\text{H}_2\text{O})^a_6\}\text{Br}_2$) to $\{\text{Ta}_6\text{Br}_{12}\}^{3+/4+}$ ($\{\text{Ta}_6\text{Br}_{12}^i(\text{H}_2\text{O})^a_6\}\text{Br}_{3/4}$) by air oxidation is fairly rapid [2], that reduces the coordination of water and metal atoms. In the nonaqueous media, the $\{\text{Ta}_6\text{Br}_{12}\}^{3+ \text{ or } 4+}$ cluster species are more stable than the $\{\text{Ta}_6\text{Br}_{12}\}^{2+}$ cluster species [2]. During the oxidation by air medium in slight acidic acetone medium, the OH anion is generated from the oxidation reaction of O_2 and H_2O molecules to coordinate with the Ta metal or replace the apical H_2O ligands that reverse the zeta potential on the surface of the cluster particle in the suspension. In addition, the hydrolysis of water involved in acetone or MEK strongly generate OH^- groups, replacing the apical water in the $\{\text{Ta}_6\text{Br}_{12}(\text{H}_2\text{O})_6\}\text{Br}_n$ (brown) to form the $\{\text{Ta}_6\text{Br}_{12}^i(\text{H}_2\text{O})^{a-6-x}(\text{OH})^a_x\}\text{Br}_{n-x}$ ($n = 2, 3, 4$). It means that the $\{\text{Ta}_6\text{Br}_{12}^i(\text{H}_2\text{O})^{a-6-x}(\text{OH})^a_x\}$ cluster could exist as the negatively charged state. It can be seen that the value of the zeta potential is slightly positive for original acetone and MEK suspensions. As the result, only $\{\text{Ta}_6\text{Br}_{12}^i(\text{H}_2\text{O})^{a-6-x}(\text{OH})^a_x\}^{n-x}$ ($n = 2, 3, 4$) anions would move to the anode under the application of the electric field. At the anode, the protons created at the surface of the electrode would neutralize the cluster anion to form an $\{\text{H}_3\text{O}\}_x \cdot n\{\text{Ta}_6\text{Br}_{12}^i(\text{H}_2\text{O})^{a-6-x}(\text{OH})^a_x\}$ ($n = 2, 3, 4$) neutral ion pair. Then, the $\{\text{H}_3\text{O}\}_x \cdot n\{\text{Ta}_6\text{Br}_{12}^i(\text{H}_2\text{O})^{a-6-x}(\text{OH})^a_x\}$ ($n = 2, 3, 4$) clusters would transform to the stable state of $\{\text{Ta}_6\text{Br}_{12}^i(\text{H}_2\text{O})^{a-6-x}(\text{H}_2\text{O})^a_x\} \cdot y\text{H}_2\text{O}$ ($n = 2, 3, 4$) clusters and would be immobilized on the surface of the ITO glass. In the case of n value is 2, the cluster would contain the $\{\text{Ta}_6\text{Br}_{12}\}^{2+}$ core which could be oxidized to form $\text{Ta}_6\text{Br}_{12}\}^{3+/4+}$ core at the anode at low pH value. Similar mechanism of the deposition of the $\{\text{Mo}_6\text{Br}_8^i(\text{Br}^a)_4(\text{H}_2\text{O})_2\}$ cluster have been proven in our previous work [18]. This result agrees with the absorption spectrum of the brown suspension. This mechanism well explains the fabrication of the Ta_6 cluster film by the EPD process. However, the expectation is to fabricate the green film containing the $\{\text{Ta}_6\text{Br}_{12}\}^{2+}$ cluster species. The detail mechanism of the deposition of the Ta_6 cluster film in aqueous and non-aqueous medium by EPD process should be investigated in near future.

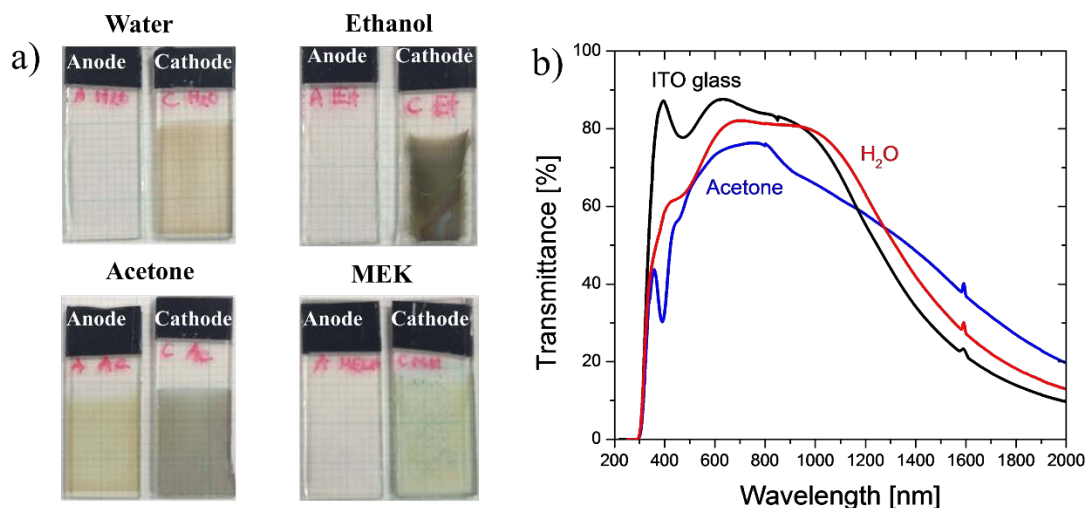


Figure 5.3. a) Deposition of the Ta₆ cluster film on ITO glass as both electrodes, and b) the UV-Vis absorption spectra of the Ta₆ cluster film prepared from different dispersing medium.

5.2.2. Optimization of the ratio of the {Ta₆Br₁₂ⁱ(H₂O)^a}₆Br₂ cluster and water in EPD suspension

It is realized that the existence of water can retain the emerald-green color for the {Ta₆Br₁₂}²⁺ cluster species and acetone is a good dispersing medium in order to fabricate the octahedral cluster film by the EPD process^[19]. The ratios of the {Ta₆Br₁₂(H₂O)^a}₆Br₂ cluster particles and water in acetone solution were optimized to obtain the homogeneous suspensions (**Fig. 5.4a**).

The concentration of the water is limited to use in the EPD process due to the gas generation at the anode and cathode by the electrolysis of water under the application of the electric field. The color of the solution and solubility of the {Ta₆Br₁₂(H₂O)^a}₆Br₂ cluster particles in the dispersing medium depends on the ratio of the Ta₆ cluster with water. It can be observed that S1-H15 is the critical ratio to retain the emerald-green of the {Ta₆Br₁₂}²⁺ cluster species and large amount of the cluster were still not dissolved (not shown here). For this reason, the suspension with the H20 ratio is selected as the suitable ratio to prepare the EPD suspension.

The deposition of the Ta₆ cluster was observed on the cathodic ITO glass electrode at 10 V for 60 s. The zeta potential and electric conductivity of S1-H20 are 1.13 (±0.04) mV and 2.49± (0.07) mS/cm, respectively. These values are close to those of the suspension in acetone. As the result, 0.2 ml of water was enough to support the complete dissolution of 10 mg Ta₆ cluster in 10 ml acetone solution. However, the green-colored film exhibiting the deposition of the {Ta₆Br₁₂}²⁺ core cluster species was interestingly obtained by the cathodic EPD process.

Figure 5.4b (upper) shows the surface morphology of the {Ta₆Br₁₂}²⁺ cluster film prepared from the suspensions (concentration of 1 g per litre) with different concentrations of acetone and water. It can be seen that the surface of S1-H20 film is condensed while some crack lines appear in the S1-H25 film. Interestingly, the obviously porous film consisting of flat lamellar is observed for the film prepared from S1-H50 suspension. By increasing the concentration of water, the cracking formation and

recrystallization of the Ta₆ cluster occur.

The S0.7 suspension was prepared by adding more acetone than S1 suspension to reduce the particle size. In all the S0.7 deposit films, it can be seen that the granular-shaped particles as discrete entity are essentially immobilized on the surface accompanying with continual phase (**Fig. 5.4b bottom**). Obviously, the lamellar pieces in the S0.7-H50 film were obviously replaced by condensable crystal packaging.

By adding small amounts of water in acetone, the {Ta₆Br₁₂}²⁺ core species will strongly be hydrated to improve the hydrogen bonds between the {Ta₆Br₁₂(H₂O)^a₆}²⁺ cluster particles, resulting the retention of the green color of the suspension, similarly to the dissolution in water. The {Ta₆Br₁₂(H₂O)^a₆}²⁺ cluster surrounded by water molecules will create the hydrogen bonds with H₂O molecules coordinating to neighbor {Ta₆Br₁₂(H₂O)^a₆}²⁺ clusters ^[11]. As the result, the {Ta₆Br₁₂(H₂O)^a₆}²⁺ cluster crystal will be strongly broken by the hydration in H₂O medium. However, the small cluster particles could exist through the hydrogen bond bridges with neighbor particles. It reduces the recognition of the Stern-layer on the surface or the zeta potential of the cluster particles (low positive zeta potential in water). In acetone medium, the hydrated cluster particles will separate by acetone molecules and reduce the agglomeration. For example, the S1-H20 suspension needed to be sonicated for 40 min to dissolve all the clusters in the solvent medium while only for 30 min to prepare the S1-H50 suspension. The formation of the green Ta₆ film on cathode indicates that the {Ta₆Br₁₂(H₂O)^a₆}²⁺ cluster always retain the positive charges on the surface during the EPD process. The role of water is to improve the dissolution and stabilization of the positive charges on the surface of the {Ta₆Br₁₂(H₂O)^a₆}²⁺ cluster particles while acetone contributes to the good processability of the EPD process. The detail mechanism of the deposition is still necessary. However, it must be noted that the green color of the film changed to red-brown color probably due to the oxidation after drying for several days. The loss of water partially causes the oxidation of the green-colored {Ta₆Br₁₂(H₂O)^a₆}²⁺ clusters film.

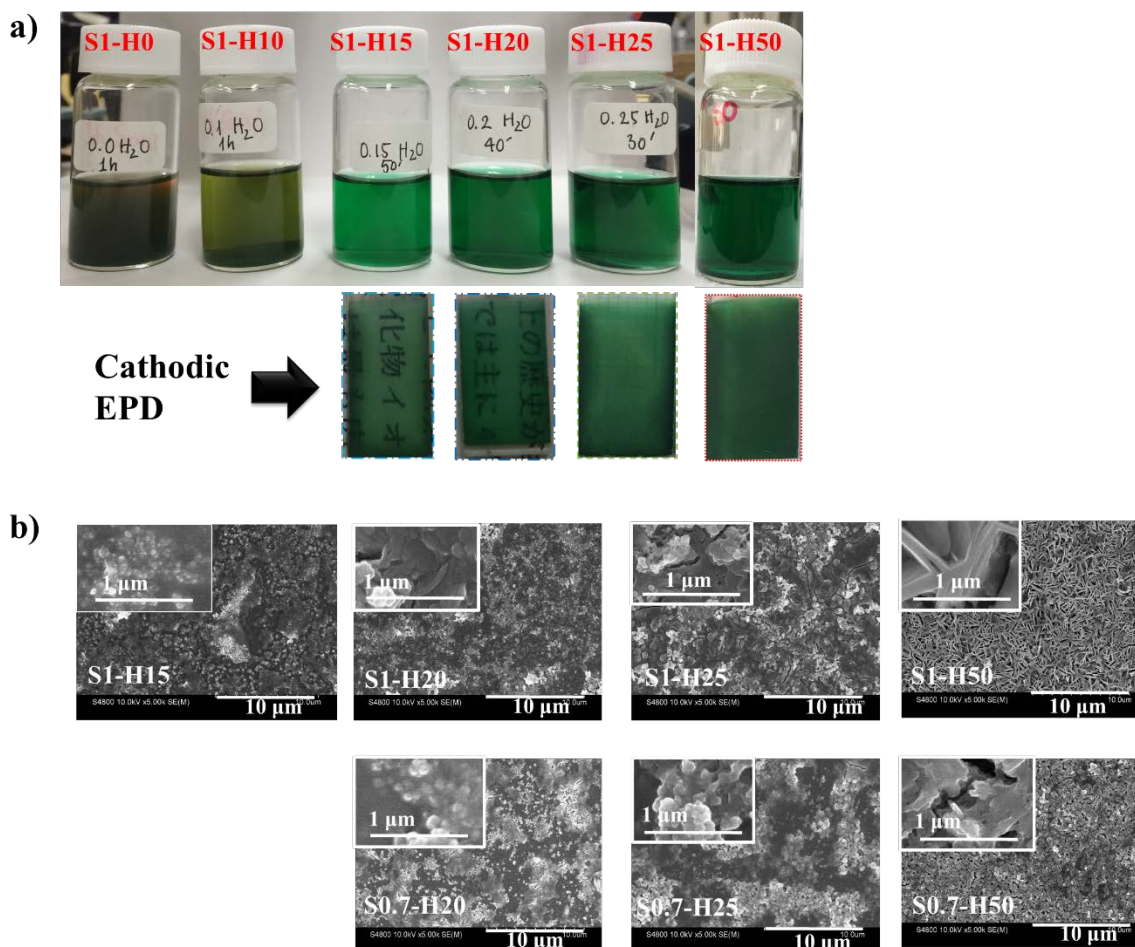


Figure 5.4. a) The obtained color and solubility of the suspension depend on the ratio of $\{\text{Ta}_6\text{Br}^{i}_{12}(\text{H}_2\text{O})^a_6\}^{2+}$ clusters and water in acetone solution and b) the SEM images of the $\{\text{Ta}_6\text{Br}^{i}_{12}(\text{H}_2\text{O})^a_6\}^{2+}$ green cluster film on the ITO glass by the cathodic EPD process at 10 V for 60 sec.

In order to confirm the existence of the $\{\text{Ta}_6\text{Br}^{i}_{12}(\text{H}_2\text{O})^a_6\}^{2+}$ core cluster species, the measurement of the UV-vis absorption was performed for all the Ta_6 cluster films listed in **Table 5.2**. The spectra show the specific absorption bands of the $\{\text{Ta}_6\text{Br}_{12}\}^{2+}$ core species at the wavelength of 760, 650 nm and under 500 nm (**Fig. 5.5a**). At high water concentration (S1-H50), the transmittance of the cluster film becomes low and a little absorption appears at the wavelength of 890 nm which is ascribed to the $\{\text{Ta}_6\text{Br}_{12}\}^{3+/4+}$ core species. This result agrees with the existence of the obvious lamellar crystals recognized in SEM image (**Fig. 5.4b**). The S1-H20 film presents the positive transmittance without the sign of the existence of $\{\text{Ta}_6\text{Br}_{12}\}^{3+/4+}$ core species. The decrease of the concentration of the cluster in the dispersing medium makes the improvement of the transmittance and absorption ability as shown in the spectra of S0.7 suspension. The S0.7-H20 can obtain the transmittance higher than 60 %, exhibiting a good property for the application of the UV-Vis blocker film. In summary, the water can improve the solubility and processability of the green $\{\text{Ta}_6\text{Br}^{i}_{12}(\text{H}_2\text{O})^a_6\}^{2+}$ cluster film by selecting the suitable ratio of H_2O and cluster as 20:1. At the ratio of 50:1, water can accelerate the oxidation of the cluster or quick

diffusion of oxygen medium during the sonication due to easy hydration of the Ta₆ clusters.

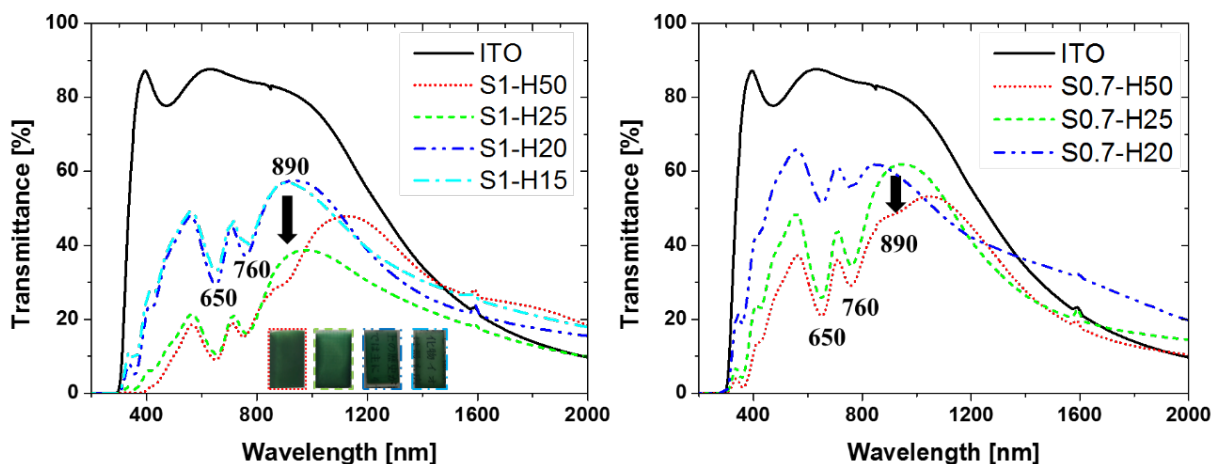


Figure 5.5. The optical absorption spectra of the film prepared from the suspension containing the $\{\text{Ta}_6\text{Br}_{12}(\text{H}_2\text{O})_6\}^{2+}$ cluster concentration of 1 g/l and 0.7 g/l in different dispersing medium. The films were deposited at 10 V for 60 s.

5.2.3. Optimization of the EPD process to fabricate $\{\text{Ta}_6\text{Br}_{12}(\text{H}_2\text{O})_6\}^{2+}$ cluster film

Figure 5.6 shows the morphology change of the Ta films with different applied voltages at a fixed deposition time for 60 s. In the case of S1-H20 suspension, the coagulation of the $\{\text{Ta}_6\text{Br}_{12}(\text{H}_2\text{O})_6\}^{2+}$ cluster particles of which size is smaller than 100 nm in the film is realized by SEM measurement. The homogeneity of the morphology is improved by increasing the applied voltage, followed by the increase of the coagulation to form big cluster particles. The uniformity of the particle size of the $\{\text{Ta}_6\text{Br}_{12}(\text{H}_2\text{O})_6\}^{2+}$ clusters deposited from the S0.7-H20 suspension is improved with the intercalation of the homogeneous phase containing a lot of the tiny clusters. In addition, at higher applied voltage, the surface become flat by dense packing tiny clusters.

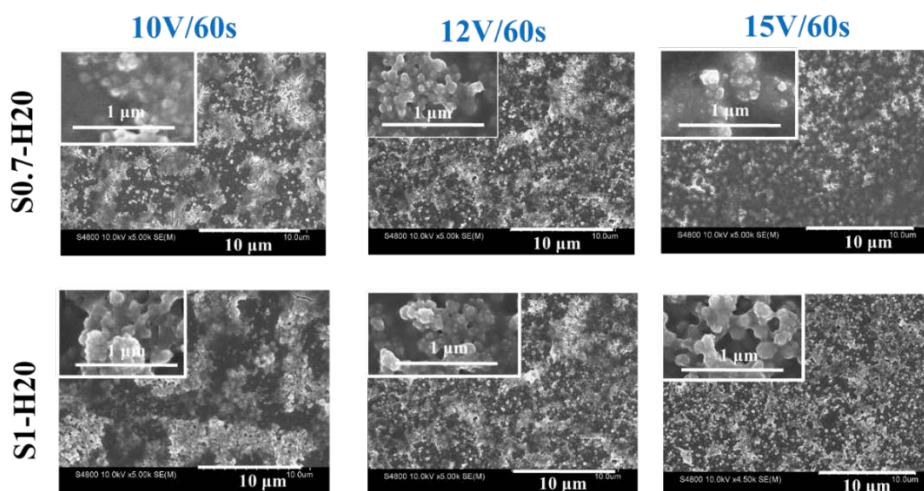


Figure 5.6. The SEM images of the $\{\text{Ta}_6\text{Br}_{12}(\text{H}_2\text{O})_6\}^{2+}$ green cluster film with the concentration of 1 g/l and 0.7 g/l, deposited at different voltages for 60 sec in different dispersing mediums.

The influence of the applied voltage for the fabrication of the green $\{Ta_6Br_{12}(H_2O)_6\}^{2+}$ cluster film is clearly evaluated by the UV-Vis spectroscopy. **Figure 5.7** presents the absorption of the $\{Ta_6Br_{12}(H_2O)_6\}^{2+}$ cluster film prepared at different applied voltages for 60 s. The increase of the applied voltage causes the reduction of the transmittance for both of the concentrations. The absorption of the $\{Ta_6Br_{12}(H_2O)_6\}^{2+}$ cluster film prepared from S.07-H20 suspension shows better relative transmittance but the absorption intensity is not significantly changed.

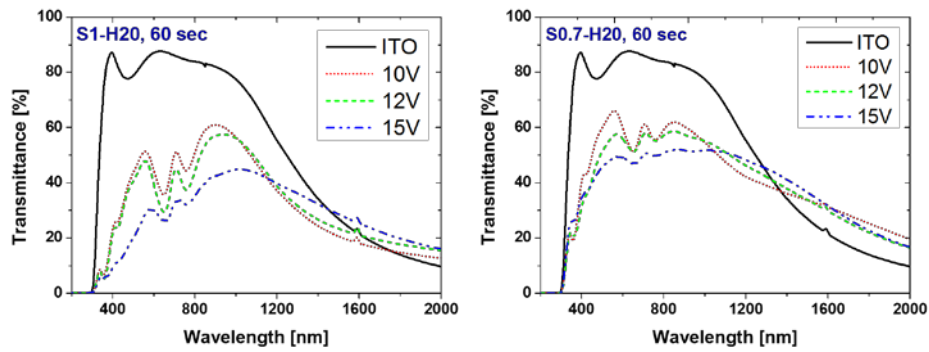


Figure 5.7. The optical absorption spectra of the films prepared from the suspension containing the $\{Ta_6Br_{12}(H_2O)_6\}^{2+}$ cluster concentration of 1 g/l and 0.7 g/l in different dispersing medium. The films were deposited at different voltages for 60 s.

Based on the results, 10 V is the most suitable applied voltage to obtain high transmittance. The deposition time to fabricate the green $\{Ta_6Br_{12}(H_2O)_6\}^{2+}$ cluster film was optimized from 30 s to 60 s. The UV-Vis absorption of the $\{Ta_6Br_{12}(H_2O)_6\}^{2+}$ cluster film prepared at 10 V for different deposition time is shown in **Figure 5.8**. The absorption curves are insignificantly changed for all the $\{Ta_6Br_{12}(H_2O)_6\}^{2+}$ cluster films prepared at any deposition time. However, all Ta_6 cluster films prepared from the S.07-H20 suspension still give the transmittance better than that from S01-H20 suspension.

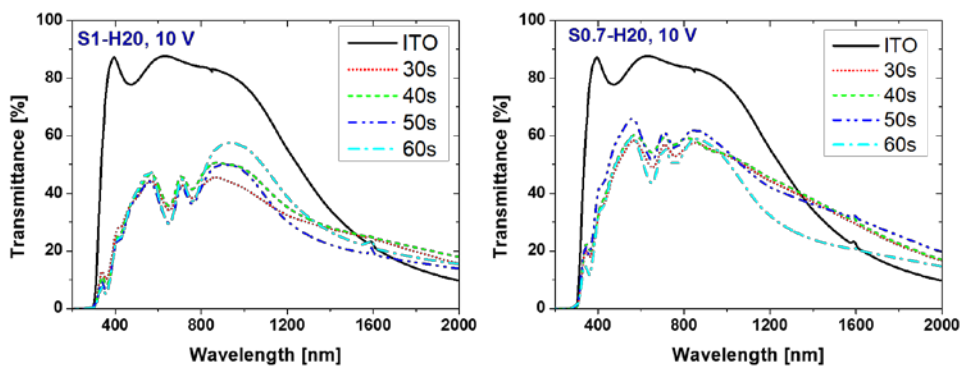


Figure 5.8. The optical absorption spectra of the films prepared from the suspension containing the $\{Ta_6Br_{12}(H_2O)_6\}^{2+}$ cluster concentration of 1 g/l and 0.7 g/l in different dispersing medium. The films were deposited at 10 V for different deposition time.

Summary

The green $\{\text{Ta}_6\text{Br}_{12}\}^{2+}$ core cluster films have successfully been fabricated by the cathodic EPD process. A major emphasis in this work is to prepare the green-colored $\{\text{Ta}_6\text{Br}_{12}\}^{2+}$ cluster suspension without being oxidized. The water plays an important role to enhance the dissolution of the $\{\text{Ta}_6\text{Br}_{12}(\text{H}_2\text{O})_6\}^{2+}$ cluster in dispersing medium and retain the positive charge of the $\{\text{Ta}_6\text{Br}_{12}(\text{H}_2\text{O})_6\}^{2+}$ cluster during the EPD process. The applied voltage and deposition time were optimized to obtain the uniform $\{\text{Ta}_6\text{Br}_{12}(\text{H}_2\text{O})_6\}^{2+}$ cluster film exhibiting high transmittance. However, the oxidation stability of the green-colored $\{\text{Ta}_6\text{Br}_{12}\}^{2+}$ cluster film was not maintained for a long time. The green-colored $\{\text{Ta}_6\text{Br}_{12}(\text{H}_2\text{O})_6\}^{2+}$ film was probably transferred to brown color due to the formation of the $\{\text{Ta}_6\text{Br}_{12}\}^{3+/4+}$ core species though the oxidation in an open air. The next step in this work is to improve the oxidation prevention by using polymer as stabilizing medium.

5.3. Fabrication of the $\{\text{Ta}_6\text{Br}_{12}(\text{H}_2\text{O})_6\}^{2+}$ @PVP film by EPD process

In order to improve the oxidation stability of the green-colored $\{\text{Ta}_6\text{Br}_{12}(\text{H}_2\text{O})_6\}^{2+}$ cluster film in ambient atmosphere after the EPD process, polyvinylpyrrolidone (PVP) was used to blend to the $\{\text{Ta}_6\text{Br}_{12}(\text{H}_2\text{O})_6\}^{2+}$ cluster suspension. The parameters to prepare the comparative Ta_6 film were presented in **Table 5.4**. All the deposited Ta_6 films were characterized by SEM and UV-Vis absorption measurements.

Table 5.4. The parameters of the suspension and EPD process to prepare the Ta_6 cluster film.

Suspension	Concentration	EPD
Brown: ($\{\text{Ta}_6\text{Br}_{12}(\text{H}_2\text{O})_6\}^{3+/4+}$)	~ 0.01 g Ta_6 /15 ml Acetone	25 V, 60 s
Green: ($\{\text{Ta}_6\text{Br}_{12}(\text{H}_2\text{O})_6\}^{2+}$)	S0.7-H20	15 V, 60 s
Green@PVP: ($\{\text{Ta}_6\text{Br}_{12}(\text{H}_2\text{O})_6\}^{2+}$) + PVP	10 ml S1-H20 5 ml (2 g PVP/ml acetone)	30 V, 30/ 60/ 90 s

Figure 5.9 shows the surface morphology observed high resolution SEM for the brown-cluster film, green-cluster film and green-cluster@PVP film deposited at different EPD parameters. While the green-cluster film and brown-cluster film still display the Ta_6 cluster crystal smaller than 1 μm , the green-cluster@PVP film shows the flat and homogeneous surface without clear appearance of the Ta_6 cluster crystals. In addition, the photos of the green-cluster@PVP film at the different EPD parameters also show the dark green color and excellent transmittance. These results indicate the efficiency of the PVP polymer mixture for the fabrication of the green film containing the $\{\text{Ta}_6\text{Br}_{12}(\text{H}_2\text{O})_6\}^{2+}$ clusters.

The thickness of the green and brown films, which is about 0.5 μm (**Fig. 5.9 a**) and 1 μm (**Fig. 5.9 b**), respectively, is recognized by cross section SEM images. The thickness of the green-cluster@PVP film is about 1.8 μm by the deposition at 30 V for 30 s (**Fig. 5.9 c**). When the deposition time increase to the 90 s, the thickness of the green-cluster@PVP film is saturated at 3.3 μm (**Fig. 5.9 c**).

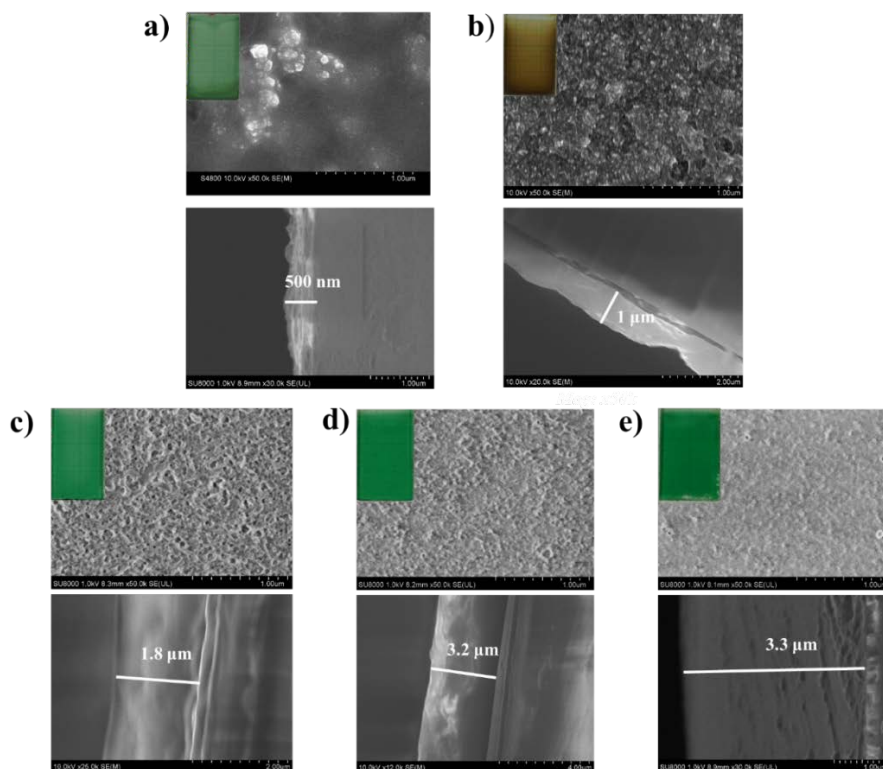


Figure 5.9. The morphology and cross section images by high resolution SEM measurement of: a) the $(\{\text{Ta}_6\text{Br}^{i}_{12}(\text{H}_2\text{O})_6\}^{2+})$ green-cluster films (15 V, 60 s), b) the $(\{\text{Ta}_6\text{Br}^{i}_{12}\}^{3+/4+})$ brown-cluster film (25 V, 60 s), c) the $(\{\text{Ta}_6\text{Br}^{i}_{12}(\text{H}_2\text{O})_6\}^{2+})$ green-cluster@PVP film prepared at 30 V for 30 s, d) the $\{\text{Ta}_6\text{Br}^{i}_{12}(\text{H}_2\text{O})_6\}^{2+}$ green-cluster@PVP film prepared at 30 V for 60 s, and e) the $\{\text{Ta}_6\text{Br}^{i}_{12}(\text{H}_2\text{O})_6\}^{2+}$ green-cluster@PVP film prepared at 30 V for 90 s.

The role of the PVP polymer as an agent to improve the dispersion of the $\{\text{Ta}_6\text{Br}^{i}_{12}(\text{H}_2\text{O})_6\}\text{Br}_2$ in the acetone medium is clearly recognized in the XRD patterns (**Fig. 5.10**). The layers of the Ta_6 cluster films are enough thick not to exhibit the XRD pattern of the ITO glass. The relatively uniform brown Ta_6 film gives the XRD pattern at 2θ angles of 10° and 17° specified for the tiny crystals. The green-cluster film appears a shape peak at 2θ angle of 10° with high intensity specified for detectable amounts of small crystals. However, this peak disappears in the XRD diagram of the green-cluster@PVP film. In the PVP medium, the coagulation of the Ta_6 cluster reduces and the occurrence of some kind of interaction between the cluster and PVP chains is suggested.

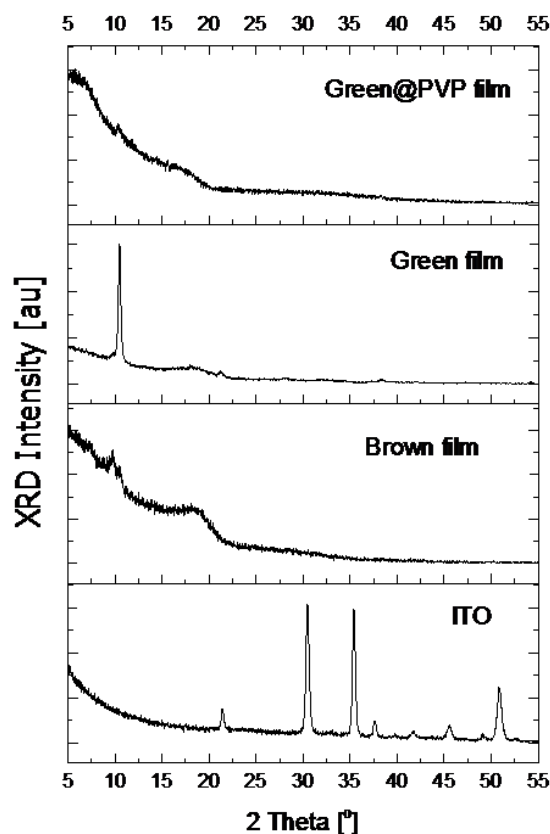


Figure 5.10. The XRD patterns of the brown film, green film and green-cluster @PVP film.

The chemical element ratios of the Br and Ta atoms in the brown-cluster, green-cluster and green-cluster @PVP films by EDX measurement are shown in **Table 5.5**. The result is the average value measured from 5 random positions on the films. Generally, the theoretical ratio of the $\{\text{Ta}_6\text{Br}_{12}^i(\text{H}_2\text{O})_6^a\}\text{Br}_2$ cluster should be about 2.33. However, the obtained ratio value for the T_6 cluster powder by EDX measurement is slightly different, which is about 2.16. The possible reason is that the residual salt based on tantalum metal still exists after the purification of the synthesizing process. The ratio value in the brown-cluster film is indicated as about 2.31. This result is reasonable because beside the deposition of the $\{\text{Ta}_6\text{Br}_{12}^i(\text{H}_2\text{O})_6^a(\text{OH})_x^a\}^{n-x}$ ($n = 3, 4$) cluster on anode, the Br^- ion also is gathered on the anode under the electric field. On the other hand, the deposition of the green $\{\text{Ta}_6\text{Br}_{12}^i(\text{H}_2\text{O})_6^a\}^{2+}$ cluster film on cathode shows the ratio value lower than 2. It is suggested that there is a simultaneous deposition of the Ta cation from residual tantalum salt. Interestingly, this ratio in the green-cluster @PVP film is opposite with the behavior of the green-cluster film, corresponding to the value of about 2.27 (± 0.21).

H. M. Kamari et al. ^[20] gave a suggestion about the possible interaction of the zinc ferrite nitrate with polyvinylpyrrolidone (PVP): The pyrrolidone group always exists an electrostatic ion pair, negative charge on O atom and positive on N atom. During the diffusion of the $\{\text{Ta}_6\text{Br}_{12}^i(\text{H}_2\text{O})_6^a\}\text{Br}_2$ cluster in the PVP medium, similarly, the ion interaction between the $\{\text{Ta}_6\text{Br}_{12}^i(\text{H}_2\text{O})_6^a\}^{2+}$ with negative polar on O atom and Br anion with positive polar on N atom may exist too.

Table 5.5. The atomic ratio of bromide and tantalum by EDX measurement.

Sample	Atomic ratio (%Br/%Ta)
Theoretical index: $\{\text{Ta}_6\text{Br}_{12}^i(\text{H}_2\text{O})_6^a\}\text{Br}_2$	2.33
Ta ₆ cluster: $\{\text{Ta}_6\text{Br}_{12}^i(\text{H}_2\text{O})_6^a\}\text{Br}_2$	2.16 ± 0.11
Brown film: $(\{\text{Ta}_6\text{Br}_{12}^i(\text{H}_2\text{O})_6^a\}^{3+/4+})$	2.31 ± 0.05
Green film: $(\{\text{Ta}_6\text{Br}_{12}^i(\text{H}_2\text{O})_6^a\}^{2+})$	1.77 ± 0.15
Green@PVP film1: $(\{\text{Ta}_6\text{Br}_{12}^i(\text{H}_2\text{O})_6^a\}^{2+})$	2.27 ± 0.21

The optical absorption bands of the brown-cluster film, green-cluster film and green-cluster @PVP film fabricated at different EPD parameters are presented in **Figure 5.11**. The green-cluster and brown-cluster films give similar optical properties compared with the brown-cluster and green-cluster suspension (**Fig. 5.2**). However, the transformation of the optical absorption bands of the green-cluster film is realized from green line to green dot line (**Fig. 5.11a**) after storing 4 days in air. The absorption peaks at the wavelength of 660 nm and 740 nm ascribed to the $\{\text{Ta}_6\text{Br}_{12}\}^{2+}$ core species disappear; that is replaced by absorption peak ascribed to the $\{\text{Ta}_6\text{Br}_{12}\}^{3+/4+}$ core species at the wavelength of 890 nm. Interestingly, these phenomena have not occurred in the green-cluster@PVP film after the storage during the same period. In addition, the transmittance and absorption intensity of the green-cluster@PVP film are excellent accompanying with the wavy curves in the infrared wavelength range. The phenomena has also been observed in the case of the Mo₆ cluster films ^[18]. It should be noted that the wavy curves appear only when the film obtains excellent transmittance originated from the interference of the incident light and diffraction light between the top of ITO layer and the surface of the Ta₆ film. The transformation of the core species from $\{\text{Ta}_6\text{Br}_{12}\}^{2+}$ to $\{\text{Ta}_6\text{Br}_{12}\}^{3+/4+}$ have not been realized in the optical absorption. This result proves that the PVP play an important role to prevent the oxidation reactions in ambient atmosphere or limit the diffusion of oxygen into the composite networks. The green-cluster@PVP films with different thickness synthesized by changing the EPD conditions give different optical property as presented in **Figure 5. 11b**. The increase of the deposit time makes the enhancement of the oxidation of the $\{\text{Ta}_6\text{Br}_{12}\}^{2+}$ core cluster, contributing to the appearance of the absorption band at the wavelength of 890 nm in dot line (60 s) and dash line (90 s). Moreover, the transmittance of the films prepared by the deposition for 60 s and 90 s, even though higher thickness reduces, the Ta₆ film obtains the same absorbing intensity. For this result, the $\{\text{Ta}_6\text{Br}_{12}\}^{2+}$ core green-cluster@PVP film fabricated at 30 V for 30 s is selected as the optimal film with the excellent optical property.

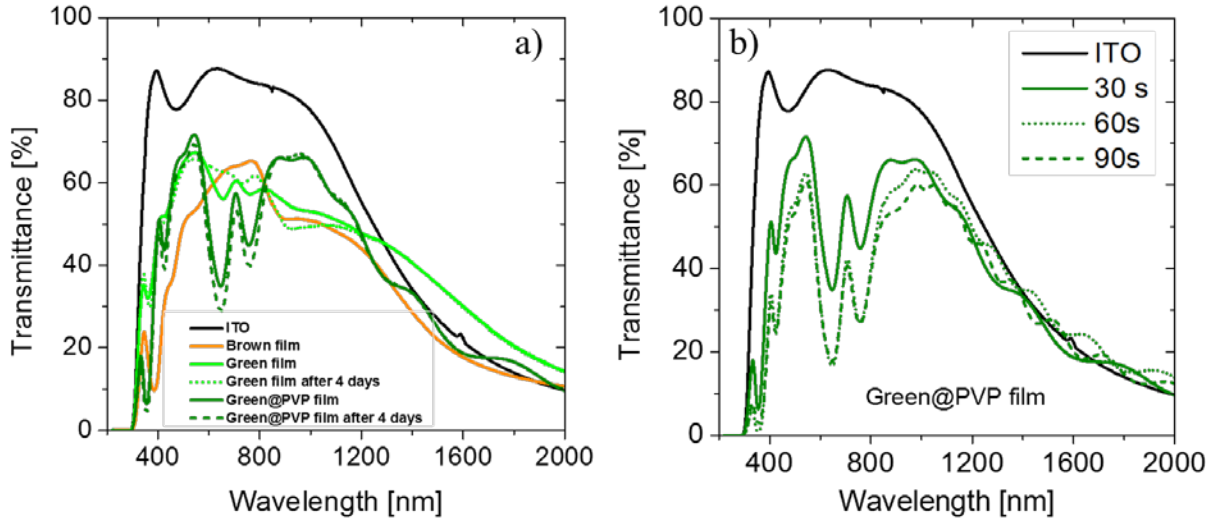


Figure 5.11. The UV-Vis absorption spectra of the brown film, green film and green@PVP film.

In order to evaluate the efficiency of the cluster coating as energy saving materials, different figure of merit (FOM) values, T_{vis} , T_{sol} , and T_{vis}/T_{sol} [21, 22] and the color coordinates (x , y , z and L^*a^*b) were calculated for each film (ITO, brown-cluster film and green-cluster film and green-cluster @PVP film). The solar transmittance, T_{sol} , is the integrated spectral transmittance of a window weighted with the normalized solar energy distribution spectrum. The visible transmittance, T_{vis} , was calculated in a similar way, but the solar transmittance is now weighted with the photonic response of the human eye. The FOM values are reported in **Table 5.6** and **Figure 5.12**.

T_{vis} and T_{sol} can be calculated by the following formula [23]

$$T_{vis}, T_{sol} = \frac{\int_{300}^{2500} T(\lambda) \times X(\lambda) \times d\lambda}{\int_{300}^{2500} X(\lambda) \times d\lambda}$$

Where T is the transmission spectrum as measured and X represents the Air Mass 1.5 (AM 1.5) which is equivalent to the spectrum of solar radiation after passing through 1.5 times the perpendicular atmospheric thickness in T_{sol} or the human eye spectral response in T_{vis} . The CIE Colorimetric System (the CIE 1931 with 10° Standard Observer from 1964 and D65 source) was used for color analysis.

The results for the color coordinates (x , y , z) of the green-cluster@PVP films are also shown in **Table 5.6** and **Figure 5.12**. For comparison, UV-vis-NIR spectra and FOM values for green-cluster@PVP films after several weeks of exposure in air are shown in **Table 5.7**. The green-cluster@PVP film clearly has a high impact in terms of the T_{sol} with a small increase in the ratio T_{vis}/T_{sol} . Thus, the incorporation of PVP into the green-cluster film is clearly beneficial for the optical properties with a T_{vis}/T_{sol} ratio equal to 1.25. The deposition process was also performed on a 4x5 cm ITO glass substrate and the film showed a high transparency, which indicates the possible scalability of the EPD process.

Table 5.6. x, y, z color coordinates and FOM values of the ideal blocker, ITO glass substrate and the brown-cluster and green-cluster films.

Name	x	y	z	Tvis	Tsol	T _{vis} /T _{sol}
ITO 6-7 Ω/sq	0.318	0.340	0.342	87.6	76.2	1.15
Brown film 30V 60s	0.352	0.374	0.274	54.1	46.5	1.16
Green film 15V 60s	0.326	0.361	0.313	50.6	41.8	1.21
Green @PVP 30V 30s	0.296	0.359	0.345	62.7	50.0	1.25
GREEN@PVP 30V 60s	0.284	0.382	0.334	50.4	41.0	1.23
GREEN@PVP 30V 90s	0.287	0.383	0.330	48.9	39.1	1.25
Ideal blocker	0.314	0.331	0.355	90.0	48.7	1.85

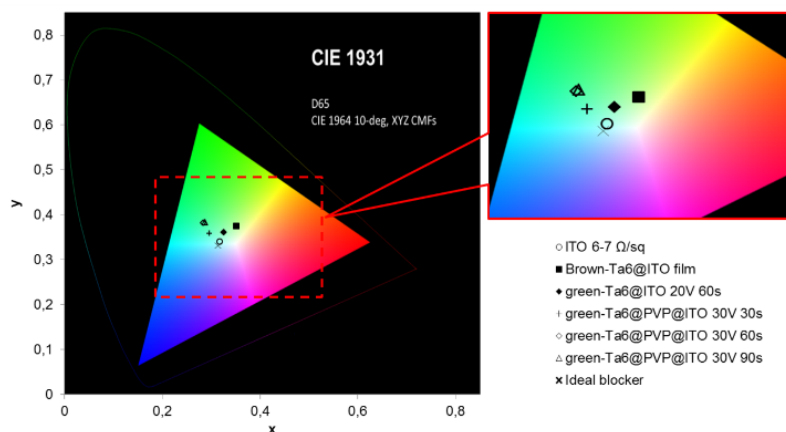


Figure 5.12. CIE chromaticity coordinates of the ideal blocker, ITO glass substrate and the brown-cluster and green-cluster films.

Table 5.7. FOM values for green-cluster film and green-cluster@PVP films after several weeks' exposure in air.

Name	x	y	z	Tvis	Tsol	T _{vis} /T _{sol}
Green film 15V 60s after several weeks	0.342	0.363	0.295	52.74	42.83	1.23
Green @PVP 30V 30s after several weeks	0.291	0.362	0.346	59.33	47.58	1.25
Green @PVP 30V 60s after several weeks	0.282	0.381	0.338	50.53	41.27	1.22
GREEN @PVP 30V 90s after several weeks	0.287	0.383	0.330	48.90	39.14	1.25

5.4. Conclusions

The green $\{Ta_6Br_{12}(H_2O)_6\}^{2+}$ cluster film has successfully been fabricated by the cathodic EPD process with the homogeneous EPD suspension prepared in the water and acetone solutions. The brown-cluster film prepared from the $\{Ta_6Br_{12}(H_2O)_6\}^{3+/4+}$ core cluster suspension in only acetone was obtained by the anodic EPD process. The PVP matrix plays an important role in retaining the green color for the deposition film or excellent preventing the oxidation of the $\{Ta_6Br_{12}(H_2O)_6\}^{2+}$ cluster in air medium.

References

1. F. W. Koknat, J. A. Parsons, and A. Vongvusharintra. Metal cluster halide complexes. I. efficient synthesis of hydrated hexanuclear niobium and tantalum cluster halides $M_6X_{14} \cdot 8H_2O$. *Inorg. Chem.*, **13**, 1699-1702, 1974.
2. B. G. Hughes, J. L. Meyer, P. B. Fleming, and R. E. Mccarley. Chemistry of polynuclear metal halides. iii. synthesis of some niobium and tantalum $[M_6X_{12}]^{2+}$ cluster derivatives. *Inorg. Chem.*, **9**, 1343-1346, 1970.
3. F. A. Cotton. Metal atom clusters in oxide systems. *Inorg. Chem.*, **3**, 1217-1220, 1964.
4. X. Zarate, E. Schott, L. A. Soto, and R. R. Tagle. A family of octahedral molybdenum cluster complexes $[Mo_6Cl_8(H_2O)_n(OH)_{6-n}]^{n-2}$ with $n = 0-6$ as a pH-sensors: A theoretical study. *Chem. Phys. Lett.*, **567**, 39-42, 2013.
5. D. J. Robbins, and A. J. Thomson. Magnetic circular dichroism spectra of the octahedral niobium and tantalum subhalide clusters $[M_6X_{12}]^{n+}$. *J. Chem. Soc., Dalton Trans.*, **0**, 2350-2364, 1972.
6. J. Knaeblein, T. Neufeind, F. Schneider, A. Bergner, A. Messerschmidt, J. Loewe, B. Steipe and R. Huber. $[Ta_6Br_{12}]^{2+}$, a tool for phase determination of large biological assemblies by x-ray crystallography. *J. Mol. Biol.*, **270**, 1-7, 1997.
7. T. Neufeind, A. Bergner, F. Schneider, A. Messerschmidt, and J. Knaeblein. The suitability of $Ta_6Br_{12}^{(2+)}$ for phasing in protein crystallography. *Biol. Chem.*, **378**, 219-221, 1997.
8. S. Cordier, F. Grasset, R. Boukherroub, N. Saito, H. Haneda, Y. Molard, S. Ravaine, M. Mortier, M. Amela-Cortes, and N. Ohashi. Inorganic molybdenum octahedral nanosized cluster units, versatile functional building block for nanoarchitectonics. *J. Inorg. Organomet. Polym.*, **25**, 189-204, 2015.
9. A. Renaud, F. Grasset, B. Dierre, T. Uchikoshi, N. Ohashi, T. Takei, A. Planchat, L. Cario, S. Jobic, F. Odobel, and S. Cordier. Inorganic molybdenum clusters as light-harvester in all inorganic solar cells: a proof of concept. *Chemistry Select*, **1**, 2284 – 2289, 2016.
10. A. Renaud, M. Wilmet, T. G. Truong, M. Seze, P. Lemoine, N. Dumait, W. Chen, N. Saito, T. Ohsawa, T. Uchikoshi, N. Ohashi, S. Cordier and F. Grasset. Transparent tantalum cluster-based UV and IR blocking electrochromic devices. *J. Mater. Chem. C*, **5**, 8160-8168, 2017.
11. A. V. Anyushin, M. N. Sokolov, E. V. Peresyphkina, and V. P. Fedin. Crystal structure of a tantalum cluster with tetraphenylborate-anion: $[Ta_6Br_{12}(H_2O)_6](BPh_4)_2 \cdot 4H_2O$. *J. Struct. Chem.*, **54**, 454-458, 2013.
12. D. N. T. Hay, and L. Messerle. Low-temperature, high yield synthesis, and convenient isolation of the high-electron-density cluster compound $Ta_6Br_{14} \cdot 8H_2O$ for use in biomacromolecular crystallographic phase determination. *J. Structural Biol.*, **139**, 147-151, 2002.
13. M. Vojnovi, S. Antoli, B. Kojik-Prodit, N. Brnizevi, M. Miljak, and I. Aviani. Reactions of hexanuclear niobium and tantalum halide clusters with Mercury(II) Halides. I synthesis and structures of the semiconducting compounds $[M_6Br_{12}(H_2O)_6][HgBr_4] \cdot 12H_2O$, $M = Nb, Ta$. *Z. Anorg. Allg. Chem.*, **623**, 1247-1254, 1997.
14. U. Beck, A. Simon, S. Sirac, and N. Brneevik. Crystal structures of trans- $[Ta_6Cl_{12}(OH)_4(H_2O)_2]$.

- 10 H₂O and (NMe₄)₂[Ta₆Cl₁₂(OH)₆]. 21 H₂O. *Z. Anorg. Allg. Chem.*, **623**, 59-64, 1997.
15. N. E. Cooke, T. Kuwana, and J. Espension. Electrochemistry of tantalum bromide cluster compound. *Inorg. Chem.*, **5**, 1081-1083, 1971.
16. M. Vojnovic, N. Brnicevica, I. Basica, P. Planinica, and G. Giesterb. The cocrystallization of the Cubic [Ta₆Br₁₂(H₂O)₆][CuBr₂X₂]·10H₂O and Triclinic [Ta₆Br₁₂(H₂O)₆]X₂·trans-[Ta₆Br₁₂(OH)₄(H₂O)₂]·18H₂O (X=Cl, Br, NO₃) phases with the coexistence of [Ta₆Br₁₂]²⁻ and [Ta₆Br₁₂]⁴⁻ in the Latter. *Z. Anorg. Allg. Chem.*, **628**, 401-408, 2002.
17. C. B. Thaxtox, and R. A. Jacobson. The crystal structure of H₂[Ta₆Cl₁₈].6H₂O. *Inorg. Chem.*, **10**, 1460-1463, 1971.
18. T. K. N. Nguyen, B. Dierre, F. Grasset, A. Renaud, S. Cordier, P. Lemoine, N. Ohashi, and T. Uchikoshi. Formation mechanism of transparent mo₆ metal atom cluster film prepared by electrophoretic deposition. *J. The Electrochemical Soc.*, **164**, 412-418, 2017.
19. T. K. N. Nguyen, F. Grasset, B. Dierre, C. Matsunaga, S. Cordier, P. Lemoine, N. Ohashi, and T. Uchikoshi. Fabrication of transparent thin film of octahedral molybdenum metal clusters by electrophoretic deposition. *ECS J. Solid State Sci. and Tech.*, **5**, 178-186, 2016.
20. H. Mohamed Kamari, M. G. Naseri, and E. B. Saion. A novel research on behavior of zinc ferrite nanoparticles in different concentration of poly(vinyl pyrrolidone) (PVP). *Metals*, **4**, 118-129, 2014.
21. N. L. Stokes, A. M. McDonagh, J. A. Edgar, and M. B. Cortie. Spectrally selective coatings of gold nanorods on architectural glass. *J. Nanopart. Res.*, **12**, 2821-2830, 2010.
22. M. Carboni, M. Carravetta, X. L. Zhang, and E. Stulz. Efficient NIR light blockage with matrix embedded silver nanoprism thin films for energy saving window coating. *J. Mater. Chem. C*, **4**, 1584-1588, 2016.
23. G. B. Smith. C. A. Deller. P. D. Swift. A. Gentle. P. D. Garrett, and W. K. Fisher. Nanoparticle-doped polymer foils for use in solar control glazing. *J. Nanopart. Res.*, **4**, 157-165, 2002.

Chapter 6

Conclusions and outlooks

Chapter 6

Conclusions and outlooks

6.1. Conclusions

In this thesis, the main theme is to perform basic research focuses on the fabrications and characterizations of nano-architecture materials based on metal atom cluster that is applicable to windows in building saving energy based on the optical and electrochromic properties. Metal atom cluster exhibits interesting photochemical and redox properties that are allocable in variety of fields, such as in energy, photo catalyst or biotechnology. In the first time, the processability of the octahedral Mo_6 and Ta_6 cluster film by the EPD process have been demonstrated through the detailed investigation of (i) the dispersion medium of the Mo_6 and Ta_6 cluster precursors or suspension parameters (pH, concentration, zeta potential, conductivity, etc.) and (ii) the parameters of the EPD process (deposition time, applied voltage, distance between electrodes, etc.) in order to obtain pure Ta_6 and Mo_6 cluster films exhibiting thin, transparent, homogeneous microstructure, and good optical properties.

Chapter 2

In this work, we did succeed the fabrication of thin, transparent and homogeneous films based on the derivations of the Mo_6 octahedral cluster units, such as, $\text{Cs}_2\text{Mo}_6\text{Br}_{14}$, $\text{TBA}_2\text{Mo}_6\text{Br}_{14}$, $(\text{NH}_4)_2\text{Mo}_6\text{Br}_{14}$, $\text{Cs}_2\text{Mo}_6\text{I}_{14}$, by the EPD process. The Mo_6 octahedral cluster film still retained the excellent optical properties by the optimization of the EPD suspension and EPD parameters. The formation mechanism of the Mo_6 octahedral cluster on ITO-coated glass by the EPD process was suggested from the analysis of their multilayered structure composed of the stacking of Br^- anions, $[\text{Mo}_6\text{Br}_8^i\text{Br}_4^a(\text{H}_2\text{O})_2]$ and $(\text{H}_3\text{O})_2[\text{Mo}_6\text{Br}_8^i\text{Br}_4^a(\text{OH})_2]$ cluster units in the absence of the original counter cations (Cs or $(n\text{-C}_4\text{H}_9)_4\text{N}$). The disappearance of the counter cation brought a new crystal pattern in the metal atom networks that makes an electron-state change, resulting the change in luminescence behavior compared with the original precursor.

Chapter 3

In order to improve the stabilization of the Mo_6 octahedral cluster film in ambient atmosphere, some polymers have been selected for coating or directly incorporating by the EPD process.

➤ Poly Dimethyl Siloxance (PDMS) with the viscosity of 1.5 and 2 centistocks (CS) was used as the top coating on the surface of the Mo_6 octahedral cluster film after the EPD process. The work resulted that the coating process was performed after the incubation time of 90 min after the EPD procedure. The incorporation of the PDMS have not affected to the homogeneity or optical property of the Mo_6 octahedral cluster film. The Mo_6 cluster film could be stabilized more than 6 months with the limitation of the crack hairlines.

➤ Poly methyl methacrylate (PMMA) and cellulose acetate phthalate (CAP) also were directly

blended with the $\text{Cs}_2\text{Mo}_6\text{I}_8(\text{OCOC}_2\text{F}_5)_6$ octahedral cluster in acetone medium to prepare the homogeneous EPD suspension. By using the EPD process at low voltage, thin and good transparent Mo_6 -cluster@polymer films were fabricated while maintaining the excellent luminescent property accompanied by highly hydrophobic property. The luminescent property of the $\text{Cs}_2\text{Mo}_6\text{I}_8(\text{OCOC}_2\text{F}_5)_6$ cluster was stabilized in the polymer matrix even after continuous exposure to the atmosphere medium of RH70% at 50°C for 1 month.

As the results, the chemical stabilization of the Mo_6 cluster in polymer would be a good solution to not only improve the processability of the Mo_6 cluster film by the EPD process but also enhance the mechanical property leading to a potential use for window application.

Chapter 4

Some of the good properties of the Mo_6 octahedral clusters including excellent luminescent property of $\text{Cs}_2\text{Mo}_6\text{Cl}_{14}$ and $\text{Cs}_2\text{Mo}_6\text{I}_8(\text{OCOC}_2\text{F}_5)_6$ was lost during the EPD process due to the poor stability of those cluster units in the suspension. In order to overcome this limitation, the Mo_6 octahedral cluster was encapsulated in hollow silica nanoparticles (HSNs).

➤ The introduction of the Mo_6 octahedral cluster ($\text{Cs}_2\text{Mo}_6\text{Cl}_{14}$ and $\text{Cs}_2\text{Mo}_6\text{I}_8(\text{OCOC}_2\text{F}_5)_6$) into the pores of the wall of the hollow silica nanoparticles was performed by the vacuum impregnation process (VIP) at room temperature with high efficiency. The results illustrated that a lot of the Mo_6 clusters were incorporated in the mesoporous hollow silica nanoparticles, which was confirmed by the TEM image. The strong interaction between the Mo_6 cluster and HSNs caused the strong luminescent property and retention of the optical property up to 200°C.

➤ The Mo_6 cluster@silica nanoparticle was used to prepare the nanocomposite film by the EPD process. The Mo_6 cluster@silica nanoparticles were dissolved in the iodine-acetone dispersing medium containing the poly ethylene imine (PEI). After optimizing the suspension and EPD parameters, the obtained homogeneous nanocomposite film gave out the luminescent property only in the case of the $\text{Cs}_2\text{Mo}_6\text{I}_8(\text{OCOC}_2\text{F}_5)_6$ cluster.

➤ The Mo_6 cluster@silica nanoparticle has been tried to fabricate the film by dip coating in the nitro cellulose-based suspension. The dip coat suspension is able to immobilize the Mo_6 cluster@silica nanoparticle on the soda lime glass while giving good hydrophobic property which is potential in the application of the insulation and UV blocking materials for window application.

Chapter 5

The success of the fabrication of the Mo_6 octahedral cluster film by the EPD process motivated the preparation of the octahedral cluster film based on the tantalum (Ta) metal ($[\text{Ta}_6\text{Br}_{12}(\text{H}_2\text{O})_6]\text{Br}_2$). With the change of the color of the Ta_6 octahedral cluster in different dispersing medium, the expectation to fabricate the thin and green film has been demonstrated.

➤ The color of the Ta_6 film depends on the stability of the Ta_6 octahedral cluster in the dispersing medium, for example, the green color exhibits the existence of the $\{\text{Ta}_6\text{Br}_{12}\}^{2+}$ core cluster

species meanwhile the brown color exhibits the existence of the $\{\text{Ta}_6\text{Br}_{12}\}^{3+/4+}$ core cluster. Some fundamental experiments were carried out to determine the optimal processing parameters, which were essential to control the color of the the Ta_6 octahedral cluster film. The green-colored film containing the $\{\text{Ta}_6\text{Br}_{12}\}^{2+}$ core cluster species was more interesting due to strong oxidation-reduction property.

➤ By the EPD process, the green-colored film based on the $\{\text{Ta}_6\text{Br}_{12}\}^{2+}$ core species was successfully fabricated, however, the stability of the oxidation state and transmittance of the Ta_6 octahedral cluster film were limited. To eliminate the problem, poly vinyl pyrrolidone (PVP) was used to improve the dispersion of the Ta_6 octahedral cluster in the EPD suspension with reducing the crystal size and prevent the interaction with the oxygen in air of the Ta_6 octahedral cluster in the network film. As the result, thin and high transmittance Ta_6 octahedral cluster film with emeral-green color exhibiting the strong UV absorption under 400 nm was successfully fabricated.

The results of the thesis contribute to demonstrate the advantages of the EPD technique to fabricate the metal cluster-based nanoparticle film. In the first time, the mechanism of the deposition of the metal cluster nanoparticles on the ITO-coated glass have been illustrated, which opens a series of new study to fabricate the different metal atom nanocluster film.

6.2. Outlooks

The works have firstly obtained some positive results for the fabrication of the pure Mo_6 and Ta_6 octahedral cluster films with thin, homogeneous microstructure and transmittance exhibiting the excellent absorption in the UV range. The successful fabrication of the cluster films by the EPD process at the laboratory level would open a new chance to apply at the industrial scale with many prominent advantages. Using small concentration of the cluster compared with dip coating, the preparation of thin and transparent cluster film on the glass with high efficiency and good optical property have been demonstrated: it will be a promising technology to reduce the cost of the production. Therefore, the expectation to improve the optical and mechanical properties of the Mo_6 and Ta_6 octahedral cluster films should be carried out in the application. The excellent optical property of the Mo_6 and Ta_6 octahedral cluster could be a potential UV-blocking material for the building application. However, to confirm the applicable possibility of the Mo_6 and Ta_6 octahedral cluster, some of the experiments still remain as the future work:

- i) Clarification of the mechanisms of the fabrication of the Ta_6 octahedral cluster film by EPD process
- ii) Modification of the Mo_6 cluster@silica surface for the luminescent application in biotechnology.
- iii) Investigation of the electrical conducting property of the Mo_6 octahedral cluster film prepared by the EPD process.
- iv) Incorporate the metal cluster with layer double hydroxide (LDH) by directly polymerization for photocatalyst.

In summary, the results of thesis effectively modify the knowledges relating to the characteristics of the optical nanoarchitecture materials based on the octahedral metal atom cluster or the processable techniques to extend the energy saving application for the building.

Achievements

Publications

1. Fabrication of Transparent Thin Film of Octahedral Molybdenum Metal Clusters by Electrophoretic Deposition

T. K. N. Nguyen, F. Grasset, B. Dierre, C. Matsunaga, S. Cordier, P. Lemoine, N. Ohashi and T. Uchikoshi. ECS J. Solid State Sci. and Tech., 5, 178-186, 2016.

Based on results of chapter 2.

2. Formation Mechanism of Transparent Mo₆ Metal Atom Cluster Film Prepared by Electrophoretic Deposition

T. K. N. Nguyen, B. Dierre, F. Grasset, A. Renaud, S. Cordier, P. Lemoine, N. Ohashi, and T. Uchikoshi, J. The Electrochemical Soc., 164, 412-418, 2017.

Based on the results of chapter 2

3. Electrophoretic Coating of Octahedral Molybdenum Metal Clusters for UV/NIR Light Screening

T. K. N. Nguyen, B. Dierre, F. Grasset, N. Dumait, S. Cordier, P. Lemoine, A. Renaud, H. Fudouzi, N. Ohashi and T. Uchikoshi, Coatings, 7, 114-127, 2017.

Based on the results of chapter 3

4. New ultra-violet and near-infrared blocking filters for energy saving applications: fabrication of tantalum metal atom cluster-based nanocomposite thin films by electrophoretic deposition

T. K. N. Nguyen, A. Renaud, M. Wilmet, N. Dumait, S. Paofai, B. Dierre, W. Chen, N. Ohashi, S. Cordier, F. Grasset and T. Uchikoshi, J. Mater. Chem. C, 5, 10477-10484, 2017

Based on the results of chapter 5

5. Visible tunable lighting system based on polymercomposites embedding ZnO and metallic clusters: from colloids to thin films.

T. G. Truong, B. Dierre, F. Grasset, N. Saito, N. Saito, T. K. N. Nguyen, K. Takahashi, T. Uchikoshi, M. Amela-Cortes, Y. Molard, S. Cordier and N. Ohashi, Sci. Tech. Adv. Mater., 17, 443–453, 2016.

6. Electrophoretic deposition for obtaining dense lanthanum silicate oxyapatite (LSO)

G. Suarez, T. K. N. Nguyen, N. M. Rendtorff, Y. Sakka, T. Uchikoshi, Cer. Inter., 42, 1619283-19288, 2016.

7. Observation of stacking faults and photoluminescence of laurate ion intercalated Zn/Al layered double hydroxide.

K. Harada, T. K. N. Nguyen, Y. Matsui, K. Fujii, F. Grasset, N. Ohashi, M. Matsuda, T. Uchikoshi, Mater. Letters, <https://doi.org/10.1016/j.matlet.2017.11.054>, 2017.

8. Preparation of Double-shelled Fluorescent Silicon Nanocrystals and Fabrication of Its Thin Layer by Electrophoretic Deposition Process

N. Shirahata, T. Uchikoshi, T. K. N. Nguyen and Y. Sakka, J. Jap. Soc. Powder and Powder Metallurgy, 65 (2), 2018 (Accepted).

Presentations at international Conferences:

- 1. The 9th International conference on the Science and Technology for Advanced Ceramics (STAC-9), Tsukuba, 2015, Japan.** Electrophoretic Deposition of $[\text{Mo}_6\text{Br}_{14}]^{2-}$ Nano Clusters. T. K. N. Nguyen, F. Grasset, B. Dierre, S. Cordier, P. Lemoine, N. Ohashi and T. Uchikoshi (poster).
- 2. The 32nd International Japan-Korea Seminar on Ceramics, Nagaoka, 2015, Japan** Fabrication the thin film based on $[\text{Mo}_6\text{Br}_{14}]^{2-}$ Nano Clusters by Electrophoretic Deposition, T. K. N. Nguyen, F. Grasset, B. Dierre, S. Cordier, P. Lemoine, N. Ohashi and T. Uchikoshi (poster)
- 3. The 15th international Conference on Advanced Materials, Kyoto, 2017, Japan.** Octahedral Metal Cluster Film for UV/NIR Light Screening. T. K. N. Nguyen, A. Renaud, B. Dierre, F. Grasset, S. Cordier, P. Lemoine, H. Fudouzi, N. Ohashi and T. Uchikoshi
- 4. Engineering Conference International: Electrophoretic Deposition IV, Gyeongju, 2017, Korea,** Fabrication of Octahedral Tantalum Cluster Film by Electrophoretic Deposition. T. K. N. Nguyen, Adele Renaud, Maxence Wilmet, Benjamin Dierre, Stephane Cordier, Naoki Ohashi, Fabien Grasset, Tetsuo Uchikoshi. (poster)

Presentations at domestic conferences:

- 1. The 54th Symposium on Basic Science of Ceramics, Saga, 2016, Japan.** Characterization of Molybdenum Metal Cluster Thin Film Fabricated by Electrophoretic Deposition, T. K. N. Nguyen, F. Grasset, B. Dierre, S. Cordier, P. Lemoine, N. Ohashi, T. Uchikoshi (oral)
- 2. 26th Annual Meeting of the Materials Research Society of Japan, Yokohama, 2016, Japan.** Fabrication and Characterization of Luminescent Nanoparticles Composed of Octahedral Molybdenum Cluster and Hollow Silica. T. K. N. Nguyen, B. Bouteille, F. Grasset, S. Cordier, P. Lemoine, N. Ohashi and T. Uchikoshi (oral).
- 3. The 55th Symposium on Basic Science of Ceramics, Okayama, 2017, Japan.** Luminescent hollow silica nanoparticle containing molybdenum octahedral cluster. T. K. N. Nguyen, B. Bouteille, F. Grasset, S. Cordier, P. Lemoine, N. Ohashi and T. Uchikoshi (oral).
- 4. The Ceramic Society of Japan The 30th Fall Meeting, Kobe, 2017, Japan.** Electrophoretic Deposition of Octahedral Molybdenum Metal Clusters. T. K. N. Nguyen, F. Grasset and B. Dierre, S. Cordier and P. Lemoine, N. Ohashi and T. Uchikoshi (poster).
- 5. The 56th Symposium on Basic Science of Ceramics, Tsukuba, 2018, Japan.** Electrophoretic Deposition of Octahedral Tantalum Cluster Film for the UV-NIR blocker. T. K. N. Nguyen, A. Renaud, M. Wilmet, B. Dierre, S. Cordier, N. Ohashi, F. Grasset, T. Uchikoshi (oral).

Award

Best Poster Presentation – First place

JECS Trust Sponsored award, Electrophoretic Deposition VI: Fundamentals and Applications, October, 2017, Gyeongju, South Korea.

Grant

Study abroad grant for foreign students, grant from CNRS funding and Rennes Metropole hosted by University of Rennes 1, France, 2016/09 – 2016/11 (3 months).